UNIVERSIDAD POLITÉCNICA DE MADRID

ESCUELA TÉCNICA SUPERIOR
DE INGENIEROS DE TELECOMUNICACIÓN

TESIS DOCTORAL

RESEARCH ON INTERMEDIATE BAND SOLAR CELLS AND DEVELOPMENT OF EXPERIMENTAL TECHNIQUES FOR THEIR CHARACTERIZATION UNDER CONCENTRATED ILLUMINATION

Pablo García-Linares Fontes
Ingeniero de Telecomunicación
2012

UNIVERSIDAD POLITÉCNICA DE MADRID

Instituto de Energía Solar

Departamento de Electrónica Física

Escuela Técnica Superior de Ingenieros de Telecomunicación

TESIS DOCTORAL

RESEARCH ON INTERMEDIATE BAND SOLAR CELLS AND DEVELOPMENT OF EXPERIMENTAL TECHNIQUES FOR THEIR CHARACTERIZATION UNDER CONCENTRATED ILLUMINATION

AUTOR: **Pablo García-Linares Fontes**
Ingeniero de Telecomunicación
DIRECTOR: **Antonio Martí Vega**
Doctor en Ciencias Físicas

2012

Tribunal nombrado por el Magfco. Y Excmo. Sr. Rector de la Universidad Politécnica de Madrid.

PRESIDENTE:

VOCALES:

SECRETARIO:

SUPLENTES:

Realizado el acto de defensa y lectura de la Tesis en Madrid,
el día ___ de _____ de 201__.

Calificación:

EL PRESIDENTE LOS VOCALES

EL SECRETARIO

Abstract

This work is a contribution to the research and development of the intermediate band solar cell (IBSC), a high efficiency photovoltaic concept that features the advantages of both low and high bandgap solar cells. The resemblance with a low bandgap solar cell comes from the fact that the IBSC hosts an electronic energy band -the intermediate band (IB)- within the semiconductor bandgap. This IB allows the collection of sub-bandgap energy photons by means of two-step photon absorption processes, from the valence band (VB) to the IB and from there to the conduction band (CB). The exploitation of these low energy photons implies a more efficient use of the solar spectrum. The resemblance of the IBSC with a high bandgap solar cell is related to the preservation of the voltage: the open-circuit voltage (V_{OC}) of an IBSC is not limited by any of the sub-bandgaps (involving the IB), but only by the fundamental bandgap (defined from the VB to the CB).

Nevertheless, the presence of the IB allows new paths for electronic recombination and the performance of the IBSC is degraded at 1 sun operation conditions. A theoretical argument is presented regarding the need for the use of concentrated illumination in order to circumvent the degradation of the voltage derived from the increase in the recombination. This theory is supported by the experimental verification carried out with our novel characterization technique consisting of the acquisition of photogenerated current (I_L)-V_{OC} pairs under low temperature and concentrated light. Besides, at this stage of the IBSC research, several new IB materials are being engineered and our novel characterization tool can be very useful to provide feedback on their capability to perform as real IBSCs, verifying or disregarding the fulfillment of the "voltage preservation" principle.

An analytical model has also been developed to assess the potential of quantum-dot (QD)-IBSCs. It is based on the calculation of band alignment of III-V alloyed heterojunctions, the estimation of the confined energy levels in a QD and the calculation of the detailed balance efficiency. Several potentially useful QD materials have been identified, such as $InAs/Al_xGa_{1-x}As$, $InAs/Ga_xIn_{1-x}P$, $InAs_{1-y}N_y/AlAs_xSb_{1-x}$ or $InAs_{1-z}N_z/Al_x[Ga_yIn_{1-y}]_{1-x}P$.

Finally, a model for the analysis of the series resistance of a concentrator solar cell has also been developed to design and fabricate IBSCs adapted to 1,000 suns.

Resumen

Este trabajo contribuye a la investigación y al desarrollo de la célula solar de banda intermedia (IBSC), un concepto fotovoltaico de alta eficiencia que aúna las ventajas de una célula solar de bajo y de alto gap. La IBSC se parece a una célula solar de bajo gap (o banda prohibida) en que la IBSC alberga una banda de energía -la banda intermedia (IB)- en el seno de la banda prohibida. Esta IB permite colectar fotones de energía inferior a la banda prohibida por medio de procesos de absorción de fotones en dos pasos, de la banda de valencia (VB) a la IB y de allí a la banda de conducción (CB). El aprovechamiento de estos fotones de baja energía conlleva un empleo más eficiente del espectro solar. La semejanza antre la IBSC y una célula solar de alto gap está relacionada con la preservación del voltaje: la tensión de circuito abierto (V_{OC}) de una IBSC no está limitada por ninguna de las fracciones en las que la IB divide a la banda prohibida, sino que está únicamente limitada por el ancho de banda fundamental del semiconductor (definido entre VB y CB).

No obstante, la presencia de la IB posibilita nuevos caminos de recombinación electrónica, lo cual degrada el rendimiento de la IBSC a 1 sol. Este trabajo argumenta de forma teórica la necesidad de emplear luz concentrada para evitar compensar el aumento de la recombinación de la IBSC y evitar la degradación del voltage. Lo anterior se ha verificado experimentalmente por medio de nuestra novedosa técnica de caracterización consistente en la adquisiciń de pares de corriente fotogenerada (I_{L})-V_{OC} en concentración y a baja temperatura. En esta etapa de la investigación, se están desarrollando nuevos materiales de IB y nuestra herramienta de caracterizaciń está siendo empleada para realimentar el proceso de fabricación, comprobando si los materiales tienen capacidad para operar como verdaderas IBSCs por medio de la verificación del principio de preservación del voltaje.

También se ha desarrollado un modelo analítico para evaluar el potencial de IBSCs de puntos cuánticos. Dicho modelo está basado en el cálculo del alineamiento de bandas de energía en heterouniones de aleaciones de materiales III-V, en la estimación de la energía de los niveles confinados en un QD y en el cálculo de la eficiencia de balance detallado. Este modelo ha permitido identificar varios materiales de QDs potencialmente útiles como $\mathrm{InAs/Al_xGa_{1-x}As}$, $\mathrm{InAs/Ga_xIn_{1-x}P}$, $\mathrm{InAs_{1-y}N_y/AlAs_xSb_{1-x}}$ ó $\mathrm{InAs_{1-z}N_z/Al_x[Ga_yIn_{1-y}]_{1-x}P}$.

Finalmente, también se ha desarrollado un modelado teórico para el análisis de la resistencia serie de una célula solar de concentración. Gracias a dicho modelo se han diseñado y fabricado IBSCs adaptadas a 1.000 soles.

Contents

List of Figures

List of Tables

List of acronyms

PV photovoltaics

IB intermediate band

IBSC intermediate band solar cell

BOS balance-of-system

QD quantum dot

CPV concentrating photovoltaics

PR photoreflectance

PL photoluminescence

XRD X-ray diffraction

FTIR Fourier transform infrared spectroscopy

CB conduction band

VB valence band

AM1.5D Air Mass 1.5 Direct

LED light-emitting diode

PCB printed circuit board

DAQ data acquisition system

PCI peripheral component interconect

PC personal computer

BNC Bayonet Neill-Concelman

TTL transistor-transistor logic

IES-UPM Insituto de Energía Solar-Universidad Politécnica de Madrid

NRR non-radiative recombination

DOS density of states

QFL quasi-Fermi level

QWRs quantum wires

QWs quantum wells

S-K Stranski-Krastanov

WL wetting layer

DenQuIBand High density quantum dot arrays for intermediate band solar cells

RCAST Research Center for Advance Science and Technology

UPM Universidad Politécnica de Madrid

MBE molecular beam epitaxy

MOCVD metal organic chemical vapor deposition

IR infrared

SRL strain relief layer

ML monolayer

AFM atomic-force microscopy

TEM transmission electron microscopy

CBO conduction band offset

VBO valence band offset

SRH Shockley-Read-Hall

BAC band anticrossing model

QE quantum efficiency

ARC anti-reflective coating

BSF back surface field

FF fill factor

EL electroluminescence

IMM-CSIC Instituto de Microelectrónica de Madrid-Consejo Superior de Investigaciones Científicas

SEM scanning electron microscope

RTA rapid thermal annealing

S-Q Shockley-Queisser

CIS $CuInS_2$ chalcopyrite solar cell

CGS $CuGaS_2$ chalcopyrite solar cell

IBPOWER IB materials and solar cells for PV with high efficiency and reduced cost

HIT heterojunction with intrinsic thin layer

SIMS secondary ion mass spectrometry

HEBAM heterojunction energy band alignment model

BP bowing parameter

DL deep level

BEP beam equvalent pressure

TF thin-film

List of symbols

I	current, A
V	voltage, V
V_{OC}	open-circuit voltage, V
E_{G}	energy of the fundamental bandgap, eV
T	temperature, K
η	efficiency, dimensionless
E_{H}	largest sub-bandgap of an IBSC, eV
E_{L}	smallest sub-bandgap of an IBSC, eV
I_{SC}	short-circuit current, A
I_{L}	photogenerated current, A
q	electron charge, C
r_{S}	series resistance, $\Omega\mathrm{cm}^2$
m	ideality factor, dimensionless
k	Boltzmann constant, $8.617\,10^{-5}\mathrm{eV\,K^{-1}}$
r_{P}	parallel resistance, $\Omega\mathrm{cm}^2$
$I_{0\mathrm{RS}}$	saturation dark current calculated with the Roosbroeck-Shockley formula, $\mathrm{A\,cm^{-2}}$
h	Planck constant, $4.135\ 10^{-15}$ eV s
c	speed of light, $\mathrm{m\,s^{-1}}$
F_{CV}	coefficient of $I_{0\mathrm{RS,CV}}$ in the multiple-level model, dimensionless
$I_{0\mathrm{RS,CV}}$	Roosbroeck-Shockley saturation dark current between CB and VB, $\mathrm{A\,cm^{-2}}$
$F2$	coefficient of $\sqrt{I_{0\mathrm{RS,CV}}}$ in the multiple-level model, dimensionless
F_{Vi}	coefficient of $I_{0\mathrm{RS,Vi}}$ in the multiple-level model, dimensionless
F_{Ci}	coefficient of $I_{0\mathrm{RS,Ci}}$ in the multiple-level model, dimensionless

$I_{0\mathrm{RS,Vi}}$	Roosbroeck-Shockley saturation dark current between each of the E_{ti} levels and the VB, $\mathrm{A\,cm^{-2}}$
$I_{0\mathrm{RS,Ci}}$	Roosbroeck-Shockley saturation dark current between the CB and each of the E_{ti} levels, $\mathrm{A\,cm^{-2}}$
$I_{0\mathrm{RS,VT}}$	sum of the Roosbroeck-Shockley saturation dark currents between each of the E_{ti} levels and the VB, $\mathrm{A\,cm^{-2}}$
F_{VT}	coefficient of $I_{0\mathrm{RS,VT}}$ in the multiple-level model, dimensionless
$I_{0\mathrm{RS,CT}}$	sum of the Roosbroeck-Shockley saturation dark currents between the CB and each of the E_{ti} levels, $\mathrm{A\,cm^{-2}}$
F_{Ci}	coefficient of $I_{0\mathrm{RS,Ci}}$ in the multiple-level model, dimensionless
α_{V}	α Varshni parameter, meV/K
β_{V}	β Varshni parameter, meV/K
Δ_{so}	spin orbit splitting, eV
$E_{\mathrm{v,av}}$	average of three uppermost VB at k=Γ, eV
T_{ij}/D	ternary/quaternary bowing parameters,
a_{v}	VB deformation potential, eV
a_{c}	CB deformation potential, eV
c_{11}, c_{12}, c_{44}	elastic constants, GPa
b	shear deformation potential, eV
E_{P}	interband matrix element (Kane energy), eV
F	Kane parameter, dimensionless
E_{t}^{*}	transversal effective mass, dimensionless
E_{l}^{*}	longitudinal effective mass, dimensionless
γ_1, γ_2	Luttinger parameters, dimensionless
m_{hh}^{*}	heavy-hole effective mass, dimensionless
m_{lh}^{*}	light-hole effective mass, dimensionless
h_1 and h_2	thicknesses of two contiguous layers, nm
r	radius of the quantum sphere (QD), nm
a_{lc}	lattice constant, $\mathring{A}$
h_{c}	critical thickness, ML
$\underline{\epsilon}$	strain tensor, m
$\underline{\sigma}$	stress tensor, $\mathrm{N\,m^{-2}}$
$\epsilon_{\parallel,i}$	epitaxial strain, dimensionless (m/m)

$C_{\mathrm{nm},i}$	elastic constants, Pa
E^{N}	energy of the isoelectronic impurity, eV
V_{int}	interaction potential (BAC model), eV
m_{e}^{*}	electron effective mass, dimensionless
J_0	reverse saturation current density, $\mathrm{Acm^{-2}}$
β	current gain, dimensionless
n_{n}	n-type electron doping concentration, $\mathrm{cm^{-3}}$
p_{p}	p-type hole doping concentration, $\mathrm{cm^{-3}}$
X	concentration factor, suns
ρ	resistivity, Ωcm
r_{B}	base series resistance, $\Omega\mathrm{cm}^2$
r_{subs}	substrate series resistance, $\Omega\mathrm{cm}^2$
r_{E}	emitter series resistance, $\Omega\mathrm{cm}^2$
r_{M}	metallization series resistance, $\Omega\mathrm{cm}^2$
$r_{\mathrm{m\text{-}s}}$	metal-semiconductor series resistance, $\Omega\mathrm{cm}^2$
f_{s}	shadowing factor, dimensionless
R_{c}	specific contact resistance, $\Omega\mathrm{cm}^2$
μ	carrier mobility, $\mathrm{cm^2\,V^{-1}\,s^{-1}}$
T	temperature, K
c_{r}	compensation rate, dimensionless
I_{mpp}	current maximum power point, A
V_{mpp}	voltage maximum power point, V
E_{dir}	direct irradiance, $\mathrm{Wm^{-2}}$

Chapter 1

Introduction

The intermediate band solar cell (IBSC) concept has been proposed as a means to obtain high efficient solar cells [Luque and Martí, 1997b, Martí et al., 2003]. This Thesis aims to provide insights on the relevance of the use of concentrated light for the operation of IBSCs. There are two fundamental operation principles in IBSCs: 1) the generation of an extra current (I) by means of the exploitation of sub-bandgap photons in two-step absorption processes through the intermediate band (IB) and 2) the preservation of the output voltage (V) of the cell, i.e. the open-circuit voltage (V_{OC}) of the IBSC is exclusively limited by its fundamental bandgap, E_{G} and not by any of the IB delimited gaps. This Thesis mainly deals with the second of the two aforementioned pillars of this high-efficiency photovoltaic concept, i.e. the preservation of the voltage and its implications regarding the use of concentrated light.

In this work, a theoretical analysis of the recombination in an IBSC is developed, which ultimately prescribes the use of concentrated light in order to recover the initially degraded open-circuit voltage (V_{OC}) of an IBSC operating at 1 sun. Experimental evidence confirming this voltage recovery in IBSCs fabricated with quantum dots (QDs) is then presented. The need for low temperature (T) operation linked to the IBSC technology available to date is also addressed. The experimental work is completed with an extensive review of a number of IBSC technologies of different nature (others than InAs/GaAs QDs) that have been fabricated in collaboration with other research groups in the context of the research projects in which the Silicon and Fundamental Studies Group at Insituto de Energía Solar-Universidad Politécnica de Madrid (IES-UPM) has been involved.

1.1 Research on novel concepts in PV

There are several reasons that justify the need for a fast development of photovoltaics (PV). Reducing gas emissions to the atmosphere is the most widespread but not the only one. The national self-control of the energy resources aimed to the production of electricity is also important and directly related to the reduction of tensions among countries. Furthermore, the availability of the fuel of the energy source (the sun) is infinite in terms of a human timescale and the amount and distribution of energy reaching each country on Earth is, in most of the cases, several orders of magnitude larger than their national energy consumption.

The use of solar energy for the production of electricity is inherently and fundamentally inefficient because it is very diluted compared to other sources of energy. This causes the exploitation of the sun as a direct source of energy for cheap electricity production to be very challenging.

Once the importance of the solar energy as a massive source of electricity for both the near and long term future has been stated, the perspectives for its development and integration into the current electricity production system have to be considered. The goal of high grid penetration can only be achieved if the overall cost associated to the energy produced by a PV power plant is reduced so that this electricity source becomes cost competitive with respect to the other sources in the system.

There are two ways of reducing the cost of PV: 1) reducing the solar cell manufacturing cost and/or 2) boosting the solar cell efficiency (η), which implies PV concepts with a high efficiency ceiling. Both strategies cannot be compared under the same standards. The cost associated to the PV module is expected to be approximately half of the price of the whole PV power plant with the balance-of-system (BOS) accounting for the other half. The cost of the solar cell, at least for current Si flat panels, approximately represents 60% of the PV module cost [del Cañizo et al., 2009]. This implies that any strategy for the reduction of the manufacturing cost of the cell affects only approximately 30% of the overall cost, while the strategy for the increase of the efficiency affects the entire cost of the investment. This last statement is explained by the fact that the marginal cost of operation and maintenance can be neglected in conventional PV and therefore, the generation cost of solar electricity ultimately depends on the electricity produced and thus, on the efficiency.

According to the predictive model presented in Ref. [Luque, 2001], only a breakthrough in PV can modify the relatively slow growth of PV so that the associated learning curve promotes a sufficiently fast development. Concentrating photovoltaics (CPV) will likely be the raison d'être of the novel concepts oriented to very high efficiency. The reason

is that the CPV strategy dramatically reduces the amount of semiconductor material required [Swanson, 2003] and therefore, the use of these novel concept technologies under concentrated light enables much more expensive (complex and efficient) devices. Besides, the higher the efficiency of a PV module, the smaller the area required for the power generation plant, with the subsequent reduction in the BOS cost, resulting in a lower turn-key price of the system. All of the previous supports the research in PV new concepts.

1.2 The intermediate band solar cell

1.2.1 Review of the concept

One of the paths leading to a possible PV breakthrough is the IBSC concept, with a limiting efficiency as high as 63.2% [Luque and Martí, 1997b] to be compared to the 40.7% maximum efficiency of a conventional solar cell [Araújo and Martí, 1994, Shockley and Queisser, 1961]. The IBSC is based on the so-called IB materials, which can be regarded as a new type of materials engineered so that an energy band or a collection of energy levels are inserted within the semiconductor bandgap. IB materials are capable of absorbing sub-bandgap photons, which otherwise would be useless for PV conversion.

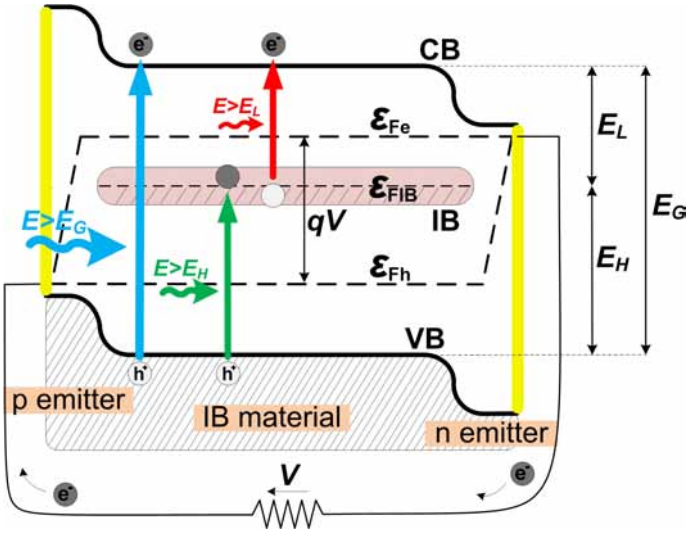

Figure 1.1: Band diagram of an IBSC where the quasi-Fermi levels (QFLs) associated to each of the bands (VB, IB, and CB) are represented together with their corresponding transitions and bandgap distribution.

These low-energy photons are collected via two-step electronic transitions through the IB, thus enabling the pumping of an extra electron flux to the conduction band (CB). This mechanism is sketched in Fig. 1.1. The first step of the sub-bandgap transition of the IBSC is depicted by a green arrow in the figure and represents the pumping from the valence band (VB) VB to the IB, through the bandgap E_{H}. The second of the sub-bandgap

steps is denoted by a red arrow and represents the electron pumping from the IB to the CB (through the bandgap defined as E_{L}). The conventional transition from the VB to the CB is represented by a blue arrow (and takes place through E_{G}). The choice of the location of the IB closer to the CB and therefore in the upper half of the host material bandgap has been arbitrarily made in this example. In this respect, the IB concept is symmetric, i.e. E_{L} can be above E_{H} in the band diagram and vice versa.

The overall effect of this double absorption causes a larger portion of the solar spectrum to become useful for the extraction of carriers. At the same time, these photogenerated carriers must preserve their electrochemical potential. As a result, the IBSC has the potential to achieve a short-circuit current (I_{SC}) enhancement without a significant degradation of the V_{OC}. The latter occurs under the assumption that three electron gases coexist, each of them associated to each of the three bands: VB, IB and CB. Out of the equilibrium, these electron gases are identified by their own quasi-Fermi level (QFL) and they are respectively denoted as $\varepsilon_{\mathrm{Fh}}$, $\varepsilon_{\mathrm{FIB}}$ and $\varepsilon_{\mathrm{Fe}}$, in Fig. 1.1. The existence of three well defined and separated electronic populations associated to each band is on the basis of a V_{OC} not limited by any of the sub-bandgaps (E_{L} or E_{H}, in this case), but only limited by the host or barrier material bandgap, E_{G}.

Another important condition is the need for electric isolation of the IB from the contacts so that the electron and hole QFL split does not collapse at these contacts [Luque and Martí, 2001, Luque et al., 2000]. This isolation is achieved by inserting two conventional semiconductors, called emitters, on both sides of the IB material. When this configuration is not implemented, no QFL separation can be achieved between $\varepsilon_{\mathrm{FIB}}$ and $\varepsilon_{\mathrm{Fe}}$ or $\varepsilon_{\mathrm{Fh}}$ and the voltage cannot be preserved, thus limiting the efficiency ceiling to that of a single gap solar cell.

1.2.1.1 Photon selectivity and photon recycling

The absorption coefficient determines the probability of an optical transition to occur as a function of the photon energy. In an IBSC, three of them are identified for each transition: α_{CV}, α_{IV} and α_{CI} (respectively corresponding to transitions VB→CB, VB→IB) and IB→CB.

In the general case of an IBSC, a photon of the appropriate energy could be absorbed producing an electronic transition between any of the three bands. However, as stated in the original reference [Luque and Martí, 1997b], the absorption coefficient profiles have to be spectrally selective in any of the transitions for an optimized IBSC performance. In other words, no energy overlap is permitted between them, what implies that for maxi-

mum performance, an incident photon should exclusively pump an electron in one of the transitions, but not in the others.

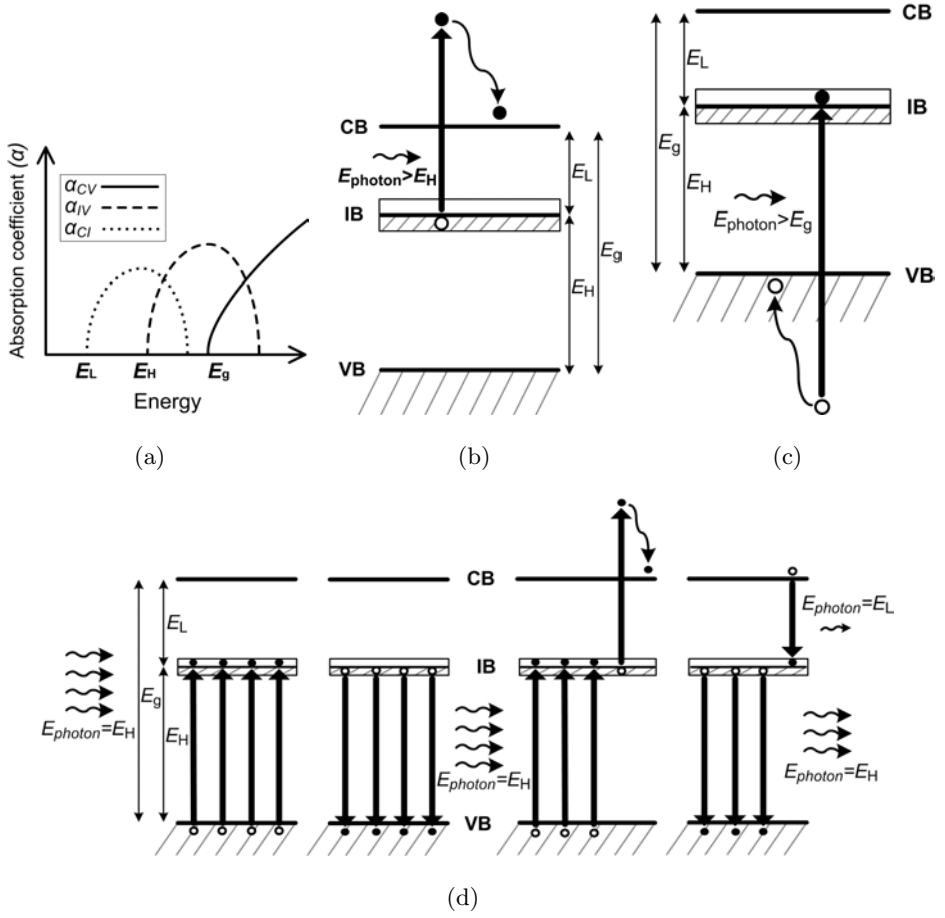

Figure 1.2: Different situations implying the absorption of a high energy photon in a low bandgap. The key point is that the absorption does not take place at the highest possible bandgap but at a lower one and therefore, the energy in excess above the bandgap is wasted. (a) Example of non-idealized absorption coefficients. (b) A photon with $E_{\text{photon}} > E_{\text{H}}$ produces an IB→CB transition. (c) A photon with $E_{\text{photon}} > E_{\text{G}}$ produces a VB→IB transition. (d) Example of process involving photon recycling and not optimum reabsorption.

The reason why this photon selectivity renders the maximum possible efficiency can be understood from Fig.1.2 [Linares et al., 2012a], where different cases of high energy photons being absorbed in low energy bandgaps are displayed. Fig. 1.2(a) sketches a qualitative absorption coefficient diagram where the different absorption functions overlap, i.e. their value is not zero in some of the energy ranges where the other functions are also defined. Fig. 1.2(b) exemplifies one of the cases in which the absorption of a high energy photon ($E_{\text{photon}} > E_{\text{H}}$) in a low energy transition (of only E_{L} eV) is associated with an energy loss mechanism. The excess of energy is wasted via the thermalization of the electron within the CB. Fig. 1.2(c) exemplifies another analogous case in which the loss

mechanism occurs for $E_{\text{photon}} > E_{\text{G}}$ and the production of a transition through E_{H} (and the subsequent thermalization of a hole in the VB). An IBSC efficiency degradation effect equivalent to those of the previous examples is shown in Fig. 1.2(d), where the overlap between absorption coefficients causes the energy loss throughout the photon recycling process [Cuadra et al., 2004, Linares et al., 2012a].

When taking into account the possibility of absorption coefficient overlap, one has to realize that the cell thickness (W) becomes a parameter to be optimized, even within the detailed balance realm. The reason for this dependence of the efficiency on the thickness is related to the loss mechanisms shown in Fig. 1.2(d). These losses are produced during the photon recycling processes and they are caused by the reabsorption of photons in a transition with an energy threshold lower than that in which it was created. Even though these recombination processes are of radiative nature, energy is lost in the thermalization process, thus degrading the cell efficiency. The optimum thickness of the cell will be the result of the trade-off between the absorptivity (a), typically given when a plain back reflector exists by [Cuadra et al., 2004]:

$$a(E) \sim 1 - exp[-(\alpha_{\text{CV}} + \alpha_{\text{IV}} + \alpha_{\text{CI}})\, 2\, W] \tag{1.1}$$

which increases as W increases, and the recombination, which depends on the bulk semiconductor volume (and therefore, also on W) and is caused by the inefficient photon recycling; therefore, it also increases when W increases.

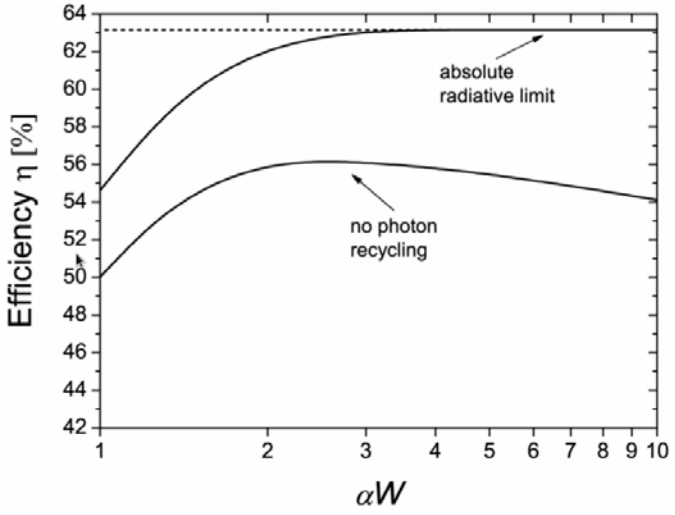

Figure 1.3: Efficiency versus cell thickness for two IBSC scenarios: with and without photon recycling. The model assumes an IBSC with optimum bandgaps, maximum concentration, and 6000K blackbody irradiance. Constant and non-overlapping absorption coefficients are considered in both cases. This figure has been reprinted from Ref. [Martí et al., 2008a]).

The photon recycling mechanism is important in radiatively dominated single gap solar cells as well as in IBSCs. The latter can be deduced from Fig. 1.3, where the efficiency of an IBSC of optimum bandgap is calculated for maximum concentration (46050 suns), constant and non overlapping absorption coefficients and the sun modeled as a blackbody at 6000K [Martí et al., 2008a]. The simulation is carried out for two different cases: an IBSC operating at the radiative limit and an IBSC in which no photon recycling takes place. Both calculations are represented with respect to the cell thickness. In the first case, the efficiency increases towards the 63.2% as the thickness increases, when all photons are absorbed ($\alpha W \gg 1$) and then remains constant for higher values. However, when photon recycling is not taken into account in the model (lower curve in Fig. 1.3), the efficiency initially increases, reaching a maximum at 56.1% and then decreases because of the increased radiative recombination without, however, recycling of photons.

However, when more than one absorption coefficient (corresponding to the different transition in the IBSC) are nonzero in the same energy range, a drop in the limit efficiency occurs even in a purely radiative case, e.g. at 1000 suns the efficiency decreases from 57% to 32%, when considering α_{CV}=α_{IV}=α_{CV}=4 10^4 cm^{-1} (value in the range of the GaAs absorption coefficient). But this harmful effect can be mitigated if the IBSC is engineered so that a large difference between each of the values of the absorption coefficients exists, i.e. $\alpha_{\mathrm{CV}} \gg \alpha_{\mathrm{IV}}$ as well as $\alpha_{\mathrm{IV}} \gg \alpha_{\mathrm{CI}}$. This situation causes one absorption coefficient to dominate in each of the three energy ranges ($E_{\mathrm{L}} < E < E_{\mathrm{H}}$, $E_{\mathrm{H}} < E < E_{\mathrm{G}}$ and $E > E_{\mathrm{G}}$), approaching the non-overlapping condition. A problem derived from such scenario is associated to the weakness of the absorption related to the lowest absorption coefficient, which in turn implies a reduced IB→CB transition. A possible solution relies on the use of light trapping techniques, such as the texturing of the IBSC or the use of a cavity [Luque et al., 1991], which increases the optical path length inside the cell. Other light management techniques can be implemented through the use of metal nanoparticles. The effect of these particles has been calculated using the near-field approximation, which has rendered encouraging results for the amplification of the desired components of the light, which could be used to enhance the corresponding absorptions. This amplification is produced by plasmonic resonance and depends on the metal material and shape of the metal nanoparticles [Luque et al., 2008, Mendes et al., 2009]. On the other hand, micrometric patterned diffraction grids have also been postulated for their calculation under the far-field approximation as another possible strategy for light trapping applied to the IR range [Tobías et al., 2008, Mellor et al., 2011].

1.2.1.2 Partial filling of the IB

It must be noticed that an electron pumped from the VB to the IB does not necessary have to be the same one that is promoted to the CB by the absorption of the second low-energy photon from the IB to the CB. If this had to be the case, the associated probability of the process would be similar to that of a three-particle collision (involving two photons and one electron), which is much more unlikely than a process involving a regular photon absorption (two-particle collision). A steady state carrier population is then required in the IB in order to assist the second sub-bandgap transition. For the VB→IB transition to occur, the IB states cannot be completely occupied with electrons, otherwise there would not be room for any other electron to be pumped from the VB and the associated probability would be zero. For the fulfillment of both IB population constrains, the IB has to be partially filled [Luque and Martí, 2001].

There are several ways to achieve such partial occupation condition. The IBSC may be engineered so that the IB is naturally partially filled at room temperature. However, if empty or completely filled it may be "artificially" doped to tune the desired IB filling level (in QD-IBSCs, this can be attained by modulation doping in the barrier as explained in Ref. [Martí et al., 2001]. Also, in steady state conditions, it could also be photofilled with the electrons from the first transition [Luque and Martí, 2010a, Strandberg and Worren, 2009], although this case only seems to be valid for very high concentrations.

If the photofilling strategy is not pursued, the QFL associated to the carrier population at the IB has to remain clamped at its equilibrium position, which depends on the density of states (DOS) of the IB. When the IB exhibits a high capture cross section for electrons in the CB (i.e. the IB is practically connected to the CB by means of a strong recombination), a low filling factor seems to improve the IBSC quantum efficiency (QE) profile [Martí et al., 2012]. However, the voltage and thus the efficiency will then be fundamentally limited by the IB→CB transition. The latter is simulated using the Generalized Shockley Read Hall model applied to the IBSC [Luque et al., 2006b] in the study of the influence of the filling factor [Luque and Martí, 2010a], where the effect of a pre-filled IB is discussed for different cases of QD-IBSCs.

All the models presented so far are analytical and may be improved in the future through the use of numerical-based models that solve the semiconductor equations that also account for the specific IB material physics [Tobías et al., 2011].

1.2.2 Detailed balance modeling

The detailed balance theory [Shockley and Queisser, 1961] analyzes the performance of a solar cell for the case of purely radiative recombination, disregarding any non-radiative recombination (NRR) mechanism. Therefore, it allows the study of the limiting efficiency of the solar cell as a function of the bandgap. The detailed balance can be applied to the computation of the limiting efficiency of new IB candidate materials, allowing the determination of the ideal bandgap distribution for any concentration factor, spectrum of incident light and cell temperature. In the case of the IBSC, this bandgap distribution is basically a function of the fundamental bandgap of the material and the energy of the IB with respect to the band edges (E_{L} and E_{H}), provided that the spectrum of the sun is known (usually assumed as that of a blackbody at T=6000 K).

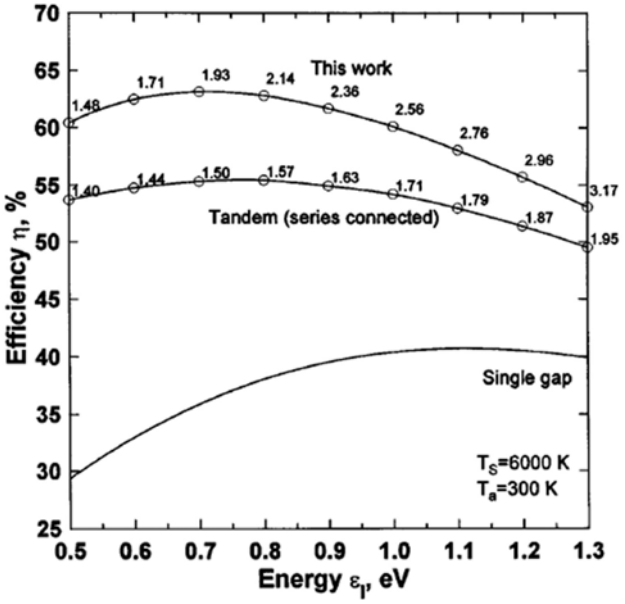

Figure 1.4: Detailed balance efficiency limit of the IBSC with respect to the minimum bandgap, E_{L} (denoted as ϵ_{l} in the figure), compared to that of a double-junction tandem solar cell and a conventional solar cell. The plot is reprinted from Fig. 2 in Ref. [Luque and Martí, 1997b].

Fig. 1.4 shows the detailed balance efficiency limit of an IBSC compared to a double junction tandem solar cell as a function of the lowest of the bandgaps involved in each structure (E_{L}) calculated for maximum concentration. The limiting efficiency of a single gap solar cell is also shown for comparison. This plot illustrates the high efficiency potential of the IBSC concept as well as the bandgap distribution that optimizes the efficiency in each case. Strandberg and Reenas [Strandberg and & Reenaas, 2010] have recalculated the IBSC limiting efficiency considering the possibility of using selective energy reflector filters. They have found out that this efficiency increases with respect to the original calculation

without filters for the case of operation at low concentrations. Another IBSC configuration with the potential for exceeding the previous 63.2% limit relies on the implementation of a tandem of two IBSCs [Antolín et al., 2006]. This IBSC tandem has a detailed balance limit efficiency of 73.2% when the cells are independently connected. When the cells are connected in series, the system exhibits a slightly lower efficiency limit of 72.7% [Antolín, 2010]. Regarding the number of bandgaps involved in the structure, each of the aforementioned IBSC tandem configurations is equivalent to a multiple-junction solar cell (MJSC) with six junctions, which respectively achieve 74.4% and 73.3% for the independently and series connected cases. When comparing both the tandem IBSC and the MJSC for the two-terminal case (monolithically grown), the obvious benefit derived from the use of the IB concept is the need for only one tunnel junction, instead of the five tunnel junctions that are required for a MJSC with six junctions. The problem, however, would still be the difficulty for engineering IBSCs endowed with such optimal configurations. In this respect, other works have identified the possibility of combining a single gap solar cell and an IBSC in a tandem configuration. This could be a more realistic device, with a sufficiently high limiting efficiency as to remain attractive compared to its equivalent 4-junction single gap solar cell [Antolín et al., 2010b]. An example of this tandem configuration could be based on a GaAs-based IBSC monolithically grown with a single gap AlGaAs-based top cell with a low Al content (<20%). This idea has a limiting efficiency above 64% and it is regarded as a specifically feasible configuration because: 1) the IBSC may be more easily achievable for the case of the well known GaAs technology; 2) the AlGaAs single gap solar cell seems to be a feasible technology when implemented with a low Al content; and 3) both cells are lattice-matched.

1.3 IB materials

So far, none of the existing semiconductors have proven to be endowed with the singular features required for a proper operation of an IBSC. This implies that a new generation of IB materials has to be engineered. For this reason an extensive research has recently begun on the identification of appropriate IB candidate materials. So far, most part of the research has been focused on two different families: the quantum dot (QD) IB approach and the bulk approach, which will be reviewed in the following sections. Nevertheless, other interesting configurations have been proposed, as for example the molecular approach [Ekins-Daukes and Schmidt, 2008] which are out of the scope of this work.

At the beginning of the IB research, the detailed balance model [Shockley and Queisser, 1961] was used to calculate the optimum bandgap distribution of an IBSC. Under maxi-

mum concentration (46050 suns at the surface of the Earth) and the irradiance distribution of a black-body at approximately 6000 K, the following values attain the theoretical 63.2% efficiency: E_H=1.24 eV, E_L=0.71 eV and E_G=1.95 eV [Luque and Martí, 1997b].

During the first years after the concept was released, more IB features were modeled, either to analyze the suitability of the different IB materials or the impact of non-idealizations regarding the practical implementation of the IBSC. In an initial stage the operating principles of the IBSC have to be tested, which requires the implementation of dedicated experimental set-ups in order to solidly assure the verification of such evidences, i.e. the production of sub-bandgap photocurrent and the preservation of the voltage.

1.3.1 State of the art of IB materials

Up to now, most practical attempts to manufacture an IBSC have been based on the introduction of nanostructured stacked layers into a III-V host material. In practice, these nanostructures have to be 0-dimensional in order to provide a true zero DOS between the IB and the CB and VB, ultimately allowing the existence and split of the corresponding QFL. Although the InAs/GaAs QD system does not satisfy the characteristics for optimal IBSC performance in terms of room temperature bandgaps, it is a relatively mature technology. On the other hand it is based on GaAs, which is an excellent semiconductor in terms of optical and electronic characteristics. These are two of the main reasons why this QD system has been selected as a prototype material to verify the fundamental principles of operation of the IBSC. Furthermore, MBE and metal organic chemical vapor deposition (MOCVD) technologies have proven to produce excellent crystalline results for this system [Bimberg et al., 1999]. The QD approach for the implementation of the IBSC will be extensively reviewed in section 5.

Besides QDs, the other large group of IB materials is the one based on bulk semiconductors. Several research lines have been proposed in this direction, which are, in most cases, based on the introduction of suitable impurity atoms. Different material systems containing impurities of the appropriate nature, located in the adequate locations in a periodic crystal have been theoretically investigated [Luque and Martí, 2010b, Luque et al., 2012b]. As we will review, a common condition for any of these impurities to form an IB is to be present in a sufficiently high concentration.

Deep-level (DL) impurities, i.e. atomic species that introduce an energy level inside the host material bandgap far from the band edges, traditionally referred to as traps or recombination centers, are considered "lifetime killers" in conventional semiconductors. Therefore, their use in high efficiency solar cells requires further justification. The answer to why impurities at high concentration inside the crystal might not increase the Shockley-

Read-Hall (SRH) recombination [Luque et al., 2006a] is related to the so-called lattice relaxation multiple phonon emission [Lang and Henry, 1975]. The latter is believed to be the main responsible mechanism for SRH recombination, since the simultaneous emission of several phonons is considered highly improbable in bulk semiconductors. The electron is de-excited from the CB to a DL trap, which implies a transition from a delocalized state to a localized one, causing an important swift movement of the charge, because it was initially distributed throughout many atoms and it is afterwards highly packed next to the impurity atom. Then, the atom vibrates violently (in real space) in a mode other than the usual lattice phonons, the so-called breathing mode. This violent vibration is then attenuated through the successive emission of phonons produced by conventional electron-phonon interaction. Therefore, if the impurities giving rise to the IB are present within the bulk material in a sufficiently high concentration as to produce the overlapping of their wavefunctions, the recombination through these intermediate states takes place between delocalized states, which can "share" or dilute the charge increase along the lattice. This distributed charge transfer process between states can inhibit the production of breathing modes as well as the corresponding lattice relaxation by multiple phonon emission. As a result, the SRH recombination is also inhibited.

The idea of using DLs to study the possibility of sub-bandgap photon absorption comes from the 60's. Wolf introduced the concept of multitransition solar cell in 1960 with the purpose of improving the solar cell performance [Wolf, 1960] and a year later, based on Wolf proposals, Grimmeiss manufactured and tested a DL impurity-based solar cell with negative results [Grimmeiss and Koelmans, 1961]. This is not surprising because both the theoretical proposal and the experimental implementation paid no attention, for example, to the need for selective contacts, i.e. they did not identified the need for non-DL-doped portions of semiconductor separating the IB material from the metal contact. Also, in the proposals by Wolf, there was no explicit mention to the need for a high enough impurity concentration as to enable the formation of a band with the aforementioned NRR blockade. Thanks to the IBSC theory, we now know that because of the previous considerations were not taken into account, the voltage of the DL solar cell proposed by Wolf and implemented by Grimmeiss was fundamentally limited. The efficiency ceiling of such configuration was, in the best case, the one of a low bandgap conventional solar cell.

DLs introduced by impurities of any kind can be considered as an option for bulk IB materials if they are located at an appropriate energy and they can be half filled with electrons at room temperature. Actually, even DLs associated to a vacant or an interstitial atom might also lead to adequate configurations.

The first stage after the IBSC concept was first presented in 1997 dealt with theoretical analysis of possible IB candidate materials. In this respect, some bulk materials doped with transition metal impurities were proposed, as for example, Ti-substituted GaAs or GaP [Wahnón and Tablero, 2002], as well as other substituting impurities such as Sc, V or Cr. An experimental research line has been proposed using an MBE reactor for the insertion of a high impurity concentration of Ti inside a GaAs matrix [Linares et al., 2013, Martí et al., 2009].

Another bulk-based IB candidate material is a well-known semiconductor for PV applications: silicon. In spite of its low limiting efficiency (according to the IBSC theory) because of its reduced bandgap, it can be used to test some of the principles of the IBSC theory that are related to the insertion of impurities. In this respect, high doses of Ti are implanted in the Si matrix by means of ion-implantation techniques combined with pulsed laser melting in order to recover the crystallinity of the implanted sample ([Olea et al., 2008, González-Díaz et al., 2009]). Some important conclusions, such as the verification of the lifetime recovery in highly Ti-doped silicon samples have been extracted from this work [Antolín et al., 2009].

IB solar cells based on thin-film-based materials, such as $CuInS_2$, $CuGaSe_2$ and $CuGaS_2$, which can also be doped with transition metals, such as Ti, V, Cr or Mn [Martí et al., 2008c, Palacios et al., 2007, Tablero and Fuertes Marrón, 2010] have also been proposed. This research line seems to be very encouraging since chalcopyrite structures can constitute an easy and versatile way to produce IB materials, i.e. the insertion of certain transition metal species seems realizable (in a sufficient concentration) from a thermodynamic point of view. An experimental line has also begun in this topic [Martí et al., 2009].

Another research line also based on the thin-film technology is being developed at the University of Michigan for the ZnTe material doped with oxygen [Weiming et al., 2009]. So far, it has rendered promising results, including the measurement of the absorption of two below bandgap energy photons.

In-thiospinels such as In_2S_3 including a high vanadium concentration have also been proposed. This last work allowed the recent implementation of the IB material by solvothermal synthesis, in which sub-bandgap absorption was measured [Lucena et al., 2008].

Recent works on bulk IB materials are based on the so-called highly mismatched materials [Yu et al., 2006], e.g. the GaNAsP alloy, which has also shown IB properties through photo-reflectance measurements. This kind of nitrogen dilute alloys is believed to experience the splitting of the CB because of the interaction between the nitrogen level and the CB of the non-nitrogen-doped host matrix (in this case, the GaAsP). In some cases, a real bandgap is created between the two split CBs as a result of this interaction and the

lower split CB is then regarded as the IB. The mechanism leading to this effect is known as band anticrossing [Shan et al., 1999].

InGaN-based alloys have also been presented as feasible IB material candidates [Martí et al., 2008c], since they present exceptionally high solubility ranges for some metal transition impurities (e.g. Mn) while the ternary alloy also covers a wide range of energy bandgaps.

1.4 The IBSC under concentrated illumination

The IBSC benefits from the advantages of both small bandgap and large bandgap solar cells. This means that the IBSC resembles a small bandgap solar cell from the current (I) point of view, in the sense that it is able to produce a relatively large photocurrent (because a wide portion of the solar spectrum is exploited). Nevertheless, it also resembles a large bandgap solar cell in terms of the output voltage (V) that it can provide (because the IBSC is only limited by the fundamental bandgap, E_{G} of the host semiconductor).

As regards of the first of the aforementioned statements (i.e. similarity between the IBSC and a low bandgap solar cell) the current enhancement of the IBSC is produced by the absorption of sub-bandgap photons that would otherwise be wasted in photovoltaic conversion. Conventionally, an increase of the photocurrent can be achieved by reducing the bandgap of a single gap solar cell, but this is accompanied by a reduction of the voltage. In contrast, the current increase in the IBSC can be achieved without degradation of the voltage [Luque and Martí, 2001, Martí et al., 2003]. For fundamental thermodynamic reasons [Luque and Martí, 1997a, Luque et al., 2002] this requires that two photons are used for the generation of a net electron-hole pair [Luque et al., 2003, Luque and Martí, 1997b].

Regarding the second statement (i.e. similarity with respect to the high bandgap solar cell), it has to be recalled that the V_{OC} of a solar cell is closely related to its carrier recombination. And the carrier recombination in an IBSC has often been regarded as being inherently larger than that of a single gap solar cell with the same fundamental bandgap because of the additional electronic de-excitation paths originating from the intermediate levels, even if these pathes are radiative. Increased recombination in a solar cell is associated with a drop in output voltage, which can be counteracted with the use of concentrated light [Linares et al., 2012b, Martí et al., 2008b]. This will be broadly discussed next.

1.4.1 The analysis of the recombination in an IBSC

1.4.1.1 The equivalent electrical circuit of an IBSC

Even in the ideal case, the recombination of the IBSC is larger than that of a single gap solar cell with the same total bandgap, and the reason is the presence of the IB, through which carriers can also recombine. Actually this recombination mechanism has to be necessarily allowed since it is the inverse mechanism of the photogeneration, which is necessary for the generation through the IB. On the other hand, the fabrication of the IBSC may introduce spurious extra confined levels (e.g. excited confined states in the case of the QD-IBSC), which are not regarded as useful in the photogeneration process (although the probability of such process is not zero), but contribute to the total recombination.

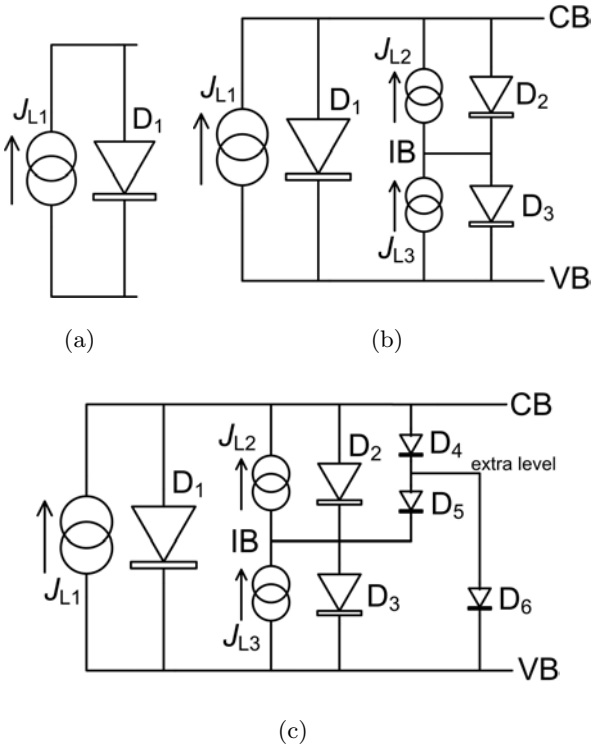

Figure 1.5: Equivalent circuits of different ideal solar cells: (a) Conventional solar cell. (b) IBSC with no overlap of the absorption coefficients. (c) IBSC with an extra level.

Fig. 1.5 has been conceived to help understand the generation/recombination process of the IBSC compared to those of the conventional solar cell. Subfigures in Fig. 1.5 represent the equivalent electrical circuit of different solar cells, in which the current generators represents the photogenerated current (I_{L}) and the diodes represent the recombination taking place between each pair of bands. Fig. 1.5(b) shows the equivalent electrical circuit of a conventional solar cell, where the generation/recombination process ideally occurs only

between the VB and CB. Fig. 1.5(b) shows the equivalent electrical circuit for the case of an ideal IBSC, where in addition to the VB↔CB transitions, the electronic transitions from/to the IB also take place: J_{L2} and D_2 accounts for the generation/recombination processes between the IB and CB and J_{L3} and D_3 accounts for the generation/recombination processes between the VB and IB. In this model and in the text, no overlap between the absorption coefficients has been considered. Ref. [Martí et al., 2006b] details a more elaborated model with an equivalent circuit that includes overlap. The last case, represented in Fig. 1.5(c) shows the equivalent electrical circuit of an IBSC with one extra level (besides the IB), which is a simplified version of the more realistic case of an IBSC where extra recombination centers appear, increasing the recombination of the cell.

1.4.1.2 Impact of the recombination on the V_{OC} and the effect of concentrated light

The effect of this increased recombination is specially evident at 1 sun illumination, where the IBSC, even under ideal operation conditions, is characterized by a V_{OC} which is severely degraded with respect to that of a single gap solar cell of the same bandgap. A detailed balance analysis will be used to simulate the electrical behavior of both the IBSC and the reference cell under the aforementioned ideal conditions. Under this realm, the solar cells operate at the radiative limit and their temperature is fixed to 300 K. The sun is treated as a black body at 6000 K.

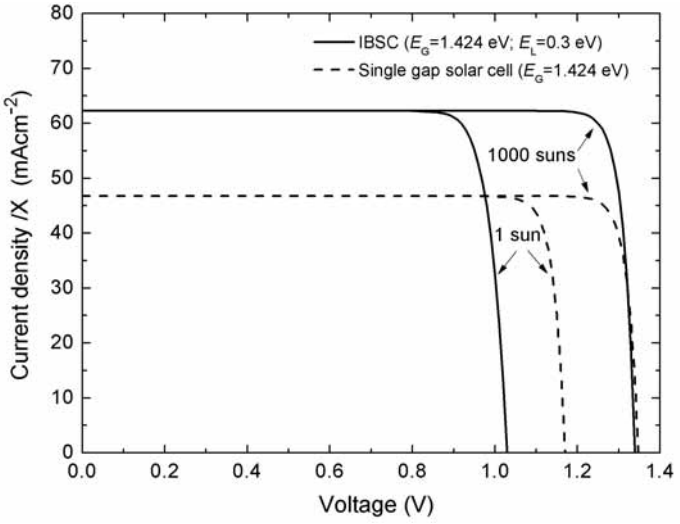

Figure 1.6: Detailed balance modeling of the 1 sun and 1,000 suns illumination J-V curves of an IBSC (E_G=1.424 eV and E_L=0.3 eV, thus representing an approximately ideal InAs/GaAs QD-IBSC) compared to an also ideal GaAs single gap solar cell (reference).

In this respect, Fig. 1.6 represents the J-V curves under 1 sun and 1,000 suns illumination conditions of an InAs/GaAs ideal QD-IBSC (E_{G}=1.424 eV and E_{L}=0.3 eV) and a GaAs reference solar cell of the same fundamental bandgap. In both illumination cases, the IBSC has a considerably larger J_{SC}, because it converts the photons from a larger portion of the spectrum. Nevertheless, the IBSC at 1 sun, has a remarkably reduced V_{OC} (approximately 150 mV lower) caused by the enhanced recombination with respect to the solar cell without intermediate levels, which only makes the IBSC efficiency to be marginally higher than the reference cell efficiency (34.5% compared to 30.7%). But the V_{OC} difference becomes almost negligible (8 mV) when the applied irradiance is enhanced to 1,000 suns, making the IBSC efficiency limit to rise up to 47.2%, compared to the 35.8% limit of the single gap solar cell. This larger efficiency difference is caused by the more rapid increase of V_{OC} for the IBSC compared to the reference cell.

1.4.2 V_{OC} larger than the absorption energy threshold

The "voltage preservation" principle applied to IBSCs is fulfilled when the output voltage is larger than the energy of any of the sub-bandgap transitions (divided by the electron charge, q) or, in other words, it is defined as the capability of the IBSC to provide a V_{OC} which is only limited by the fundamental bandgap of the semiconductor (E_{G}). Thus, the voltage preservation principle can be verified by checking whether the absorption energy threshold (in eV) of the IB semiconductor is surpassed by the maximum $q\,V_{\mathrm{OC}}$ reached by the cell when illuminated by concentrated light. In the case of a solar cell, the absorption threshold can be directly measured by QE or Fourier transform infrared spectroscopy (FTIR) and indirectly by photoreflectance (PR) or a luminescence technique, such as photoluminescence (PL) or electroluminescence (EL) [Martí et al., 2012]. Nevertheless, the latter is not a sufficient, but a necessary condition for the proper operation of an IBSC. The absorption of low-energy photons in two-step transitions is the other necessary condition of the IBSC. Only the combination of the two conditions allows exceeding the Shockley-Queisser (S-Q) efficiency limit, resulting in a high current and high voltage solar cell.

1.4.3 Dark J-V for the analysis of the voltage recovery in IBSCs

Technological problems of practical nature, such as the larger series resistance (r_{S}) of actual IBSCs prevent us from measuring this predicted efficiency increase, i.e. a QD-IBSC operating at 1,000 suns has a worse FF than its reference cell and hence, the efficiency can be lower. Although there is no conceptual problem for developing low r_{S} contacts for the QD-IBSC. This supposes at present a considerable technological effort that, after all,

could be worthless if the QD-IBSC does not operate as such. For this reason, another strategy for the verification of the voltage preservation is the analysis of the dark J-V characteristic, because this feature provides an insight into the recombination taking place in the device. Moreover, by means of the analysis of the dark J-V curves, the large voltage difference existing at very low current densities (which in turn correspond to low voltages) between the IBSC and the single gap cell can be visualized, as well as the decrease of the voltage gap between the two cells as their current densities increase.

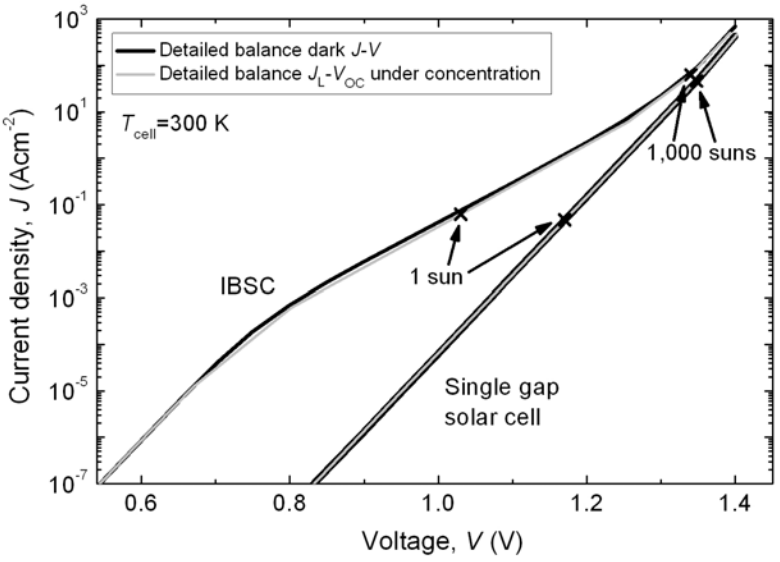

Figure 1.7: Detailed balance modeling of the J-V dark characteristic of an InAs/GaAs QD-IBSC (E_{G}=1.424 eV and E_{L}=0.3 eV) plotted together with a GaAs single gap solar cell. The J_{L}-V_{OC} curves of both cells calculated for different concentrations are also represented in the graph.

The dark J-V curve is conventionally divided into two recombination regimes: the low-voltage regime, dominated by Shockley-Read-Hall recombination in the space-charge region and characterized by a low exponential slope typically in the range of $e/2kT$ (i.e. an ideality factor m_2=2); and the high-voltage regime, dominated by recombination in the neutral zones and characterized by an exponential slope of e/kT (m_1=1) at low injection. However, as shown in the detailed balance calculations of Fig. 1.7 (resulting in a purely m=1 dark current), the recombination processes in an IBSC differs from those of the conventional solar cells [Linares et al., 2012b, Linares et al., 2012c]. In solid, black lines, the dark J-V characteristics for both an IBSC (E_{G}=1.42 eV, E_{H}=1.12 eV and E_{L}=0.3 eV) and its reference cell are represented. Within the low J range, up to $\sim$1 mAcm^{-2}, both curves remain parallel and are separated by a significant gap (of almost 300 mV), i.e. the IBSC recombination is much larger because it is dominated in this range by only one of the electronic transitions to or from the IB (D_2 and D_3 in of Fig. 1.5(b)). Between J=1 mAcm^{-2} and J=2.5 10^4 mAcm^{-2}, an operating regime with a lower exponential slope (and

influenced by the second of the electronic transitions to or from the IB) becomes dominant and leads to the recovery of V_{OC}. Above the current density of a typical GaAs solar cell operating under 1,000 suns illumination (25 A cm^{-2}), the two recombination characteristics nearly converge (their difference in voltage is reduced to barely 8 mV), meaning that the VB-CB transition (D_1 in Fig. 1.5(b)) is now dominating the recombination in the IBSC. In other words, under this regime, the contribution of diodes D_2 and D_3 to the total recombination is negligible compared to that of D_1, which is necessary for the recovery of the V_{OC}, as will be later demonstrated experimentally.

1.4.4 J_L-V_{OC} characterization

Nevertheless, as advanced in the previous section, the r_S of actual devices prevents the experimental observation of this convergence. When a dark J-V curve is measured in practice, the r_S of the solar cell affects the high current range, bending the curve toward higher voltages, thus making the comparison between the different recombination of both cells (IBSC and reference) difficult to interpret. As a consequence, the analysis of the recombination and the verification of the corresponding voltage recovery principle in IBSCs cannot be undertaken by means of the dark curve.

However, the impact of r_S in this measurement can be circumvented by means of the acquisition of J_L-V_{OC} pairs measured at different concentrations [Linares et al., 2012b, Linares et al., 2012c], thus representing the dark curve (recombination) of the solar without the detrimental impact of the r_S. This can be verified in Fig. 1.7, where the solid gray curve of the single-gap (reference) cell superimposes its dark curve. The analytical demonstration comes from the Shockley equation for an illuminated solar cell, as it can be deduced from equation 1.2, where J and V are respectively the solar cell current and voltage, J_{01} and J_{02} are the reverse saturation current densities of the two-diode model, m_1 and m_2 are the diode ideality factors, k is the Boltzmann constant, r_P is the parallel resistance, T is the cell temperature and q is the electron charge. In the equation [Linares et al., 2012c], V=V_{OC} is imposed by making I=0. The terms are then reorganized and an equation similar to that corresponding to the solar cell under dark conditions is obtained, where V=V_{OC} and J=J_L and also with the absence of the r_S component.

$$J = J_{\mathrm{L}} - J_{01}\left[\exp\left(\frac{q\,(V + r_{\mathrm{S}}\,J)}{m_1\,k\,T}\right) - 1\right] - J_{02}\left[\exp\left(\frac{q\,(V + r_{\mathrm{S}}\,J)}{m_2\,k\,T}\right) - 1\right] - \frac{V + r_{\mathrm{S}}\,J}{r_{\mathrm{P}}}$$

$$\text{If } J = 0 \;\; (V = V_{\mathrm{OC}}) \tag{1.2}$$

$$J_{\mathrm{L}} = J_{01}\left[\exp\left(\frac{q\,V_{\mathrm{OC}}}{m_1\,K\,T}\right) - 1\right] + J_{02}\left[\exp\left(\frac{q\,V_{\mathrm{OC}}}{m_2\,K\,T}\right) - 1\right] + \frac{V_{\mathrm{OC}}}{r_{\mathrm{P}}}$$

The first line of equation 1.2 represents the solar cell under illumination. When J is set to zero (and V=V_{OC}), the equation varies to the one shown in the lower line, which resembles the equation of the solar cell under dark conditions, where J is substituted by J_{L}, V is substituted by V_{OC} and there is no effect of r_{S}. Hence, we can state that, at least for the Shockley's equation for the conventional solar cell, the superposition principle is fulfilled and the J_{L}-V_{OC} pairs under different concentrations reproduce the dark J-V curve without r_{S}. An equivalent argument cannot be stated concerning the IBSC, which in general, does not mathematically fulfill the superposition principle. Nevertheless, the detailed balance analysis illustrated in Fig. 1.7 also represents the J_{L}-V_{OC} pairs at different concentrations and the curve described accurately matches the dark J-V curve.

Regarding the measurement of the V_{OC} and the J_{L} of a QD solar cell under concentrated light, a similar analysis was carried out by Hubbard et al. using InAs/GaAs QD solar cells, strain-balanced with GaP and grown by low-pressure organometallic vapor phase epitaxy [Hubbard et al., 2009]. Concentrator solar cells with 5, 10 and 20 QD layers were fabricated and J_{SC}-V_{OC} curves were measured under concentrated light at room temperature. An absolute efficiency improvement of ∼1% compared to the *p-i-n* GaAs control cell was obtained due to the J_{SC} enhancement produced by the tuning of the bandgap. Nevertheless, the V_{OC} of the QD solar cell did not approach the V_{OC} of the reference as the concentration increased. This phenomenon is, nevertheless, in agreement with theory as it will be explained next.

1.4.5 Need for low temperature operation

When the verification of the convergence of the dark curves is attempted experimentally at room temperature we face the problem of an IB-to-CB transition likely "short-circuited" in practice due to the electron thermal escape [Antolín et al., 2010a], which means that the electronic transfer through the E_{L} sub-bandgap is characterized by a thermalization rate much higher than the photogeneration rate. The latter makes a large IB-CB QFL split difficult to achieve at room temperature. At this point, the use of low temperatures is prescribed so that thermal radiation, instead of solar photons, does not pump electrons

from the IB to the CB [Luque et al., 2011a]. Also, at low temperature, there are less phononic modes available to interact with the solar cell and also pumping electrons from the IB to the CB.

In order to operate at low temperature, the concentration set-up is combined with a closed-cycle He cryostat. A convex lens is specially designed to focus the flash light on the solar cell so that the it receives a 1,000 suns equivalent irradiance while operating down to T=6 K (the 10,000 suns figure can only be achieved out of the cryostat, in the room temperature set-up, where more optimized optics can be used). Moreover, at low temperatures, the r_S of our solar cells increases, making even more difficult the voltage recovery analysis by means of the dark curve. The J_L-V_{OC} pairs measured under a wide range of concentrated illuminations and low temperatures can be acquired with the new characterization system explained in chapter 6, which combines a multi-flash concentration system with a cryostat.

1.4.6 Detailed balance efficiency as a function of concentration

The detailed balance model has been already reviewed in section 1.2.2, where it has been applied to the IBSC in order to state the potential of the concept with respect to the conventional solar cell. Such analysis is usually carried out for maximum concentration (46050 suns) in order to set a maximum limit for the radiation of the sun that reaches the Earth. Nevertheless, this concentration might seem unrealistic regarding the application of the concept to actual devices. For this reason a study of the efficiency of the IBSC in accordance with the concentration is shown here.

The detailed balance model has also been used to define the limiting efficiencies in accordance with the concentration. Plots in Fig. 1.8 represent the efficiency of the IBSC for different concentration factors (X=46,050 (maximum concentration), X=1,000 and X=1). The y axis stands for the fundamental bandgap energy (E_G) and the x axis for the energy of the IB with respect to the closest band (E_L). The sun is again modeled as a blackbody at 6000K and the IBSC remains at room temperature (T=300 K).

The 3D plots show a limiting efficiency that increases as the concentration increases, which is expected in this idealized case where r_S is disregarded. Fig. 1.8(a) presents the detailed balance efficiencies for maximum concentration and thus shows the highest values of η, whose maximum is the well known 63.2 % [Luque and Martí, 1997b] for an IBSC bandgap configuration of E_G=1.95 eV and E_L=0.71 eV. Figs. 1.8(b) and 1.8(c) respectively show the detailed balance efficiency for X=1,000 and X=1, which maxima are displaced to higher values of E_G (the lower the concentration, the higher the E_G that optimizes the IBSC for maximum efficiency). The latter is in agreement with our

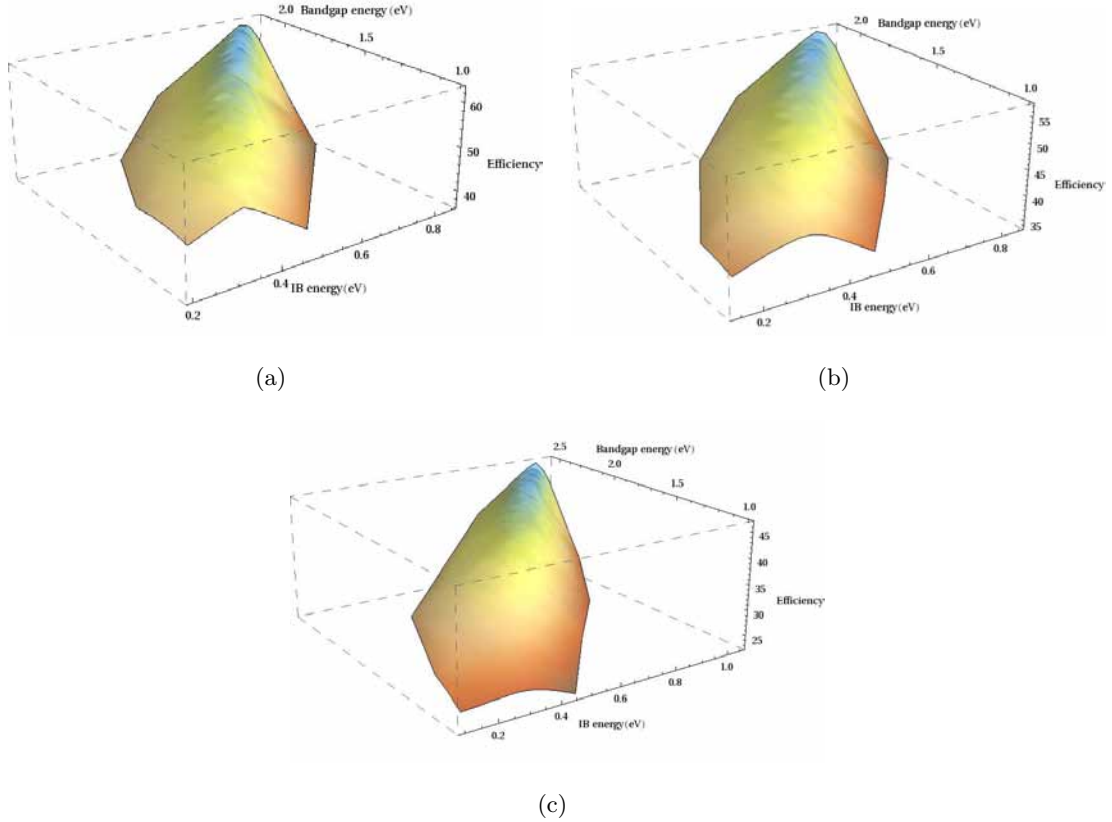

Figure 1.8: Detailed balance efficiency of an IBSC calculated for different concentrations: (a) 46,050 suns. (b) 1,000 suns. (c) 1 sun. All plots are represented with respect to the energy of the fundamental bandgap (E_{G}) and the energy of the IB with respect to the closest band (E_{L}).

aforementioned statements regarding the impact of the concentration on the recombination of an IBSC, i.e. at low concentrations, the impact of recombination through the IB is more significant and thus, higher E_{G} values are required so that the trade-off between collection of photons from the sun and carrier recombination is compensated. The values of E_{G} and E_{L}, as well as the optimized efficiencies for the calculated concentration factors are collected in Table 1.1. A similar study can also be found in Ref. [Cuadra, 2004].

Another interesting fact about the 3D plots is that the efficiency seems to be more sensitive to the displacement of the IB from its optimum position for lower concentration. Or in other words, a cross section of η throughout the x axis (E_{L}) in the 1 sun plot of Fig. 1.8(c) shows a more abrupt contour than the 1,000 suns plot and this is in turn more abrupt than the 46,050 suns plot. The reason of this higher sensitivity of the low concentration curve may be again the larger impact of the recombination through the IB.

The impact of the concentration on the efficiency of an IBSC compared to that of a conventional solar cell (only one gap) has also been studied. Two cases, have been considered which data are presented in Table 1.2: a) a large bandgap IBSC (E_{G}=1.95

Table 1.1: Detailed balance efficiency of the IBSC optimized for different concentrations: 46,050X, 1,000X and 1X. The E_{G} and E_{L} values that optimize the efficiency for each concentration are also indicated.

Concentration (X)	Maximum η (%)	$\{E_{\mathrm{G}}$ (eV),E_{L} (eV)$\}$
46,050	63.2	{1.95,0.71}
1,000	57.3	{2.07,0.76}
1	46.8	{2.38,0.91}

Table 1.2: Comparison between the detailed balance efficiency of a large bandgap IBSC (and corresponding single gap cell) and a small bandgap IBSC (and single gap cell) calculated for X=1 and X=1,000.

Cell bandgap (eV)	Concentration (suns)	η (%)
E_{G}=1.95 (single gap cell)	1	25.2
E_{G}=1.95, E_{L}=0.71 (IBSC)	1	45
E_{G}=1.95 (single gap cell)	1,000	28.1
E_{G}=1.95, E_{L}=0.71 (IBSC)	1,000	57.1
E_{G}=1.25 (single gap cell)	1	30.9
E_{G}=1.25, E_{L}=0.3 (IBSC)	1	32.5
E_{G}=1.25 (single gap cell)	1,000	36.9
E_{G}=1.25, E_{L}=0.3 (IBSC)	1,000	47.4

eV and E_{L}=0.71) and corresponding reference (single gap) cell and b) a small bandgap IBSC (E_{G}=1.25 eV and E_{L}=0.3 eV) and reference cell, both compared at 1 sun and at 1,000 suns. Both IBSC bandgap distributions optimize the detailed balance efficiency at maximum concentration.

These data allows us to outline the efficiency enhancement derived from the use of concentrated light (1 sun operation compared to 1,000 suns) in an IBSC compared to its corresponding reference cell. Besides, the theoretical analysis is carried out for the two cases of large and small bandgap solar cells. In accordance with our theory of the faster V_{OC} recovery of the IBSC compared to the single gap cell [Linares et al., 2012b, Martí et al., 2008b], the efficiency experiences a similar recovery when concentrated light is used. The data from the Table reveals an absolute efficiency improvement of $\Delta\eta$=2.9 % for the high bandgap single gap cell and $\Delta\eta$=12.1 % for the high bandgap IBSC, when the incident light increases from 1 to 1,000 suns. In the case of the low bandgap cells: $\Delta\eta$(single gap cell)=6 % and $\Delta\eta$(IBSC)=14.9 %. The faster efficiency recovery of the IBSC is evident both in the high bandgap as well as in the low bandgap cells. Although both the high and the low bandgap IBSCs seem to experience a similar efficiency improvement,

the relative improvement of the low bandgap cell is more pronounced, i.e. its 14.9 % absolute improvement implies a 45.8 % relative improvement, while the 12.1 % absolute improvement of the high bandgap IBSC implies a 26.9 % relative improvement.

1.5 Scope and outline of the Thesis

The main goal of this Thesis is the understanding of the performance of the IBSC under concentrated light and the verification of the voltage recovery in these high-efficiency devices. For such purpose, a novel experimental technique is presented which combines the use of concentrated light and low temperature operation. This characterization technique is applied to a relatively large number of the currently available IBSC technologies.

After this introduction (first chapter), a second chapter is devoted to the study and verification of the voltage recovery in QD-IBSCs, where different QD technologies are compared. The voltage preservation principle will be verified for at least one of the existing QD technologies.

In the following chapter of this Thesis, the rest of the IBSC technologies will be analyzed regarding the preservation of the voltage, for which the low temperature concentrated light characterization system will be also employed. In this third chapter, IBSC technologies based on bulk semiconductors will be studied.

The fourth chapter is devoted to the identification of new candidate materials for the implementation of the QD-IBSC concept. For such purpose, an algorithm has been implemented for the calculation of the heterojunction band alignment of two III-V semiconductor alloys. The algorithm combines the formalism of the Model Solid Theory [Van de Walle, 1989], which includes the effect of strain caused by the lattice mismatch, as well as set of equations to interpolate the different electronic parameters of ternary and quaternary alloyed semiconductors.

The following chapter is devoted to the fabrication of QDs for the implementation of the so-called QD-IBSC, explaining the intricacies underlying the features of the nanoparticles (size, shape, aspect ratio, growth temperature, etc.) and their performance as IB materials. The experimental progress regarding the $InAs/GaAs_{1-x}N_x$ QD-IBSC developed in collaboration with The University of Tokyo, including both the fabrication in molecular beam epitaxy (MBE), processing and characterization of the solar cells, is explained in this section.

The sixth chapter is devoted to the new characterization system developed for the measurement of solar cells at very high concentration and under very low temperatures. The constraints of each of the main components employed for the conception of this low-

temperature and concentrated-light set-up are reviewed, as well as the intricacies of this new type of measurement.

The appendices are focused on the design and fabrication of concentrator QD solar cells. In particular, on the analysis of the front grid pattern for the metallization of the device as well on the methodology of the processing of concentrator solar cells. A thorough analysis of the r_S is then carried out in this chapter and some examples are shown of the front grid designs optimized for the QD-IBSC used at IES-UPM and RCAST.

Chapter 2

Characterization of QD-IBSCs under concentrated light

2.1 Introduction

In this chapter, we demonstrate experimentally how the recombination in the IBSC can be reduced at low temperature and under operation at high-irradiance, leading to the recovery of the initially degraded V_{OC} and verifying our initial theoretical prediction. This is particularly promising for IBSCs to be used in CPV systems.

The operation principle known as "voltage preservation" is here experimentally verified in actual operating devices. In this chapter the discussion will be focused on IB materials based on QD technology. The relatively mature QD technology applied to the IBSC will be subjected to concentrated light characterization. As it has been already outlined in the introductory chapter, the use of low temperatures is prescribed in order to make these non-idealized cells behave as actual IBSCs.

The different intricacies of the novel low temperature concentrated light characterization technique, as well as other applications of the aforementioned technique will also be discussed in this chapter.

2.2 Experimental characterization of QD-IBSCs

Several IBSCs candidates have been tested with our concentration system. The main results that have been obtained using QDs will be summarized in this section.

2.2.1 Characterization of the InAs/GaAs QD-IBSCs

2.2.1.1 InAs/GaAs QD-IBSC with thick spacers

A 30 layer InAs/GaAs QD-IBSC and a GaAs reference solar cell (control sample) were fabricated at the University of Glasgow by MBE. A detailed sketch of the layer structure of this QD-IBSC is presented in Fig. 2.1, together with the specifications of the composition, doping and thickness of each layer. The bottom layer consists of a 625 μm thick n-type

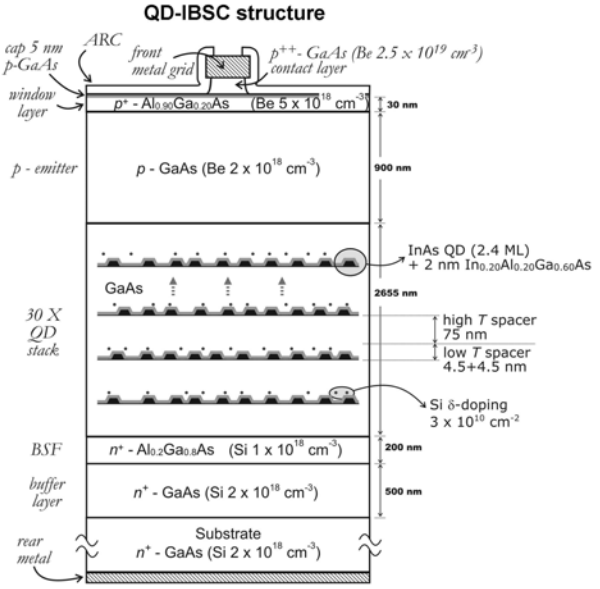

Figure 2.1: QD-IBSC layer structure including doping and thickness data for each layer. The IB region consists of 30 stacked QD layers, each of which is separated by a thick spacer which incorporates the Si δ-doping. Courtesy of Dr. Elisa Antolín.

GaAs wafer on top of which the device was grown. Next, a buffer layer was grown to smooth the surface. Then, an n^+-$Al_{0.2}Ga_{0.8}As$ layer that acts as the n-emitter of the cell, was added. The IB material was grown next and consists of 30 layers of self-assembled InAs QDs built up in the Stranski-Krastanov (S-K) growth mode and separated by thick, intrinsic GaAs spacers to prevent material dislocations (because of the accumulation of strain) and the carrier tunneling between the QD layers and the host material CB [Antolín et al., 2010a]. A quaternary $In_{0.2}Al_{0.2}Ga_{0.6}As$ capping was added to preserve the QD height/base aspect ratio, to red-shift the E_H transition [Ustinov et al., 2000] and to eliminate the CB discontinuity with the GaAs barrier layer and thus, prevent the formation of an additional quantum well (QW) [Linares et al., 2010a] in an effort to isolate the IB from the CB (this will be reviewed in section 4.5). Si δ-doping was included to half-fill the IB with electrons, so there are both empty states to enable the electrons to be pumped from the VB to the IB and filled states to assist in the IB-CB transition [Martí et al., 2001].

After the IB material region, a p-type GaAs emitter completes the electrically active part of the solar cell. Finally, an AlGaAs window, a p^+-GaAs contact layer and an ARC layer complete the IBSC structure. The reference cell structure is identical except for the lack of the QD-IB region and the substitution of the n^+-$Al_{0.2}Ga_{0.8}As$ emitter by a 2 10^{17} cm^{-3} doped, 3.1 μm n-type base layer on top of a 200 nm n^+-$Al^{0.2}Ga^{0.8}As$ back surface field (BSF) layer.

The experimental results were analyzed and compared to the predictions explained in section 1.4. For this purpose, the J_L-V_{OC} characteristics of both the QD-IBSC and the reference cell were obtained at different light concentration levels and at four different temperatures [Martí et al., 2012]. Fig. 2.2(a) shows the results of the room temperature experiment, in which the recombination associated with the QD-based technology still appears to be too large (non-radiative recombination is also present) and the voltage recovery effect is not observed, i.e., both J_L-V_{OC} curves remain approximately parallel. This is consistent with the fact that, under room temperature conditions, a large IB-CB QFL split is difficult to achieve, and the QD-IBSC behaves as a low-bandgap conventional solar cell [Antolín et al., 2010a]. The dark J-V curves are presented in solid,dark lines in order to verify the fulfillment of the superposition principle in the range where they are not strongly affected by r_S. In Fig. 2.2(b), the experimental temperature was lowered to T=150 K, and the first evidence of an IBSC recombination actually approaching the reference cell recombination is observed. The latter shows the trend of IBSC recombination moving with a slope higher than e/kT and converging to the reference cell as the concentration increases and as predicted by the theory. In addition, the maximum V_{OC} obtained in this measurement exceeds the photon energy absorption threshold, which is of approximately 0.95 eV (corresponding to the E_H sub-bandgap energy at room temperature), as experimentally observed in the QE of the device shown in Fig. 2.3. This plot shows the results from a QD cell and a GaAs reference cell equivalent to the the ones employed in Fig. 2.2 and which are extensively reviewed in Ref. [Antolín et al., 2010a].

Fig. 2.2(c) shows the results of the experiment performed at T=77 K, in which the IBSC voltage recovery is complete at a high concentration; V_{OC} values close to 1.4 eV are reached by both cells, and the IBSC recombination matches that of the reference cell, thus verifying the proposed IBSC voltage recovery model. Under these conditions, an exponential slope of e/kT fits the low-voltage range of the QD-IBSC J_L-V_{OC} characteristic, which may be interpreted as an operating regime close to the radiative limit. Nevertheless, the low-voltage range of the reference cell J_L-V_{OC} does not behave in such radiative way, since it shows a much lower exponential slope. Finally, Fig. 2.2(d) presents the same measurements at T=20 K, showing the full IBSC recombination characteristic lying below the

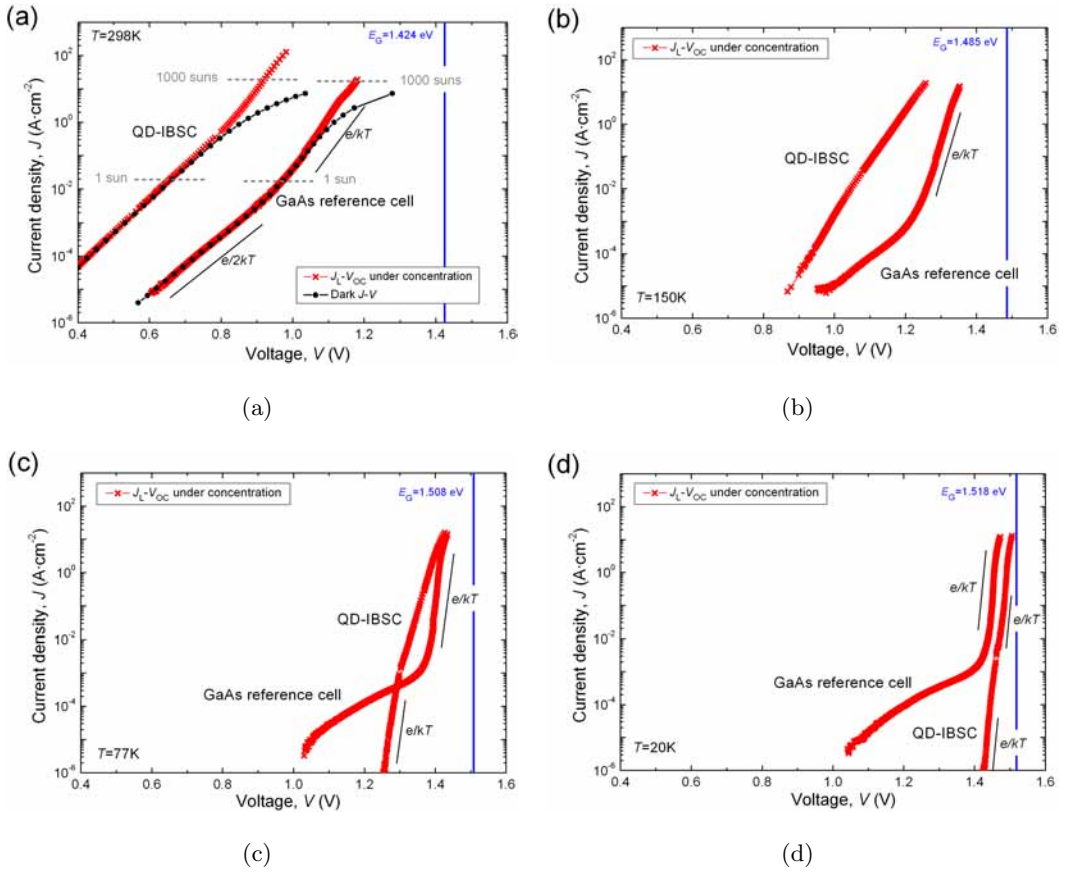

Figure 2.2: Concentrated light J_L-V_{OC} characteristics of both the QD-IBSC and the reference cell at different temperatures [Linares et al., 2012b]. (a) Dark J-V and concentrated light J_L-V_{OC} characteristics measured at T=298 K. The concentration levels are indicated with horizontal gray dashed lines. (b), (c) and (d) show concentrated light J_L-V_{OC} measurements at T=150 K, T=77 K and T=20 K, respectively. The solar cells fundamental bandgap is represented with a solid, blue line for each temperature and the e/kT and $e/2kT$ exponential slopes are also indicated when present.

reference cell recombination. This may be justified by the of use of the n^+-$Al_{0.2}Ga_{0.8}As$ rear n-type emitter for the QD-IBSC, which decreases the contribution to the total recombination provided by this emitter, in contrast to the use of a conventional n-GaAs emitter in the reference cell and supports that recombination is dominated by the emitters and not by the QD-region. The largest IBSC output voltage value measured at this temperature corresponds to V_{OC}=1.506 V. It is exceptionally high, although consistently lower than the QD-IBSC E_G/e (1.516 eV), which accounts for the bandgap of a properly operating IBSC at T=20 K.

Fig. 2.3 also shows, in the logarithmic scale plot to the right, the energy corresponding to the wetting layer (WL), which is a QW associated to the growth of self-assembled QDs by S-K (further insight of the WL concept is addressed in chapter 5) and several confined energy levels of the QD cell. Besides the WL, up to three levels were identified.

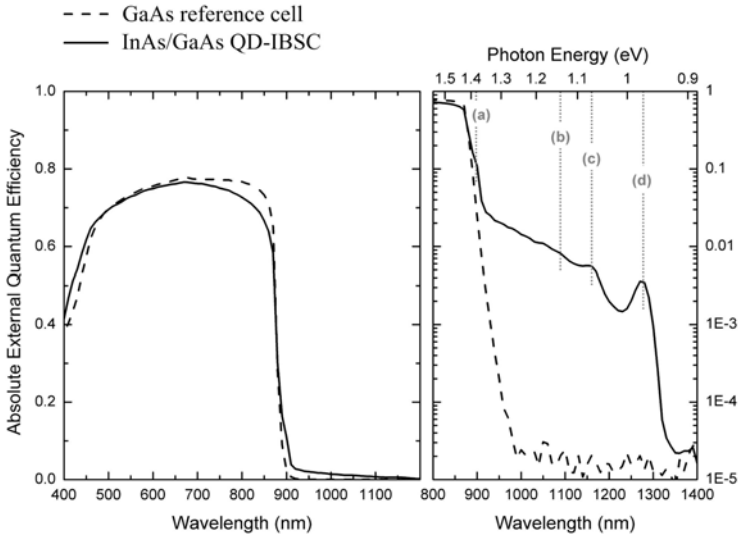

Figure 2.3: Absolute external QE measurements of the 30 layer InAs/GaAs QD-IBSC and GaAs reference cell plotted in linear and logarithmic scale. The WL, denoted as (a) and three confined levels are identified in the sub-bandgap region of the QD solar cell and labeled from (b) to (d), where (d) is the confined ground-state. Courtesy of Dr. Elisa Antolín.

2.2.1.2 InAs/GaAs QD-IBSC with thin spacers

The previous results have addressed the experimental verification of the voltage preservation principle in InAs/GaAs QD-IBSCs with thick spacers. These thick GaAs layers can dilute the strain (generated by the InAs deposited for the growth of each QD layer) before the next layer is grown. From a morphology point of view, this type of structures is meant to avoid material dislocations and irregular formation of the QDs, both originated because of the strain (this point will be reviewed in detail in section 5). From an electronic point of view, the thick spacers also prevent carrier tunneling between the QDs and the CB [Antolín et al., 2010a] and the absence of this thick spacers may contribute to the practical "short-circuiting" of the IB-CB transition.

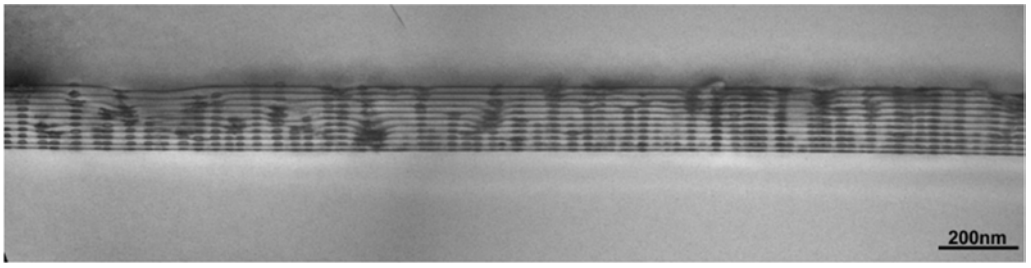

Figure 2.4: Dark field 002 TEM image of the InAs/GaAs QD-IBSC where the ten InAs QD layers and the seed layer are shown. The QD layers are separated by thin GaAs spacers, which large lattice mismatch with InAs produce the accumulation of strain in the upper QD layer. The QD layers are packed between the GaAs n- and p-emitters, also visible in the image.

QD cells with thin spacers fabricated at the University of Glasgow have also been tested in our low temperature concentrated light set-up to try to provide insights on the effect of tunneling to the voltage recovery. The devices corresponding to this experiment consist of InAs/GaAs QD-IBSC with 10 QD layers (plus the so-called seed-layer, reviewed in chapter 5) separated by 13 nm thick GaAs spacers. The main difference with respect to the solar cell layer structure shown in Fig. 2.1 (besides the number of QD layers and the QD spacer layer thickness) is the existence of a 3.1 μm thick n-type emitter, between the n^+-$Al_{0.2}Ga_{0.8}As$ layer (that now acts as a BSF layer). A dark field 002 transmission electron microscopy (TEM) image of the cell is presented in Fig. 2.4. The strain produced by the large mismatch between InAs and GaAs and accumulated in the upper QD layer is easily observable in the TEM image.

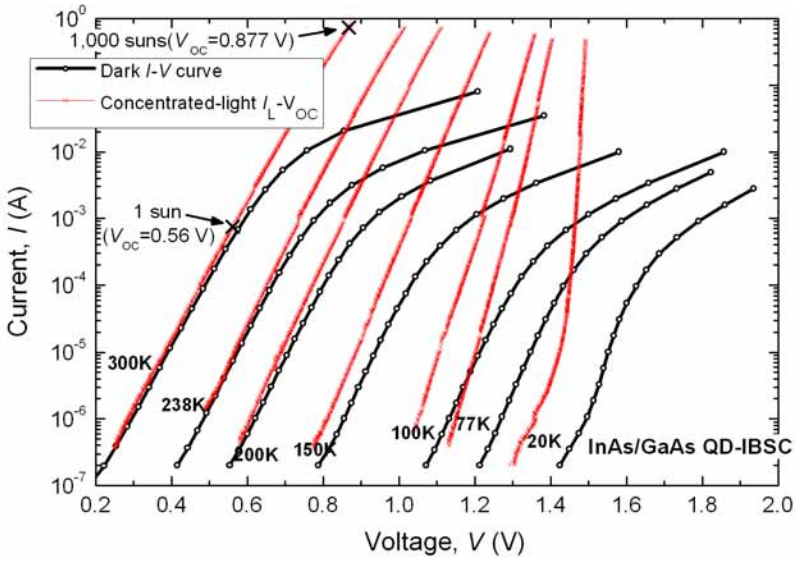

Figure 2.5: Concentration I_L-V_{OC} and dark I-V characteristics in which T is varied from 300 K to 20 K. The 1 sun and 1,000 suns points are indicated as well as their corresponding V_{OC} values.

Concentrated light low temperature I_L-V_{OC} characteristics have been measured together with the corresponding dark I-V curves for the verification of the voltage preservation principle in these cells. The results from these experiments are represented in Fig. 2.5, showing how the initially degraded V_{OC} of the QD cell (0.56 V at 1 sun) is not very much recovered at 1,000 suns (0.877 V) when the cell remains at T=300 K. This is caused by very high electronic thermal escape occurring in the IB-CB transition [Antolín et al., 2010a, Luque et al., 2011a, Martí et al., 2006b]. The temperature is then lowered in order to verify whether the IB is effectively isolated from the CB, i.e. the thermal escape is sufficiently inhibited so that the QD cell behaves as an actual IBSC. A study of the QD-IBSC under low temperature operation can be found elsewhere [Luque et al., 2012a].

The superposition principle between the I_L-V_{OC} and the dark I-V curves is fulfilled in the low-current range where the product $r_S\, I$ should be negligible and in the QD sample only for $T \geqslant 200$ K. In this cell, the dark I-V curves deviate toward higher voltages (note that the I-V curve is almost entirely located beyond 1.5 V) with respect to their corresponding concentrated-light I_L-V_{OC} curves as the temperature is decreased. This effect is likely produced by a large increase of the r_S value, which can be perhaps attributed to the presence of an intrinsic region in the cell (where the InAs QDs are hosted) activated at low temperature. The possibility of cell heating because of the effect of the concentrated light is disregarded because the incident luminous power that produces an $I_L < 10^{-5}$ A (equivalent to $\sim 10^{-2}$ suns) is too small at that current range. A possible heating derived from the active (reverse) biasing is not possible either, because the cell remains under dark conditions (i.e. with $I \sim I_0$ in the range of nA) when it is reverse biased prior to receiving the flash light. Besides, both heating mechanisms are also disregarded because they do not take place for the reference cell (see Fig. 2.2(a)), which fulfills the superposition principle.

Table 2.1: Maximum V_{OC} obtained under concentrated-light for the QD-IBSC operated at different temperatures.

Temperature (K)	V_{OC} (V) at maximum concentration
300	0.877
238	1.015
200	1.111
150	1.239
100	1.358
77	1.404
20	1.492

The evolution of the maximum V_{OC} achieved at maximum concentration corresponding to each of the different operating temperatures of the QD cell is shown in Table 2.1. It can be observed how the voltage gradually recovers, until it reaches V_{OC}=1.492 V at T=20 K, which is a value very close to the E_G/q of the (GaAs) fundamental bandgap at T=0 K (1.519 eV [Vurgaftman et al., 2001]). The latter demonstrates the complete voltage recovery of the QD cell at low temperature. Nevertheless, the progression of the V_{OC} experienced by the QD sample with thin spacers operated under low temperature and high concentration is different from the QD sample with thick spacers. In that case (especially evident in Figs 2.2(c) and 2.2(b)), the slope of the upper part of the J_L-V_{OC} curve has a higher exponential slope than the lower part, which cannot be explained by

the "classical" theory for conventional solar cells but fits with the IBSC theory [Linares et al., 2012b, Martí et al., 2008b]. In the samples with thin spacers, approximately the same slope dominates the high and the low current ranges for most temperatures. This may be due to the effect of tunneling in these cells, although further analysis is required.

However, the fact that the V_{OC} is not limited by E_L or E_L is a verification of the voltage preservation principle, even in this cell with thin spacers and consequently with an escape component assisted by tunnel that could be suppressed when, at forward bias, the bands become progressively flat.

2.2.2 InAs/GaAsN QD-IBSCs manufactured at the University of Tokyo

The InAs/GaAsN QD-IBSCs fabricated at Prof. Okada's Lab at the Research Center for Advance Science and Technology (RCAST) at the University of Tokyo were also subjected to low temperature concentrated light experiments. The layer structure of these cells consists of a top 50 nm layer corresponding to the contact layer, a 150 nm thick GaAs p-emitter, 50 stacked InAs QD layers separated by 20 nm thick GaAsN intrinsic spacers, a 1,000 nm thick GaAs n-emitter and a 250 nm thick n-GaAs buffer layer. The reference cell is similar except for hosting a 1,000 nm thick intrinsic GaAs layer instead of the QD region.

Concentration measurements in Fig. 2.6(a) show the QD and reference cell J_L-V_{OC} and dark J-V characteristics at room temperature, where the two red curves (representing the concentration measurements) remain approximately parallel. This result confirms that the very high electronic thermalization and tunneling rates make the QD cell to behave as a single gap solar cell (of reduced bandgap) at this temperature. The latter implies that both the reference and QD cells recover their V_{OC} with an equivalent trend (when the concentration is increased), i.e. they both have same slopes, conversely to the case explained in the previous section, where low temperatures apply and the QD cell behaves as a real IBSC.

Fig. 2.6(b) shows the J_L-V_{OC} and dark curves of the QD cell measured at different temperatures. The recombination characteristic of this cell decreases as the temperature decreases, as expected from the increase of the bandgap (which strongly affects the amount of radiative recombination) and the reduction of the non-radiative component due to the progressive extinction of the phononic modes that favor this type of recombination. All of the foregoing makes the V_{OC} to increase when the temperature decreases, up to a value slightly above 1.2 V (reached for the lowest temperature, T=20 K). Conversely to the previous InAs/GaAs solar cell fabricated at the University of Glasgow, this value does not correspond to the bandgap of the host material (GaAs, with which the emitters are made

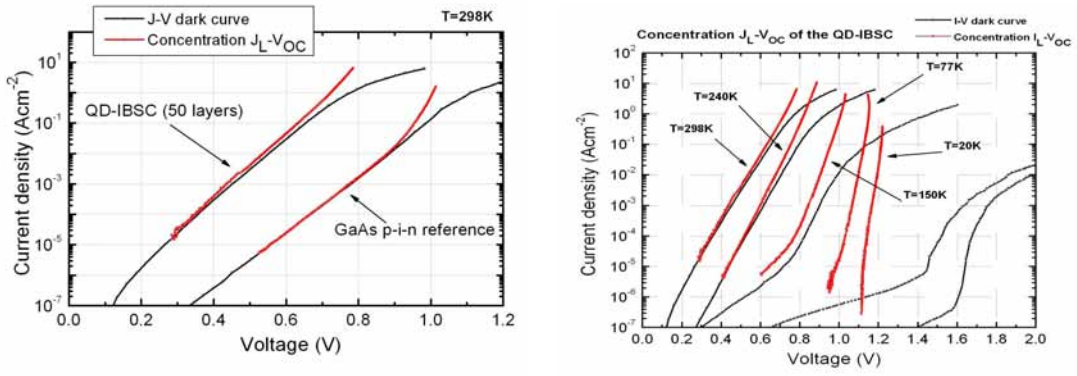

(a) (b)

Figure 2.6: Concentrated light J_L-V_{OC} and dark characteristics of a 50 stacked QD layer IBSC from RCAST, plotted together with their corresponding dark curves. (a) Room temperature comparison between the *p-i-n* GaAs reference cell and the InAs/GaAsN QD-IBSC. (b) QD-IBSC measured at different temperatures from T=298 K down to T=20 K. The plot shows the voltage recovery not being completely achieved in this case.

of), but most likely to the bandgap of the GaAsN. We can, hence, infer that the voltage preservation principle is not fulfilled for this QD technology or at least that it is limited by the bandgap (divided by the electron charge) of the GaAsN, that is notably lower than that of the emitters (GaAs).

Nevertheless, even if the electronic thermal escape is almost completely suppressed at this low temperature, the thin spacers (of 20 nm) that separate each QD layer will not prevent the electronic tunneling. It would be so, especially because the spacer material is made of GaAsN instead of GaAs, and it has a lower energy CB due to the BAC effect produced by the dilute nitrogen, i.e. the smaller the energy between the QD ground state and the CB of the barrier material, the larger the tunneling component.

A remarkable measuring problem occurs in these cells at low temperatures. When the concentrated light factor surpasses approximately 100 suns (in these cells, this is equivalent to about 10^{-2} mAcm^{-2}), one of the problems that will be explained in section 6.3.3.1 and referred to as the unavoidable heating of the cell when exposed to very high irradiances takes place. It can be observed in the upper part of the J_L-V_{OC} curve at T=77 K. It is probably caused by a defective processing of the device, which could hinder the evacuation of the heat generated during the exposure of the cell to a very high irradiance. As a consequence, the bending of the J_L-V_{OC} curve takes place toward lower voltages as the concentration increases, which is counterintuitive. Conversely to the conventional heating that usually occurs in this type of concentrated light measurement, which affects the cell temperature constantly during the whole flash pulse (provoking a parallel displacement of

the curve), in this case, the heating (and the subsequent V_{OC} decrease) is more pronounced in the very first part of the flash pulse and then progressively disappears. As a result, the V_{OC} at the higher part of the T=77 K plot is not correctly measured. The higher part of the curve at T=20 K has not been represented because this effect is even more pronounced.

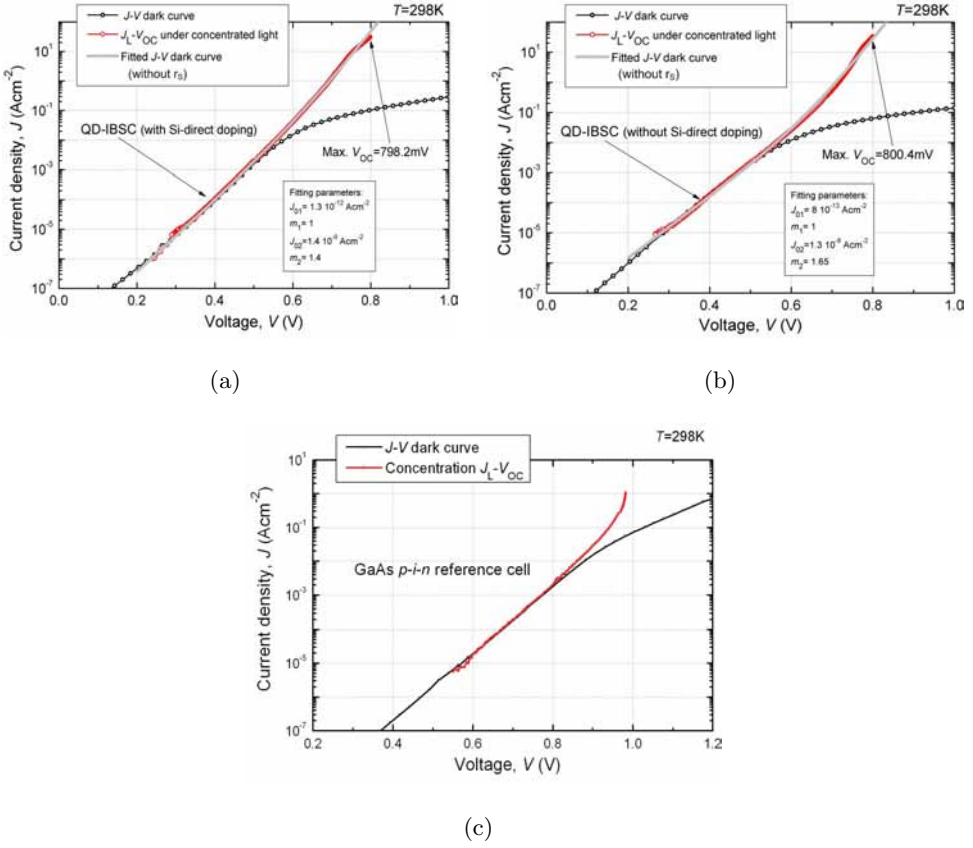

Figure 2.7: Concentrated light J_L-V_{OC} characteristics of the second batch of samples from RCAST. (a) QD-IBSC with Si-direct doping including a two-diode fitting (with r_S=0). (b) QD-IBSC without QD doping (also with fitting). (c) *p-i-n* GaAs reference cell.

Regarding the second batch of samples provided by RCAST, Fig. 2.7 represents the room temperature J_L-V_{OC} and dark J-V plots, together with a fitting to a two-diode recombination model, with r_S=0 in order to reproduce the J_L-V_{OC} curve. The results of the fitting: J_{01}, J_{02} and the slopes corresponding to each diode, are also indicated. The maximum V_{OC} obtained in the experiments is also represented in the plots. The fact that these QD cells operate as single gap solar cells at room temperature, make possible a quite accurate fitting of the recombination curves. Otherwise, it would not be possible to fit them, since there is not an analytical model of the IBSC recombination that is equivalent to the Shockley's model for a conventional solar cell.

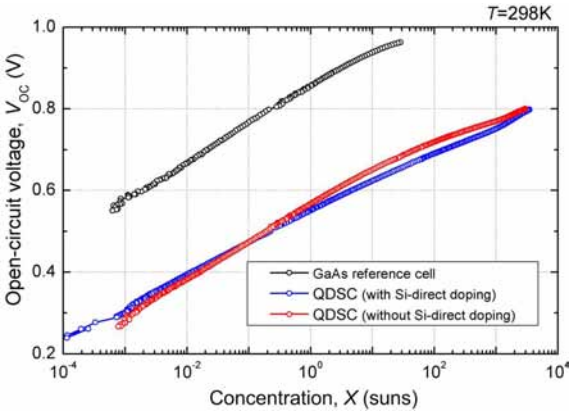

Figure 2.8: V_{OC} obtained from the solar cells of the second batch of samples fabricated at RCAST and processed at IES-UPM. The batch consists of two 30 QD stacked layer InAs/GaAsN QD-IBSCs, with and without Si-direct doping and a *p-i-n* GaAs reference cell. The measurements were performed at room temperature and for a wide range of concentrated lights.

In order to verify whether the trend of the V_{OC} of any of these QD cells (with and without Si-direct doping) approaches the V_{OC} of the reference cell as the concentration increases, another type of representation can be performed consisting of plotting the $V_{OC}(X)$ functions represented in semilogarithmic scale (X being the concentration). These functions, plotted in Fig. 2.8, show similar behavior both for the QDs with doping as well as for the QDs without doping. The difference in V_{OC} between the GaAs *p-i-n* reference cell and the QD cells is roughly constant (300 mV), verifying that the V_{OC} of the QD cells does not recover faster than the GaAs reference cell at room temperature. As it can be observed in Fig. 2.7(c), the reference cell suffers again from the same unavoidable heating and thus, it cannot be subjected to very high concentrations.

The third batch of QD solar cells, which layer structure is discussed in Fig. 5.23, is aimed to solve the problems encountered in the previous batches, where the GaAsN barrier material limits the performance of the device and the thin spacers do not block the carrier tunneling between QD layers. The results of the low temperature concentrated light measurements are plotted in Fig. 2.9. The *p-i-n* GaAs reference cell, represented in Fig. 2.9(a), apparently fulfills the superposition principle at the four different temperatures, even at T=20 K (of course, only in the low concentration range, where the effect of the series resistance is not very pronounced), which also occurred for the *p-n* GaAs reference cell from Glasgow. This cell almost reaches a V_{OC} of 1.5 V, while the QD cell slightly surpasses this value (but does not surpass the E_G/q value), accurately reproducing the voltage recovery result exposed in section 2.2.1 and published in Ref. [Linares et al., 2012b]. The confirmation of this result is important regarding the voltage preservation principle of InAs/GaAs QD-IBSCs at low-temperature.

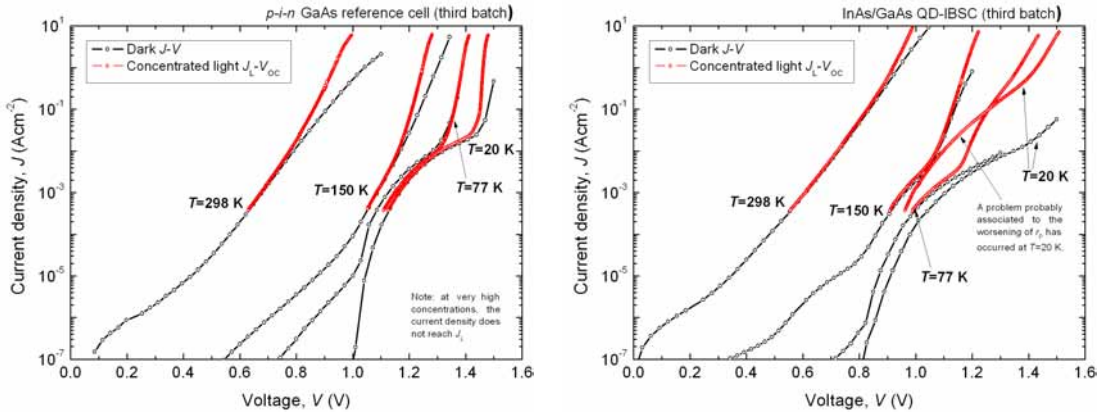

(a) (b)

Figure 2.9: Concentrated light J_{L}-V_{OC} and J-V dark characteristics of the third batch samples (the one in which GaAsN barriers are replaced by thick GaAs ones) fabricated at RCAST and processed, encapsulated and measured at IES-UPM. (a) p-i-n GaAs reference. (b) InAs/GaAs QD-IBSC. Both figures are measured at different temperatures from T=298 K down to T=20 K.

The concentrated light experiment carried out with the GaAs cell of this first batch of samples could not measure J_{L}-V_{OC} at the highest concentration (∼800 suns, inside the cryostat), because the large r_{S} of this cell required a reverse bias more negative than -6 V, which cannot be provided by our set-up. Therefore, the J_{L} is slightly underestimated, although this effect is almost unnoticeable. On the other hand, the QD sample experienced a deterioration of the r_{P} only at T=20 K, which is apparent only throughout the low concentration range (which crosses the curve at T=77 K).

2.2.3 InAs/GaAs QD-IBSCs manufactured at Rochester Institute of Technology

Another type of strain-compensation QD cells have also been characterized in this Thesis work. In this case, a batch of QD-IBSCs with 5 InAs/GaP stacked QD layers, similar to the ones used in Ref. [Hubbard et al., 2008], were fabricated at the Rochester Institute of Technology in collaboration with NASA Glenn Research Center. These samples were also characterized at low temperature and concentrated light. The GaP, as well as the GaAsN, also has a smaller lattice constant than the GaAs, exerting a tensile strain that compensates the compressive strain introduced by the InAs QDs. The main difference between the GaP strain-compensating technique used in this case compared to the GaAsN used from RCAST is that the GaP layer is sandwiched between a thicker GaAs barrier material, instead of being GaAsP alloy. The resulting band diagram is then different than the one generated by a single alloyed material barrier layer, although this, in principle,

will not significantly affect the results. Regarding the electronic properties, the GaP has a larger bandgap than GaAs, conversely to the GaAsN case. For this experiment, no reference cells were provided to IES-UPM as a benchmark.

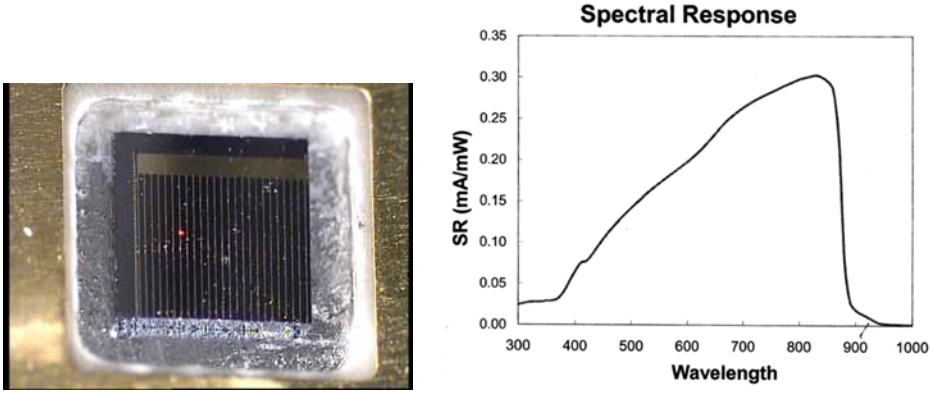

(a) (b)

Figure 2.10: (a) Microscope picture of the encapsulated InAs/GaAsP QD-IBSC from Rochester. The solar cell is in this case a small portion of a 1x1 cm^2 solar cell that was cut into smaller pieces in order to appropriately measure it under concentrated light. (b) Spectral response of the QD cell. A small response in the sub-bandgap region is observed.

Fig. 2.10(a) shows a microscope picture of the QD cell used in this experiment, taken in the wire-bonding system. The cell is a small portion of a larger (squared 1 cm^2) cell, which was too large for our concentration system because the source-meter cannot handle large currents (it is limited to 6 A). The spectral response of the cell is represented in Fig. 2.10(b), where the GaAs bandgap signature can be observed at 870 nm as well as a sub-bandgap response as large as 2% of the integrated photocurrent. Nevertheless, this sub-bandgap photoresponse is very likely almost exclusively related to the WL.

The result of the low temperature concentration experiment is shown in Fig. 2.11. It is remarkable how the superposition principle is almost completely fulfilled for all the temperatures, even at T=20 K. In this case, the voltage recovery is produced up to 1.43 V at T=20 K, which is 86 mV below the E_G/q value of 1.516 eV. Nevertheless, this can be qualitatively considered as having fulfilled the voltage preservation principle (taking into account that the same concentration could not be achieved at T=20 K).

It can then be concluded that the GaP (or any related alloyed compound such as GaAsP) is a valid strain compensation material for the InAs/GaAs based QD technology, regarding its operation as an IBSC, conversely to the GaAsN material, which reduced bandgap dramatically limits the electrical performance.

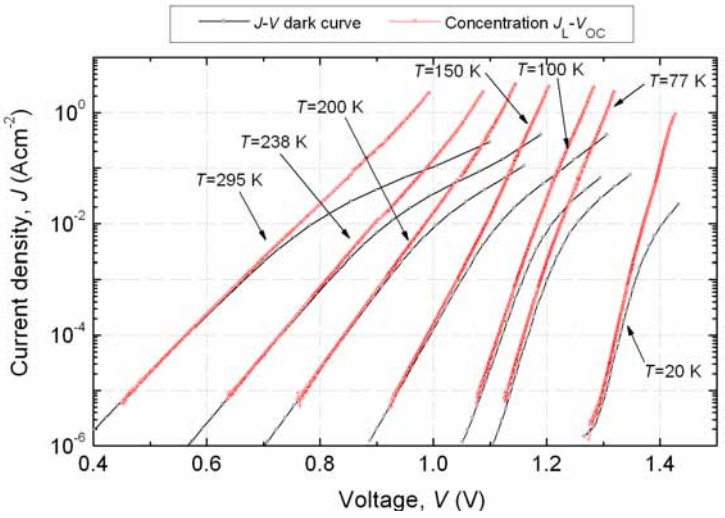

Figure 2.11: Concentrated light J_L-V_{OC} characteristics of the InAs/GaAsP strain compensated QD-IBSCs (with 5 stacked QD layers) fabricated at NanoPower Research Laboratories at Rochester Institute of Technology. Seven different measurements acquired from T=298 K down to T=20 K are shown, including their corresponding dark curves for comparison.

2.3 Other applications of the concentration experiment

2.3.1 The multiple-level IBSC

A model including several IB levels has been proposed [Luque et al., 2010a, Linares et al., 2010b]. In this section, the presence of multiple energy levels in the IBSC is studied by detailed balance calculations under ideal conditions. As it has already been mentioned, the QD structures included in the QD-IBSCs discussed in this Thesis are far from the optimal size and hence, besides the confined ground-state, they have other confined levels (up to four, in the samples that have been experimentally characterized [Cánovas et al., 2008]). The results from the concentrated light J_L-V_{OC} measurements are presented here together with their fitting to a multiple-level IBSC model to gain insight on the recombination associated to each of the transitions.

2.3.1.1 The equivalent circuit model of a multiple-level IBSC

In Fig. 1.5, the equivalent electrical circuits of the conventional solar cell and two representative IBSC cases were presented. These equivalent circuits can be upgraded to include the multiple-level case, leading to the more realistic model shown in Fig. 2.12(a). On the left part of the figure, the host subcell model consisting of a photocurrent generator in parallel with a diode is represented. It accounts for the VB→CB pumping and recombination mechanisms respectively. In parallel with this host subcell, we can find a combination in series of two other subcells, representing the VB→IB and IB→CB transitions of the

IBSC. There is a total of four of these secondary subcell sets representing pumping and recombination through each of the four confined levels.

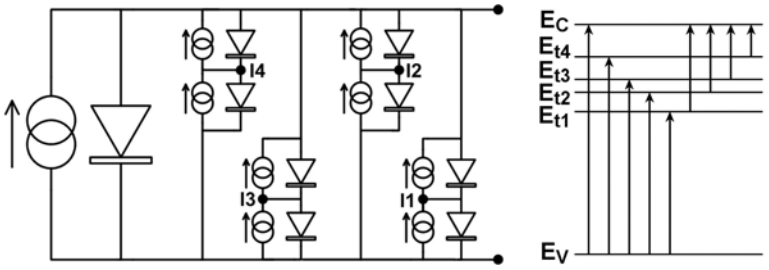

(a) (b)

Figure 2.12: (a) Equivalent circuit for a four-level IBSC. The big current generator/diode set on the left corresponds to the transition through the fundamental bandgap. The other four double series-connected current generator/diode sets correspond to the transitions through each of the four QD energy levels. (b) Schematic of all possible transitions involving the three existing bands (VB, IB and CB) that have been considered in our 4-level multiple-level model.

Fig. 2.12(b) shows a simplified sketch of the three bands present in an IBSC (the IB being in this case substituted by four energy levels). The arrows represent each of the possible transitions occurring from the VB to the CB, from the VB to any of the IB levels (first step of the sub-bandgaps generation and recombination processes) and the ones from the IB levels to the CB (second step of the same processes). E_{V} represents the top of the effective VB and E_{C} the bottom of the effective CB. $E_{\mathrm{ti}}(i{=}1,\ 2,\ 3,\ 4)$ represents the energy of the IB levels. There are many confined hole levels in the VB offset and therefore, many different transitions are allowed between them and the electron confined levels in the CB. On the other hand, the strongest interband transitions are produced between hole and electron confined states of the same quantum numbers [Luque et al., 2011b]. These complex scenario is simplified considering that a single E_{V} energy exists accounting for all the levels in the VB. The values for E_{ti} are then calculated from this reference energy.

2.3.1.2 The multiple-level detailed balance analysis

In our detailed balance analysis we will consider that no transition can occur among the four (electron) confined levels considered in the model, but only between each of them and any energy level located within the CB (i.e. the energy range from E_{C} to positive infinity) or the VB (from negative infinity to E_{V}). The reason arises from the fact that these confined levels are regarded as fine lines or δ functions in energy, and therefore, the associated energy interval for integration for a transition between confined levels is zero, contrary to what it is discussed in Ref. [Levy and Honsberg, 2008a], where the IB

is assumed to be of finite width. In turn, E_{C} is actually considered to be located at the energy of the WL, because the DOS function in a WL is continuous, as it is the case in any two-dimensional nanostructure, and thus, the absorption probability increases abruptly from such energy. Furthermore, the condition of non-overlapping absorption coefficients is assumed in our detailed balance analysis [Cuadra et al., 2004] which implies that every photon is absorbed in the largest possible transition, even if its absorption in a less energetic transition is physically possible.

On the other hand, the possibility of the existence of a strong NRR component among confined levels is considered in our model. This assumption is represented by the physical connection between the points I1, I2, I3 and I4 in the circuit represented in Fig. 2.12(a) and implies that the four levels share a single QFL. In the following, this case will correspond to the case of study named as "connected", which will have its corresponding mathematical expression. In consequence, two different models are proposed: on the one hand, the "disconnected" one, with four isolated QFLs corresponding to each of the four IBs and represented by the equivalent electrical circuit shown in Fig. 2.12(a) and on the other hand, the aforementioned "connected" model.

The saturation dark current of the recombination term employed in our theoretical model is based on the Roosbroeck-Shockley formula [van Roosbroeck and Shockley, 1954] shown in equation. 2.1

$$\frac{I_{0\mathrm{RS}}\left(E_{\mathrm{m}}, E_{\mathrm{M}}\right)}{A_{\mathrm{cell}}} = \frac{2\,\pi}{h^3\,c^2}\int_{\mathrm{E_m}}^{\mathrm{E_M}} E^2 \exp\left[-\left(E - F_{\mathrm{t}}\right)/k\,T\right]\,dE \tag{2.1}$$

where $I_{0\mathrm{RS}}$ is the saturation dark current calculated with the Roosbroeck-Shockley formula in $\mathrm{A\,cm^{-2}}$, $(E_{\mathrm{m}}, E_{\mathrm{M}})$ is the energy interval of integration of the Roosbroeck-Shockley formula in eV, A_{cell} is the area of the cell in $\mathrm{cm^{-2}}$, h is the Planck constant in eV, c is the speed of light in $\mathrm{m\,s^{-1}}$, F_{t} represents the energy of the IB QFL (located at the level E_{t}), k is the Boltzmann constant in $\mathrm{eV\,K^{-1}}$ and T is the cell temperature in K. The assumption of constant QFL throughout the whole cell volume (i.e. infinite mobility) is also made.

The constants parameterizing the different recombination terms in our model constitute the central point of our analysis. F_{CV} is the coefficient of the saturation dark current ($I_{0\mathrm{RS,CV}}$) corresponding to the fundamental transition (VB→CB) calculated with the Roosbroeck-Shockley formula from equation 2.1. It is then a correction factor that represents the number of times that this component of the recombination is higher in the fitted solar cell than in the purely radiative case. In order to take into account the recombination between VB and CB associated to the term $\exp(\mathrm{eV}/2KT)$, the parameter $F2$

has been included in our model. It then corresponds to the dark saturation current of the recombination term $\sqrt{I_{\mathrm{CV}}}$, being I_{CV} the recombination in the fundamental transition.

The parameters F_{Vi} and F_{Ci} are respectively the coefficients or correction factors of the $I_{0\mathrm{RS}}$ terms associated to VB$\rightarrow E_{\mathrm{ti}}$ ($I_{0\mathrm{RS,Vi}}$) and $E_{\mathrm{ti}} \rightarrow$CB ($I_{0\mathrm{RS,Ci}}$) transitions calculated for the disconnected model. On the other hand, in the connected model there is only one coefficient corresponding to the recombination between the IB levels and the VB ($I_{0\mathrm{RS,VT}}$), denoted as F_{VT} and another one for the recombination between the CB and the IB levels ($I_{0\mathrm{RS,CT}}$), denoted as F_{Ci}. These recombination terms are calculated as the sum of the Roosbroeck-Shockley dark saturation currents corresponding to the different transitions between the VB or the CB and each of the four confined levels located at E_{ti}, as shown in equation 2.2.

$$I_{0\mathrm{RS,VT}} = \sum_{\mathrm{i}=1}^{4} I_{0\mathrm{RS,Vi}} \qquad \text{and} \qquad I_{0\mathrm{RS,CT}} = \sum_{\mathrm{i}=1}^{4} I_{0\mathrm{RS,Ci}} \tag{2.2}$$

2.3.1.3 The multiple-level experiment

The detailed balance model does not consider r_{S} effects and thus, in order to fit the recombination characteristic of actual IBSCs, the measurement of the J_{L}-V_{OC} characteristic arises as an excellent tool, because, as it has already been explained (and justified in equation 1.2), the J_{L}-V_{OC} pairs measured under different concentrations represent the recombination characteristic of the cell without the impact of the r_{S}.

Three different QD-IBSCs and one GaAs reference cell (all fabricated at the University of Glasgow) have been measured under concentrated light up to approximately 10,000 suns and the J_{L}-V_{OC} curves have been obtained at room temperature [Linares et al., 2010b]. Each of the QD samples has been manufactured with a different technological approach. The QD cell denoted as "sample A", which layer structure and detailed characteristics are explained in Ref. [Martí et al., 2007], was manufactured with 10 stacked InAs/GaAs QD layers. The QDs in this sample are relatively small and hence, their ground-state is quite high in energy (enlarging the E_{H} transition and reducing E_{L}). The QD layers are separated by very thin spacers of 10 nm, which produces the accumulation of strain in the vertical direction. The QD cell labeled as "sample B", corresponds to sample SC in Ref. [Antolín et al., 2010a]. The main differences with respect to sample A are the slightly thicker GaAs spacers of 13 nm, the 2 nm thick quaternary $\mathrm{In_x[Ga_yAl_{1\text{-}y}]_{1\text{-}x}As}$ capping layer [Antolín et al., 2010a, Linares et al., 2010a] introduced right after the InAs QDs and the presence of the QD seed layer (explained in section 5.2 and schematically represented in Fig. 5.5). These last two features were included with the purpose of enhancing the QD

size while preserving the QD aspect ratio, so that the IB is more separated from the CB. Sample B also includes the so-called field damping layers [Martí et al., 2008b]. "Sample C" in this work is the one with a layer structure as the one depicted in Fig. 2.1. It is similar to sample B except for the lack of a thick n-emitter (the 200 nm n^+ AlGaAs BSF layer acts as the n-emitter in this case) and also because of the higher number of stacked QD layers (30 instead of 10) and the thicker spacers (84 nm instead of 13 nm). The latter are meant to prevent both carrier tunneling effects and the accumulation of strain. Table 2.2 collects information from different sources about the location of the energy of the confined states and CB minima (actually, the energy of the WL) comes from: the room temperature external QE from Fig. 3 Ref. [Antolín et al., 2010a] for samples B and C and for sample A, the data are taken from the PR data in Ref. [Cánovas et al., 2008].

Table 2.2: Energy (in eV) of the four confined levels identified in each of the QD-IBSC samples used in this multiple-level model [Linares et al., 2010b].

Energy level	Sample A	Sample B	Sample C
E_{C}	1.35	1.21	1.39
E_{t4}	1.225	1.144	1.18
E_{t3}	1.175	1.105	1.14
E_{t2}	1.137	1.015	1.175
E_{t1}	1.052	0.953	0.974

E_{V}, is considered as the zero potential energy

The fitting to the three QD-IBSCs and the GaAs reference cell (which layer structure is explained in section 2.2.1) are shown in Fig. 2.13. Sample A can only be fitted with the connected model, while samples B and C have to be fitted using the disconnected model.

The fitting to the concentrated light J_{L}-V_{OC} plot of the reference cell (Fig. 2.13(d)) reveals that F_{CV}=150 (150 times the Roosbroeck-Shockley term), meaning that the total recombination in our GaAs cell is 150 times the minimum theoretical value (radiative limit). This value can be seen as the baseline for comparison with the QD-IBSC prototypes. $F2$=0.13, which has no physical meaning, except for giving an idea of the magnitude of the non-radiative recombination for further analysis of QD solar cells.

The fitting to sample A provides an F_{CV}=27,000, which implies a considerably high deterioration of the host subcell and an $F2$=2.8, meaning that the introduction of the QDs has severely increased the non-radiative recombination. F_{VT}=12 and F_{CT}=2, which will have to be compared with further fittings.

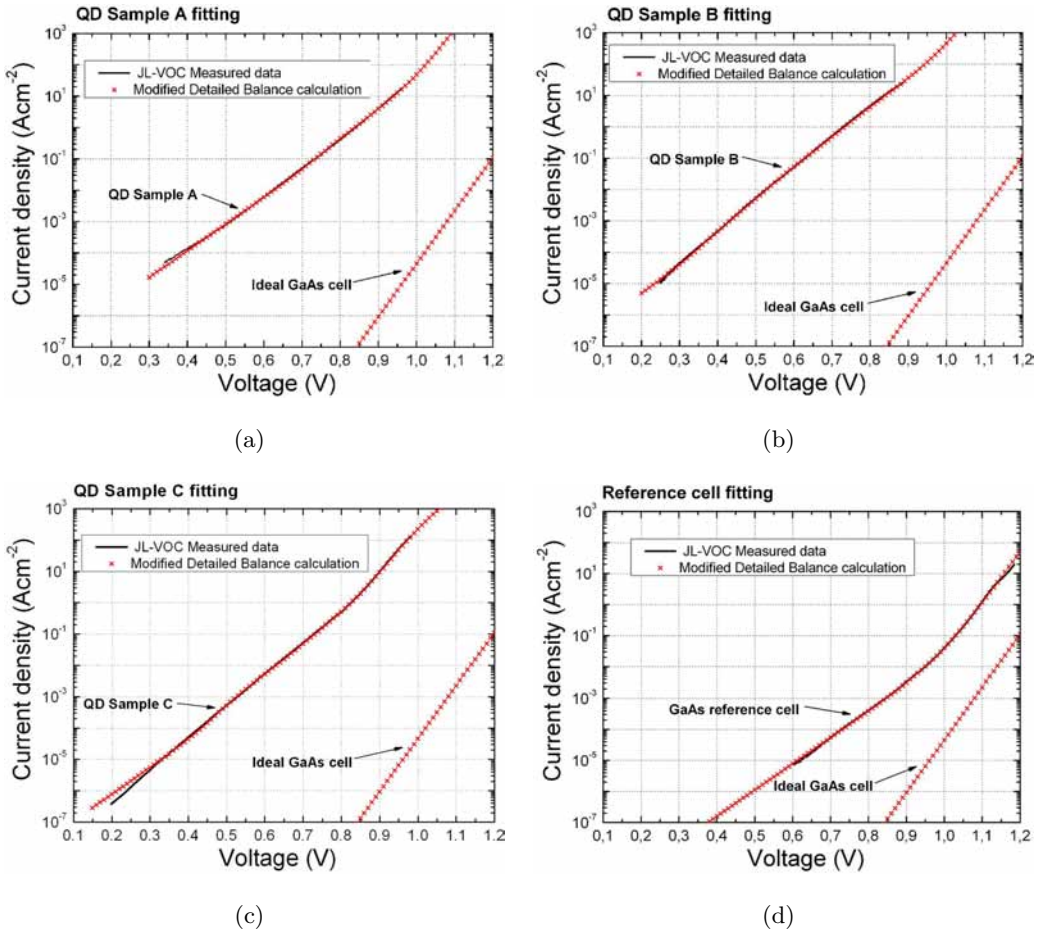

Figure 2.13: Detailed balance fitting performed with with the multiple-level model. The values of the different fitting parameters can be found in the text. (a) Sample A. (b) Sample B. (c) Sample C. (d) GaAs reference cell [Linares et al., 2010b]. The fitting of the purely radiative GaAs cell (F_{CV}=1 and $F2$=0) is shown in all figures for comparison.

The fact that samples B and C require the disconnected level model (four independent QFLs) is probably related to their larger QDs and the better aspect ratio of these QDs with respect to sample A. On the other hand, the fact that sample B has such low E_{C} value (as shown in Table 2.2) is related to the large number of QD confined states that are located very close to each other (almost producing a continuum of states) from E_{C}=1.21 eV, probably influenced by the larger QDs formed in the upper QD layers due to the accumulation of strain.

The following Roosbroeck-Shockley parameters fit the concentrated light J_{L}-V_{OC} curve measured in sample B with the disconnected model: F_{CV}=1,400; $F2$=1.8; F_{V1}=2,000; F_{V2}=1,300; F_{V3}=1,300; F_{V4}=0.01; F_{C1}=0.3; F_{C2}=2; F_{C3}=6; F_{C4}=0.01. And these other factors fit sample C with the same model: F_{CV}=300; $F2$=18; F_{V1}=90; F_{V2}=50; F_{V3}=130; F_{V4}=160; F_{C1}=100; F_{C2}=200; F_{C3}=100,000; F_{C4}=100,000.

It is important to remark that a low Roosbroeck-Shockley factor does not necessary imply a strong radiative behavior of the transition, since it can also be related to a poor absorption [Luque et al., 2010a]. Actually, the two mechanisms (increased recombination and poor absorption) are combined in the fitting parameter. This is because the detailed balance model assumes total absorption of the incoming photons and therefore, even in the radiative limit, the associated fitting parameter of a transition may be below 1 (although it may seem against intuition).

The treatment given to the concentrated light J_{L}-V_{OC} curves presented in this section can be useful to gain insight on the magnitude of the different components of the IBSC recombination.

2.3.2 Characterization of the bandgap energy by means of an electrical measurement (fitting of the $J_{01}(t)$)

The semiconductor bandgap can be obtained by means of electrical characterization by plotting $m_1 \,\mathrm{Ln}(J_{01})$ with respect to $1/T$, where m_1=1 is the ideality factor of the diode and J_{01} is the reverse saturation current density corresponding to radiative recombination in the neutral zones. Different values for $J_{01}(T)$ of a GaAs solar cell have been obtained from the fitting to the concentrated light J_{L}-V_{OC} curve at different temperatures. This allows plotting the curve presented in Fig. 2.14. Then, the material bandgap can be determined from the slope of the curve. A value of E_{G}=1.51 eV is obtained for the GaAs solar cell characterized in this example, which seems to be quite accurate.

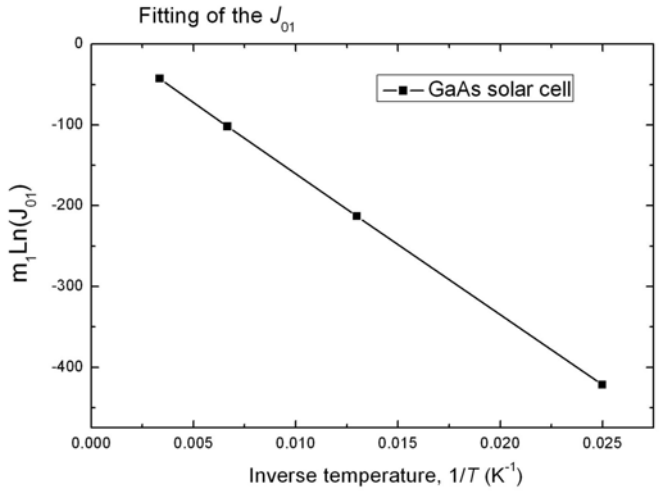

Figure 2.14: Logarithm of the fitted J_{01} plottedvs the inverse of the inverse temperature at which the cell is measured.

This is hence, another use of the concentrated light measurements applied to the characterization of solar cells.

2.3.3 Temperature-dependent modeling of the QD-IBSC

The low temperature concentrated light J_L-V_{OC} characterization can also be used to provide feedback to further IBSC modeling as the one presented in Ref. [Luque et al., 2012a]. The model has allowed fitting to the temperature-dependent recombination curves presented in Fig. 2.2 with a reasonable accuracy.

2.4 Summary

It was predicted that the increased recombination and the associated strong reduction of the device V_{OC} observed in the IBSC operating at 1 sun could be counteracted by the use of concentrated illumination. This theory has been verified experimentally by means of characterization at low temperature, which is necessary to slow down the fast IB-CB thermalization rate that takes place in InAs/GaAs QD-IBSCs at room temperature.

The trend of the QD-IBSC J_L-V_{OC} characteristic under concentrated light towards an exponential slope closer to e/kT is identified as the mechanism responsible for the rapid voltage recovery. The change in slope can be explained by a recombination initially dominated by the IB that evolves toward a recombination only dominated by the fundamental transition, i.e. that from the CB to the VB, making the IBSC recombination equivalent to that of a single gap solar cell. The latter has been verified experimentally using low temperatures.

In addition, the maximum measured IBSC V_{OC} (1.5 V) corresponds to a QFL separation that is very close to E_G/q (1.52 eV at T=20 K). This largely exceeds the photon energy absorption threshold. An output voltage that is not limited by its absorption threshold is a proof of the voltage preservation operation principle.

Other characterization techniques also carried out from the results obtained with the concentrated light experiments, such as the determination of the material bandgap by means of electrical characterization and the fitting of multiple-level IBSCs depending on the energy of the different confined states of the QD-IBSC, have also been presented in this chapter.

Chapter 3

Characterization of bulk-IBSCs under concentrated light

3.1 Introduction

Besides QDs, bulk IB semiconductors constitute another type of promising IB materials [Luque and Martí, 2010b, Luque et al., 2012b]. Several bulk IB semiconductors have been fabricated (some of them for the first time) and characterized during the European project IB materials and solar cells for PV with high efficiency and reduced cost (IBPOWER). These new IB materials have allowed the implementation of IBSCs and most of them (except the QD-IBSC) have been implemented by means of the incorporation of a transition element into a conventional bulk semiconductor.

In this chapter, four new families of IB materials and corresponding IBSCs have been engineered in the framework of the IBPOWER project. This European research initiative, coordinated by IES-UPM, has brought together four research lines devoted to the fabrication of IB materials from which IBSCs have also been manufactured. Each of the four partners of IES-UPM in this European venture have specialized in one type of IB material:

- The research group of Prof. Colin Stanley, from the University of Glasgow (UK), was in charge of the InAs/GaAs QD-IBSC
- The research group of Prof. Tom Foxon, from the University of Nottingham (UK), was in charge of the bulk-based InGaN:X and GaAs:Fe IBSCs
- The research group of Prof. Hans-Werner Schock, from the Helmholtz-Zentrum Berlin (Germany), was in charge of the thin-film (TF) $CuInS_2$:X and $CuGaS_2$:X IBSCs

- The research group at the company RIBER (France), led by Dr. Catherine Chaix was in charge of the bulk-based GaAs:Ti IBSC

In addition to the coordination tasks, IES-UPM has conducted the characterization of all the IBSCs fabricated during the development of the project. In this respect, the low temperature concentrated light characterization technique has played an important role. It has been employed to determine whether the voltage preservation principle was fulfilled by these novel devices and thus, whether they behaved as actual IBSCs. The results are shown in this chapter.

3.2 Characterization of chalcopyrite TF-IBSCs under concentrated light and low temperature

IB chalcopyrite thin-film technology [Palacios et al., 2007] is a versatile technology, developed by one of the IBPOWER project partners, the Helmholtz-Zentrum Berlin für Materialien und Energie GmbH, expert in thin film solar cells. This low-cost technology is meant to perform at 1 sun illumination. Under this low irradiance conditions the detailed balance analysis of IBSCs based on host materials with bandgaps of energies lower than 1.14 eV shows that they cannot lead to solar cells wth efficiencies higher than their counterparts without IB.

Fig. 3.1(a) shows with a solid black line, the 1 sun IBSC limiting efficiency as a function of the total bandgap, with the sub-bandgap energy, E_{L}, also indicated next to each of the points of the plot [Martí et al., 2008c]. The figure represents, with solid black dots, the optimum efficiency of IBSCs implemented with three common Cu-containing chalcopyrite thin film technologies, together with the state of the art data corresponding to 2008 from reported performance (solid black squares) of solar cells based on these materials. A dashed line shows the single gap efficiency limit for comparison.

Fig. 3.1(b) shows the detailed balance efficiency limit of one of the thin film chalcopyrite IBSC candidates as an example: the $CuGaS_2$ IBSC implemented with different transition elements and plotted with respect to the energy from the gap between the IB and the VB and CB of the chalcopyrite host semiconductor.

Two types of Cu-containing chalcopyrite thin-film materials have been explored in this work: the $CuInS_2$ chalcopyrite solar cell (CIS) and the $CuGaS_2$ chalcopyrite solar cell (CGS), both of them incorporating transition elements acting as DLs that give rise to the IB. Ti, Fe and Sn have been either incorporated by diffusion from the substrate ($CuInS_2$:Fe and $CuInS_2$:Ti) or by co-evaporation ($CuInS_2$:Sn, $CuGaS_2$:Ti, $CuGaS_2$:Fe and $CuGaS_2$:Sn). $CuIn_{1-x}Ga_xS_2$ alloys allow tuning the bandgap of the host semiconductor so

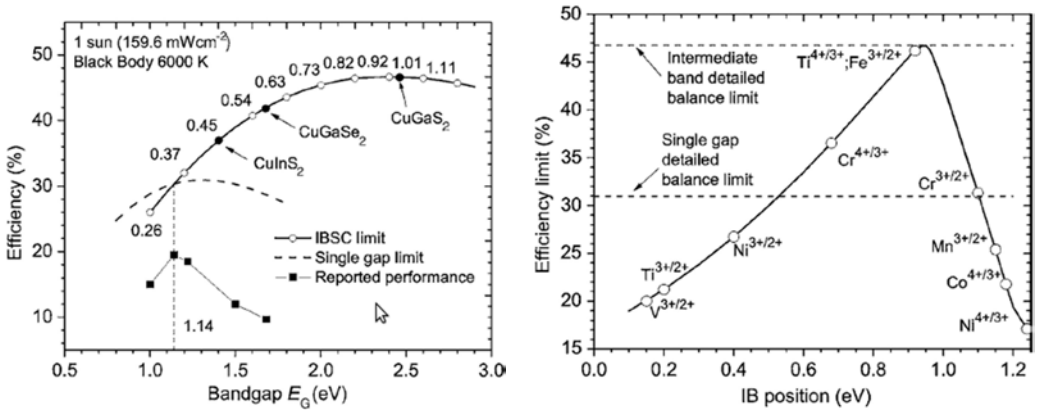

(a) (b)

Figure 3.1: Theoretical efficiencies of thin-film IBSC cells calculated for 1 sun illumination. (a) As a function of the total bandgap, E_G. The lower sub-bandgap energy is also indicated, as well as experimental data from three cases of common Cu-containing chalcopyrite thin film technologies. The actual reported efficiency of these technologies and the limiting efficiency of a single gap solar cell are also plotted for comparison. (b) Detailed balance efficiency of the $CuGaS_2$ IBSC with respect to the energy separation of the IB from either the VB or the CB. The cases corresponding to the different transition elements, each of them creating the IB at a different position within the host material bandgap, are also indicated. These figures are reproduced from Figs. 2 and 3 in Ref. [Martí et al., 2008c].

that it can be optimized for IBSC purposes, however, the growth of a pentanary compound, i.e. $CuIn_{1-x}Ga_xS_2$:X, may be complicated to implement because different phases can appear during the formation of the alloy.

3.2.1 CIS solar cells

CIS materials are not the best candidates for implementing IBSCs from the theoretical efficiency point of view, however, as pointed out in Ref. [Marsen et al., 2010], a good electronic quality can be obtained with this technology at the moment, which made it a good starting point for exploring the IBSC concept. Even if this type of technology is not designed for its use under concentrated light, these type of experiments are still very useful as characterization tool.

The cells were fabricated with a $Mo/CuInS_2/CdS/ZnO$ device structure. In fact, due to the technological difficulty regarding the fabrication of an n-type $CuInS_2$, the IB material ($CuInS_2$:Ti) is not isolated from the contacts as the IB theory states. In this case, the IB material is in direct contact with the Mo, which acts as the metallic contact. This fact will have important implications.

Only the $CuInS_2$:Ti technology has been considered in this study. Fig. 3.2 shows the concentrated light I_{SC}-V_{OC} characteristic of the CIS reference cell without Ti measured at

room temperature. This plot is shown as an example of concentration measurement carried out on a thin film solar cell. J_{L} values could not be appropriately measured (projected gray dashed curves in the figure) in these cells, due to the combined effect of high r_{S} and low r_{P} present in these cells. As a consequence, current-deficient J_{SC} (compared to the J_{L} values) polarization points had to be obtained instead. The chalcopyrite I_{SC}-V_{OC} curve did not seem to be affected by severe heating problems during its measurement and it apparently superimposed well to the dark curve in the low current range.

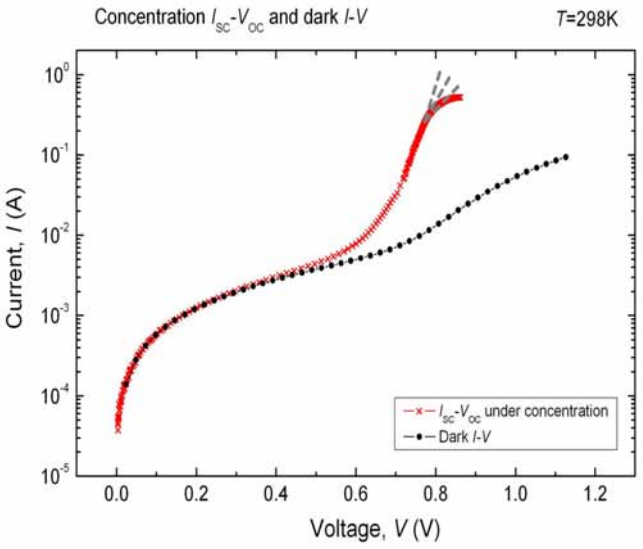

Figure 3.2: I_{SC}-V_{OC} characteristic under concentrated light of the CIS reference cell (without Ti) measured at room temperature. This example shows the different issues concerning the measurement of thin-film chalcopyrites. The gray dashed lines indicate possible extrapolations of the I_{L}-V_{OC} curves where the r_{S} does not affect.

In general, the concentrated light measurements at low temperature performed in these chalcopyrite solar cells are complex, because the device is not meant to operate under concentration. Nevertheless, low temperature concentrated light characterization was successfully performed in the CIS reference cell. Fig. 3.3 represents the electrical response as a function of the temperature of this cell. In Fig. 3.3(a) the evolution of the maximum V_{OC} obtained for temperatures ranging from 300 K to 20 K can be observed. The maximum V_{OC} is obtained at T=200 K, where it reaches a value of 911 mV, still very far from the E_{G}/q value of the chalcopyrite (∼1.5 V). The CdS layer and/or the band offsets at the CIS/CdS interface may be responsible for the reduced V_{OC} value. $V_{\mathrm{OC}}(T)$ slightly decreases for T=150 K and then progressively diminishes for lower temperatures which may be due to the deterioration of the device under such temperature conditions.

Regarding the measurement of the $I_{\mathrm{SC}}(T)$ under concentrated light shown in Fig. 3.3(b), we observe that this magnitude also improves from T=298 K to T= 200 K, but

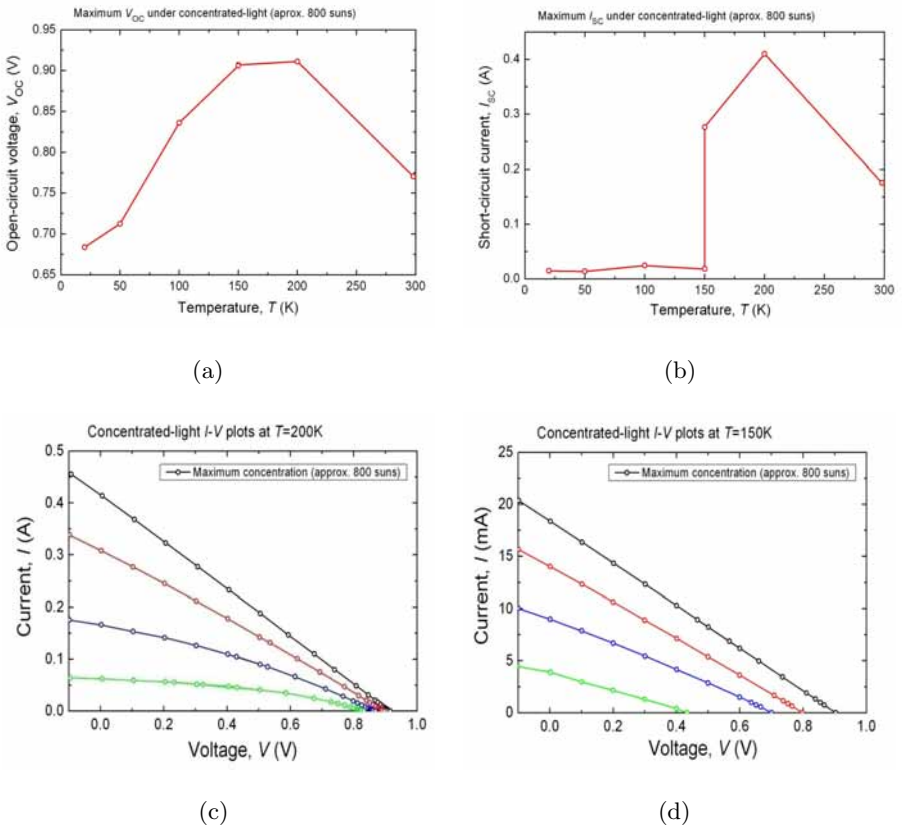

Figure 3.3: Plots of the electrical characteristics obtained for the CIS reference cell measured under approximately 800 suns (inside the cryostat) and for a wide range of temperatures, from T=298 K down to T=20 K. (a) Maximum $V_{\rm OC}(T)$. (b) Maximum $I_{\rm SC}(T)$. (c) and (d) show concentrated light I-V curves respectively performed at T=200 K and at T=150 K measured at a maximum concentration of approximately 800 suns.

then, when T=150 K, it suddenly decreases. Actually, at this temperature, the cell experiences a quite bizarre and unexpected electrical behavior: besides the reasonable worsening suffered with respect to $I_{\rm SC}(T$=200K), the $I_{\rm SC}$ dramatically decreases, at least one order of magnitude, when the experiment is repeated and then it never recovers again to the original values.

Figs. 3.3(c) and 3.3(d) show concentrated light I-V curves again from the reference cell and respectively performed at T=200 K and at T=150 K, when the experiment is performed at this temperature for the second time, in order to exemplify the dramatic drop in $I_{\rm SC}$ between the electrical characteristics acquired at this two temperatures. Actually, it is remarkable that the $r_{\rm S}$ of the measurement at T=150 K has increased with respect to the measurement at T=200 K, i.e. the concentrated light I-V curve is almost a straight line, even when the current is much smaller. But the $V_{\rm OC}(T$=150K) is not significantly diminished, at least the one corresponding to the highest concentration. The cell keeps

providing this reduced current and no longer recovers for lower temperatures. A potential barrier for the carriers may appear at low temperature, making the extraction of carriers difficult. Fig. 3.4(a) shows a sketch of the electronic band diagram of the CIS cell which may eventually help to understand its electrical behavior.

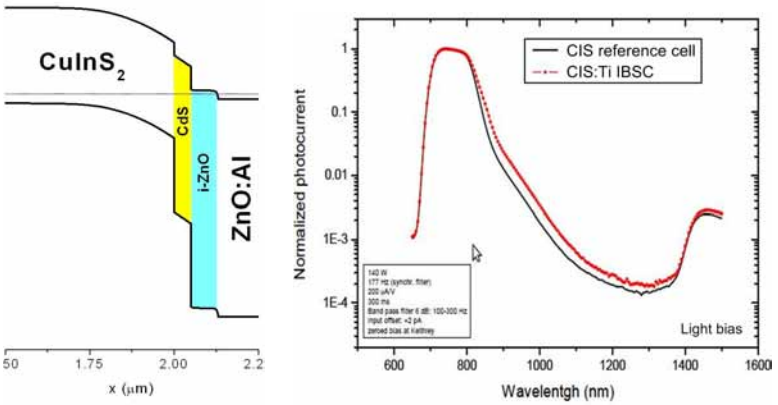

(a) (b)

Figure 3.4: (a) Sketch of the electronic band diagram of the CIS thin-film solar cell fabricated at HZB. (b) Normalized PC absorption of both the CIS reference and IB cells. The measurement features are indicated in the figure. Courtesy of Dr. David Fuertes.

It may be important to remark that these measurements have been progressively performed from room temperature to low temperature and not the other way around. The reason is that the cell is degraded at low temperature and this degradation can be irreversible. Proceeding in this way, at least the characteristics at higher temperatures might be obtained.

All of the foregoing is also related to the so-called "memory effect", which can difficult the proper electric characterization of these cells at low temperatures. This effect can be originated by the metastabilities produced by the large number of defects inherent to this type of technology. Besides, this memory effect can be responsible for the aforementioned non-repeatability found in the I_{SC} signal at T=150 K, which was further explored in Fig. 3.5, where the degradation of the thin-film solar cell is observed by measuring the I-V dark curves several times under the same set of conditions. The characteristics progressively worsen as new tests are carried out, but the recovering of the initial performance is not assured.

In Fig. 3.6, the concentrated light I_{SC}-V_{OC} characteristics of the CIS:Ti cell corresponding to room and low temperature are shown. After the measurement at T=200 K, the cell breaks and thus, the concentration measurement cannot be measured at lower temperatures. Nevertheless, the results show that, although the IBSC partially recovers

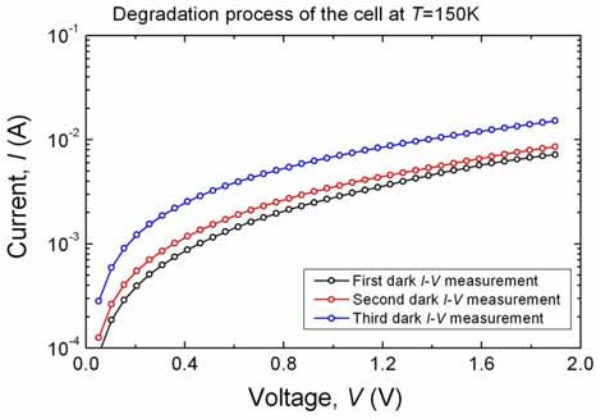

Figure 3.5: Memory effect observed during the measurement of the CIS reference cell dark I-V curves at low temperature (T=150 K). The dark curves were consecutively acquired after the measurement of the solar cell under concentrated light.

the degraded V_{OC}, it is limited by either the electronic band structure or the lack of one of the emitters that should be sandwiching the IB material. Therefore, according to the IBSC theory, the QFL split between the IB and one of the other bands (the VB or the CB) cannot not possibly take place anyway.

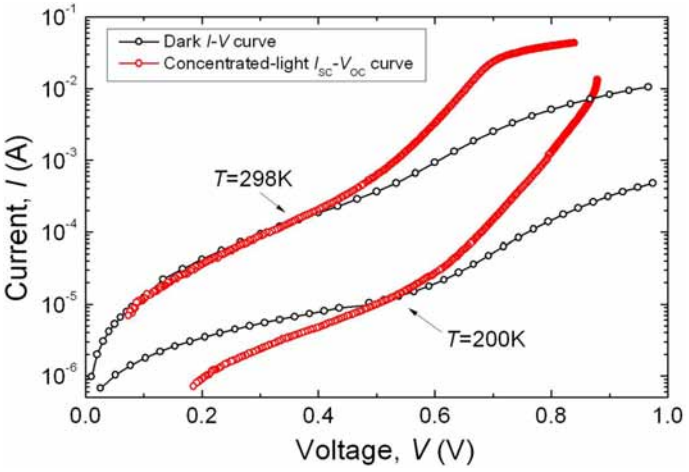

Figure 3.6: Concentrated light I_{SC}-V_{OC} characteristics of the CIS IBSC (with Ti) measured at room and low temperature. Several problems affect the experiment and prevent the low temperature measurements to be appropriately characterized. Nevertheless, the results show that, although the IBSC partially recovers the degraded V_{OC}, it is limited by either the electronic band structure or the lack of one of the emitters sandwiching the IB material.

The fact that Fig. 3.4(b) shows sub-bandgap photocurrent for both the CIS reference cell and its counterpart with Ti, indicates that the presence of the IB may not be responsible for this sub-bandgap absorption. Actually, this phenomenon is usually observed in chalcopyrite cells and it is very likely produced by the high density of defects of this type

of crystals. Anyway, the maximum $q\,V_{OC}$ does not reach the energy absorption threshold of approximately 1.2 eV, that is deduced from the extended low-energy tails of the photocurrent.

The Ti-containing cells systematically showed higher conversion efficiencies than Ti-free $CuInS_2$ reference cells [Marsen et al., 2010] due to increased V_{OC}. However, no increase (nor reduction) in the I_{SC} was detected.

3.2.1.1 Other problems regarding the characterization of thin-film solar cells under concentration

As well as the other IBSCs with intentionally incorporated large amounts of impurity levels and/or defects in the crystal structure that will be described later, the $CuInS_2$:Ti cell also presents capacitive effects that become apparent when measuring the V_{OC} under concentrated light. These capacitive effects are more pronounced at low temperatures and may ultimately prevent the measurement of the cell under high irradiances. The only solution is lowering the concentration factor, typically by one order of magnitude from the 800 suns top reference that can be reached inside the cryostat, until the electrical signal can be properly acquired. An example of this problem is depicted in Fig. 3.7, where the $V_{OC}(T{=}200\text{K})$ of the CIS:Ti cell (top panel) saturates at a voltage slightly lower than 0.9 V. This $V_{OC}\,(t)$ signal does not follow the irradiance signal acquired with the photodetector. The two signals shown in the figure are plotted within the same temporal axis during a flash light discharge of approximately 20 ms.

These V_{OC} saturation and desynchronization effects are very likely related to a large capacity originated by these defects. These problems are similar to the ones that will be described in section 6.3.3.1 (Fig. 6.15).

3.2.2 CGS:Fe solar cells

The thin-film IBSCs implemented with GGS:Fe were also measured under low temperature and concentrated light. In principle, this high bandgap chalcopyrite doped with Fe is characterized by one of the maximum limiting efficiencies, as pointed out by Fig. 3.1(b). The major inconvenient is that CGS technology is not as mature as the CIS technology and hence, worse starting performances are expected.

$CuGaS_2$:Fe solar cells, also with a Mo/$CuInS_2$/CdS/ZnO device structure, were fabricated (in large area devices) at the Helmholtz-Zentrum Berlin and sent to IES-UPM, where they were encapsulated and measured. The CGS solar cell studied in this work was nominally doped with Fe at a considerably high concentration, although compositional

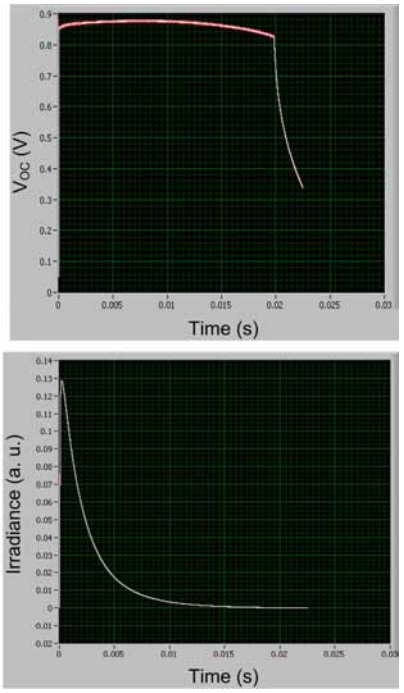

Figure 3.7: (Top) Plot of the $V_{OC}\,(t)$ signal of the CIS:Ti cell measured at T=200 K and directly acquired by the DAQ card (prior to the processing of the data) during the flash light pulse. (Bottom) Irradiance (in arbitrary units) during the flash pulse.

measurements revealed the lack of such Fe impurities, at least at the nominal concentrations.

External QE experiments [Martí et al., 2012] performed on CGS solar cells at room temperature (Fig. 3.8(b)) showed sub-bandgap photoresponse until roughly 1.68 eV (it must be recalled that the total bandgap of this chalcopyrite is approximately 2.4 eV), although even the reference cell (with nominally 0% of Fe) showed a similar response. This result implies that again the sub-bandgap tails may come from structural defects from the chalcopyrite crystals and not by the transition metal impurity.

Low temperature concentrated light characterization was carried out on these devices, obtaining the I_{SC}-V_{OC} curves in Fig. 3.8(a). Again, the electrical characterization could not be performed at very low temperatures, because the cells broke again at T=150 K. The maximum V_{OC}, obtained at T=200 K, corresponds to 726 mV, well below from the absorption threshold. These CGS structures are also affected by the two major drawbacks advanced in the CIS case: 1) the CdS layer and/or the band offsets at the CGS/CdS interface may be limiting the total bandgap of the structure and 2) the region with transition metal impurities (in case they are incorporated to some extent) is not separated at both sides from the contacts by non-doped (conventional) semiconductor layers.

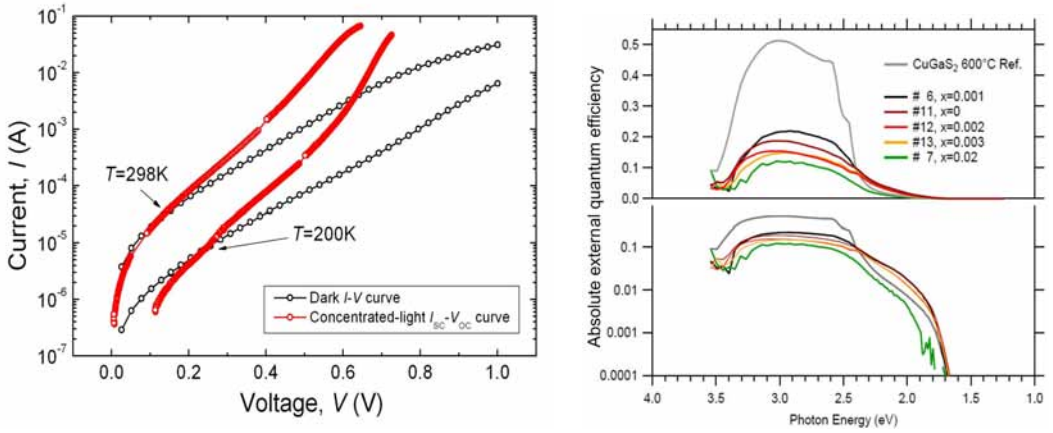

(a) (b)

Figure 3.8: (a) Concentrated light I_{SC}-V_{OC} characteristics of the CGS:Fe cell measured at room and low temperature. (b) Absolute external QE of several CGS:Fe solar cells, (black, brown, red, yellow and green lines) nominally with different concentration of Fe, as well as of the CGS reference solar cell (gray line). The lower part of the figure shows the absolute external QE in logarithmic scale, where the absorption threshold can be identified in all cells approximately at 1.7 eV. The QE plots are a courtesy of Dr. Björn Marsen.

A study of the decay of the $V_{OC}(t)$ with time was also performed in this cell in order to verify whether the electrical characterization was appropriately synchronized with the light as well as to qualitatively measure the equivalent capacity of the chalcopyrite solar cells. The experiment, shown in Fig. 3.9, is performed by abruptly interrupting the concentrated light pulse at different instants of time (represented with different colors in the figure) while monitoring the V_{OC} even after the light has completely vanished. Actually, depending on the capability of these defects to host and release electric charge that flows to/from the CB (or the VB) and the DL defects, the so-called persistent photovoltage (and photocurrent) can be observed. The experiment is performed at low temperature (T=200 K), where this capacitive effect results magnified.

3.3 Characterization of other bulk-IBSCs

The presence of DL impurities in the semiconductor bandgap has been traditionally considered detrimental for the performance of solar cells. However, the IB theory predicts [Luque et al., 2006a] that when incorporated at sufficiently high concentration, the wave-function of foreign species can delocalize, inhibiting the so-called breathing modes and thus suppressing the emission of multiple phonons and therefore the detrimental Shockley-Read-Hall non-radiative recombination.

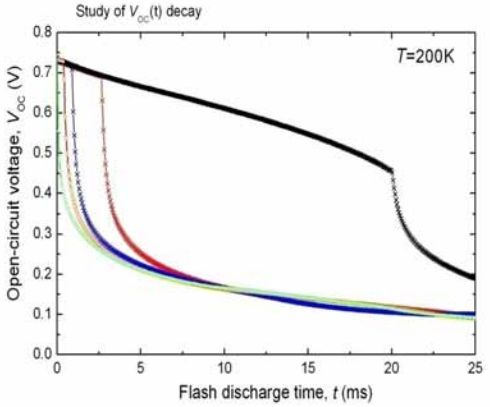

Figure 3.9: $V_{\mathrm{OC}}(t)$ decay experiment performed by abruptly interrupting the concentrated light pulse coming from the flash at different instants of time. This effect is produced by the DLs present in this type of solar cells and it can be seen as mostly responsible for the large equivalent capacity of the cell.

3.3.1 Transition element impurity silicon-based IBSCs

Manyof the IBSCs presented in this Thesis are based on III-V materials, which show a number of advantages regarding the high ratio of radiative to non-radiative recombination, the relatively high absorption coefficients, the possibility of tunning alloyed compounds, etc. However, crystalline Si (Si-c) technology is very important in PV because of the availability of the material, the reduced cost, the maturity of the technology, etc. Regarding the IBSC, Si does not have an adequate bandgap for implementing an efficient IBSC, because this is too small and far from the optimum. Besides, any IB created within such a small semiconductor bandgap energy (∼1.12 eV) will very likely have a high thermal escape rate. Nevertheless, Si, as InAs QDs is an excellent workhorse for studying the implementation of the IBSC concept.

The incorporation of large amounts of Ti in c-Si has been proposed as a possible candidate material for IBSCs [Olea et al., 2008]. As it has been demonstrated in Ref. [Antolín et al., 2009], the initially degraded carrier lifetime of a semiconductor doped with a DL impurity (Ti on Si, in this example), can be recovered if the impurity is incorporated in very high concentrations. This experiment verified the theory presented in Ref. [Luque et al., 2006a], where it was stated that at sufficiently high concentration, the delocalization of the electronic wave-function in DLs in meant to inhibit non-radiative recombination.

In our case, a Si-based IBSC with Ti has been implemented thanks to the collaboration of the Universidad Complutense de Madrid (UCM) and the Universidad Politècnica de Cataluña (UPC). This IB material is based on crystalline Si where a highly doped Ti-layer is incorporated by ion implantation and subsequent recrystallization by pulsed-laser melting (PLM). The IB region is grown on an n-type Si layer and the isolation from the

contacts is completed by adding a hydrogenated amorphous Si (a-Si:H) p-type layer as in a heterojunction with intrinsic thin layer (HIT) [Taguchi et al., 1990, Tanaka et al., 1992]. The HIT technology is a promising and relatively cheap Si-based technology with a reported efficiency of 22% [Tsunomura et al., 2009].

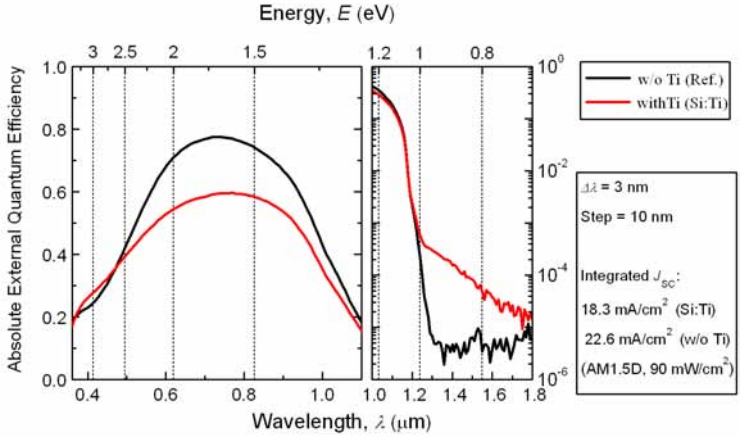

Figure 3.10: Absolute external QE measurements of the HIT Si:Ti solar cell and its reference cell (without Ti). On the left part of the figure, the measurement in linear scale is shown, then the low energy range of the external QE represented in logarithmic scale and on the right, the values of the integrated J_{SC} of both cells. Courtesy of Mrs. Esther López.

Fig. 3.10 shows the absolute external QE plot of the HIT Si:Ti IBSC implemented in this work, together with the results of an equivalent cell (except for the incorporation of Ti) used as benchmark. The QE experiment shows that the reference cell (solid black line) has a higher response than the Si:Ti cell (solid red line) in the supra-bandgap range, although the Si:Ti has a weak but noticeable response in the sub-bandgap region, until approximately 1.8 μm.

Characterization under concentrated light has also been performed on these cells. Low temperature concentrated light experiments are only shown in the J_{SC}-V_{OC} format for the HIT Si reference cell (see Fig. 3.11(a)), because equivalent results from the HIT Si:Ti cell present some anomalies and its interpretation can be confusing. Actually, in this case, the more simple J-V curves under concentration are preferred. The experiment is strongly affected by a very large r_P which again prevents the measurement at reverse bias, thus obtaining J_{SC} and not J_L. An electronic noise typically associated to the source-meter biasing of relatively bad quality solar cells in the low photocurrent range, prevents the measurement of the concentrated light J_{SC}-V_{OC} pairs below 10^{-2} mAcm^{-2}. On the other hand, the desynchronization of both the $I_{SC}(t)$ and the $V_{OC}(t)$ signals with respect to the received irradiance (from the flash light) can be observed in Fig. 3.11(b). The saturation of the $V_{OC}(t)$, severely hinders the appropriate acquisition of this measurement. It is specially

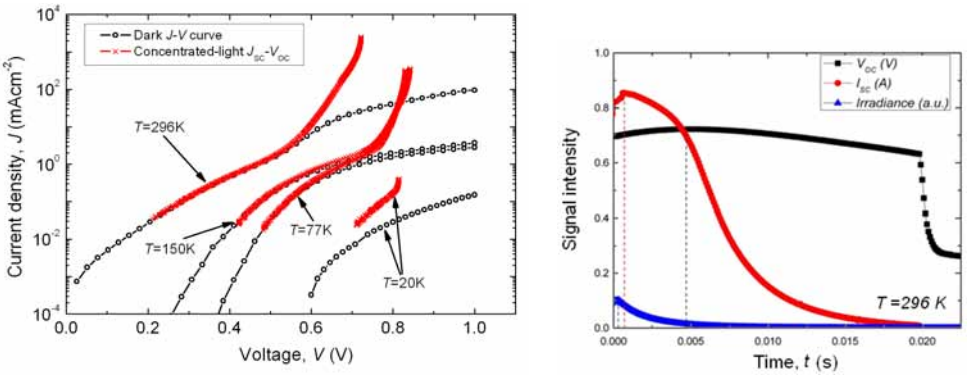

(a) (b)

Figure 3.11: (a) Concentrated light J_{SC}-V_{OC} characteristics of the HIT Si reference cell measured at room and low temperatures. A very strong noise and a pronounced desynchronization of the V_{OC} signal affects the measurement at low temperatures. (b) V_{OC}, I_{SC} and irradiance signals represented in accordance with time. The uncorrelated maximums of these signals are represented with dashed lines.

pronounced at low temperatures. The superposition principle is fulfilled in three out of the four curves. Only at T=20 K this superposition cannot be verified. Nevertheless, this may be due to the impossibility of acquiring sufficient data in the low current range because of the high electronic noise. The behavior of the J_{SC}-V_{OC} at T=150 K and T=77 K in the high concentration range is very similar. Surprisingly, the T=77 K curve is even displaced towards the left, which is counterintuitive regarding the conventional V_{OC} enhancement that takes when the temperature is lowered. Actually, the maximum V_{OC} (841 mV) is obtained for the measurement at T=150 K.

Fig. 3.11(b) presents an example (at room temperature) of the desynchronization between the I_{SC} and the V_{OC} signals with respect to the evolution of the flash irradiance over time. As deduced from the previous low temperature curves under concentration, besides being desynchronized, the V_{OC} saturates. Even the current response is desynchronized, which is not very common in this type of measurement.

Fig. 3.12 shows the concentrated light J-V curves of the HIT Si:Ti IBSC measured at a maximum concentration (approximately 800 suns). Two main results can be extracted from these plots. On the one hand, the V_{OC} of the IBSC recovers from 387 mV at room temperature up to 540 mV at T=20 K, which is a remarkable increase, but still very far from the absorption threshold energy: 0.73 eV at room temperature (deduced from an absolute external QE measurement, not shown in this work). On the other hand, such maximum V_{OC} is obviously still far from E_G/q of the cell, which in this case would correspond to the c-Si emitter bandgap (which is more restrictive than the a-Si:H): 1.12 V at room temperature.

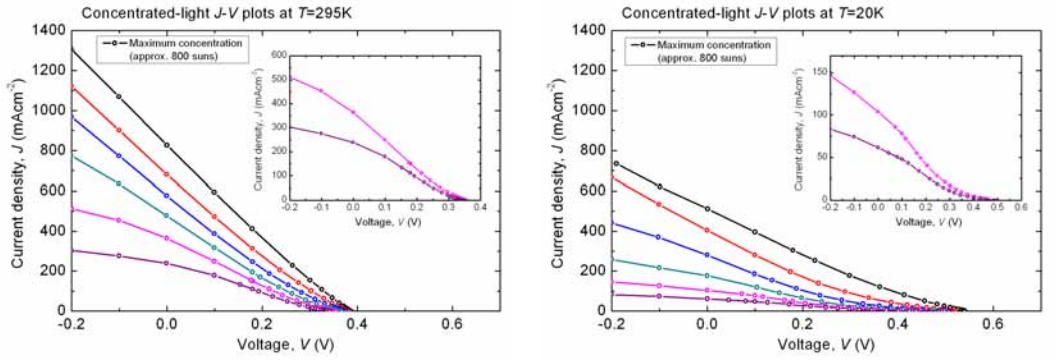

(a) (b)

Figure 3.12: Concentrated light J-V curves of the HIT Si:Ti IBSC measured at a maximum concentration of approximately 800 suns. (a) At room temperature. (b) At very low temperature (T=20 K). This experiment demonstrates that the voltage preservation principle is not fulfilled in these cells.

3.3.2 Transition element impurities in III-V IBSCs

Two different III-V semiconductor material hosts have been studied during this Thesis for the implementation of an IBSC: $In_{1-x}Ga_xN$ and GaAs.

The $In_{1-x}Ga_xN$ ternary alloy has the inconvenient of not being a mature semiconductor for PV applications. Nevertheless, $In_{1-x}Ga_xN$ doped with high concentrations of Mn impurities has been theoretically proposed as an IB material [Martí et al., 2009, Martí et al., 2008d]. Such new challenging material has been fabricated by Prof. Foxon's research group at the School of Physics and Astronomy, at the University of Nottingham. $In_{1-x}Ga_xN$ alloys were selected as semiconductor hosts for IB materials mainly because of two reasons. The first of them is that they cover a wide range of bandgaps. This can be deduced from Fig. 3.13(a), where a theoretical calculation of the $In_{1-x}Ga_xN$ ternary bandgap is shown. The (constant) position of the energy level introduced by the Mn impurities that form the IB and the corresponding sub-bandgaps in which E_G is divided are also shown in the figure. The second reason is that some transition metals, such as Mn, present a high solubility in this host semiconductor, which is important regarding the incorporation of the large amounts of impurities required for the delocalization of their wavefunction.

Fig. 3.13(b) shows the limiting efficiency of the $In_{1-x}Ga_xN$:Mn IBSC and the reference cell (without Mn) calculated as a function of the Ga content for both the black body and the AM1.5G spectra. A quite wide range of the efficiency curve corresponding to the low Ga content region has an IBSC limiting efficiency surpassing 50%, justifying the research on this new IBSC prototype.

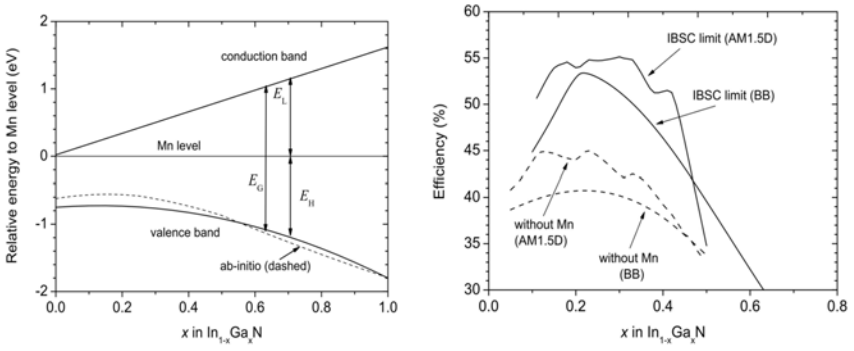

(a) (b)

Figure 3.13: Theoretical calculation of the performance of $In_{1-x}Ga_xN$:Mn material as an IBSC. (a) The bandgap of the $In_{1-x}Ga_xN$ ternary alloy can be calculated as the difference between the CB and the VB. The energy of the level of the Mn can also be calculated. (b) Limiting efficiency of the $In_{1-x}Ga_xN$:Mn IBSC and reference cell (without Mn) calculated as a function of the Ga content. These figures are reproduced from Figs. 2 and 3 in Ref. [Martí et al., 2008d].

GaAs is a semiconductor limited by radiative semiconductor, but its major advantage regarding the possible engineering of a new IB material may be that it is one of the most studied III-V semiconductors and it already has a large background in PV applications. This makes it a very interesting host for the co-doping with transition metal impurities as IB material candidate. Besides, its bandgap, being not optimum, still could lead to IBSCs with reasonable efficiencies. Fig. 3.14(a) shows the detailed balance limiting efficiency of the GaAs:X IBSC, where X is the transition element incorporated in GaAs [Martí et al., 2009]. The solar cell is assumed to be at T=300 K and to receive photons from the sun, modeled as a black body at 6000 K, at the maximum concentration of 46050 suns. The limiting efficiency (solid black line) is plotted with respect to the energy difference between the IB and one of the two host material bands (VB or CB). Each of the transition elements (indicated with empty dots in the figure) are meant to produce an IB at a different energetic position within the bandgap, thus, providing IBSCs with different potentials for harvesting the sunlight. Ti and Fe are the elements used in the two families of IBSC prototypes fabricated during this Thesis. They both have a limiting efficiency close to 58% when incorporated in a GaAs matrix. The dashed lines of the figure represent the best case scenario for the single gap solar cell efficiency and for the IBSC (with optimized bandgaps).

Simple GaAs solar cell structures with neither anti-reflecting coatings nor AlGaAs window were grown by MBE at the research group at RIBER. Since in this study we were interested in the possible photoresponse from the IB, it was considered that inserting these layers at this stage could eventually complicate the manufacturing of the cell, as well as the

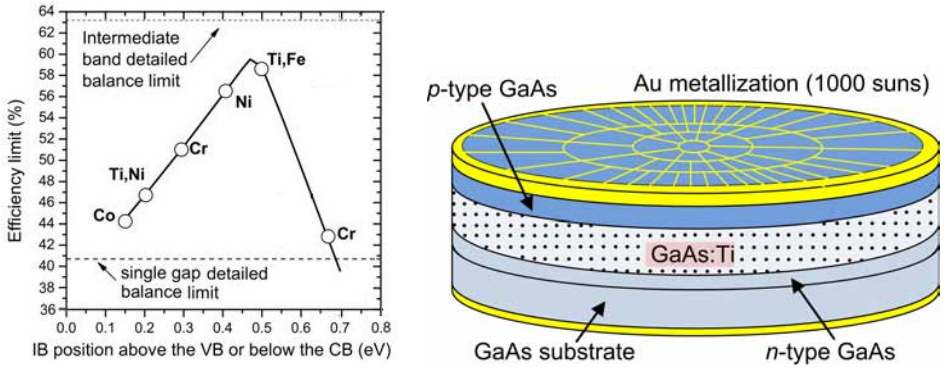

(a) (b)

Figure 3.14: (a) Theoretical analysis of the detailed balance limiting efficiency of bulk-based IBSCs fabricated with a transition element X incorporated in GaAs [Martí et al., 2009]. (b) Artistic depiction of the layer structure of the GaAs:Ti IB solar cell fabricated during this Thesis. The front metallization grid is designed for 1,000 suns operation [Linares et al., 2013]. Note: the drawing is not to scale.

interpretation and modeling of the results. The structure of the GaAs:Ti cell is sketched in Fig. 3.14(b) [Linares et al., 2013]. As required by the IBSC theory, the IB material of 1 μm thick in our experiments, is isolated from the metal contacts by Ti-free p- and n-type GaAs (emitter) layers. These two conventional semiconductor layers were grown at high temperature, T=580 ℃, which may have annealed out some of the lattice defects formed during the low temperature growth of the GaAs:Ti layer. A GaAs cell in which the IB material region has been replaced by an undoped low temperature GaAs layer with the same thickness was also fabricated as a benchmark. All devices were processed with a metallization grid designed for a concentrated light of 1,000 suns described in appendix B.

3.3.2.1 $In_{1-x}Ga_xN$:Mn

Crystalline $In_{1-x}Ga_xN$ alloy in zincblende configuration is a material difficult to grow, specially because of the difficulty found on the temperature control of the InGaN film growth sample inside the MBE due to a rapid rise in temperature at the early stages of growth [Hall et al., 2010]. Such rise does not match with the typical shutter transients experienced in MBE and it is detrimental to the production of a high quality material. The explanation may be related to the free carrier absorption of radiation during the growth [Hall et al., 2010]. Special techniques had to be developed for the control of the temperature during InGaN film growth.

As indicated in Fig. 3.13(b) the maximum efficiencies are predicted for $In_{1-x}Ga_xN$ with x in the range of 0.2-0.3. That is the reason why the growth of $In_{0.79}Ga_{0.21}N$ IB materials

with 1% of Mn was chosen. Such impurity concentration is actually well above the necessary limit for the delocalization of the impurity wave-function [Luque et al., 2006a], since this threshold is, at room temperature, between 10^{19} and 10^{20} cm^{-3} and the atoms that represent the 1% of a crystalline cubic lattice of these characteristics are between 10^{21} and 10^{22} cm^{-3}. The $In_{1-x}Ga_xN$:Mn IBSC was fabricated with the GaAs/$In_{1-x}Ga_xN$:Mn/GaN device structure, using GaAs as the substrate and also as the n-type emitter, then growing the $In_{1-x}Ga_xN$:Mn and finally a GaN layer as the p-type emitter, isolating the $In_{1-x}Ga_xN$:Mn IB material from the contacts. The cells were grown without ARC layer, passivating layer, window layer or BSF layer for simplicity. No reference cell was fabricated in this case.

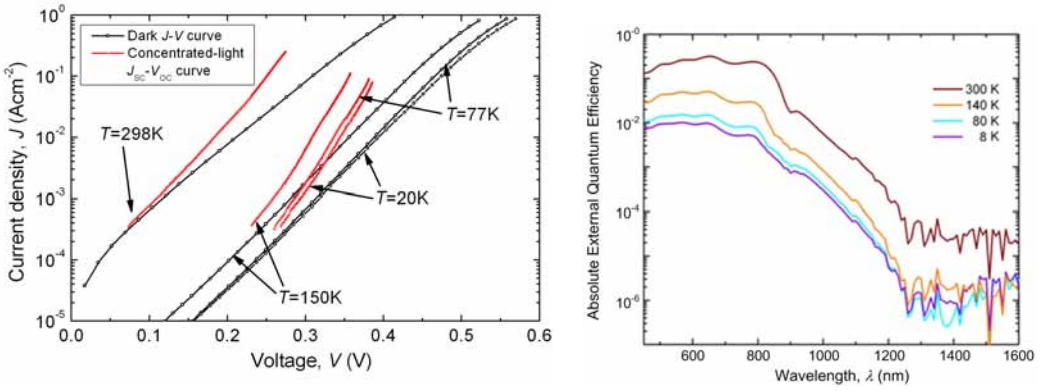

(a) (b)

Figure 3.15: Characterization of the $In_{0.79}Ga_{0.21}N$:Mn IBSC at room and lower temperatures. (a) Concentrated light J_{SC}-V_{OC} showing a maximum V_{OC}=0.386 V for T=20 K, well below the absorption threshold. (b) Absolute external quantum efficiency. The QE plots are a courtesy of Mrs. Esther López.

The $In_{0.79}Ga_{0.21}N$:Mn IBSC was characterized at room and low temperatures under concentrated light. Fig. 3.15(a) represents the concentrated light J_{SC}-V_{OC} curves measured at T=298 K, T=150 K, T=77 K and T=20 K. The very low r_P of the cell again prevented polarizing it at reverse bias, thus avoiding the possibility to reach the J=J_L value. Also in this case a strong noise related to the electrical connection to the cryostat and its interaction with the source-meter working as voltage source prevented the measurement of very low currents (below 10^{-5} A, which is equivalent to approximately 3 10^{-4} Acm^{-2}). This time, the measurement did not suffer from signal desynchronization. The very degraded V_{OC} value at 1 sun (∼150 mV) recovered up to 386 mV at approximately 800 suns and very low temperature (T=20 K), however, this value is still very far from the absorption threshold measured in this technology, which corresponds to a wavelength of approximately 1250 nm (∼1 eV), as deduced from the low temperature absolute external QE plots of Fig. 3.15(b). On of the reasons for this small value of the V_{OC} is likely related to the fact that the heterojunction band alignment between the GaAs rear emitter and

the $In_{0.21}Ga_{0.79}N$:Mn *i*-region or the GaN front emitter creates such band discontinuity that prevents further splitting of the QFLs. No sub-bandgap absorption is measured for wavelengths longer than 1250 nm. Conversely, the GaAs reference cell bandgap is observed starting from 870 nm at room temperature and decreasing as temperature decreases, as it is expected.

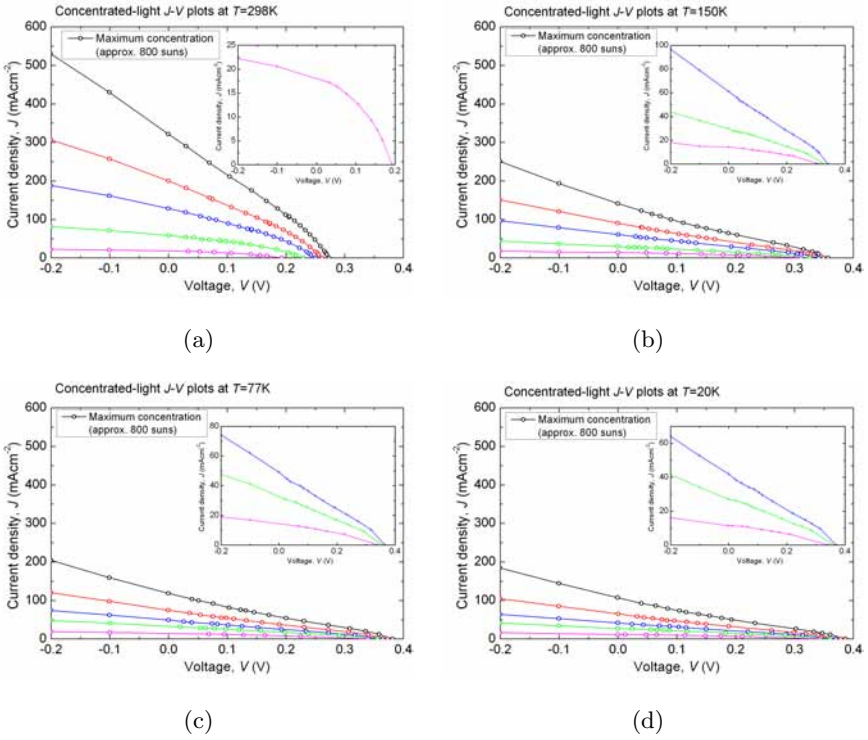

Figure 3.16: Concentrated light *J-V* curves of the $In_{0.75}Ga_{0.25}N$:Mn IBSC measured at different temperatures. (a) T=298 K; (a) T=150 K; (a) T=77 K; (a) T=20 K.

For the sake of a better clarity, Fig. 3.16 shows the evolution of the *J-V* curves under different concentrations (maximum of 800 suns) as the temperature is reduced to 20 K.

3.3.2.2 GaAs:Ti

The growth of GaAs:Ti layers with a very high Ti concentration is complicated by the low solid solubility [Zhang et al., 2010] of Ti in GaAs. An inverse relationship exists between solubility and temperature so that Ti could be incorporated in GaAs at high concentration if grown at a sufficiently low temperature [Campion et al., 2003]. However, the low-temperature growth of GaAs can produce an excessive number of As antisites [Zhao et al., 2005] and Ga vacancies (and a negligible amount of As interstitials) [Liu et al., 1995], which are all well known as lifetime killers. These intrinsic defects can be avoided by growing with the Ga:As atomic ratio carefully adjusted to ∼1:1, rather than employing an

excess of As which is typical for growth at high temperatures (500 ℃ and above) by, for example, molecular beam epitaxy. For our experiments, a target temperature of 200-250 ℃ and a growth rate of 0.3 μm/h were set.

The incorporation of Ti in GaAs was corroborated by secondary ion mass spectrometry (SIMS). Fig. 3.17(a) shows the SIMS analysis of a GaAs:Ti layer grown at a beam equvalent pressure (BEP) of Ti of 3.7 10^{-9} Torr and a substrate temperature estimated at ∼200 ℃. Constant values of Ti concentration in the range of 1.3 10^{20} cm^{-3} for both the ^{47}Ti and the ^{48}Ti isotopes were detected throughout the whole GaAs:Ti layer. Furthermore, the concentration of incorporated Ti was found to be proportional to the partial pressure of the Ti in the reactor chamber, verifying the controlled growth of this novel GaAs:Ti material.

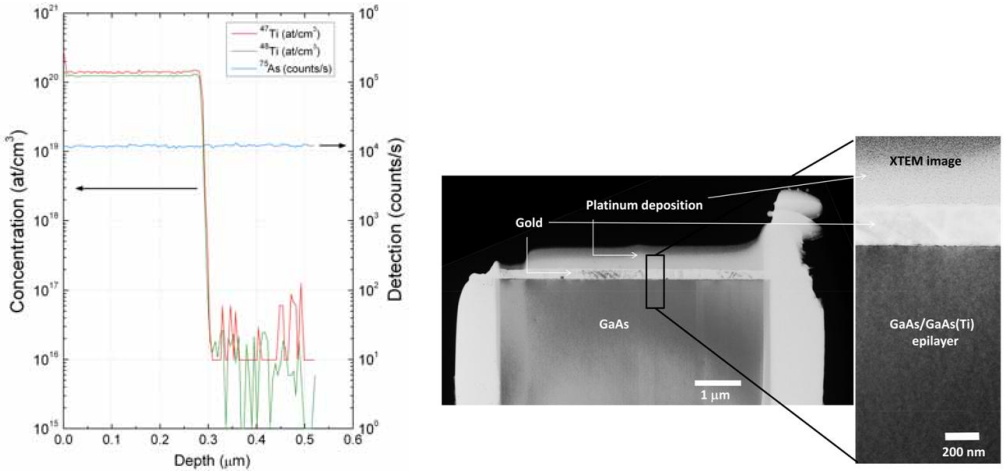

(a) (b)

Figure 3.17: Compositional and morphological characterization of the GaAs:Ti material and device. (a) SIMS analysis performed on a GaAs:Ti layer. A uniform Ti concentration of 1.3 10^{20} cm^{-3} is measured throughout the first 0.3 μm of the sample. (b) Bright Field (BF) TEM image of a processed GaAs:Ti solar cell; the inset shows an image taken in 220BF conditions, where no extended defects are observed.

On the other hand, the incorporation of large concentrations of atomic species characterized by a different atomic radius may result in lattice deformation. For this reason, the possibility of structural defects in the GaAs:Ti has to be considered. TEM characterization was carried out to gain insight into the crystal quality of the sample and the result is shown in Fig. 3.17(b). The whole sample is apparently free of structural defects.

Fig. 3.18(a) shows the absolute external QE of both the GaAs:Ti IB and the GaAs reference solar cells, both of which show sub-bandgap response. Although the sub-bandgap response is higher in the GaAs:Ti than in the reference cell, this below bandgap response cannot be attributed exclusively to the creation of an IB from the insertion of Ti since it

exists also in the reference cell. Bandgap states induced by As antisites and Ga vacancies defects may also be involved.

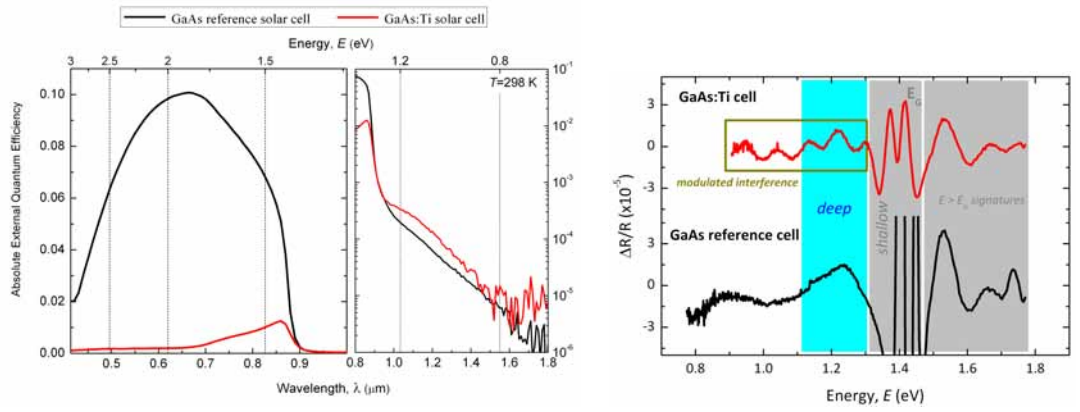

(a) (b)

Figure 3.18: Absolute external QE measurement and PR. (a) External QE of the GaAs:Ti IBSC (red) and the GaAs reference cell (black) measured at room temperature. Both cells show photoresponse to sub-bandgap energy photons. Courtesy of Dr. Elisa Antolín, Mr. Íñigo Ramiro and Mrs. Esther López. (b) PR characterization of the GaAs:Ti and reference GaAs cells. The sub-bandgap structure is different in both cells. Courtesy of Dr. David Fuertes.

The existence of a sub-bandgap electronic structure is also confirmed by the PR characterization carried out on both samples and represented in Fig. 3.18(b). The shallow and deep sub-bandgap PR signatures are different in each of the cells, showing the likely presence of a GaAs defect at around 0.9 eV in the reference cell and a modulated interference of unknown origin in the case of the GaAs:Ti cell.

In addition, the EQE of the GaAs reference cell (solid black line) is low (EQE_{max}=0.1), which is not explained entirely by the lack of a passivating window layer and anti-reflective coating. PC1D simulations reveal that this low EQE signature can only be explained when bulk lifetimes are in the order of 3 picoseconds. Hence, the degradation of the cell is most likely due to the presence of excessive As antisites and Ga vacancies caused by the growth of the GaAs layer at low temperature with too much As. The cell with Ti is even more degraded, perhaps due to the incorporation of additional species captured by the reactive Ti during growth, or because of the diffusion of Ti atoms into the GaAs emitters during the subsequent high temperature GaAs layer growth. Lifetimes in the order of 0.1 ps are necessary to model its performance.

To test the operating principle of the IB solar cell relating to voltage preservation, we have measured the *I-V* characteristics at 1 sun and under concentrated light of both the reference and the GaAs:Ti cells. The V_{OC} of the GaAs reference cell and the GaAs:Ti solar cell at 1 sun are respectively 0.400 V and 0.136 V, as shown in Fig. 3.19. The voltage

Table 3.1: Maximum V_{OC} (mV) obtained under concentrated-light. The approximated value for the concentration level used is also indicated.

Temperature	V_{OC}(GaAs) [mV]	V_{OC}(GaAs:Ti) [mV]
298 K	834 (800 suns)	690 (80 suns)
150 K	1,182 (800 suns)	1,161 (80 suns)
77 K	1,317 (800 suns)	1,321 (8 suns)
20 K	1,390 (800 suns)	1,361 (8 suns)

recovery in these cells has been verified experimentally by the measurement of the V_{OC} of both cells under concentrated light at different temperatures (see summary of data in Table 3.1).

At room temperature, it was possible to recover the V_{OC} of the GaAs:Ti cell from 0.136 to 0.690 V and the V_{OC} of the reference cell from 0.400 to 0.834 V by the use of concentrated light. On the other hand, at 20 K, the V_{OC} of the reference and GaAs:Ti cells recovered to 1.390 V and 1.361 V respectively. In addition, notice also that the concentration required to reach these values in the GaAs:Ti cell case was substantially lower than in the GaAs reference cell. A graphical representation of this voltage recovery is shown in Fig. 3.19, where plots of the J-V characteristics of the GaAs:Ti solar cell are shown. The experiment was carried out under three different sets of conditions: the black curve represents the 1 sun J-V curve at room temperature, the red curve corresponds to the concentrated-light J-V characteristic at room temperature and the blue curve shows the response to concentrated light and low temperature.

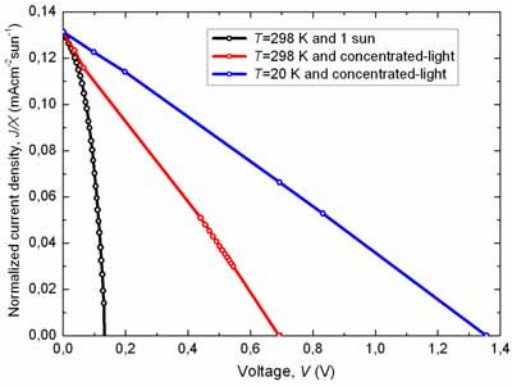

Figure 3.19: Normalized J-V characteristics of the GaAs:Ti IB solar cell for different temperatures and illumination intensities ($X_{T=298K}$ ∼80 and $X_{T=20K}$ ∼). The "normalized" term refers to the fact that J has been divided by X, for an easier comparison.

Thanks to this research line, the manufacture of GaAs:X IBSCs has been attempted for the first time. In order to incorporate Ti at high concentrations, the MBE growth

temperature was decreased, but the overall material quality was poor probably due to the presence of As antisites and Ga vacancies, even for the reference cell. In spite of this, both the reference and the GaAs:Ti cells have shown photoresponse to below-bandgap energy photons, which we speculate arises mainly from As antisite and Ga vacancy defects appearing in the bandgap, although we cannot discount the introduction of additional states inside the bandgap by the Ti atoms also contributing to the generation of photocurrent. We have shown that these states do not limit the V_{OC} of the cells that has shown a recovery from a few hundreds of mV to values above 1.3 V when concentrated light is used and the temperature is lowered.

3.3.2.3 GaAs:Fe

The last IB material that will be presented in this chapter is GaAs:Fe, which similarly to the GaAs:Ti and the $In_{1-x}Ga_xN$:Mn technologies, was grown by MBE. The GaAs:Fe IBSC, with a layer structure similar to the GaAs:Ti cell, has also been fabricated by Prof. Foxon's research group at the University of Nottingham.

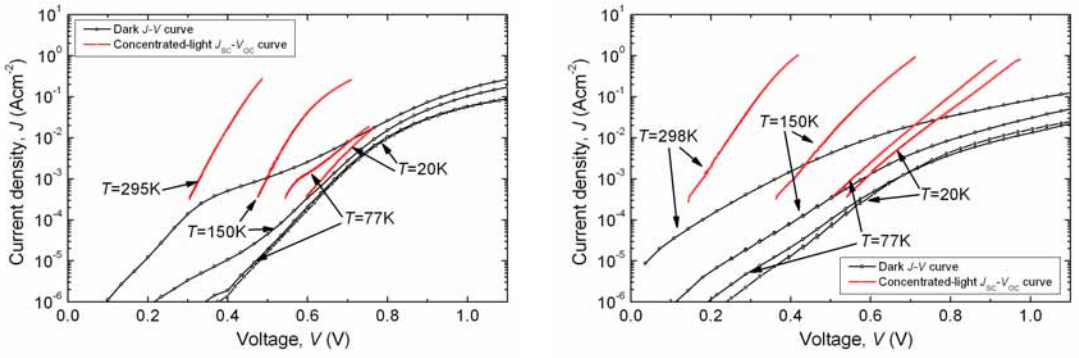

Figure 3.20: Dark J-V and concentrated light J_{SC}-V_{OC} characterization at room and low temperatures of another GaAs:X IBSC fabricated in the University of Nottingham. The cells were processed, encapsulated and measured at IES-UPM. (a) GaAs:Fe IBSC. (b) GaAs:Fe reference cell.

The concentrated light J_{SC}-V_{OC} curves of the GaAs:Fe IBSC and the reference cell measured at room and low temperatures are shown in Fig. 3.20. The reference cell (Fig. 3.20(a)) recovers the voltage very fast as the temperature decreases, going from $V_{OC} \simeq$400 mV at room temperature, to V_{OC}=974 mV at T=20 K. The cell with Mn, surprisingly, presents a larger V_{OC} when subjected to maximum concentration at room temperature, but it then recovers more slowly, contrary to what the IBSC theory predicts and reaches only 763 mV, very far from its reference counterpart. The value of the absorption threshold of the GaAs:Mn cell, which is not shown in this work, is approximately 1 eV. Therefore,

we can then conclude that the voltage preservation principle is not fulfilled either for this cell.

3.3.2.4 PC1D analysis of the GaAs:X cells

The concentrated light J_{SC}-V_{OC} characteristics from the previous GaAs-based IBSCs present very poor voltages, including those without intentional incorporation of impurities (reference cells), grown at high temperature. Nevertheless, it would not be fair to compare them with the excellent performance of state of the art GaAs solar cells. The reason is that, for simplicity, we have decided not to include a window layer or an ARC layer in the solar cell structure and therefore, their best performance under such non-ideal conditions is very degraded when compared to that of the state of the art GaAs technology (J_{SC}(1 sun)$\sim$25 mAcm^{-2} and V_{OC}(1 sun)$\sim$1.1 V). To illustrate this idea, Fig. 3.21 shows the PC1D [Basore,] modeling of the 1 sun I-V characteristic of the GaAs reference cell under these non-ideal conditions. It must be noticed that the V_{OC} of the modeled cell is limited to 0.85 V and the I_{SC} is slightly above 8.6 mAcm^{-2}. The resulting efficiency is, in this case, only 6.5%.

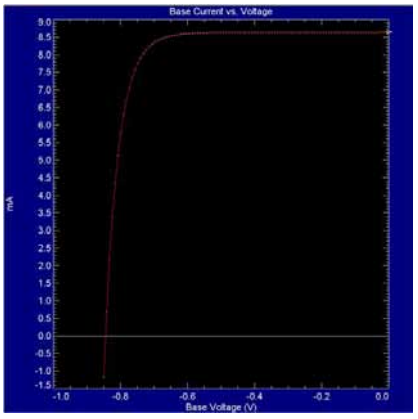

Figure 3.21: Plot of the 1 sun I-V characteristic of a GaAs solar cell modeled with PC1D. The solar cell has neither window layer nor ARC.

3.4 Summary

Several bulk-IBSC technologies have been measured with the low-temperature concentrated light technique developed in this Thesis, providing interesting conclusions on their performance as actual IBSCs regarding one of the two operation principle fundamentals: the voltage preservation.

Two families of chalcopyrite TF-IBSCs have been characterized under concentrated light and low temperature. The first of them, $CuInS_2$:Ti, has shown a moderate improve-

ment of the V_{OC} until T=200 K and a dramatic loss of both V_{OC} and I_{SC} for temperatures below 150 K. The second family is based on $CuGaS_2$:Fe alloys, which have a larger bandgap. This type of cells showed an even poorer electrical response when they were subjected to concentrated illumination, which also improved slightly at T=200 K. Lower temperatures resulted in the breakage of the cells. Both $CuInS_2$:Ti and $CuGaS_2$:Fe were far from fulfilling the voltage preservation principle, among other things because their IB material was not isolated from the contacts and also because the band alignment of the heterostructure limited the maximum effective bandgap. Besides, they suffered remarkable problems during the measurements, specially because the so called "memory effect".

Si:Ti HIT IBSCs were also characterized during this Thesis. A noticeable increase of the V_{OC} is produced: from 387 mV at room temperature to 540 mV at T=20 K at maximum concentration, although it remains far from the energy of the absorption threshold (divided by the electron charge), located at approximately 730 mV at room temperature.

Two types of bulk-IBSCs based on III-V materials have been developed during these Thesis: $In_{1-x}Ga_xN$:Mn and GaAs:X:

- $In_{0.21}Ga_{0.79}N$:Mn IBSCs have been fabricated with a Mn concentration of approximately 1%. They have been subjected to concentrated light J_{SC}-V_{OC} characterization under low temperature, obtaining a maximum V_{OC} of 386 mV for T=20 K. This value, although largely improved with respect to the 150 mV measured at room temperature, is still very far from the absorption threshold of approximately 1 eV. The reason may be likely related to the fact that the heterojunction band alignment between the GaAs rear emitter and the $In_{0.21}Ga_{0.79}N$:Mn i-region or the GaN front emitter creates such discontinuity that prevents further splitting of the QFLs.

- GaAs:Ti IBSCs have also been fabricated. The SIMS signature shows an incorporation of Ti above 10^{20} atoms/cm^3 and the TEM characterization indicates the absence of structural defects. External QE measurements show sub-bandgap photoresponse, although the reference cell (without Ti) also presents this type of absorption. The As antisites very likely produced during the low temperature growth and not the Ti of the IB region may be responsible for this sub-bandgap response. The initially degraded V_{OC} at 1 sun and room temperature (136 mV) increases to 690 mV under the operation under concentrated light and it suffers a dramatic recovery at low temperature, reaching 1,361 mV, which is above the absorption threshold and actually almost as large as the host material bandgap divided by q.

- GaAs:Fe IBSCs have also been implemented. They surprisingly obtained larger V_{OC} than their reference counterparts under concentrated light and room temperature,

although the low temperature response was clearly favorable to the GaAs benchmark. The maximum V_{OC} obtained by the GaAs:Fe cell does not surpass its absorption threshold.

- In order to progress in this research we anticipate that it will be necessary to exercise a more rigorous control over the growth at low temperature (with the Ga:As atomic ratio close to 1 and with intentional n-doping) to produce good quality material before attempting a high efficiency cell under this approach [Missous, 1995, Missous, 1996]. Besides, the so-called Migrated Enhanced Epitaxy [Horikoshi et al., 1986, Horikoshi et al., 1987] technique could be used to better adjust the low temperature Ga:As atomic ratio.

In view of these results we can conclude that the new low temperature concentrated light characterization technique presented in this Thesis is a powerful tool for the analysis of the validity of new candidate materials for their performance as IBSCs.

Chapter 4

Modeling of III-V heterojunction alloys for the identification of new QD IB materials

4.1 Introduction

QDs have been proposed as a means to achieve the practical implementation of the IBSC concept. So far, only few QD material systems, such as In(Ga)As/GaAs [Luque et al., 2004, Zhou et al., 2010] and related compounds (e.g. adding small amounts of P or N to the host material to strain balance the QD stacks [Hubbard et al., 2008, Oshima et al., 2008, Popescu et al., 2008, Alonso-Álvarez et al., 2008, Zhou et al., 2010]) have been tested experimentally, giving rise to two important conclusions: the verification of the concept fundamentals [Martí et al., 2006a, Antolín et al., 2010c, Linares et al., 2012b] and the need to seek new QD candidate materials in order to produce high efficiency devices. Concerning the latter, in this chapter an analytical model is presented to assess the potential of QD-IBSCs [Linares et al., 2011]. It consists of the following steps: 1) calculation of the heterojunction band alignment taking material strain into account, 2) calculation of the QD confined energy levels constituting the IB and 3) calculation of the efficiency limits in the detailed balance realm and optimization of the QD systems in terms of QD size and material composition. The search criteria are reviewed and several QD systems, such as InAs/$Al_xGa_{1-x}As$, InAs/$Ga_xIn_{1-x}P$, $InAs_{1-x}N_x$/GaAs, $InAs_{1-y}N_y$/$AlAs_xSb_{1-x}$, $InAs_{1-z}N_z$/$Al_x[Ga_yIn_{1-y}]_{1-x}P$, $InAs_{1-y}N_y$/$Ga_xAs_{1-x}P$, type-II VBO compounds and PbSe/ZnTe are identified and their optimum QD sizes are calculated. Limiting efficiencies over 60% are calculated at maximum light concentration.

4.1.1 The QD approach

So far, the choice of InAs/GaAs as QD system (QD and barrier materials) has not been made on the basis of an optimized band alignment for best IBSC performance, but simply because InAs/GaAs and related systems are readily available and exhibit a relatively mature technology.

There are other approaches for the practical implementation of IB materials [Ekins-Daukes and Schmidt, 2008, Luque and Martí, 2010b, Martí et al., 2009], although so far the QD based IBSC (QD-IBSC) remains as one of the most mature for its manufacture. A QD structure causes the electron to be confined in the three spatial directions, which allows a discrete (delta function like) density of states. The lower of these confined electron levels (in the most favorable case there is only one confined state) acts as the IB. The QDs are manufactured from two different materials; 1) the barrier material, which has a larger bandgap (E_{G}) and 2) the QD material, which must have the CB edge below that of the barrier material, so that a potential well is formed.

As it will be reviewed in the next chapter, the QD size is an important parameter in the design and manufacture of a QD-IBSC. A rather small QD size allows the existence of fewer confined states inside the conduction band offset (CBO), although the smaller the QD, the higher the energy of the fundamental confined state and subsequent excited states. An aspect ratio close to unity stresses their zero-dimensionality, making them differ from the quantum well behavior (for which the IB-CB optical transition is forbidden for front illumination [Loehr and Manasreh, 1993]) and favors a strong IB-CB absorption [Luque et al., 2010b]. A low QD size dispersion also enables fewer different confined energy levels to appear, which is detrimental to the IBSC operation [Luque et al., 2010a].

From a theoretical point of view, the IB concept is symmetric with respect to the position of the IB (that is, E_{L} can be above E_{H} or the other way around). However, for practical reasons this is not believed to be the case when the IBSC is implemented with QDs. This statement is based on the relatively high value of the hole effective mass in most III-V materials. This situation makes confined hole levels arising in the valence band offset (VBO) not sufficiently separated from each other as to give the option of producing an IB well separated from the VB, as will be shown as a corollary of this work.

The IBSC theory states that the efficiency limit for a single gap solar cell will not be overcome unless there is an actual splitting of the three QFLs. But, as stated and experimentally verified in chapter 2, in the case of the InAs/GaAs system the IB-CB QFL split is difficult to achieve at room temperature [Martí et al., 2006b] and this occurs mainly because of the presence and proximity of the many confined levels arising in the CBO. This situation can be reverted by attaining smaller QDs and choosing a material combination

for them to produce a larger CBO (so the electron confined levels remain well separated from each other).

Several models for the analysis of the QD-IBSC material systems have been proposed so far [Martí et al., 2002, Levy et al., 2005, Popescu et al., 2008, Levy and Honsberg, 2008b, Dahal et al., 2010]. In some cases [Martí et al., 2002, Levy et al., 2005, Levy and Honsberg, 2008b, Dahal et al., 2010] only the material composition is taken into account so that the band diagram can be obtained, but the confined energy levels are not specifically calculated. The model presented in this chapter relies on several simplifications (e.g. the QDs are assumed to be spherical). Although more rigorous analyses based on numerical calculations, such as the one presented in Ref. [Popescu et al., 2008], are more precise and reliable, they take too long for a screening of the many possible III-V alloy combinations.

4.2 QD-IBSC optimization model

Our analysis is based first on the calculation of the heterojunction band alignment favoring appropriate band offsets, the subsequent calculation of the confined levels arising in the QDs as a function of the effective mass in order to foresee where the IB would be located and finally, the determination of the efficiency potential as IBSCs.

In order to illustrate how our model works, the InAs/GaAs QD system will be calculated as a working example and the results from each of the calculation steps will be presented.

4.2.1 Modeling of the heterostructure band alignment including the effect of strain

The first step of our analysis consists of the elaboration of the heterojunction energy band alignment model (HEBAM) that includes strain effects. This model is, in turn, based on the so called Model Solid Theory by C. G. Van de Walle [Van de Walle, 1989], upgraded with more recent data for all required III-V parameters and completed with the calculation of the electron and hole effective masses of the alloys involved. The HEBAM has been implemented to calculate the band alignment at the interface of ternary and quaternary alloys, accounting for their corresponding interpolations through appropriate bowing parameters (BPs).

In this analysis, only type II quaternary alloys will be analyzed. These are compounds of the type $(B_2)_x(B_{1y}B_{4(1-y)})_{1-x}$ (e.g., $Al_x[Ga_yIn_{1-y}]_{1-x}P$), whose solid solutions can be considered as the aggregation of three III-V binary compound semiconductors: B_1, B_2 and B_4 (GaP, AlP and InP respectively in the example). As it will be described later,

the interpolation of a quaternary parameter requires, not only its quaternary BP and the binary parameter values from which it is formed, but also the BPs related to all the ternary alloys involved: B_2B_1, B_2B_4 and B_1B_4 (AlGaP, AlInP and GaInP respectively in the example).

A compilation of the most significant equations used in our model is presented in Table 4.1, including those derived from the Model Solid Theory, those leading to specific material parameter calculation and also those related to non-linear ternary and quaternary alloy parameter interpolation.

Table 4.1: Equations used in the HEBAM

Notation	Value	Meaning	Model	
E_{G}	$E_{\mathrm{G}}^{0} - \dfrac{\alpha T^2}{T+\beta}$	Binary bandgap for a given temperature	Varshni formula [Varshni, 1967]	(4.1)
$Q(x,y)$	$\mathbf{Y}\begin{bmatrix} C_1 & T_{12} & C_2 \\ T_{14} & D & T_{23} \\ C_4 & T_{34} & C_3 \end{bmatrix}\mathbf{X}$	Interpolation of a quaternary alloy parameter	Generalized Thompson-Woolley formula [Donaty et al., 2003]	(4.2)
$T_{v,av}^{B_iB_j}$	$3\left(-a_{\mathrm{v}}^{B_i} + a_{\mathrm{v}}^{B_j}\right)\dfrac{\Delta a_{\mathrm{lc}}}{a_{\mathrm{lc},0}}$	BP for the interpolation of the $E_{\mathrm{v,av}}$ of a ternary alloy	Model Solid Theory [Van de Walle, 1989]	(4.3)
m_{e}^{*}	$\left[(1+2F) + \dfrac{E_{\mathrm{P}}\left(E_{\mathrm{G}}+2\Delta_{\mathrm{so}}/3\right)}{E_{\mathrm{G}}\left(E_{\mathrm{G}}+\Delta_{\mathrm{so}}\right)}\right]^{-1}$	Electron effective mass at k=Γ		(4.4)
m_{e}^{*}	$\dfrac{3}{1/E_{\mathrm{l}}^{*} + 2/E_{\mathrm{t}}^{*}}$	Electron effective mass of a $k \neq \Gamma$ ellipsoidal valley		(4.5)
ΔE_{i}	$a_{\mathrm{i}}\left(2\epsilon_{\parallel} + \epsilon_{\perp}\right)$	Band energy displacement due to hydrostatic strain	Model Solid Theory [Van de Walle, 1989]	(4.6)
ΔE_{hh}	$1/3\Delta_{\mathrm{so}} - b\left(\epsilon_{\perp} - \epsilon_{\parallel}\right)$	HH energy displacement due to biaxial strain	Model Solid Theory [Van de Walle, 1989]	(4.7)
ΔE_{lh}	$-1/6\Delta_{\mathrm{so}} + 1/2b\left(\epsilon_{\perp} - \epsilon_{\parallel}\right) + 1/2[\Delta_{\mathrm{so}}^2 + \Delta_{\mathrm{so}}2b\left(\epsilon_{\perp} - \epsilon_{\parallel}\right) + 9b^2\left(\epsilon_{\perp} - \epsilon_{\parallel}\right)^2]^{1/2}$	LH energy displacement due to biaxial strain	Model Solid Theory [Van de Walle, 1989]	(4.8)

4.2.1.1 Compound material parameters and their interpolation

Equation 6.1 in Table 4.1 represents the Varshni formula used to calculate binary bandgaps in accordance with the temperature T (in K) and the Varshni parameters α_{V} (in meV/K) and β_{V} (in K). Equation 6.2 shows a generalization of the Thompson-Woolley formula [Thompson and Woolley, 1967, Donaty et al., 2003] used to carry out non-linear inter-

polations of the following III-V quaternary alloy parameters: E_{G}, the unstrained alloy bandgap (in eV); Δ_{so}, the spin orbit splitting (in eV); and $E_{\mathrm{v,av}}$, the average energy of the three uppermost VBs at k=Γ (in eV). Vectors $\mathbf{Y}$ and $\mathbf{X}$ respectively correspond to $[y,\, y\,(1-y)\,,\, 1-y]$ and $[1-x,\, x\,(1-x)\,,\, x]^{\mathrm{T}}$; C_{i} corresponds to the parameter value of the i^{th} binary compound; and T_{ij}/D are the ternary/quaternary BPs (look at Ref. [Donaty et al., 2003] for precise definition). When a type II quaternary alloy parameter is to be computed, one of the binary values is assigned twice in one row or column of the matrix in equation 6.2 and the associated ternary BP is zero (e.g., B_2=B_3 and T_{23}=0 in the aforementioned example). When any of the BP data are lacking, the value 0 is taken. On the other hand, as explained in 5.3.3.1 the estimation of dilute nitride alloy bandgaps, in general, does not accurately correspond to any single BP and thus, it should be computed following the BAC model (equation 5.5). Because of the interaction between the energy levels of the nitrogen impurity and the host CB, the dilute alloy presents a split CB.

Equation 6.3 describes how to compute the $E_{\mathrm{v,av}}$ BP for a ternary compound ($B_{\mathrm{i}}B_{\mathrm{j}}$) [Van de Walle, 1989]. Δa_{lc} is defined as $a_{\mathrm{lc}}^{B_i} - a_{\mathrm{lc}}^{B_j}$ in the previous formula; where $a_{\mathrm{lc,0}}$ is defined as $x a_{\mathrm{lc}}^{B_i} + (1-x)\, a_{\mathrm{lc}}^{B_j}$; and a_{v} (in eV) is the VB deformation potential.

Nevertheless, most interpolations are carried out through Vegard's Law, because of the lack of appropriate data or simply because a linear interpolation is most appropriate. In this respect, the following parameters are linearly interpolated: a_{lc}; a_{v}; a_{c} (the CB deformation potential in eV); c_{11}, c_{12}, c_{44} (in GPa), the elastic constants; and b (in eV), the shear deformation potential.

The value of the electron and hole effective masses of the strained materials will be essential in the following step in our analysis. When the electron effective mass of a direct bandgap compound is to be calculated, equation 6.4 is used, for which the interband matrix element E_{P} (in eV) and the Kane parameter F are linearly interpolated. On the other hand, both the indirect bandgap ($k \neq \Gamma$) electron effective mass (with ellipsoidal constant energy surface) and the hole effective mass, require a linear interpolation from the masses of the binary compounds. The first is obtained from equation 6.5, where E_{t}^{*} and E_{l}^{*} are the transversal and longitudinal effective masses. The second is always deduced from the Luttinger parameters (γ_1, γ_2) as m_{hh}^{*}=$(\gamma_1 - \gamma_2)^{\text{-}1}$ and m_{lh}^{*}=$(\gamma_1 + \gamma_2)^{\text{-}1}$ for the heavy-hole (HH) and light-hole (LH) effective masses respectively. The interpolation of the following parameters: γ_1, γ_2, E_{t}^{*} or E_{l}^{*} would be physically meaningless and hence, the individual properties of the binary compounds have to be calculated in order to interpolate from them the property of the alloy. The crystal orientation is taken to be 001 for simplicity.

4.2.1.2 Computing the effect of strain

Once all alloy parameters are interpolated, the Model Solid Theory is applied taking into account the hydrostatic and biaxial strain of two contiguous layers, corresponding to both barrier and QD materials with unstrained thicknesses h_1 and h_2 respectively. To simulate the strain to which the QD material is exposed, we will set the ratio h_1/h_2=30 which is related to the ratio of InAs and GaAs deposited in each stacked QD layer and which appears to be a reasonable approximation as will be explained. The crystal orientation is again taken to be 001. The analytical equations representing the two components of the strain are shown in equations 6.6, 6.7 and 6.8. The band displacement resulting from hydrostatic strain, which intuitively accounts for changes in the unit cell volume, is presented in equation 6.6, where a_{i} [eV] is the deformation potential at the band i (VB or CB in our case) and $\epsilon_{\parallel}$ and $\epsilon_{\perp}$ are respectively the strain tensor components parallel and perpendicular to the plane of the interface. Equation 6.7 represents the HH energy displacement at k=Γ once the biaxial strain is computed, and equation 6.8 represents the same effect for the LH energy.

4.2.1.3 Working example

Most of the values for the material parameters have been taken from the extensive reference [Vurgaftman et al., 2001], although references [Donaty et al., 2003, Madelund et al., 1986, Van de Walle, 1989, Vurgaftman and Meyer, 2003] have also been used when the data in [Vurgaftman et al., 2001] was incomplete and when more recent or more reliable III-V parameter values have been published, e.g. Ref. [Vurgaftman and Meyer, 2003] updated the former review regarding the use of III-V nitride parameters.

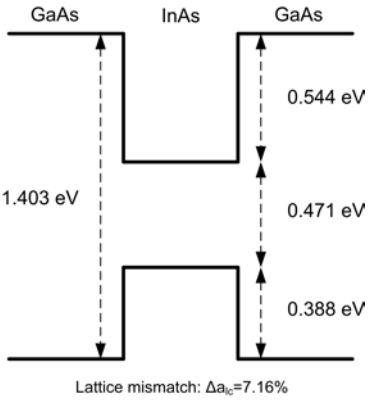

Figure 4.1: Band alignment of the InAs/GaAs QD system calculated with the HEBAM. The lattice mismatch Δa_{lc} is one the figures of merit for the QD growth.

In order to show an example of the HEBAM, we have calculated the band alignment of the InAs/GaAs QD system at T=300 K (see Fig. 4.1). The CBO in this system of only 544 meV appears to be too small for an optimized IB material, with a total $E_G \approx$=1.42 eV. This statement is made on the basis of the next step of the model, which is meant to estimate the position of the confined QD states and will show that the IB comes too close to the CB.

The resulting band diagram calculated with our model for a heterojunction has an overestimated VBO, although agrees reasonably well with the experimental and theoretical results found in the literature [Vurgaftman et al., 2001].

4.2.2 Confined energy levels

The next step in our analysis consists of the calculation of the number and energy of the different confined levels arising within the quantum structure in accordance with the QD size. The location of each confined level also depends on the size of the confining potential described by the heterojunction band diagram previously calculated (CBO or VBO) and also on the effective masses inside and outside the nanostructures, i.e. the QD and barrier material effective masses. This confined level distribution is required so we can calculate the maximum efficiency of a solar cell fabricated with such QDs.

There are many possible QD candidate materials based on III-Vs and this model suggests a rather easy and direct way for their screening in order to make a selection of the most suitable ones for the IB concept. We have carried it out assuming the QDs are quantum spheres with radius r expressed in nanometers. This approximation is better at representing real QDs when they have an aspect ratio close to unity, which is, in general, the correct trend for an optimized IBSC [Luque et al., 2010b].

For this purpose, we will use the effective mass approximation and thus, define a unique effective mass (necessary to obtain a hermetic Hamiltonian) as the geometric average of both effective masses: inside and outside the sphere. As explained in [Messiah, 1960], the solution for each of the s, p, d and f orbitals requires the n-order Bessel spherical function (with n=1, 2, 3, 4 for each of the aforementioned orbitals) to be computed and divided by its derivative (n+1-order Bessel spherical function) for the solutions inside the QD. The same procedure, although with the spherical Hankel function, must be followed to find the solutions outside the QD. Only the values that verify both the inner and outer solutions are a solution for the confined energy levels.

By means of this analytical model and defining the confining potential as the CBO (or VBO for the holes) in each case and the effective mass as the average of both electron effective masses (or hole effective masses), we will calculate both the position of the electron

(or hole) confined energy levels inside the QDs. The sphere radius, r, is taken as variable ranging from 1 to 7.5 nm.

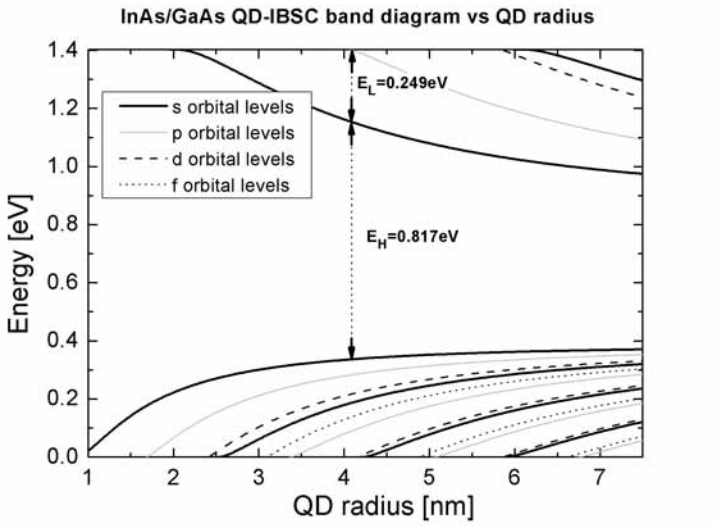

Figure 4.2: Confined energy levels for a spherical InAs/GaAs QD system. The particular case where there is only one confined level in the CBO is emphasized.

The latter is exemplified in Fig. 4.2 where again the InAs/GaAs case is shown. This step requires the previous results from the HEBAM as an input and provides the corresponding approximation for the confined energy levels in a spherical QD of radius r. The case for r=4.09 nm is emphasized in the figure because it is considered as the optimum in our model, defining what we call the effective bandgap and thus determining the actual E_{L} and E_{H} of the system. It represents the QD size limit for which there is only one electron confined level (1s orbital) inside the confining potential. The first excited level (1p orbital) is then located in the energy of the CB edge, maximizing the IB-CB transition and hence favoring a strong absorption for the electrons to reach the CB [Luque et al., 2010b]. Smaller radius values (left of the optimum in Fig. 4.2) place the electron confined levels higher in energy and larger radius values (right of the optimum) make the first excited level remain inside the confining potential, making the IB-CB absorption less efficient. Besides, in the two previous cases, a smaller E_{L} is obtained.

4.2.3 Efficiency limit of QD-IBSCs

After the band alignment has been computed, the material parameters have been calculated and the confined levels have been obtained, our calculation is completed by computing the limiting efficiency as a QD-IBSC. This last step is essential to provide feedback to

the material survey, since it distinguishes whether the selected QD material combination is fundamentally limited or it has a high potential for IB photovoltaics.

We have assumed a zero IB width in our detailed balance efficiency calculations. The motivation, as well as in the case of the solar spectrum, is the simplicity to compare our results with that of previous works. Further discussion on this topic can be found in Ref. [Cuadra et al., 2000], where the maximum IB width permitted before stimulated emission occurs for different concentrations is discussed and also in Ref. [Levy and Honsberg, 2008a], where the effect of a finite IB width is analyzed in terms of efficiency.

4.2.3.1 The detailed balance model

In this regard, the same model used in all theoretical calculations of the dark and illumination electrical performance throughout chapter 2 has been used. It is based on the detailed balance limit of *p-n* junction solar cells [Shockley and Queisser, 1961] adapted for an IBSC [Luque and Martí, 1997b]. It only requires the following data inputs: total effective bandgap, energy of one of the two sub-bandgap transitions (because the other sub-bandgap transition can be then deduced), e.g. E_{L} or energy between the IB and the CB, sunlight spectrum and concentration level. The two first inputs are provided by the previous calculation, the light spectrum is the one from a black-body at 6,000 K and the concentration level is set to the maximum (46,050 suns) for a uniform comparison. Other illumination conditions could also be suitable for this analysis (e.g. direct AM1.5 spectrum at 1000 suns), so a more realistic operating conditions are represented. Nevertheless, most of the analyses of this type (including the original one in Ref. [Luque and Martí, 1997b]) have also been carried out assuming that the incident spectrum corresponds to a black-body at a T=6,000 K and maximum concentration. In our model we have decided to use these same conditions for the sake of a proper comparison. The readers interested in the impact of the terrestrial spectrum can find further details in Ref. [Bremner et al., 2008].

4.2.3.2 Definition of the appropriate QD radius for an optimum sub-bandgap distribution

The energy of the sub-bandgap E_{H} is defined from the first hole confined level (also corresponding to a 1s orbital) and the reason for it will be explained next.

As has been already explained, the high effective mass of the holes in the VB causes the hole confined levels in the structure to be very packed and close to each other (see also Fig. 4.2). This makes us consider that a carrier in the barrier material VB edge will find enough de-excitation paths to finally end up at its lowest possible level, i.e. the

first hole confined level in the VBO. Therefore the actual effective bandgap will be defined from this first hole confined level as represented in Fig. 4.2. The little separation between electron confined levels explain the actual carrier escape behavior at T=300 K [Antolín et al., 2010c].

In our case of study, the limiting efficiency of an InAs/GaAs QD-IBSC results in 49.44% for an optimized QD size of 4.09 nm. Even if the host material is GaAs and the E_{G} ∼1.42 eV, the effective bandgap defined with our criterium is 1.066 eV, with E_{H}=0.817 eV and E_{L}=0.249 eV.

4.3 Constraints imposed in our model

The aforementioned screening method is fast enough to compute most of the possible III-V semiconductor compound candidates in a reasonable time and the combinations between them as QD and barrier materials for an optimized IBSC. Hence, we are ready to settle the constraints for potentially efficient QD candidate screening. These constraints which may limit the search for an optimized QD system are:

- The required total effective bandgap should approach that of the ideal of 1.95 eV, although values several hundreds of millielectronvolts below this value or even above it provide high efficiencies if the IB is located close to its optimum position (see Fig. 1.8).

- The CBO has to be as large as possible, preferably above 1 eV, because, as we have already checked in the aforementioned example (InAs/GaAs), the first electron confined level appears at a rather high energy when small QDs are grown, which would displace the IB to energies very close to the CB, i.e. far from the optimum position. On the other hand, small QDs are essential so that: 1) the confined energy levels are well separated from each other in order to avoid the thermalization of carriers [Antolín et al., 2010a, Luque et al., 2011a] and 2) the areal density of QDs can be sufficiently high so as to provide large sub-bandgap absorption.

- The lattice mismatch between the barrier and the QD materials has to be such that it enables the formation of self-assembled QDs, if strain is the driving force for the formation of the QDs, as in the S-K growth mode. We have limited the search for candidates to materials with a lattice mismatch between 3.5% and 9%.

- Contrary to previous works [Levy et al., 2005, Levy and Honsberg, 2008b, Dahal et al., 2010], a negligible VBO is not imposed as a requirement for an optimum QD-IBSC and the reason for it is that the effective bandgap, as it has been defined, can

be considered instead of the bandgap of the barrier material. Under this approach, the electronic transitions are considered from the fundamental hole confined state, instead of from the VB edge, which in addition, may represent the actual generation mechanism in QDs in a more accurate way.

- In this work, we will not restrict the search in terms of mismatch between the barrier material and the substrate to grow on top of. The reason is that such constraint is only practical (availability of substrates) and not of a fundamental nature. Therefore, if the desired barrier material is not lattice-matched to any currently commercially available substrate, a properly lattice-matched substrate could be researched ad hoc, which results would ultimately justify.

- No limitation is prescribed for selecting either indirect barrier or indirect QD materials. They will be subject to our candidate selection when their properties fit the latter constraints, since there is no fundamental reason why indirect materials should be disregarded.

- The size of the QD has to be optimized so that only one confined electron level appears within the CBO. This unique level is then the IB. As it has been already explained in section 4.2.2, this is a way of optimizing the performance of the QD-IBSC because there are no harmful extra confined levels and the IB-CB transition is favored.

Taking all of the aforementioned into account, several QD systems have been identified as good candidate materials. They are all discussed in the following section.

4.4 Results and discussion

4.4.1 $InAs/Al_xGa_{1-x}As$

If we first want to find a QD system that improves the performance of standard InAs/GaAs QDs without significant modification, aluminum can be added to the barrier material and form an $Al_xGa_{1-x}As$ alloy. In order to check whether this is a good idea we just calculate all possible ternary combinations, which in this case implies varying the Al content from 0 to 1 and compute the HEBAM, then the confined levels, and finally the limiting efficiency of the barrier compound ranging from GaAs to AlAs.

When performing this calculation step we must pay attention to the change from direct to indirect gap the alloy experiences at a stoichiometry (x) in the vicinity of 0.44. The reason is that the binary parameters vary as if we were dealing with a different compound

when it becomes indirect: the curvature of the k=X or k=L valleys are different from the k=Γ one, the deformation potentials may even change sign, etc. The result is represented in Fig. 4.3(a), where the efficiency is computed for the optimum radius, defined as the radius for which the energy of the first excited-state equals the energy of the host CB minimum in each case (i.e. calculated for each of the different stoichiometries). Fig. 4.3(b) shows the optimum radius in accordance with the Al content, so the different radius trends leading to the optimum case are shown. The noticeable discontinuity in both plots corresponds to the direct to indirect change, which also matches the maximum efficiency (56.32% for a 2.84 nm QD radius) of the InAs/$Al_xGa_{1-x}As$ QD system.

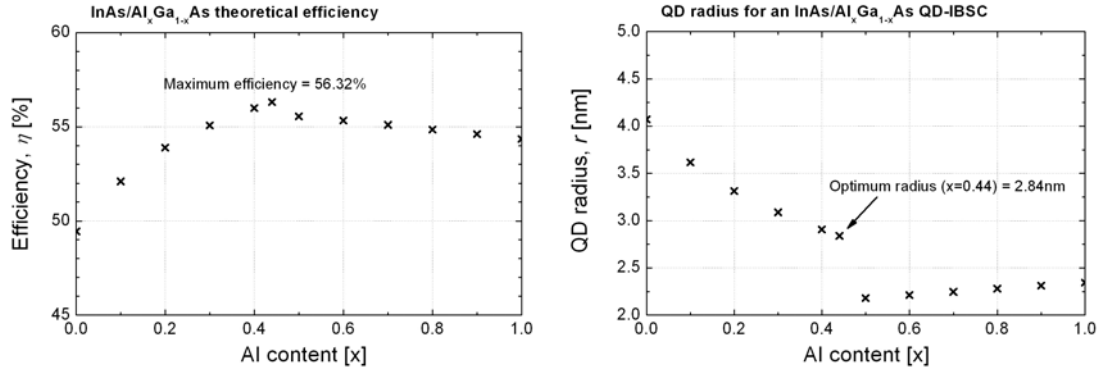

(a) (b)

Figure 4.3: (a) Theoretical efficiency limit of the InAs/$Al_xGa_{1-x}As$ QD-IBSC in accordance with the Al content and calculated for its optimum radius. (b) Radius of the optimum quantum sphere (corresponding to the first excited level appearance) in accordance with the Al content.

In this case, any $Al_xGa_{1-x}As$ compound is almost completely lattice-matched to GaAs, which is advantageous for its growth on top of currently commercially available substrates and the nucleation of QDs is assured since the accumulated strain at the interface is comparable to the well-known InAs/GaAs case.

4.4.2 InAs/$Ga_xIn_{1-x}P$

The InAs/$Ga_xIn_{1-x}P$ QD system has also been studied as a possible QD material to implement the IBSC. Its limiting efficiency is lower than the AlGaAs case, as shown in Fig. 4.4(a). In the case of a barrier material consisting of a $Ga_xIn_{1-x}P$ alloy lattice-matched to GaAs, $Ga_{0.51}In_{0.49}P$ has to be used. However, this InAs/$Ga_{0.51}In_{0.49}P$ material combination does not provide a very large improvement with respect to the InAs/GaAs QD system. The InAs/$Ga_{0.7}In_{0.3}P$ combination reaches its highest efficiency at 50.6% and this will be considered as the optimum of its family, despite being of indirect bandgap and not being lattice-matched to any commercially available substrate. However, these reasons

have not been considered as indispensable in our seek for high efficiency IB materials, as explained in section 4.3.

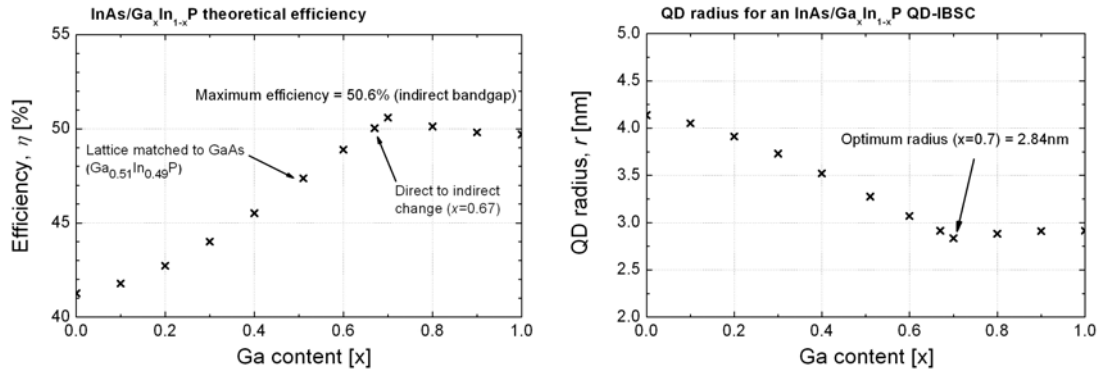

(a) (b)

Figure 4.4: (a) Theoretical efficiency limit of the InAs/$Ga_xIn_{1-x}P$ QD-IBSC in accordance with the Ga content and calculated for its optimum radius. (b) Optimum radius (radius that optimizes the efficiency for each stoichiometry and corresponding band alignment).

Fig. 4.4(b) shows the nanosphere optimum radius of the QD/barrier material for each of the Ga stoichiometries, ranging from 0 to 1. In this case, there is also an abrupt change in the trend of the optimum radius for the direct to indirect change.

4.4.3 $InAs_{1-x}N_x/GaAs$

Another relatively simple modification of the conventional InAs/GaAs QD material consists of adding small amounts of nitrogen into the InAs-based QDs. As a consequence, the so-called $InAs_{1-x}N_x$ dilute nitride is formed, which is more favorable than InAs as a QD material. There are two reasons supporting such statement. The first one is related to the fact that $E_{v,av}$ in InN is much lower than that of InAs and therefore, the nitrogen incorporation pushes the QD material VB towards the barrier VB and reduces the VBO, making the effective bandgap increase and thus bringing it closer to the optimum. The second reason is that the incorporation of small amounts of N into the InAs and the formation of a nitride dilution is related to the BAC effect, which drives its CB towards a less energetic position, and hence reduces the QD material bandgap, which is also beneficial in terms of the IB (because enhances the CBO and reduces the VBO).

The fabrication of the $InAs_{1-x}N_x/GaAs$ QD material has also been proposed and hence, the calculation of realistic nitride dilutions has been carried out. Table 4.2 shows the optimum radius (in nm) and the limiting efficiency for each of the stoichiometries ranging from 0 to 0.03. The first case (x=0) corresponds to the InAs/GaAs case.

Table 4.2: $InAs_{1-x}N_x$/GaAs QD-IBSC data

x	Optimum radius [nm]	Optimum efficiency [%]
0	4.03	49.44
0.01	3.9	50.78
0.02	3.8	52.39
0.03	3.73	53.35

4.4.4 $InAs_{1-y}N_y/AlAs_xSb_{1-x}$

When aiming to the III-V compound semiconductor screening for implementing QD-IBSCs with a high conversion potential, one can simplify the search to a reduced number of ternary/quaternary QD and barrier alloyed combinations. For an optimized barrier material, we realize at a glance that all alloy bandgaps below a certain threshold (that can be set to e.g. 1.5 eV) do not match the constraints for a maximized IBSC performance. Neither of the very wide bandgap QD materials are useful, since they create a small CBO, contrary to the desired criteria. We keep following this reasoning (under the premises given in section 4.3) and we reduce the enormous number of QD and barrier material candidates to a few potentially efficient alloys. Then, once a reduced number of alloy pairs have been selected for QD and barrier materials, their stoichiometry ranges of interest have to be analyzed so the band alignment, effective masses, confined levels and limiting efficiencies can be calculated providing feedback to the optimization process.

$InAs_{1-y}N_y/AlAs_xSb_{1-x}$ is given as a QD system made up of the combination of two ternary alloys that render a quite flat range of efficiencies (between 61.6 to 61.76%) for As contents [x] ranging from 0.75 to 1 and N contents [y] ranging from 0.07 and 0.08, as shown in Fig. 4.5. This bar chart also shows the total host material bandgap as well as the effective bandgap and the energy of the different sub-bandgaps (E_L and E_H) for each of the material combinations.

It has to be mentioned that such levels of N incorporation are currently difficult to achieve for good crystallinities, although a reduction in the N content does not significantly decrease the performance as an IBSC.

The optimum radius, as defined in section 4.2.2 ranges from 1.8 nm to 2.2 nm, increasing as the As content increases.

4.4.5 $InAs_{1-z}N_z/Al_x[Ga_yIn_{1-y}]_{1-x}P$

$InAs_{1-z}N_z/Al_x[Ga_yIn_{1-y}]_{1-x}P$ is another possible QD system offering a maximized efficiency. In this case, the stoichiometry ranges to analyze are x and y varying from 0 to 1 and z as

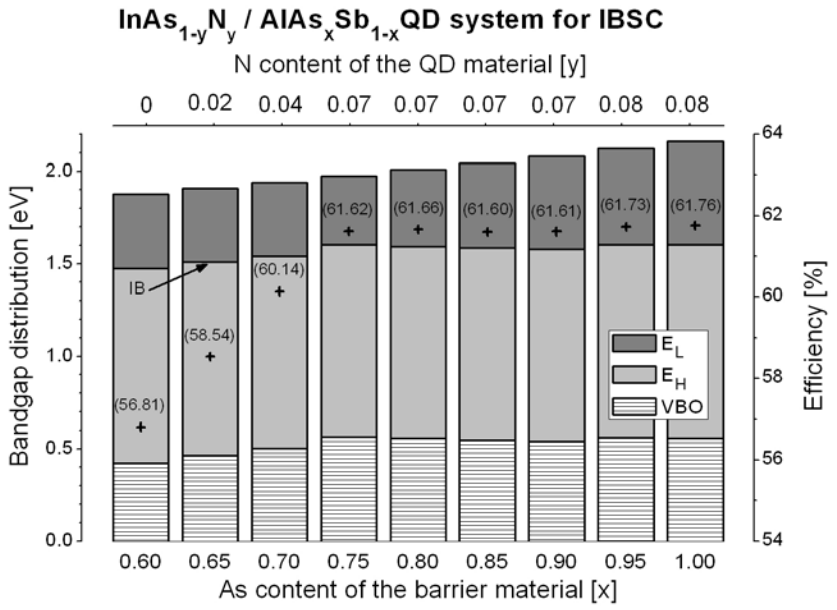

Figure 4.5: Diagram of the $InAs_{1-y}N_y/AlAs_xSb_{1-x}$ QD system representing the bandgap distribution and efficiency in function of the N and Al concentrations.

high as 0.1 (in order to make the III-V nitride alloy closer to a realistic implementation). This large amount of possible combinations are then calculated. The most suitable among them are the ones with stoichiometries that make the barrier become indirect, although a direct one has also been identified as a promising barrier material. In all cases, the phenomenon known as "ordering" will be assumed to be inexistent for AlGaInP alloys for simplicity, i.e. no ternary phases will be considered.

Special attention must be paid to the fact that a small fraction of the indirect AlGaInP alloy, close to the direct threshold, is related to the k=L valley. Once the quaternary has become indirect, the more In the alloy contains the more k=X character it has. This behavior can be explained by looking at the boundary $Ga_xIn_{1-x}P$ ternary, which is characterized by a minimum k=L valley from x=0.67 to 0.7, thus making its study more complicated because of the lack of data for most of the quaternaries.

The most significant data on the appropriate candidates is compiled in Table 4.3, where the effective bandgap as well as as the E_L values are shown. The optimum radius for the aforementioned material combinations is slightly larger than 2 nm, except for the only direct AlGaInP barrier compound, which approaches 2.5 nm. Values as high as 62.35% are reached for the most efficient QD material combinations.

Table 4.3: High efficiency $InAs_{1-z}N_z/Al_x[Ga_yIn_{1-y}]_{1-x}P$ data

x	y	z	E_G^* [meV]	E_L [meV]	Nature	Efficiency
0.42	0.05	0.06	1662.4	595.8	direct	61.65
0.02	0.68	0.08	1685.2	595.7	indirect	62.35
0.03	0.74	0.09	1683.3	606.1	indirect	61.68
0.04	0.72	0.09	1680	606.4	indirect	61.5

4.4.6 $InAs_{1-y}N_y/Ga_xAs_{1-x}P$

The $InAs_{1-y}N_y/Ga_xAs_{1-x}P$ QD material has also been studied for implementing the IBSC. In this case, the $Ga_xAs_{1-x}P$ alloy, which acts as barrier material, could be either grown on top of a GaAs matrix or on GaP, depending on the stoichiometry, although, this is not a crucial aspect in our study. The material screening has been carried out using our model and varying the N content from 0 to 0.1. Larger amounts of N do not seem realistic.

The optimum combination has been found to be $InAs_{0.9}N_{0.1}/Ga_{0.37}As_{0.63}P$. Its band diagram is sketched in Fig. 4.6(a). It has a reasonably appropriate total bandgap of 2.076 eV, although it is reduced to an effective bandgap of 1.6 eV once the confined hole levels in the VB are calculated and the aforementioned criterium is applied. The confined electronic levels are represented in the CBO energy diagram of Fig. 4.6(b), where the largest possible E_L that can be obtained without extra confined levels (criterion used to obtain the optimum radius) is indicated. The optimized nanosphere radius is 4.76 nm, which is relatively large compared to the previous calculated materials. This is probably due to the large difference existing between the electron effective masses of both materials: m_e^*(barrier)=0.089 to be compared with m_e^*(QD)=0.012. Fig. 4.6(b) shows the electron confined levels in accordance with the QD radius for a CBO=1.385 eV. The optimum radius produces an E_L of 0.415 eV. The lattice mismatch with respect to GaAs, Δa_{lc}, is 7.7%, very close to that of the InAs/GaAs QD system.

The $InAs_{1-y}N_y/Ga_xAs_{1-x}P$ QD-IBSC results in a limiting efficiency of 54.68%, although the barrier material is at Δa_{lc}=1.38% from GaP, the commercial substrate with the closest a_{lc}.

4.4.7 Type II-valence band offset (TII-VBO) QD-IBSC

Most QD/barrier material combination calculated and fabricated so far are endowed with a positive or type-I VBO, i.e. the energy of the QD material VB is higher than the barrier material VB. The possibility of manufacturing QD-IBSCs with a negative or type-

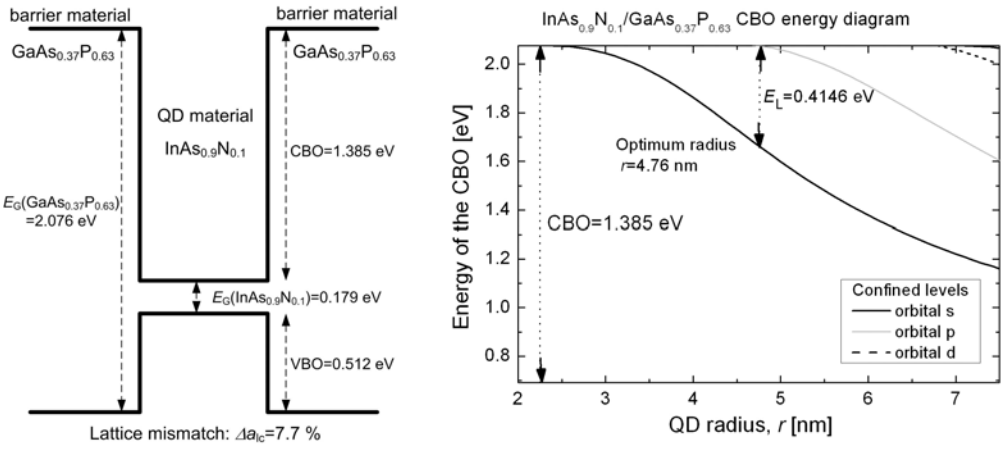

(a) (b)

Figure 4.6: Study of the electronic characteristics of the $InAs_{1-y}N_y/Ga_xAs_{1-x}P$ QD material particularized for the stoichiometry that provides an optimum QD-IBSC material (x=0.37 and y=0.1). (a) Band diagram of the $InAs_{0.9}N_{0.1}/Ga_{0.37}As_{0.63}P$ heterojunction. The lattice mismatch (Δa_{lc}) between barrier and QD materials is also indicated. (b) Energy diagram of the CBO with all the confined levels arising within the CBO up to 7.5 nm. The optimum radius is indicated.

II VBO has been identified [Tomić et al., 2011]. The idea of this type-II VBO is to extend the wavefunction of the holes in the VB so that the Auger interband relaxation can be inhibited. This Auger mechanism could be partly responsible for favoring the electronic thermalization between confined states in the CB, which ultimately blocks the phonon-bottleneck effect. In this respect, the $InAs/Al_xGa_{1-x}As_ySb_{1-y}$ heterojunction is identified as a candidate material for type-II QDs.

The $Al_xGa_{1-x}As_ySb_{1-y}$ quaternary covers a very large area in the bandgap/lattice constant ($E_G(a_{lc})$) graph, as it is represented in Fig. 4.7. Most of the III-V binary compounds are represented in the graph as well as the ternaries produced by the alloys formed by each two of these binaries. The solid lines represent the direct bandgap ternaries and the dashed lines represent the indirect bandgap ternaries. The four binaries that form the $Al_xGa_{1-x}As_ySb_{1-y}$ quaternary (Al, Ga, As and Sb) are highlighted in the graph with a red circle and the binary forming the QDs is represented with a green circle. The area of the quaternary is delimited by the contour delimited by the ternary compounds connecting the four binaries: $Al_xGa_{1-x}As$, $AlAs_xSb_{1-x}$, $Al_xGa_{1-x}Sb$ and $GaAs_xSb_{1-x}$. The stripped region inside this area approximately corresponds to the $Al_xGa_{1-x}As_ySb_{1-y}$ quaternary alloy of indirect bandgap. The indirect bandgap region is preferred in our calculation because it is associated to values of the barrier material bandgap closer to the optimum. This indirect region has been defined from the direct-indirect crosspoint of the $Al_xGa_{1-x}As$ ternary to the homologous point in the $Al_xGa_{1-x}Sb$ alloy. A bowing parameter of an approximately

intermediate value between the bowing parameter of both ternaries has been selected to delimit this indirect bandgap region.

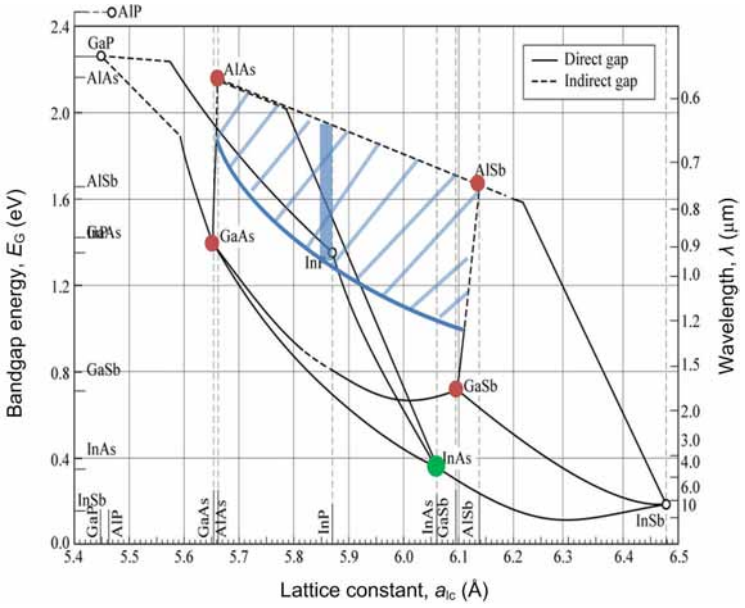

Figure 4.7: $E_G(a_{lc})$ graph representing most of the III-V semiconductors. The indirect bandgap $Al_xGa_{1-x}As_ySb_{1-y}$ quaternary alloys are represented with blue stripped area and the valid solutions for the desired host material of the type-II QD system are represented with a solid rectangle.

The definition of the indirect bandgap region is important in order to carry out the calculation of the band alignment of the alloyed heterostructure with our HEBAM. Once this region has been identified, the constraints of our QD system have to be set. The first of them is of course the negative VBO, for which the condition 0 meV>VBO(InAs/AlGaAsSb)>-100 meV is defined (a very negative VBO is not desired). A second constraint determines the lattice mismatch between the quaternary and the substrate on top of which it is grown. The only commercially available substrate far enough (in the $E_G(a_{lc})$ graph) from the $Al_xGa_{1-x}As$ alloy (that always produces type-I VBOs) seems to be InP. Actually, in this region of the graph, only GaAs and InAs are alternative substrate candidates, but unfortunately the $Al_xGa_{1-x}As_ySb_{1-y}$ alloys which are reasonably lattice matched to each of the are not suitable. In the first case (GaAs) the reason is that these $Al_xGa_{1-x}As_ySb_{1-y}$ alloys are far from producing the desired type-II VBOs and in the second case (InAs) the problem is that very little mismatch would be produce between the barrier and the QD materials so as to produce the nucleation of the dots by S-K growth mode. As this Δa_{lc}(AlGaAsSb/InP) cannot be large if a relatively thick high quality solar cell is to be grown, we impose the following condition: Δa_{lc}(AlGaAsSb/InP)<0.5%. Only the solutions with $a_{lc} > a_{lc}$(InP) are selected so that a higher Δa_{lc}(InAs/AlGaAsSb) is obtained and thus a better nucleation of the dots takes place (i.e. with a thinner WL). The two aforementioned constraints

determines the solutions of the problem, which are located within the blue solid rectangle shown in the figure. A third condition is established: |CBO|< E_{G}-100 meV. It is meant to prevent the possible carrier tunneling between the confined states in the CBO and the barrier material VB. However, no alloy is disregarded with this last constraint, although the CBOs of these heterojunctions are large (in the range of 1.3-1.5 eV, as it is represented in Table 4.4).

Table 4.4: Valid solutions for the quaternary alloys with their respective stoichiometries, bandgaps, VBO, CBO, effective masses and lattice mismatch for the InAs/$Al_xGa_{1-x}As_ySb_{1-y}$ type-II heterojunction.

Al[%]	Ga[%]	As[%]	Sb[%]	VBO	CBO	$E_{\mathrm{G,barrier}}$	$m^*_{\mathrm{e,barrier}}$	$m^*_{\mathrm{e,QD}}$	Δa_{lc}
0.64	0.36	0.54	0.46	-0.0976	-1.290	1.601	0.266	0.0254	0.0318
0.65	0.35	0.54	0.46	-0.095	-1.295	1.608	0.266	0.0254	0.0318
0.66	0.34	0.54	0.46	-0.0928	-1.299	1.614	0.265	0.0254	0.0317
0.67	0.33	0.54	0.46	-0.0905	-1.303	1.621	0.264	0.0254	0.0317
0.68	0.32	0.53	0.47	-0.0996	-1.314	1.621	0.263	0.0253	0.0308
0.68	0.32	0.54	0.46	-0.0881	-1.307	1.628	0.264	0.0254	0.0317
0.69	0.31	0.53	0.47	-0.0973	-1.318	1.627	0.262	0.0253	0.0308
0.69	0.31	0.54	0.46	-0.0857	-1.312	1.634	0.263	0.0254	0.0316
0.7	0.3	0.53	0.47	-0.0950	-1.322	1.634	0.261	0.0253	0.0308
0.7	0.3	0.54	0.46	-0.0834	-1.316	1.641	0.262	0.0254	0.0316
0.71	0.29	0.53	0.47	-0.0927	-1.327	1.641	0.261	0.025	0.0307
0.71	0.29	0.54	0.46	-0.0811	-1.320	1.647	0.26	0.0254	0.0315
0.72	0.28	0.53	0.47	-0.0904	-1.331	1.647	0.260	0.0253	0.0307
0.72	0.28	0.54	0.46	-0.0788	-1.325	1.654	0.261	0.025	0.0315
0.73	0.27	0.52	0.48	-0.0994	-1.342	1.648	0.258	0.0252	0.0298
...	...	...	...	...	...	...	...	...	...
0.98	0.02	0.55	0.45	-0.00895	-1.435	1.834	0.243	0.0254	0.0313
0.99	0.01	0.5	0.5	-0.0671	-1.479	1.812	0.237	0.024	0.0271
0.99	0.01	0.51	0.49	-0.0557	-1.472	1.818	0.238	0.0250	0.0279
0.99	0.01	0.52	0.48	-0.0440	-1.464	1.823	0.239	0.0251	0.0288
0.99	0.01	0.53	0.47	-0.0319	-1.456	1.8295	0.240	0.0252	0.0296
0.99	0.01	0.54	0.46	-0.0195	-1.448	1.835	0.241	0.0253	0.0304
0.99	0.01	0.55	0.45	-0.00684	-1.440	1.840	0.243	0.0254	0.031
1.	0.	0.5	0.5	-0.0652	-1.484	1.819	0.236	0.0249	0.0271
1.	0.	0.51	0.49	-0.0537	-1.477	1.825	0.237	0.0250	0.0279
1.	0.	0.52	0.48	-0.0420	-1.469	1.830	0.238	0.0251	0.0287
1.	0.	0.53	0.47	-0.0299	-1.461	1.83	0.240	0.0252	0.0296
1.	0.	0.54	0.46	-0.0175	-1.453	1.842	0.241	0.0253	0.030
1.	0.	0.55	0.45	-0.00474	-1.445	1.848	0.242	0.0254	0.0312

A reduced sample of the results produced by the HEBAM applied to the InAs/$Al_xGa_{1-x}As_ySb_{1-y}$ heterojunction is represented in Table 4.4. It includes data on the band alignment, e.g.

VBO and CBO, and bandgaps and effective masses of both the barrier and the QD materials as a function of the stoichiometry of such materials. The lattice mismatch is also given in the table. The model produces a very large list of results and not all of them are shown in the table. Actually, a line filled with points separates the beginning and the end of the list of valid results.

The $AlAs_{0.55}Sb_{0.45}$ quaternary alloy is taken as an example for the calculation of the limiting efficiency as QD-IBSC. Its parameters are necessary to calculate the energy of the confined electron levels (the confined holes are not necessary in these type-II structures). They can be obtained from the table: $E_{G,\,barrier}$ = 1.848 eV, CBO = 1.445 eV, $m^*_{e,barrier}$=0.242 and $m^*_{e,QD}$=0.0254084. Thanks to these data, the confined levels in the CBO can be calculated. These confined levels are shown in Fig. 4.8(a). A graphical representation of the mathematical verification of the Schrödinger equation inside and outside the potential well is also shown in Fig. 4.8(b).

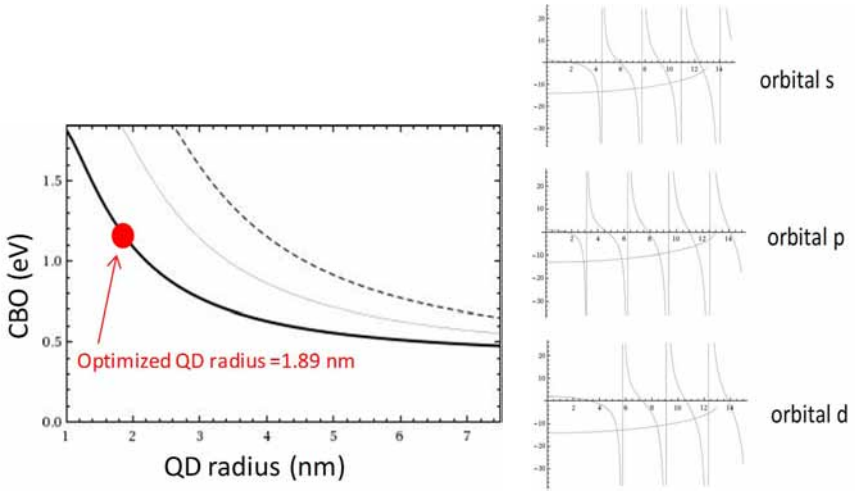

(a) (b)

Figure 4.8: (a) Confined electron levels as a function of the QD radius in an $InAs/Al_xGa_{1-x}As_ySb_{1-y}$ QD system assuming the approximation of spherical dots. (b) Graphical expression of the mathematical verification of the Schrödinger equation inside and outside the potential well that represents the QD surrounded by the barrier material.

The optimum QD radius [Linares et al., 2011] is again defined as in section 4.2.2 (in this case, it is only 1.89 nm large). The bandgap distribution (E_G and E_L) is deduced from the previous analysis and the limiting efficiency is calculated for maximum concentration. An η_{max} ≈63% is obtained with this configuration.

4.4.8 An example of the lead salt QD-IBSC: PbSe/ZnTe

An IB material from the so-called lead-salt QD-IBSC family [Antolín et al., 2011] has also been studied. It consists of a QD/barrier material combination which nucleation driving force is not the strain created by the lattice mismatch (Stranski-Krastanov growth mode), but the difference lattice structure of the QD material with respect to the barrier material (rocksalt crystalline structure in the first case and zincblende structure in the second). The concept is based on the non-strained lead salt QD (IV-VI) family [Heiss et al., 2006] such as PbTe, PbSe or PbS, which nucleate within a host material from the II-VI family: $Cd_{1-x}Mg_xTe$, $Cd_xZn_{1-x}Te$, $CdS_{1-x}Se_x$ or $ZnSe_{1-x}Te_x$.

These QDs can be lattice-matched to the barrier (a ternary alloy is required so that the lattice constant of the barrier compound material can be tuned and adjusted to the a_{lc} of the QD), thus avoiding the strain problems of the conventional III-V materials. Besides, the aspect ratio of the QDs formed by means of this difference in the crystalline structure is very close to one and the size can be easily tuned. Another advantage is that because of the growth mechanism, no wetting layer is formed, which is very positive, regarding their performance as an IBSC.

In this case, only one material combination has been selected as a case of study. The selected QD consists of PbSe, which crystallizes in rocksalt structure and ZnTe as barrier material, which crystallizes in zincblende structure. Fig. 4.9(a) represents the band diagram of the PbSe/ZnTe heterojunction, which cannot be calculated by means of our III-V HEBAM and hence has to be calculated from the material electronic affinity data found in Ref. [Madelund et al., 1986]. It has to be noted that this is probably a good approximation, since no strain affects the structure when the heterojunction is lattice-matched. An inverted configuration (small CBO and large VBO) with respect to the usual III-V material combinations is suitable in this case, because the hole effective masses are appropriate for hole confining in these materials. The host bandgap, close to 2.4 eV, a priori may result a bit large for an optimized IB material, although the confined levels could eventually modify this situation. The confined energy levels (holes and electrons) are calculated again with respect to the QD radius for this structure. The latter is shown in Fig. 4.9(b), where the sphere approximation is quite accurate, since the lead salt QDs can be almost completely rounded [Heiss et al., 2006]. This time, a rather low value and large difference between the hole effective masses, m_h^*, of the two involved materials (m_h^*(barrier)=0.2 and m_h^*(QD)=0.048) together with the large VBO make the hole confinement suitable for hosting an isolated confined hole level acting as the IB. This is clearly represented in Fig. 4.9(a), where a small QD, of a radius close to r=1.6 nm, creates an IB very deep into the bandgap that provides a limiting efficiency of η=50.43%.

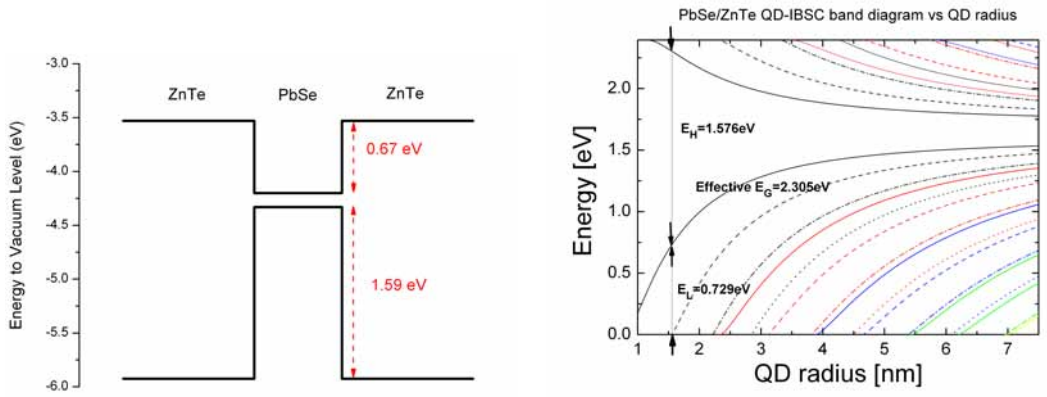

(a) (b)

Figure 4.9: Study of the electronic characteristics of the PbSe/ZnTe lead salt QD material. (a) Band diagram of the PbSe/ZnTe heterojunction. (b) Energy diagram of the confined levels (holes and electrons) arising within the PbSe/ZnTe spheric QD approximation. The optimum radius is indicated (for an IB formed by hole confining) together with the effective bandgaps and sub-bandgaps defined by the confined levels following our criterion.

4.5 Calculation of $In_x[Ga_yAl_{1-y}]_{1-x}As$ strain relief layers for the QD-IBSC

The heterojunction band alignment model or HEBAM developed in this Thesis was also used to calculate the appropriate stoichiometry of the $In_x[Ga_yAl_{1-y}]_{1-x}As$ alloy to be used as SRL in the InAs/GaAs QD-IBSCs fabricated in the University of Glasgow [Linares et al., 2010a]. The concept was introduced in section 5.2 together with the seed layer concept. It consists of calculating the quaternary alloy that fulfills the following conditions: 1) hosting approximately 20% of In; 2) matching the $In_x[Ga_yAl_{1-y}]_{1-x}As$ CB with the GaAs CB; and 3) a bandgap larger than the GaAs bandgap, so that the cap does not contribute to limiting the voltage of the IBSC.

The first condition is related to avoid the alloying produced between In and Ga adatoms during during the capping of the QDs with GaAs. This alloying or intermixing effect is induced by the strain of the QDs and it worsens the aspect ratio of the QD [Antolín et al., 2010a]. This problem has been circumvented by depositing a capping layer containing In, immediately above each of the QD layers [Ustinov et al., 2000]. The In incorporation occurs by means of a surface process in which In and other Group III adatoms (basically Ga or Al) are exchanged during the deposition of the capping layer above the QD InAs layers. The driving force for such redistribution is the strain field appearing during QD formation, responsible for the preferable relocation of indium adatoms next to InAs islands, as represented in Fig. 4.10. The SRL capping is then followed by a GaAs spacer layer

containing a Si δ-doping is introduced (schematically represented in the figure). The layer sequence is repeated to form a QD stack.

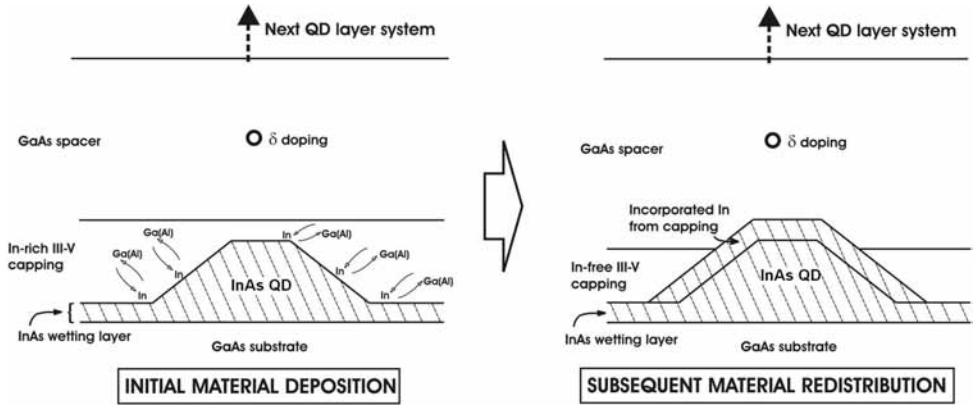

Figure 4.10: Sketch showing the In incorporation process. On the left side, the surface exchange process is shown. The right side represents the steady state case where most of the In in the capping layer has joined the InAs island contributing to QD enlargement [Ustinov et al., 2000].

There is a limit to the total amount of In that can be deposited directly during the formation of the QDs and the subsequent capping of the dots with a strain-relieving buffer before strain relaxation occurs, an effect reported by Ustinov et al. [Ustinov et al., 2000]. The total amount of InAs, Q_Σ, measured in ML, deposited in the QDs and the cap can be expressed by the following relationship:

$$Q_\Sigma = Q_{\mathrm{InAs}} + x\, L_z \tag{4.9}$$

where Q_{InAs} is the initial amount of InAs deposited for QD nucleation (usually 2ML), x is the In compositional fraction of the capping layer and L_Z its thickness, also measured in ML. The accumulated amount of InAs in the QDs and cap (Q_Σ) cannot exceed 5 ML [Ustinov et al., 2000], otherwise the QDs relax and their associated PL intensity decreases. The maximum In stoichiometry of the cap is found to be approximately 0.2 without the degradation of the QD performance, which has been identified empirically. The value has been corroborated through low temperature PL measurements on structures with different $In_xGa_{1-x}As$ cap compositions.

The second condition refers to a zero CBO between the $In_x[Ga_yAl_{1-y}]_{1-x}As$ cap and the GaAs host in order to prevent the appearance of either a detrimental intermediate energy band between the IB and CB (positive CBO) and consequent voltage loss, or a potential barrier (negative CBO) that obstructs the electron transport throughout the CB. This is sketched in Fig. 4.11, where the CBs of a ternary and a quaternary capping layers are illustrated together with the CB of the InAs QD and the GaAs barrier material. The figure

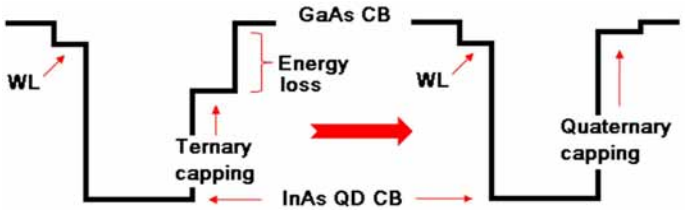

Figure 4.11: Sketch of the heterojunction CB alignment between a ternary cap (left) and the QD (InAs) and barrier materials (GaAs). The right part of the figure shows the same alignment in which the ternary is substituted by a quaternary cap.

shows how a ternary $In_xGa_{1-x}As$ cap cannot adjust its CB in order to obtain a CBO=0. No matter how large the In stoichiometry of the ternary alloy is, that the band alignment will be such that a positive CBO will be produced. Nevertheless, the $In_x[Ga_yAl_{1-y}]_{1-x}As$ can be selected so that a negligible or even a zero CBO is obtained. Besides, the quaternary allows to do so for a fixed In stoichiometry of 0.2.

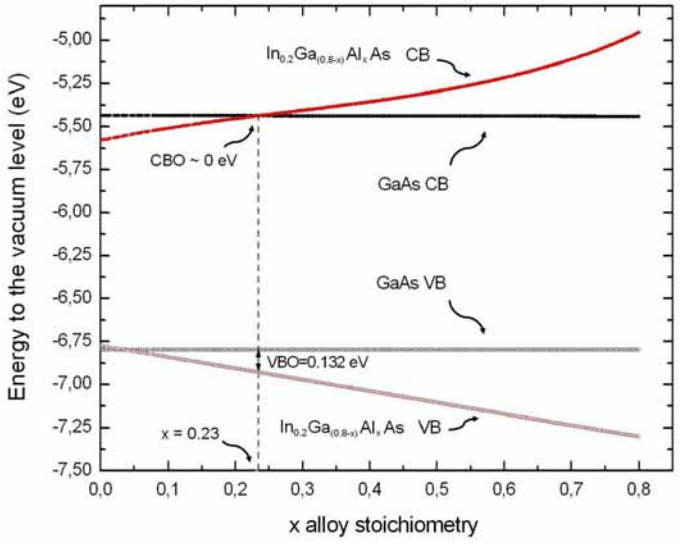

Figure 4.12: Calculated band diagram showing GaAs and $In_{0.2}Ga_{0.8-x}Al_xAs$ VB and CB lineups depending on the x stoichiometric (Al fraction in this case). Optimal x is chosen so that the CBO=0.

The quaternary cap is calculated with respect to only one variable, x, varying the $In_{0.2}Ga_{0.8-x}Al_xAs$ alloy from 0 to 1. Fig. 4.12 shows the result of this calculation, where one solution fulfills the three conditions. The vertical dashed line shows the optimal Al content and, therefore, the global stoichiometry that the quaternary barrier material must have: $In_{0.2}Al_{0.23}Ga_{0.57}As$.

The two InAs/GaAs QD-IBSCs fabricated by the University of Glasgow presented in this Thesis have been implemented using this $In_{0.2}Al_{0.23}Ga_{0.57}As$ quaternary cap. It has demonstrated the validity of the predicted performance [Antolín et al., 2010a] i.e. the E_H

transition was redshifted almost 100 meV, increasing the activation energy with respect to the QD samples without capping.

4.5.1 $In_x[Ga_yAl_{1-y}]_{1-x}As$-$Al_{0.25}Ga_{0.25}As$

As mentioned in section 4.4.1, the InAs/AlGaAs QD approach is promising because of the higher bandgap of the host semiconductor as well as for the possibly larger IB-CB transition. $InAs/Al_xGa_{1-x}As$ QD cells with x=0.25 are a reasonable candidate to

Table 4.5: Stoichiometries of the $In_x[Ga_yAl_{1-y}]_{1-x}As$ alloy that produce a CBO<5 meV with respect to an $Al_{0.25}Ga_{0.25}As$ host

In[%]	Ga[%]	Al[%]	$E_G[In_x(Ga_yAl_{1-y})_{1-x}As]$
0	0.75	0.25	1.78003
0.0072	0.7128	0.28	1.80732
0.0138	0.6762	0.31	1.8348
0.0198	0.6402	0.34	1.86273
0.0256	0.6144	0.36	1.87892
0.031	0.589	0.38	1.8957
0.036	0.564	0.4	1.91315
0.0406	0.5394	0.42	1.93135
0.5244	0.0456	0.43	1.4829
0.5096	0.0504	0.44	1.50985
0.0448	0.5152	0.44	1.95036
0.0495	0.5005	0.45	1.95671
0.4752	0.0648	0.46	1.56669
0.054	0.486	0.46	1.96347
0.4611	0.0689	0.47	1.59347
0.0583	0.4717	0.47	1.97063
0.442	0.078	0.48	1.62323
0.4284	0.0816	0.49	1.64986
0.41	0.09	0.5	1.67944
0.07	0.43	0.5	1.99468
0.392	0.098	0.51	1.70891
0.3744	0.1056	0.52	1.73828
0.3572	0.1128	0.53	1.76753
0.3404	0.1196	0.54	1.79666
0.3195	0.1305	0.55	1.82867
0.3036	0.1364	0.56	1.85751
0.2992	0.1408	0.56	1.86055
0.2795	0.1505	0.57	1.89229
0.2752	0.1548	0.57	1.89539
0.2562	0.1638	0.58	1.92696
0.252	0.168	0.58	1.93012
0.2296	0.1804	0.59	1.9647
0.2255	0.1845	0.59	1.96794
0.2214	0.1886	0.59	1.97122
0.2173	0.1927	0.59	1.97454

progress in QD-IBSC with respect to previous approaches based on InAs/GaAs. The

whole range of $Al_xGa_{1-x}As$ ternary alloys is almost completely lattice-matched to GaAs, which makes it a relatively easy heterojunction to fabricate by MBE. Hence, the quaternary $In_x[Ga_yAl_{1-y}]_{1-x}As$ SRL has to be calculated, this time to match the conditions of the $Al_{0.25}Ga_{0.25}As$ host material. The results from Table 4.5 are obtained when only the constraint of CBO<5 meV is considered for this $In_x[Ga_yAl_{1-y}]_{1-x}As$-$Al_{0.25}Ga_{0.25}As$ case.

The table includes the different stoichiometries of the quaternary alloy in the three first columns and the resulting bandgap in the fourth column. It can be observed that the first stoichiometry of the table corresponds to the host ternary itself ($Al_{0.25}Ga_{0.25}As$). However, this solution is obviously not valid as SRL material. With respect to the rest of the results, if the third constraint employed in the case of the GaAs is used in this case, all the $In_x[Ga_yAl_{1-y}]_{1-x}As$ alloys with lower bandgap than $Al_{0.25}Ga_{0.25}As$ have to be excluded. There is not certain knowledge of the validity of the second constraint (In content $\sim$0.2), but in case it is also applied, a very similar result to the GaAs case is finally obtained for the composition of the SRL of the InAs/$Al_{0.25}Ga_{0.25}As$ QD-IBSC.

4.6 Summary

We have developed a theoretical model capable of a fast analysis of III-V compound semiconductors in order to predict their suitability as QD systems for an IBSC. It consists of a calculation method based on three main steps: 1) computing the band alignment of the heterojunction formed by the barrier and QD material and also computing some important parameters from the alloy such as the effective mass; 2) determining the confined states of the QD in order to calculate the effective bandgap distribution so the three possible transitions can be calculated; and 3) determining the efficiency limit in the framework of the detailed balance theory to estimate the suitability of the QD system to perform as an IBSC.

The approximations of the model are justified by the ultimate purpose of the analysis, which is meant to act as a first screening of possible candidate materials.

Some master lines on how to carry out a proper search for III-V candidates have been given with special emphasis on the treatment of the VBO and its confined energy levels in order to define the effective bandgap of the QD-IBSC so that an isolated IB, far from the CB and from other excited levels can be obtained.

The model is applied to the standard InAs/GaAs QD system to exemplify how it operates. Subsequently, several material candidates with limiting efficiencies close to the maximum of the IBSC concept have been identified.

Chapter 5

Fabrication of strain-compensated In(Ga)As/GaAs$_{1-x}$N$_x$ QD-IBSCs

5.1 Introduction

After the fundamentals of the IBSC were first proposed in 1997 [Luque and Martí, 1997b], the need for a feasible technology to implement this new type of solar cell became apparent. The use of QDs was soon identified as a promising way for the practical implementation of IBSCs [Martí et al., 2000]. The first photovoltaic devices ad-hoc manufactured with the possibility of hosting an IB within the bandgap, together with the rest of the necessary features of the IBSC concept, were designed at IES-UPM and grown at the University of Glasgow [Luque et al., 2005]. Since then, an increasing number of research centers worldwide have pursued the implementation of the QD-IBSCs based on the InAs/GaAs system [Hubbard et al., 2008, Oshima et al., 2008, Popescu et al., 2008, Zhou et al., 2010].

Quantum dots are semiconductor crystals of nanometric size, also known as "artificial atoms" or "molecules" because their electronic properties are in some aspects similar to those of single atoms. These quantum structures can be engineered so that their electronic properties are tuned for a specific purpose. A QD system consists of a collection of small semiconductor crystals of nanometric dimension (QD material) embedded in another crystal of different nature (barrier material). The barrier (or host) material is characterized, in most cases, by the largest bandgap, so that a confining potential is created inside the dots. QDs can be treated in an ideal way as spherical, although most of them resemble a concave lens [Sugawara, 1999], a pyramid [Harrison, 2005] or a truncated pyramid [Tablero, 2009, Tomić, 2010] in practice. They are restricted to the nanometric range in the three spatial directions. This causes the appearance of discrete confined energy levels (electron,

holes or both) with a typical DOS similar to a delta-like function, as the one shown in Fig. 5.2(d) [Sugawara, 1999, Tomić, 2010].

Quantum dots can be thus used to implement the intermediate band solar cell concept [Martí et al., 2000]. Under the QD approach, the fundamental or ground-state of the QD is meant to act as the IB, as shown in Fig. 5.1, where the band diagram of a QD-IBSC is sketched. The figure shows several non-ideals that will be reviewed throughout this chapter, such as the effect of the extra confined levels or the WL. These produce the theoretical E_G, E_H and E_L bandgaps of the ideal IBSC to turn into the $E_{G,eff}$, $E_{H,eff}$ and $E_{L,eff}$ effective bandgaps, which correspond to a more realistic situation of the band diagram of a QD structure. The IB requires to be well separated from the CB so that carriers cannot easily escape from the confined states towards the CB [Antolín et al., 2010a] and thermal radiation, instead of photons from the sun is not the main contribution to electron pumping from the IB to the CB [Luque et al., 2011a]. Otherwise, the QFL split between IB and CB would be difficult to achieve. When the confined states are separated by an energy greater than that of the phonons, the carrier thermalization through the emission of a single phonon is inhibited. This non-radiative recombination (NRR) blockade is also known as phonon-bottleneck-effect [Bockelmann and Bastard, 1990].

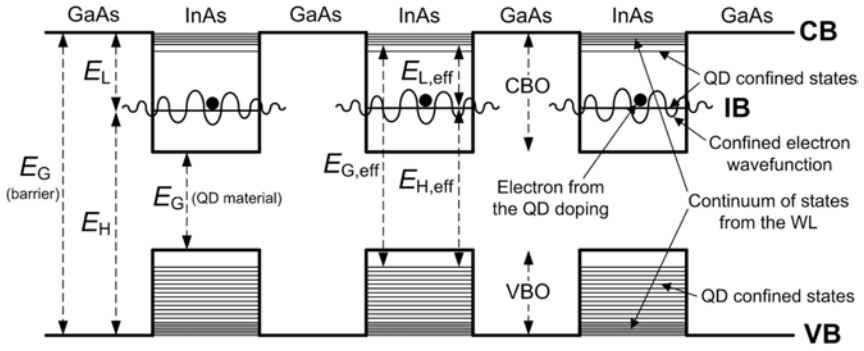

Figure 5.1: Sketch of an InAs/GaAs QD-IBSC band diagram. The effective fundamental bandgap $E_{G,eff}$ and the effective sub-bandgaps $E_{H,eff}$ and $E_{L,eff}$ are reduced with respect to the original distribution because of the non-ideals introduced by the QDs. The rest of elements in the sketch are reviewed throughout this chapter.

But not every kind of nanostructure is potentially adequate for the implementation of an IBSC. In nanotechnology approaches with lower degree of confinement, such as quantum wires (QWRs) or quantum wells (QWs), respectively characterized by one or two degrees of freedom in real space [Datta, 1989, Harrison, 2005], carriers are not spatially confined in all directions. As a consequence, these nanostructures are characterized by a continuum in the DOS function, starting from the ground-state towards higher energies. This has been represented in Fig. 5.2(b) and Fig. 5.2(c), where the DOS function for QWs and

QWRs are schematically shown. The typical DOS of a bulk material is also represented (5.2(a)) for comparison. This continuum in the DOS function prevents the existence of an IB isolated from both the VB and the CB and thereby makes the IB-CB QFL split increasingly difficult.

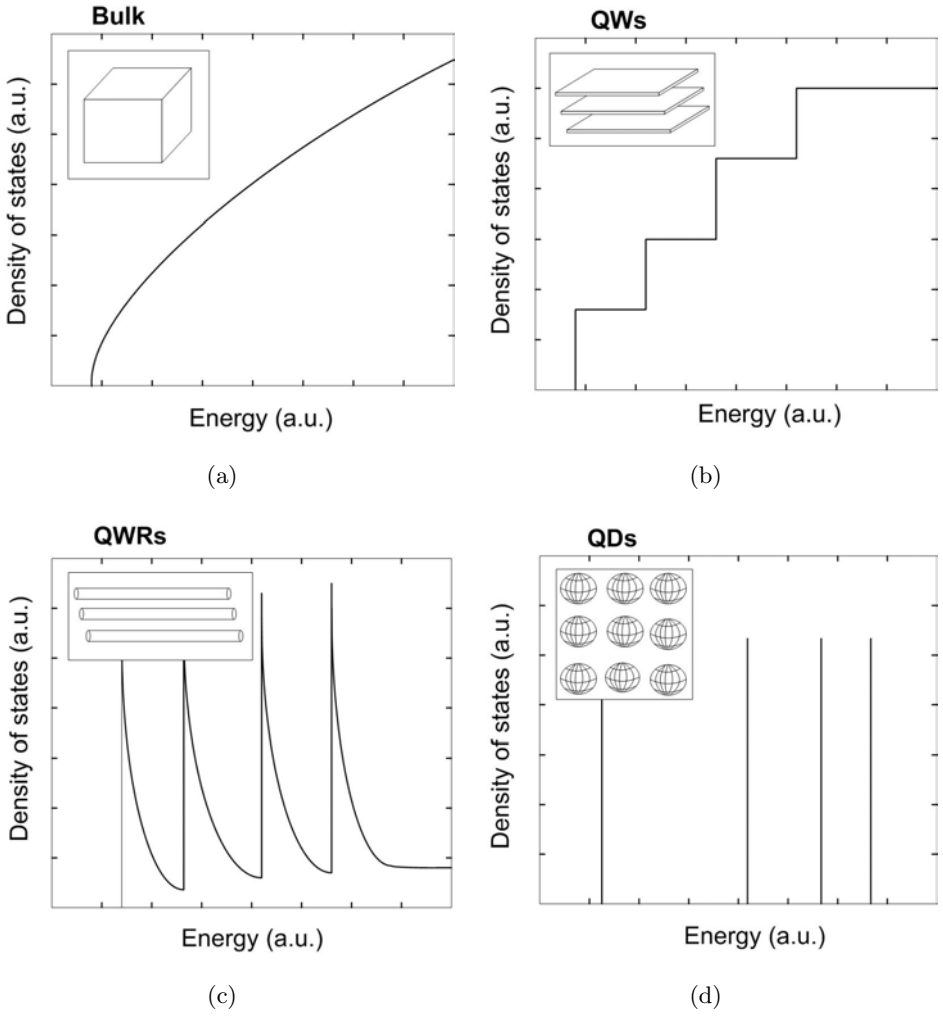

Figure 5.2: Schematics of DOS functions: (a) the crystal in bulk has a continuous DOS; (b) QWs allow two degrees of freedom for electrons and are characterized by a continuous stair-like DOS function; (c) QWRs allow one degree of freedom for electrons and present a continuous needle-like DOS function; (d) only QDs confine electrons in the three spatial directions and present a delta-like DOS function.

Several stacked QD layers have to be grown in order to increase the overall photon absorption of the QDs. The low-energy part of the spectrum, i.e. IR light, can only be absorbed in the QDs. This absorption is proportional to the number of QDs that these IR photons find throughout their optical path, which, under normal illumination, corresponds to the number of QD layers present in the solar cell structure. However, the stacking of successive QD layers presents growth problems related to the accumulation of strain.

InAs/GaAs QDs are commonly grown in the Stranski-Krastanov growth mode [Stranski and Krastanov, 1939,Sugawara, 1999,Harrison, 2005], in which the driving force leading to the formation of the QDs is the strain appearing because of the lattice mismatch between the QDs and the barrier material (7.16% of mismatch in this case). It is precisely thanks to this difference in lattice constant (a_{lc}) and the subsequent compressive strain exerted in the thin InAs layer that islands can nucleate, forming the QDs. The formation of these QDs takes place when the amount of InAs material deposited on top of the GaAs matrix surpasses a critical thickness (h_{c}) as a means to release some of the accumulated strain. The whole QD nucleation sequence is sketched in Fig. 5.3. This zero-dimensional nanostructure growth mechanism is also characterized by a thin layer of QD material which 'wets' the plane of growth of the QDs. This thin layer is a QW superimposed to the QDs, usually referred to as WL. The presence of this WL is detrimental for the QD-IBSC because it adds a two-dimensional nanostructure together with the QDs and creates a continuum of states very close to the CB (as represented in Fig. 5.1), reducing the effective bandgap and easing the recombination to the lower energy confined states.

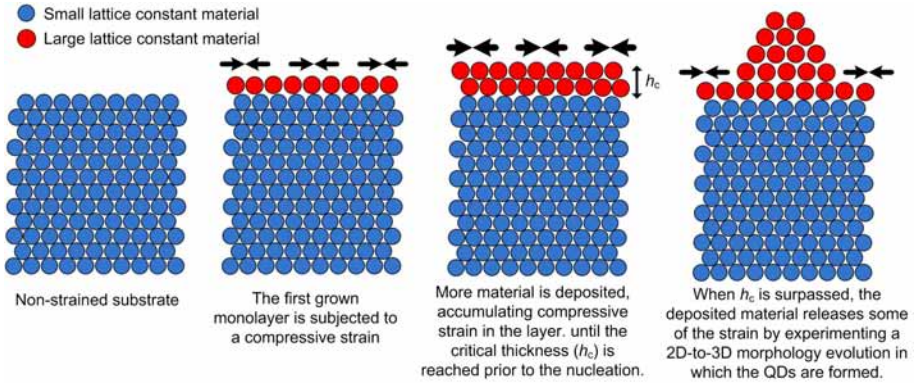

Figure 5.3: Sketch of the different steps of the S-K growth mode in which the formation of islands is induced because of the lattice mismatch between the two materials.

5.2 QD growth

III-V semiconductor QDs present different morphologies depending on the many variables involved when formed by molecular beam epitaxy (MBE) S-K growth mode [Sugawara, 1999]. Some of these variables affect the different QD features, such as the shape, size, aspect ratio, areal density, size distribution, number of QD stacked layers that can be grown, ordering, crystalline quality, etc. Hereafter, the most important of these variables are listed:

- **Choice of the QD/barrier material**. The S-K growth mode relies on the strain produced by a heterojunction of two materials with a relatively large difference in a_{lc}. As shown in Fig. 5.3, the strain is the driving force for the QD nucleation and thus, the choice of these two materials (QD and barrier) determines this parameter. In our case of study, In(Ga)As/Ga(N)As QDs, the presence of N has little influence in the QD a_{lc}, since it is introduced up to values of approximately 1.5%, however, the stoichiometry of the $In_xGa_{1-x}As$ will be of great importance, since it could, in principle, be varied from x=0.4 to x=1, inducing a strong modification in the a_{lc}. Other QD materials that deserve special mention are the ones that combine different crystalline structures and in which the driving force leading to their nucleation is not the strain but such difference in the crystal lattice [Antolín et al., 2011]. These QDs were reviewed in section 4.4.8.

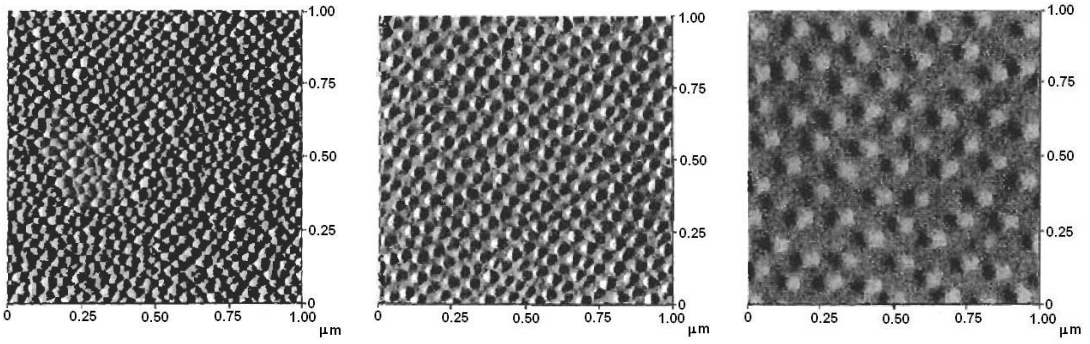

(a) (b) (c)

Figure 5.4: 1x1 μm^2 AFM images of $In_{0.4}Ga_{0.6}As$ QDs grown on GaAs(311)B at different temperatures: (a) T= 480 ℃ ; (b) T= 500 ℃ ; (c) T= 520 ℃ . This figure is reproduced from the data presented in Fig. 2 of Ref. [Akahane et al., 1998a].

- **Growth temperature**. The QD areal density strongly depends on the temperature of the substrate in which they are grown. The lower the temperature, the higher the QD areal density. An example of this statement can be found in Ref. [Akahane et al., 1998a], where a temperature-dependent study of the QD density is carried out varying the substrate temperature from 460 ℃ to 540 ℃ and showing clear evidence of the inverse relationship between temperature and QD size and density. The latter can be observed in the different atomic force microscopy (AFM) images of Fig. 5.4, where $In_{0.4}Ga_{0.6}As$ QDs grown on GaAs(311)B at different temperatures are shown. As a matter of fact, the variation in QD density is accompanied by the corresponding variation in QD size, also following an inverse relationship. The higher the dot density, the higher the light absorbed by the QDs, which is beneficial

for the IBSC performance. Nevertheless, in most cases, the low temperature MBE growth of a III-V semiconductor material has a worse crystallinity and consequently a poorer electrical performance. Thus a trade-off between QD density and crystal quality must be faced.

- **Other MBE parameters**. Besides temperature, pressure control is another important parameter regarding the growth conditions of the MBE reactor. The partial pressure of different alien species to the MBE reactor (e.g. elements and compounds which can result harmful for the growth) is monitored inside the MBE growth chamber. The partial pressure of the elements involved in the growth, as well as the growth rate of each of the epitaxial layer (0.1-0.2 μm/h for the InAs QDs and in the range of 1 μm/h for the GaAs) are other MBE parameters that have to be appropriately adjusted. They can be controlled by adjusting the temperature of each of the effusion cells as well.

- **Amount of QD material deposited per QD layer**. h_c has been defined as the minimum amount of QD material that has to be deposited in order to induce the nucleation of the QDs. This minimum material thickness depends on the lattice mismatch and increases as the mismatch decreases. The InAs h_c corresponding to the InAs/GaAs QD system is in the range of 2 monolayers (ML), while an In(Ga)As/GaAs QD system is characterized by a h_c which increases as the Ga content increases. The amount of QD material deposited also affects the size and distribution of QDs.

- **Use of atomic hydrogen in the MBE**. The beneficial effect of the use of atomic H in the MBE QD growth process has been reported [Chun et al., 1996]. It can be used not only prior to the epitaxial growth to clean the substrate's surface but also during the InAs QD epitaxial deposition. This technique is believed to improve the optical properties of the QDs (e.g. enhance its PL signature) and reduce the dot size so that the areal density is also increased.

- **Presence of seed layer and strain relief layer (SRL)** In our QD structures the SRL consists of a thin layer composed by an In$_x$[Ga$_y$Al$_{1-y}$]$_{1-x}$As quaternary alloy, with the purpose of redshifting the VB→IB transition (the one through E_H bandgap), while blueshifting the IB→CB one (through E_L bandgap) [Antolín et al., 2010a, Linares et al., 2010a]. This is achieved by improving the QD aspect ratio (height/base) and reducing the local strain in the QD by means of the redistribution of the In adatoms close to the InAs QD, which can migrate or suffer a "surface

exchange process". On the other hand, the existence of a QD seed layer allows an effective increase of the QD areal density without decreasing the QD size, which should help the E_H redshift without any sacrifice in QD absorption. The growth of several stacked QD layers including a seed layer is depicted in 5.5, where the whole growth process is sketched step by step showing the impact of the vertical strain (represented as red arrows in the figure) as the driving force leading to the formation of the QDs. Fig. 5.5(a) shows the QD seed layer, which will have a higher amount of InAs compared to the rest of the QD layers. Fig. 5.5(b) shows how a relatively large strain (which also depends on the size of the QDs) is vertically transmitted. Fig. 5.5(c) shows the second QD layer, which has a lower amount of material. It is nucleated at a relatively reduced distance from the seed layer (i.e. the spacer is thin in this case). Fig. 5.5(d) shows the increased GaAs spacer grown between the second and the third QD layers. Figs. 5.5(e) and 5.5(f) show the growth of the third InAs QD layer and corresponding GaAs spacer, which will be replicated as many times as the number of stacked QD layers. As a result of this seed layer growth technique, the QD density is fixed to that of the first (seed) layer (templating effect) [Howe et al., 2004].

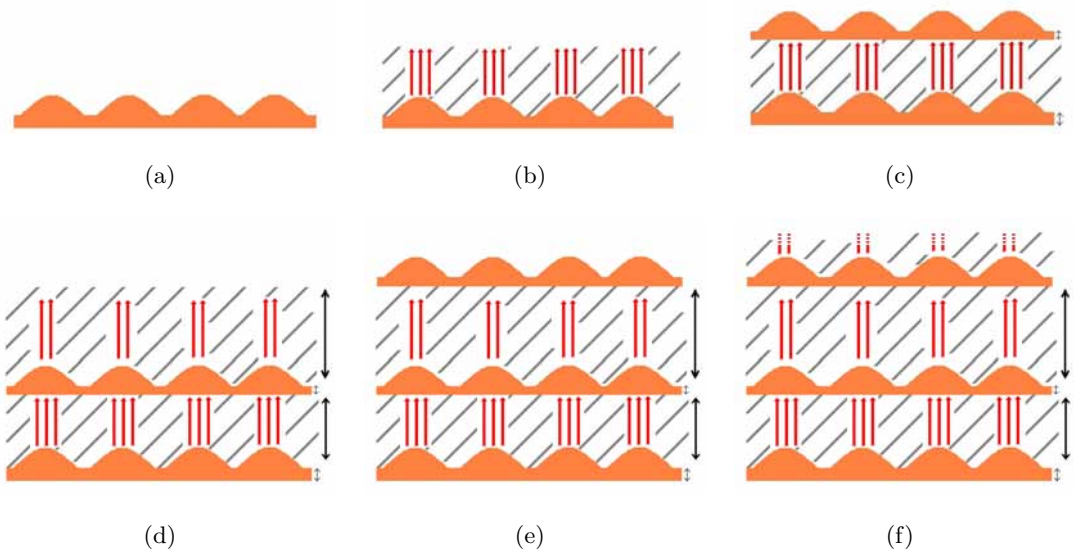

Figure 5.5: Artistic representation of the growth process of stacked QD layers using a seed layer with a higher amount of QD material and a reduced spacer used to tune the vertically accumulated strain. The depictions shown from (a) to (f) represent the different growth steps corresponding to the three first QD layers.

- **Crystal orientation of the substrate**. Akahane et. al [Akahane et al., 1998b] show how the growth of In(Ga)As/GaAs QD layers can be obtained at an increased

areal density by using a GaAs substrate of high crystallographic index (e.g. 311B). Thanks to this technique they claim to have obtained closely packed QD layers without coalescence of adjacent dots, which may be related to a different type of QD growth mode denoted as "phase separation". The AFM images shown in Fig. 5.4 (and specially the one corresponding to low temperature: 5.4(a)) are a good example of the high QD densities that can be obtained by growing on high index substrates.

- **Spacer thickness**. The thickness of the barrier material layer located between two consecutive QD layers (called spacer layer) also affects the distribution of QDs within the layer. Once the QDs are nucleated, they have to be capped and depending on the amount of barrier material deposited on top of them, the strain will be vertically transmitted or not to the next QD layer. Three scenarios are then possible: 1) if the spacer is in the range of 20 nm or less (although this and the following values vary as a function of the compressive strain created by the mismatch between the QD and the barrier materials) the strain is directly transmitted to the upper layer, inducing a columnar nucleation of QDs (templating effect), i.e. in the same position as in the previous layer; 2) if the spacer is approximately 60 nm or more, the strain is diluted throughout the barrier material and the distribution of the QDs do not follow any predefined pattern [Antolín et al., 2010a]; and 3) if the spacer is in between these two ranges, only a partial nucleation of the QDs will take place following the vertical alignment defined by the the previous QD layer. The two first cases are shown in the TEM images shown in Fig. 5.6. Fig. 5.6(a) shows a QD solar cell structure with 10 stacked QD layers with very thin spacers. The vertical strain induce the formation of columnarly aligned QDs (which in turn are larger in the upper layers compared to the ones below). On the contrary, Fig. 5.6(b) shows another InAs/GaAs stacked QD layer structure with 30 QD periods accounting for very thick spacers of 84 nm (and a 2 nm quaternary cap acting as SRL), thus preventing the vertical alignment. The compressive strain is no longer propagated to the next layer in this case, since it is completely diluted throughout the thick spacers.

  Another consequence of the thin spacers is the possibility of the IB-CB electronic escape component between the QD confined energy levels of adjacent layers: the so-called tunneling escape. The probability of this type of quantum transport depends upon the spacer thickness that the electrons have go trough (quantum tunneling) and therefore, it is a mechanism that can be efficiently blocked by means of a spacer sufficiently thick. This feature is very important regarding the performance of QD-IBSCs, since it favors electronic transport between CB and IB and thus the indistin-

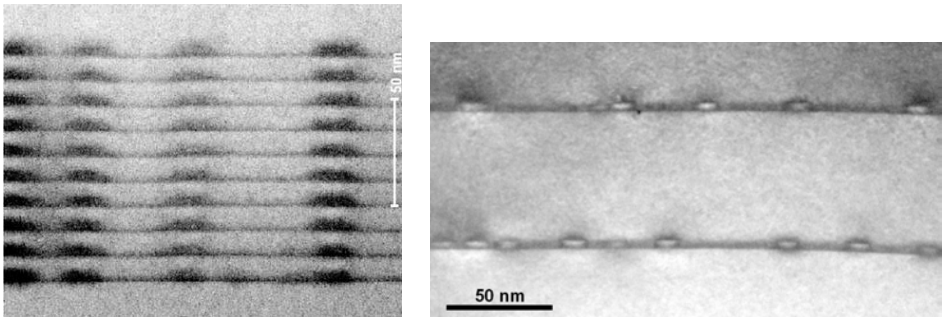

(a) (b)

Figure 5.6: (a) Bright field scanning TEM image of a 10 stacked QD layer sample fabricated with 2.7 ML InAs QDs and 10 nm GaAs spacers. The image shows the vertical alignment of dots. (b) High magnification of the dark field 002 TEM image of a multi-stacked QD solar cell with 2.4 ML InAs QDs and 84 nm thick GaAs spacers (plus 2 nm thick $In_{0.21}Al_{0.21}Ga_{0.58}As$ SRL). The TEM image in Fig. 5.6(a) is a courtesy of the University of Glasgow.

guishability between the two corresponding electronic populations, which ultimately leads to hindering the IB-CB QFL separation.

- **Continuity of the growth and temperature during the QD layer growth**. There are different strategies regarding the growth of QDs. Once the dots are nucleated at a temperature lower than good quality GaAs growth temperature (480 ℃ - 500 ℃ approximately), there are two possibilities: on the one hand the substrate's temperature can remain low, thus also growing low temperature GaAs spacers (with a worse crystal quality). This can be carried out without interrupting the growth process. The other possibility is to stop the process for each of the QD periods, so that the temperature can be increased to the GaAs growth optimum and then lowered again for the next InAs deposition. The second strategy obtains better crystal quality, nevertheless, the fact that the growth is interrupted and then the QDs are annealed due to the higher temperature also affects the QD morphology.

- **Strain-balance technique**. The issue regarding the transmission of strain through the vertical direction has been already addressed, although there are other consequences to be considered besides the aforementioned QD nucleation and templating effect. When the compressive strain is transmitted from the first to the second QD layer, it is added to the strain produced by the new QD layer. In this respect, if the stacked QD layer structure accounts for relatively thin spacers, the compressive strain is increasingly accumulated throughout the successive QD layers until it is inelastically relaxed by means of threading dislocations. Such effect can be observed in Fig. 5.7, where a multi-stacked QD solar cell with 50 InAs/GaAs periods and

GaAs spacers as thin as 15 nm is completely dislocated due to the accumulation of strain [Martí et al., 2007]. In the last 14 periods of the structure, the QDs are not even nucleated and only WLs seem to be formed because most of the strain which should act as the driving force of the QD formation is inelastically released. If such dislocation takes place, the optical and electrical quality of the crystal is very degraded. The latter implies that a maximum number of stacked QD layers are allowed, unless a strain-balance (or strain-compensation) growth technique is used. This consists of the use of a barrier material with a smaller a_{lc} than that of the substrate, thus exerting a tensile strain that compensates the compressive strain produced by the QD material.

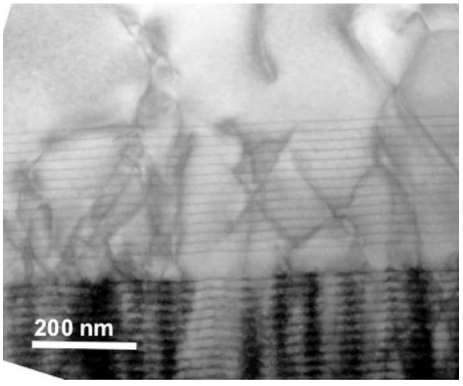

Figure 5.7: Bright field scanning TEM image of upper part of the 50 stacked QD layers of a QD solar cell formed by 3.2 ML InAs QDs and 15 nm GaAs spacers. The presence of dislocation is evident as well as the collapse of the QD growth in the last 14-16 InAs/GaAs periods, where only WLs, rather than QDs can be observed. Courtesy of the University of Glasgow.

The strain-compensation technique will be broadly studied in section 5.3.

5.2.1 QDs out of the idealized model

The same reason that is in the origin of the formation of the QDs in the S-K growth mode, i.e. the strain, is also responsible for obtaining multi-stacked QD systems which are far from the ideal. Regarding the IBSC theory, this ideal is related to a system that fulfills the following features:

1. QD/barrier material that provides a favorable energy band diagram
2. high volumetric density of QDs
3. absence of other nanostructures, such us QWs, superimposed to the QD layer (dot-in-a-well system)
4. QDs with the appropriate shape and size

5. well defined nanostructure interfaces

6. defect-free crystalline structure (good material quality)

5.2.1.1 QD/barrier material that provides a favorable energy band diagram

Any proposed QD material should approach the optimized bandgap distribution of E_G=1.95 eV, E_H=1.24 eV and E_L=0.71 eV [Luque and Martí, 1997b] if the efficiency is to be maximized, at least to some extent, since these values are optimized for maximum concentration and extraterrestrial sunlight spectrum. The choice of the appropriate QD/barrier material candidates for their use as IB materials, which is reviewed in chapter 4, could be summarized as the need for host barrier materials with larger bandgaps and an IB well separated from the CB. It has to be recalled that only confined electronic energy levels are suitable in general and not confined hole energy levels [Linares et al., 2011].

At this respect Fig. 5.8 represents the evolution of the band diagram of an InAs/GaAs QD system that is affected by the different non-ideals which are basically originated by the presence of strain in the structure. The first of the band diagrams of the figure represents the position of the VB and CB of the QD and barier materials at room temperature with respect to the energy of the vacuum as they remain isolated from each other, i.e. prior to their growth forming a heterojunction and without any influence of the strain.

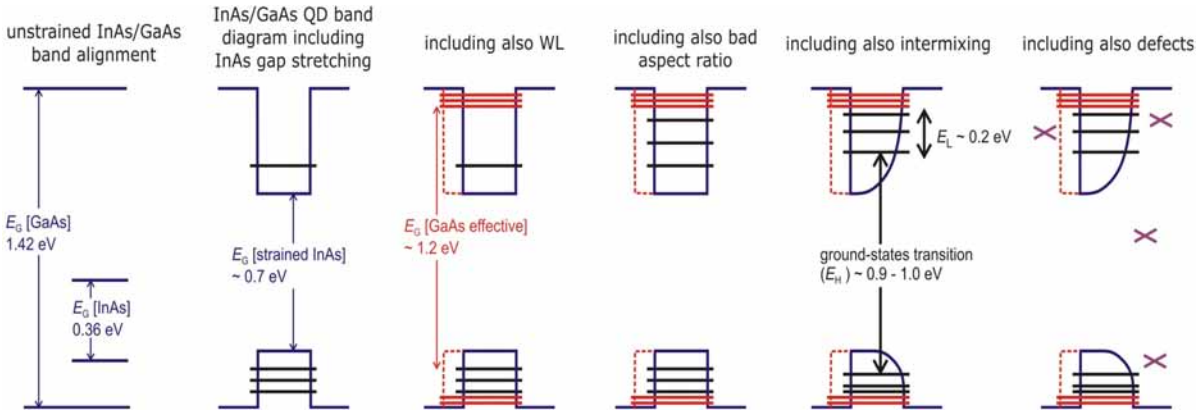

Figure 5.8: Sketch of the evolution of the energy band diagram of the InAs/GaAs QD system under the different non-ideals produced by the effect of strain. Courtesy of Dr. Elisa Antolín.

The barrier or host material (GaAs) is far from the ideal 1.95 eV at room temperature. It only has 1.42 eV, but its choice is based upon the fact that it is a very well known technology in terms of material growth, device processing and use for nanotechnology applications. The choice of the QD material seeks the creation of a relatively large discontinuity between the CB of both the barrier and the QD materials or conduction band offset (CBO) and a small discontinuity between their respective VBs (valence band

offset (VBO)). The large CBO allows a ground-state sufficiently deep into the bandgap of the host material so that it is relatively optimized regarding the exploitation of the solar spectrum: maximized sub-bandgap photocurrent generation and the radiative recombination taking place within such transitions. On the other hand, a small VBO avoids the shrinking of the barrier material effective bandgap caused by the presence of many confined hole states. These allow a fast carrier thermalization. Anyhow, as depicted in Fig. 5.8, the initial alignment between unstrained InAs and GaAs is completely modified by the strain caused by the heterojunction, producing a dramatic stretching of the InAs bandgap, from 0.36 eV to approximately 0.7 eV (as shown in the second of the band diagrams in Fig. 5.8). The strained material bandgap configuration is detrimental regarding the IBSC limiting efficiency. Other QD/barrier material configurations (with a more suitable host's bandgap, CBO and VBO) are widely studied in section 4.4 taking into account the effect of the strain for the calculation of the band alignment.

5.2.1.2 Presence of the WL

The harmful effect of the WL, can be observed in Fig. 5.1 and in the third of the band diagrams of Fig. 5.8. As any other two-dimensional nanostructure, the InAs WL creates a continuum of states located very high in energy, i.e. close to the CB in the case of the confined electronic states and close to the VB in the case of the confined hole states. The reason is that the WL typically has a thickness in the range of one monolayer which induces the confined states to be located very high in energy. This continuum of states added to the aforementioned effect of the many confined hole states in the VBO causes the effective bandgap of the host material to be reduced to approximately 1.2 eV.

5.2.1.3 QDs with the appropriate shape and size

One of the most remarkable QD non-ideals is referred to the size and shape of the QDs. A small QD size and a height/base aspect ratio close to one would be desirable so that not many excited confined electronic states (above the ground-state) arise within the host's bandgap. The QDs have the actual shape of a truncated pyramid or lens, with an aspect ratio usually in the range of 0.2-0.4. The TEM image shown in Fig. 5.9 allows measuring the size of the nanostructure, which can be approximated by a squared base of 16 nm of edge and 6 nm of height. These dimensions cause the appearance of several excited confined states (up to four are measured in a 10 stacked InAs/GaAs QD layer structure [Cánovas et al., 2008]), as sketched in Fig. 5.1 and lead to a strong thermal escape at room temperature.

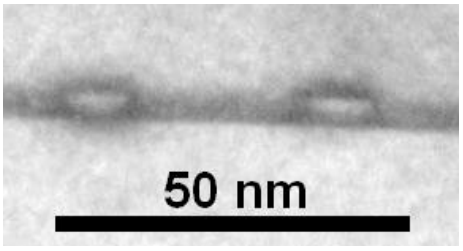

Figure 5.9: Detailed of two QDs from a high magnification dark field 002 TEM image. The dimensions of the QD are measured, resulting in an edge of 16 nm (under the approximation of a squared base) and a height of 6 nm.

The effect of the degradation of the aspect ratio is also represented in Fig. 5.8, where the fourth of the band diagrams shows multiple excited electron states that effectively shrink the total solar cell bandgap to the value E_{H}. This occurs because at room temperature, the extra confined levels assist the IB-CB electron pumping by means of the energy of the phonons.

5.2.1.4 Well defined nanostructure interfaces

The QDs do not remain unaltered once they are nucleated from the strained InAs layer. Their shape before and after being capped with the barrier material is notably different. When the QDs are capped, not only their aspect ratio worsens (becoming flatter), but also an intermixing effect is produced on their surface. This intermixing process occurs between In adatoms from the QDs and Ga adatoms from the GaAs capping, producing a rather discontinuous and undefined surface, which in turn leads to the less sharp potential well depicted in the fifth of the band diagrams of Fig. 5.8. As a result, the energy of the ground-state increases as well as that of the excited states, which also get closer to each other, facilitating the thermal escape. The aforementioned SRL is meant to avoid this intermixing problem to some extent.

5.2.1.5 Defect-free crystalline structure

Some causes of the appearance of defects in the crystalline structure of a QD system have already been reviewed. Besides the complete dislocation of the crystalline structure due to the accumulation of strain, other strain-related consequence is the formation of defects or discontinuities of the crystal lattice due to less intense inelastic lattice relaxation. For example, a certain probability exists for the coalescence of two or more QDs producing the appearance of a super-QD which acts as a very harmful recombination center and thus reduces the minority carrier lifetime and the V_{OC}. Any kind of defect within the lat-

tice increases the Shockley-Read-Hall (SRH) recombination, assisting the thermal escape component in case they are located within the IB-CB transition.

5.2.1.6 High volumetric density of QDs

As it has already been stated, a high-current device as the IBSC requires a high absorption of the sub-bandgap transitions. The absorption of the QDs is related to the number of QDs present in the structure. Nevertheless, it can be demonstrated that not only a high number of QDs is required, but also at high concentration.

The reduction of the dot size, the strain compensation technique, the high-index substrate growth and the unstrained lead-salt QD structures are some of the strategies to be followed in order to maximize the absorption of the QD-IBSC during the development of this Thesis work.

5.3 Strain-balanced InAs/GaAs$_{1-x}$N$_x$ QD-IBSCs

5.3.1 The Japanese-Spanish collaboration

Only in very recent times an epitaxy reactor has been installed at IES-UPM for the fabrication of IB materials. Throughout recent years, research collaborations with other institutions have allowed us to receive the proposed IB materials and corresponding IBSC structures from our partners. Within this framework, a research project entitled DenQuIBand ("High density quantum dot arrays for intermediate band solar cells", No. PLE2009-0045) was signed together with the Okada's research group at the RCAST, in the University of Tokyo. The DenQuIBand project is funded by both the former Spanish MICINN (Ministerio de Ciencia e Innovación - Ministry of Science and Innovation) and the JST (Japan Science and Technology Agency). The collaboration begun after the "First Bilateral Japan-Spain Meeting on Nanotechnology and New Materials for Environmental Challenges" held in Tokyo in April 2009, which coincided with the research internship made by the author of this Thesis at RCAST-University of Tokyo.

The DenQuIBand project consisted of a Japanese-Spanish collaborative venture whose two principal investigators are: Prof. Yoshitaka Okada, from the University of Tokyo, on the Japanese side, and Prof. Antonio Luque, from the UPM (Universidad Politécnica de Madrid), on the Spanish side. Each institution was engaged with a different task which were mutually complementing. On the one hand, RCAST was in charge of the QD-IBSC sample growth. They were able to undertake such task because their facilities in Tokyo are provided with several MBE reactors and they are experts in III-V semiconductor QD growth. On the other hand, IES-UPM was in charge of the measurement and characteri-

zation of the QD-IBSCs that were meant to provide feedback on the solar cells grown at RCAST. The wafer processing was first assigned to RCAST and later on this task was transferred to IES-UPM.

5.3.2 The MBE reactor at RCAST

Besides the IB materials fabricated by MBE, other techniques have also been proposed for the fabrication of IBSCs. Chemical vapor deposition for the incorporation of transition-metals in chalcopyrite-based solar cells [Marsen et al., 2010, Martí et al., 2008c], ion implantation plus laser annealing (eventually, completing the *p-n* junction by sputtering) for the implantation of Ti atoms in a Si host [Antolín et al., 2009, Olea et al., 2008] are two examples of these alternative bulk-based IB materials and their corresponding manufacturing techniques. Nevertheless, the MBE technique is of remarkable importance in the IBSC framework, since it allows the growth of III-V crystalline semiconductor devices (together with the possibility of co-doping with transition-metals [Martí et al., 2009]) as well as the growth of nanostructures.

Figure 5.10: The image shows the MBE reactor held at Prof. Okada's Laboratory at RCAST with which the QD-IBSCs of the DenQuIBand project have been grown.

Fig. 5.10 shows the MBE reactor used for the growth of the QD-IBSCs during the DenQuIBand project. The reactor is equipped with seven conventional Knudsen effusion cells containing the following elements: As, Ga(two cells), In, Al, Be, Si, an atomic hydrogen cracker cell and a plasma cell for nitrogen.

(a) (b) (c)

Figure 5.11: Images of the different parts of the MBE reactor of the RCAST. (a) Platen manipulator; (b) Effusion cells; (c) Detail of the shutter of one of the effusion cells.

Fig. 5.11 shows some pictures of important parts of the MBE reactor that were extracted from it when the reactor was disassembled during a periodic maintenance work. Fig. 5.11(a) shows the platen manipulator of the MBE with the sample holder and the sample heater in one of its ends. In Fig. 5.11(b) two Knudsen effusion cells that are being cleaned can be observed. The crucible containing the material to be molten is located in one the ends of the cell. This crucible is completed by a metallic disk or shutter shown in Fig. 5.11(c). It can adopt two positions: open, allowing the flow of the molecular beam towards the sample and close, preventing the molecular beam to leave the crucible. During the maintenance works of the MBE, special care was taken with the cleaning of the shutter.

5.3.3 The strain compensation technique applied to QD superlattices

Zincblende GaAs has $a_{\mathrm{lc}}(T = 300K)$=5.6533 $\mathring{A}$, while InAs is characterized by the larger $a_{\mathrm{lc}}(T = 300)$=6.0583 $\mathring{A}$. When a very thin InAs film (e.g. one monolayer) is grown on a GaAs substrate, the InAs atoms in the interface of the heterojunction have to accommodate their lattice parameter to that of the GaAs substrate, thus suffering a strong compressive strain. The larger the amount of InAs, the higher the strain that is exerted on the epitaxial layer, until the critical thickness, h_{c}, is surpassed, leading to the elastic deformation of the InAs epitaxial layer, i.e. nucleating the QDs. As it has been previously pointed out, not all the strain is released through the formation of the QDs and a certain component of residual strain can be transmitted along the growth direction and even increasingly accumulate throughout the different QD layers.

The strain compensation technique is based on the use of a barrier material with a smaller lattice parameter than that of the substrate, thus exerting a tensile strain that compensates in average the global strain of the QD system and leading to a zero overall in-plane stress [Popescu et al., 2008]. A couple of materials are suitable for this purpose regarding the InAs/GaAs QD system: GaP, with an a_{lc} of 5.4505 $\AA$ and GaN, with an a_{lc} of 4.5 $\AA$. They can be either used alloyed with GaAs or as pure binary thin layers (completing the spacer layer with GaAs). To this end, In(Ga)As/GaAs$_{1-x}$P$_x$ QD cells have been both theoretically and experimentally studied with a P composition ranging from 0.8 to 18 % [Popescu et al., 2008] and InAs/GaAs$_{1-x}$N$_x$ QD solar cells have also been fabricated [Oshima et al., 2008] with a lower concentration of N (in the range of 1%).

A comparative sketch of a multiple-layer QD system with and without using the strain compensation technique is represented in Fig. 5.12. The left part of the image shows a multi-stacked QD layer system in which no strain compensation has been used. The red arrows represent the compressive strain suffered by the QD material. The vertical bar located on the right side of the sketch indicates the strain accumulated throughout the structure: the white color indicates the absence of strain and the black color stands for a fully strained system. The figure shows how the accumulated strain increases as more QD layers are grown. However, when the strain compensation technique is applied (right part of the figure), the barrier material exerts a tensile strain that balances the overall strain of the system.

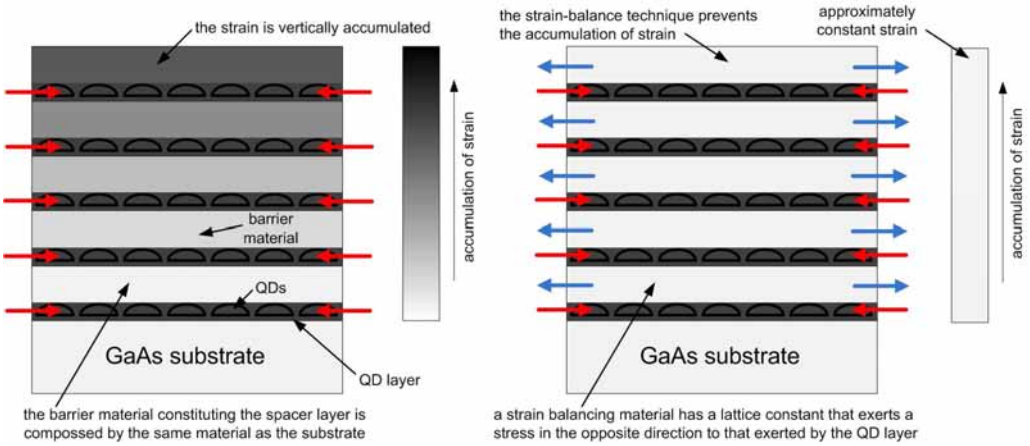

Figure 5.12: On the left part of the figure, a sketch of the stacked InAs/GaAs QD layers is shown, where the compressive strain of the QD layers is shown together with a bar indicating the strain accumulated throughout the structure in the vertical axis. On the right side of the figure, the strain-balance spacers exert a tensile strain that compensates the compressive strain produced by the QDs. The successive compressive-tensile strain components lead to a strain symmetrization where no strain is vertically accumulated.

The strain of a lattice mismatched epitaxial layer is not only proportional to the difference in a_{lc}, but also to the QD material and barrier material spacer layer thicknesses. For this reason, the choice of the appropriate composition and thickness of the strain compensation layers requires the calculation of its elastic strain energy E, which is a function of the elastic energy density, U, and the total volume of the layer, V, verifying $E{=}UV$. Equation 5.1 relates these variables to the strain ($\underline{\epsilon}$) and stress ($\underline{\sigma}$) tensors:

$$\underline{\sigma} = \frac{\partial U}{\partial \underline{\epsilon}} = \frac{1}{V}\frac{\partial E}{\partial \underline{\epsilon}} \tag{5.1}$$

The condition of a zero stress component along the in-plane growth direction must be imposed. The continuum-elasticity theory states that this condition will be fulfilled by the two consecutive layers 1 and 2 (representing in our case the GaAs$_{1-x}$P$_x$ or the GaAs$_{1-x}$N$_x$ barrier material layer and the InAs QD layer) if the following equation is verified

$$\frac{l_1}{l_2} = -\frac{G_2\,\epsilon_{\parallel,2}\,a_{\mathrm{lc},1}}{G_1\,\epsilon_{\parallel,1}\,a_{\mathrm{lc},2}} \tag{5.2}$$

where $a_{\mathrm{lc},i}$ represents the lattice constant of each of the materials involved in the heterojunction, l_{i} is the thickness of each of the two materials, i.e. in our case, the subindex 1 refers to the barrier material spacer and 2 refers to the QD material deposited in each QD period. $\epsilon_{\parallel,i}$ is the epitaxial strain, defined as

$$\epsilon_{\parallel,\mathrm{i}} = \frac{a_{\mathrm{lc,substrate}} - a_{\mathrm{lc},i}}{a_{\mathrm{lc,substrate}}} \quad \text{and } i = 1 \text{ or } 2 \tag{5.3}$$

where $a_{\mathrm{lc,substrate}}$ is the lattice constant of the substrate and G_i is a coefficient related to the shear strain, called "shear modulus" in the Model Solid Theory [Van de Walle, 1989], as it will be reviewed in chapter 4. This coefficient is calculated from

$$G_i = C_{11,i} + C_{12,i} - \frac{2C_{12,i}^2}{C_{11,i}} \quad \text{with } i = 1 \text{ or } 2 \tag{5.4}$$

where $C_{\mathrm{nm},i}$ represents each of the three linearly independent elastic constants of a crystal with cubic symmetry, e.g. zincblende structure semiconductors [Vurgaftman et al., 2001]. This condition verifies a null in-plane stress only for the case of a (001) growth plane. For the case of a higher index growth plane, section II of Ref. [Popescu et al., 2008] will have to be reviewed.

Hence, the strain compensation technique consists of choosing a certain barrier material thickness and calculating the P or N concentration of such alloy, thus making this barrier

material to exert a tensile strain that compensates the compressive strain produced by the QD material, which ultimately cancels the total stress. A trade-off then exists between the thickness and the composition of the strain-compensating layer, actually allowing to tune one or the other in order to obtain a globally strain-free epitaxial growth.

5.3.3.1 The influence of the nitrogen on the QD-IBSC performance

Within the framework of the Spanish-Japanese collaboration, the dilute nitride GaAs$_{1-x}$N$_x$ ternary alloy was used. Even if dilute nitride barrier materials (GaAs$_{1-x}$N$_x$) with very little N content (in the range of 1%) are used, the impact on the band diagram of the alloy with respect to the N-free compound is very remarkable.

As explained in [Shan et al., 1999, Wu et al., 2002] the big impact of small amounts of N in the estimation of the dilute nitride alloy bandgaps is explained by the so-called band anticrossing model (BAC). The physical explanation is related to the interaction between the energy levels of the nitrogen impurities and the CB of the host material (GaAs in this case), which splits the dilute alloy CB into two sub-bands, namely E_- and E_+. This effect is described by equation 5.5, where E^{N} is the position of the isoelectronic impurity within the host compound and V_{int} is the interaction potential between the two bands. The variable x represents the nitrogen content and $E^{\mathrm{C}}(k)$ the CB dispersion of the non-nitrogen semiconductor.

$$E_{\pm}(k) = 1/2\{\left[E^{\mathrm{C}}(k) + E^{\mathrm{N}}\right] \pm \sqrt{\left[E^{\mathrm{C}}(k) + E^{\mathrm{N}}\right]^2 + 4V_{\mathrm{int}}^2 x}\} \tag{5.5}$$

Regarding the performance of an IBSC fabricated with these dilute nitrogen alloys as the barrier material, there are two main drawbacks related to the BAC effect. On the one hand the energy of the CB of the barrier material is lowered with respect to the GaAs CB [Wu et al., 2002], which reduces the effective bandgap of the whole QD system. In turn, this creates smaller sub-bandgap transitions and allows a less favorable bandgap distribution with respect to the limiting efficiency of the IBSC [Luque and Martí, 1997b]. On the other hand, the dilute nitrogen alloy (GaAs$_{1-x}$N$_x$) is characterized by a much broader CB dispersion signature or equivalently expressed, a higher electron effective mass (m_{e}^*). This m_{e}^* enhancement produces a higher number of confined electronic states located below the barrier material CB. As a result, the ground-state energy level is closer to the barrier CB, the energy threshold between the ground-state and the first excited state is reduced, as well as the energy difference between contiguous excited states. The aforementioned effects are harmful regarding the performance of the IBSC because they

increase the thermal electronic rate between the IB and the CB, reducing the activation energy and making the QD solar cell to behave as a reduced-bandgap single-gap solar cell.

The experimental verification of the BAC effect on stacked QD solar cells and the possible drawbacks derived from the use of GaAs$_{1-x}$N$_x$ alloys as strain balance barrier materials for the QD-IBSC is studied in the next section.

5.4 The QD-IBSC layer structure design

5.4.1 First batch of samples: prototype QD-IBSC structures

During the research stay at RCAST, the author of this Thesis had the opportunity to collaborate in several MBE growth experiments that led to the fabrication of the first batch of InAs/GaAs$_{1-x}$N$_x$ QD-IBSCs and reference cells of the DenQuIBand project. Fig. 5.13 sketches the layer structures of a 30 InAs/GaAs$_{1-x}$N$_x$ stacked QD layer solar cell and

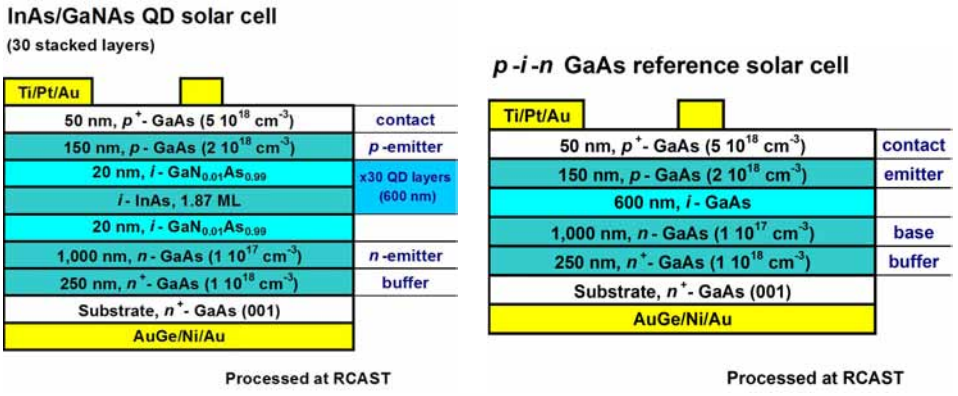

(a) (b)

Figure 5.13: Sketch of the layer structure of the first batch of InAs/GaAs$_{1-x}$N$_x$ QD-IBSCs and *p-i-n* GaAs reference cell. (a) QD cell with 30 stacked QD layers introducing GaAs$_{1-x}$N$_x$ strain balance spacers. (b) GaAs reference cell of the first batch of samples.

its corresponding reference or control *p-i-n* GaAs cell with the thicknesses and doping level details of each layer.

Fig. 5.13(a) describes the QD cell of this first batch of samples in which the top 50 nm layer corresponds to the contact layer, the layer below it consists of a 150 nm thick *p*-GaAs layer that corresponds to the *p*-emitter of the IBSC, which may result too thin regarding the requirements of a proper concentrator solar cell. Nevertheless, such thin emitter assures a good crystal quality, which is a priority at this early stage of the research. The IB material consists of 30 stacked InAs QD layers (2.0 ML) separated by 20 nm thick GaAsN intrinsic spacers. A 1,000 nm GaAs layer located under the QD layers

acts as the n-emitter of the IBSC, completing the sandwiching of the IB material by two conventional semiconductors. The first epitaxial layer that was grown in this structure is a 250 nm thick n-GaAs buffer, which is directly deposited on top of the 001 GaAs substrate. This first layer is meant to smooth the surface of the substrate, assuring a high quality crystalline material. Fig. 5.13(b) corresponds to the p-i-n GaAs reference cell that acts as the benchmark of the QD sample. Its layer structure reproduces that of the QD cell, except for the replacement of the QD region by an intrinsic layer of the same thickness.

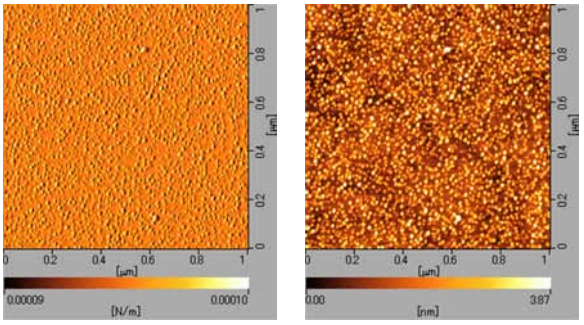

(a) (b)

Figure 5.14: 1x1 μm^2 AFM plots of the 30 InAs/GaAsN stacked QD layer sample. (a) For the calculation of the areal density. (b) For the calculation of the QD size distribution.

Two other alternative growths were also carried out within this first batch of samples: a second GaAs reference with a thicker emitter (450 nm instead of 150 nm) and a simple test structure with the 30 InAs/GaAsN QD periods on top of the buffer layer and with the last QD layer uncapped for AFM analysis. The growth experiment of the 450 nm thick emitter structure suffered from As desorption. This could be deduced from the "milky" appearance of the wafer, which could be observed once it was removed from the MBE growth chamber. This growth experience was useful, anyway, to determine the appropriate MBE growing parameters to be eventually used in future highly doped thick layers. The other alternative QD sample was used for AFM analysis with which the areal QD density and the QD size distribution could be analyzed (shown in Fig. 5.14(a)). The first of these measurements is represented in a 1x1 μm plot representing the QD contour, i.e. only the presence of the QDs can be inferred, but their size and height is not appreciable. This measurement is carried out with a relatively low pressure on the cantilever, varying from 9 10^{-5} to 10^{-4} N m^{-1}. A QD density of approximately 2 10^{11} cm^{-3} is measured. Fig. 5.14(b) shows a higher resolution AFM measurement where the size distribution of the sample can be observed. An average base range of 15-20 nm and height range of 3-3.5 nm are calculated for the QDs grown in this sample.

Three different 500 suns concentrator cell front grids and photolithography masks were calculated, designed and fabricated at RCAST. The whole processing procedure for the new devices was also redefined to adapt it to concentrator cells (see chapter C for a more detailed explanation). An example of the processed wafer is shown in Fig. 5.15(a), where three types of devices can be observed: concentrator solar cells of circular symmetry with three different sizes (1 mm, 0.5 mm and 2 mm radius cells), rectangular solar cells for QE and round diodes for dark current measurements (also with three different sizes). After the photolithography, the front grid and rear metal evaporation, the mesa etching and the annealing processes, the wafer was ready to be cut in a diamond tip station. All devices are pre-measured (measuring their V_{OC} under illumination) in a probe station, so that the best among them are selected, cut (separated from the wafer) and encapsulated in a copper disk, as shown in the picture from Fig 5.15(b). The type of encapsulation is adapted to the

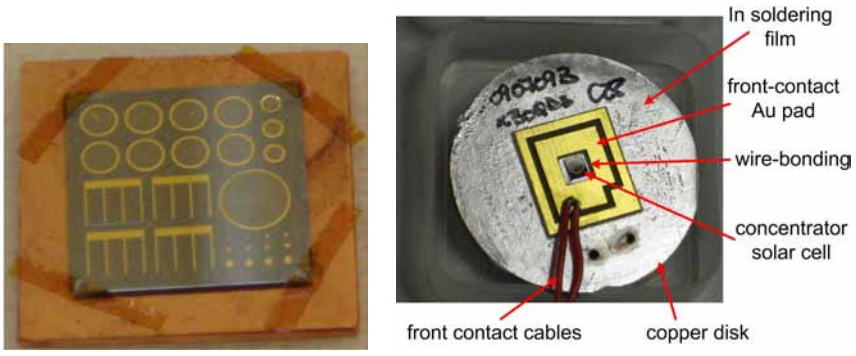

(a) (b)

Figure 5.15: (a) Image of the QD wafer showing three different types of devices: concentrator solar cells, QE solar cells and diodes. (b) Image of a 1 mm radius 500 suns concentrator solar cell encapsulated into a copper disk.

special features of the He-cryostat used at IES-UPM for low-temperature characterization. In this respect, the soldering is made with indium because of its relatively low thermal expansion coefficient so that when it is placed inside the cryostat the sample does not break because of the difference in the dilatation of the two contacted materials. The cell is wire-bonded to an Au PCB with two isolated pads for 4-wire I-V characterization. Finally, the front electrical contact is made with a wire soldered to the Au pad. The rear electrical contact is made on the copper disk.

After the processing and encapsulation of the solar cells, optical and electrical measurements are performed. A liquid nitrogen temperature (T=77 K) PL experiment was carried out at RCAST on the QD solar cell. The result is shown in Fig. 5.16(a) and shows a relatively broad emission pick centered at λ=1103 nm (equivalent to E=1.124

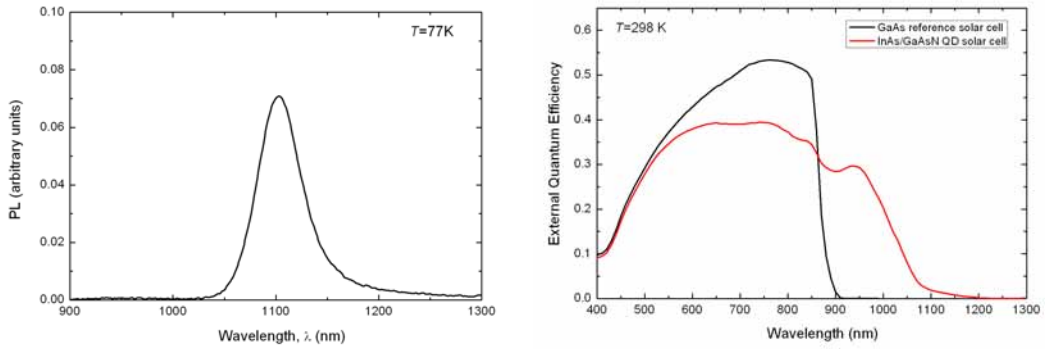

(a) (b)

Figure 5.16: (a) PL experiment (T=77 K) of the InAs/GaAsN QD solar cell corresponding to the first batch of samples. The emission pick of the PL is at λ=1103 nm. (b) Room temperature External QE experiment of both the QD cell and the *p-i-n* reference cell.

eV). This signature theoretically corresponds to the radiative recombination associated to the electronic transition from the confined ground state of the QDs to the VB. The almost symmetric broadening of the PL pick may be related to the size dispersion of the QDs. Fig. 5.16(b) represents the results from the external QE measurements carried out at room temperature on both the QD cell (solid red line) and the *p-i-n* GaAs reference solar cell (solid black line). The respective bandgaps can be deduced from the QE signature: the QE of the GaAs reference cell drops from roughly 0.5 to 0 at approximately 870 nm, which corresponds to $E_{\mathrm{G}}(GaAs)$=1.425 eV. The relatively low value of the supra-bandgap QE is consistent with the fact that the solar cell structure lacks anti-reflective coating (ARC) and window layer, which reduces the collection of carriers. The external QE signature of the QD solar cell has a poorer response in the visible range (from 400 nm to 800 nm), remaining under 0.4 (more degraded than the reference cell), probably due to the presence of the QD layers. The fundamental bandgap, corresponding to the GaAs emitters, is also at λ=870 nm, although in this case, other features related to the QD layer and to the GaAsN spacers can be observed. First, a hump at a QE level of 0.3 at λ=940 nm, (E=1.32 eV) probably corresponding to the WL. Second, a relatively sharp drop at λ=1.040 nm (E=1.19 eV), which is very likely related to the bandgap shrinking produced because by the GaAsN spacers (as explained by the BAC theory). Third, another absorption tail, with a QE signature at least one order of magnitude below: from λ=1.080 nm to λ=1250 nm (E=1.15 eV to E=0.99 eV) and corresponding to the QD absorption (in the E_{H} transition).

Electrical characterization was also carried out. The dark J-V characteristic of the two samples was measured and the results are presented in Fig. 5.17. The two exponential

slopes (m_1 and m_2) can be observed in the dark curve of the GaAs reference cell (solid black line), but only one slope with a value between 1 and 2 can be observed in the QD sample, which is, moreover, ascribable to the a much larger J_0. The latter suggests that the QDs enhance the recombination of the solar cell with respect to the sample without QDs. The red curve is affected by a larger r_S.

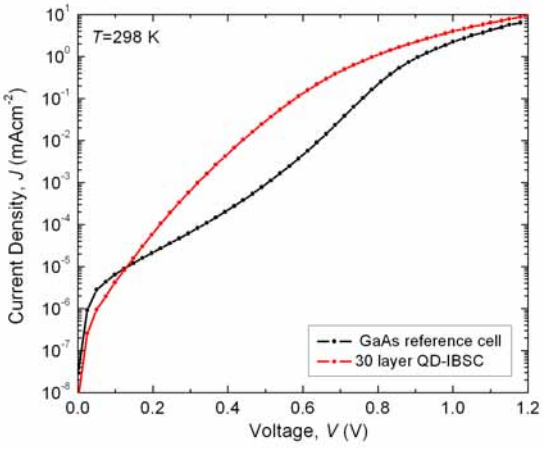

Figure 5.17: Electrical characterization carried out at IES-UPM of the *p-i-n* GaAs reference cell and the QD cell from the first batch of samples measured at IES-UPM. (a) Dark *J-V* curve. (b) One sun *J-V* illumination curve.

In order to complete the routine electrical characterization of the QD (and corresponding reference) cell, the concentration measurements (that were thoroughly reviewed in chapters 2 and 3) are also presented. Fig. 5.18(a) shows a family of *J-V* curves measured under different levels of concentrated light with the concentration system detailed in chapter 6 and conceived at IES-UPM. The concentrated-light *J-V* curves of the *p-i-n* GaAs reference solar cell are plotted in black lines and the ones corresponding to the QD cell are plotted in red lines. The concentration level is indicated with a label next to each of the curves. Fig. 5.18(b) represents the concentrated-light J_L-V_{OC} curves measured together with the dark *J-V* curves for comparison. The J_L-V_{OC} pairs measured under concentrated-light represent the dark curve of the device without the influence of the r_S.

Three more samples were grown within this first batch of samples with an equivalent structure for the QD solar cell, except for containing 50 stacked InAs/GaAs$_{1-x}$N$_x$ QD layers instead of 30. The corresponding *p-i-n* GaAs reference solar cell is also equivalent to the previous one except for an intrinsic 1,000 nm thick layer, which is equivalent to the *i*-region of the QD cell. These cells were grown with the aim of reproducing the previous results by carrying out the processing at IES-UPM. One of the samples consists of a *n-i-n* QD photodetector structure (containing 50 InAs/GaAsN QD layers) specially designed for

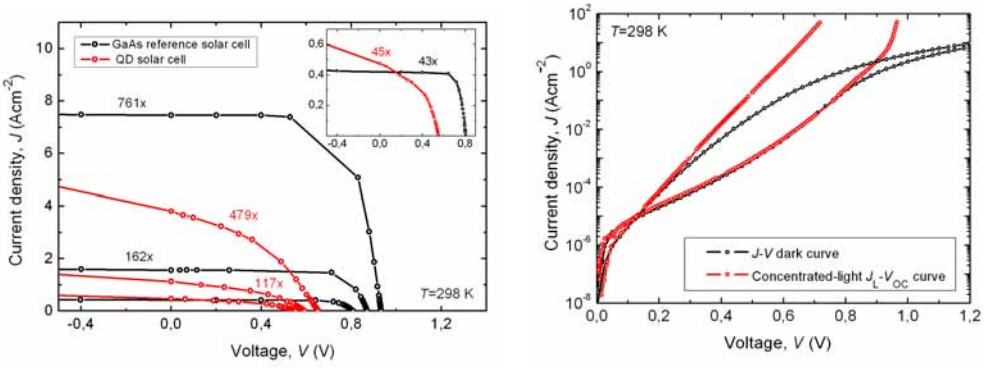

(a) (b)

Figure 5.18: Concentrated-light measurements of both the reference cell and the QD cell. (a) Family of J-V curves. (b) J_{L}-V_{OC} curves plotted together with the dark J-V curves.

detecting the IB-CB transition, however, the study of such device is outside the scope of this Thesis.

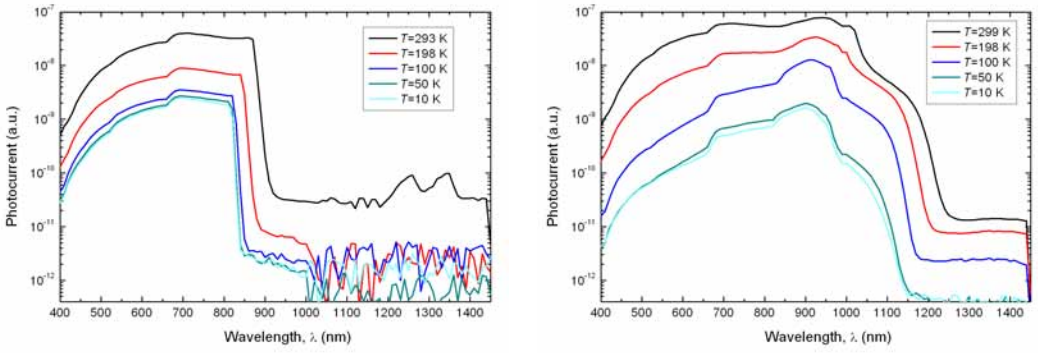

(a) (b)

Figure 5.19: Photocurrent measured at different temperatures (from room temperature to T=10 K). (a) GaAs reference sample. (b) QD solar cell. Courtesy of Mr. Íñigo Ramiro.

The photocurrent response was measured under low-temperature at IES-UPM. This measurement is performed in the QE set-up using a quartz tungsten halogen (QTH) lamp as light source. The light beam from the QTH lamp is chopped by a mechanical chopper before entering a 1/4 m monochromator. The photoresponses of the solar cells are detected using a low-noise preamplifier prior to a lock-in amplifier locked to the frequency of the chopper. Calibrated Si and Ge detectors are employed to determine the power density of the light impinging on the samples. A set of bandpass and longpass filters are used to prevent secondary beams and/or stray light exiting the monochromator from reaching the sample under test. The spectraly resolved photocurrent results are represented in Fig.

5.19, showing the evolution of the solar photoresponse from room temperature to T=10 K. The fundamental bandgap of the GaAs solar cell can be deduced from Fig. 5.19(a), which varies from approximately 1.42 eV (λ=880 nm) to 1.51 eV (λ=820 nm). The shape of the photocurrent measurements are strongly influenced by the spectral distribution of the incoming light. The two picks arising between 1,200 and 1,400 nm in the measurement are caused by second order influences of the diffracted light. Fig. 5.19(b) represents the photocurrent response of the QD solar cell, showing the signature from the GaAsN from the bandgap of the GaAs (λ ~870 nm at room temperature) until approximately 1,000 nm. The absorption produced by the confined states is shown between λ ~1,000 nm and λ ~1,250 nm, similarly to the explanation of Fig. 5.16(b).

5.4.2 Second batch of samples: QD Si-direct doping

A second batch of samples with a number of improvements with respect to the first batch was grown at RCAST and processed at IES-UPM. It consisted of three different solar cell structures which detailed layer descriptions are presented in Fig. 5.20.

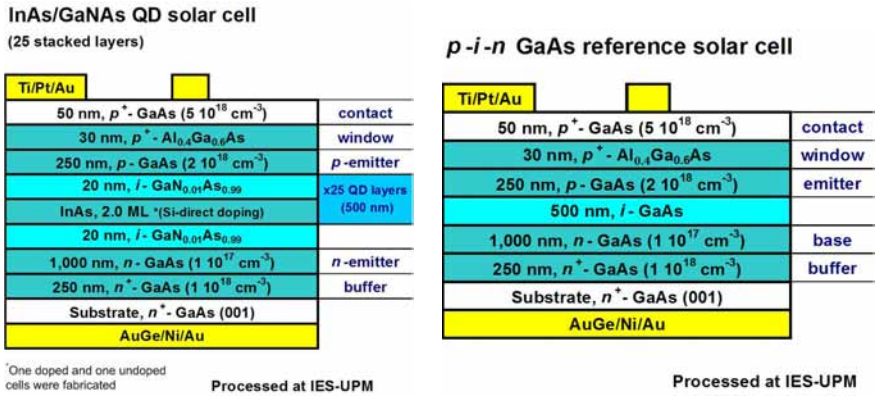

(a) (b)

Figure 5.20: Sketch of the layer structure including an AlGaAs window layer and in one of the cases, a direct Si doping. (a) Two QD cells (one with Si direct doping and another one without it) were grown with 25 stacked QD layers characterized by 20 nm thick GaAs$_{1-x}$N$_x$ strain-balance spacers. (b) *p-i-n* GaAs reference cell.

On this occasion, the two type of cells were grown with a 30 nm thick Al$_x$Ga$_{1-x}$As window layer (x=0.4) and with a slightly thicker p-emitter (250 nm instead of 150 nm). The QD region was also reduced to 25 QD layers with 20 nm GaAsN spacers. Consequently, the i-GaAs layer of the reference cell was only 500 nm thick. One of the QD cells incorporated the so-called Si-direct doping in the dot region.

The Si-direct doping of the QDs aims to half-fill the IB with electrons [Luque and Martí, 2010a] (as it is represented in Fig. 5.1), so that there are enough electrons in the IB to

assist the IB→CB transition while allowing enough empty states for the electrons being pumped at the VB→IB transition. This IB half-filling condition rules out the necessity of a very unlikely three-particle collision (which would involve one electron and two photons). It can be fulfilled with a Si-direct doping concentration equal to the QD areal density, providing one electron per QD. These electrons occupy one of the two available confined energy levels of the QD ground-state (i.e. the spin-up or the spin-down). Thanks to this intentional QD doping, the IBSC does not depend upon the photofilling [Strandberg and Worren, 2009], which is only efficient at a very high concentration.

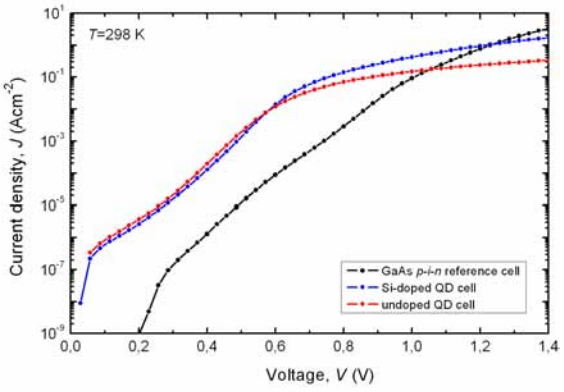

Figure 5.21: Dark J-V curve of the three solar cells of the second batch of samples measured at room temperature: the GaAs reference cell is represented with a solid black curve, the doped QD cell with a solid blue curve and the undoped QD cell with a solid red curve.

The half-filling of the IB in QD-IBSCs has been previously carried out by means of the so-called δ-doping technique [Luque et al., 2005]. The latter refers to a modulated doping technique consisting of doping the barrier layer (close to the QD layer) with a "doping-sheet" of a surface density equivalent to the QD density, so that one electron per QD is also obtained. Conversely, the Si-direct doping technique is an alternative way of implementing the doping of QDs, which is performed during the QD nucleation, introducing the donor impurities inside the QDs.

Regarding the characterization of this second batch of samples, the dark J-V curves have been measured. They are plotted in Fig. 5.21, where the reference cell shows a smaller I_0 as well as a smaller r_S. The two QD cells look relatively similar to each other, although the Si-direct doped cell has a slightly smaller J_0 and r_S values compared to the undoped sample.

The absolute external QE is also measured at room temperature for the three solar cells of this second batch of samples (Fig. 5.22). The reference cell presents a reasonably good QE signature, with a well defined bandgap at 1.42 eV and an apparent degradation of the short-wavelength QE. The two QD cells show important differences in this case:

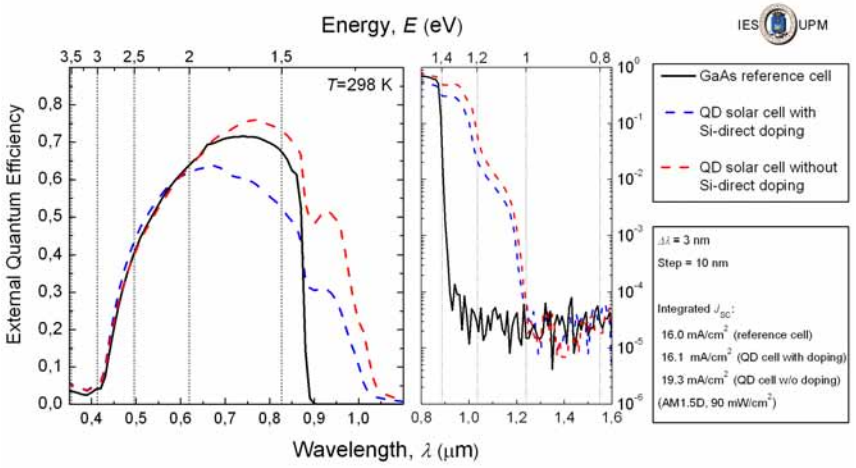

Figure 5.22: External QE of the second batch of samples. The measurement is plotted in linear scale on the left part of the figure and in logarithmic scale on the right part of the figure. The $\Delta\lambda$ used to scan the wavelength axis was 3 nm and the step was 10 nm. Each curve is integrated using the AM1.5D spectrum, resulting in the J_{SC} values shown in the right part of the figure. Courtesy of Mr. Íñigo Ramiro.

an enhanced QE response is noticeable regarding the undoped cell, both for the supra-bandgap and for the below-bandgap carrier collections. The higher sub-bandgap QE of the undoped-sample can be explained by the fact that its IB is empty of electrons and thus, there is more room for the photogenerated carriers to be absorbed from the VB to the QD ground-states, or otherwise explained, half of the doped sample ground-state levels are occupied with electrons. However, there is not any direct explanation for the higher supra-bandgap response of the undoped cell and it may be related to an undetermined problem during the cell processing. The J_{SC}, which has been calculated from the integration of the QE with respect to the Air Mass 1.5 Direct (AM1.5D spectrum, is also shown in Fig. 5.22 for each of the three cells.

5.4.3 Third batch of samples: removing the N and thickening the spacers

The layer structure of the last fabricated batch of samples (referred to as "third batch") is shown in Fig. 5.23. The new layer structure is designed to avoid two major problems encountered in the InAs/GaAsN QD cells: 1) shrinking of the bandgap produced by the dilute nitride and 2) quantum tunneling produced between QD layers. The first problem is tackled by replacing the strain-compensation GaAsN layers by thick GaAs layers, which dilute the strain throughout their 60 nm GaAs layer, thus preventing the appearance of defects derived from the accumulation of strain. The thick spacers also prevent (block) the quantum tunneling produced between contiguous QD layers as well as with the barrier material CB. This tunneling contributes to the so-called carrier escape [Antolín et al.,

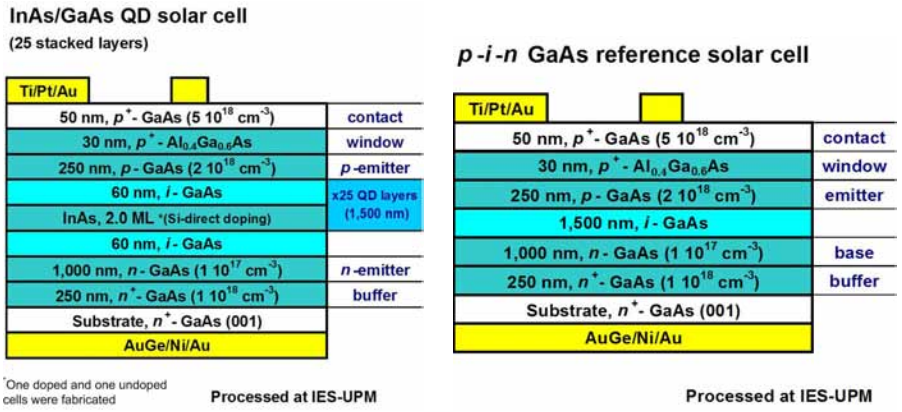

(a) (b)

Figure 5.23: Layer structures of the third batch of samples. (a) 25 InAs/GaAs QD layer cell with thick spacers. (b) *p-i-n* GaAs reference cell.

2010a], making its associated rate (together with the thermal escape component) to be much higher than the photogenerated rate and causing the IB and CB electronic populations to be indistinguishable in practice, which ultimately reduces the solar cell effective bandgap. The QD region is in this case 1,500 nm thick (25 layers times 60 nm per layer), as it is the intrinsic region of the GaAs reference sample. Regarding the rest of the layers of the structure, the solar cell is identical to the previous batch, including the fabrication of one doped and one undoped QD samples.

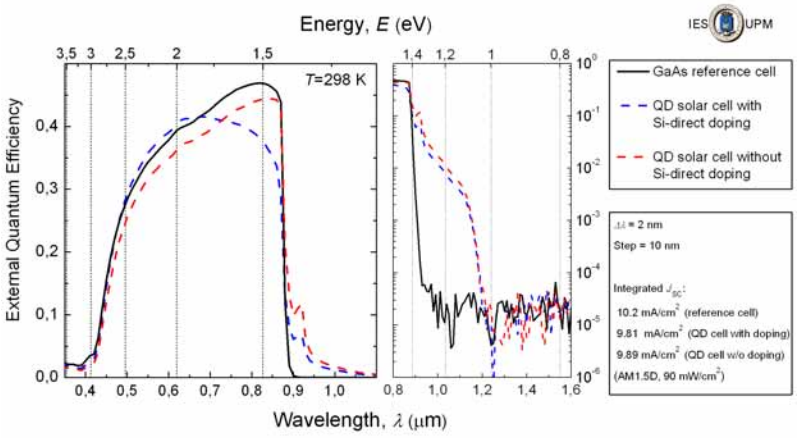

Figure 5.24: External QE of the devices from the third batch of samples at room temperature. Courtesy of Mrs. Esther López.

At the time of writing this Thesis, very few characterization experiments have been carried out on this batch of samples. The most representative may be again the external QE, which is performed at room temperature and which results are shown in Fig. 5.24. In this case, the three devices seem to have suffered from problems at processing level, which

explains the low absolute QE values and the very different behavior in the supra-bandgap response.

The most significant improvement of this new designs is that both QD cells are now only limited by the GaAs bandgap and not by the smaller GaAsN bandgap, which implies that the below-bandgap response is exclusively originated by absorption in the QDs (and in the WL). This sub-bandgap absorption is again higher in the undoped sample, which is consistent with the previous corresponding explanation. The pick at λ=920 nm (E=1.35 eV), corresponds to the WL absorption.

5.4.4 Future design: InGaAs/AlGaAs QD solar cell grown on GaAs(311)B substrate with thick spacers

The designs shown in Fig. 5.25 upgrade the previous QD cell structures and propose a couple of important improvements regarding the important tasks corresponding to the enhancement of the below-bandgap absorption and the separation of the IB electronic population from that of the CB, which should ultimately allow the preservation of the voltage, even at room temperature. In this case, the solar cell will be grown on top of a GaAs(311)B substrate, so that a higher QD density can be achieved [Akahane et al., 2002] thanks to the higher crystal index, as explained in section 5.2. Another important feature will also have to be implemented: in this case, $Al_xGa_{1-x}As$ layers with a relatively high Al content (close to the direct-to-indirect threshold) will have to be used for the spacer layers as well as for the p- and n-emitters.

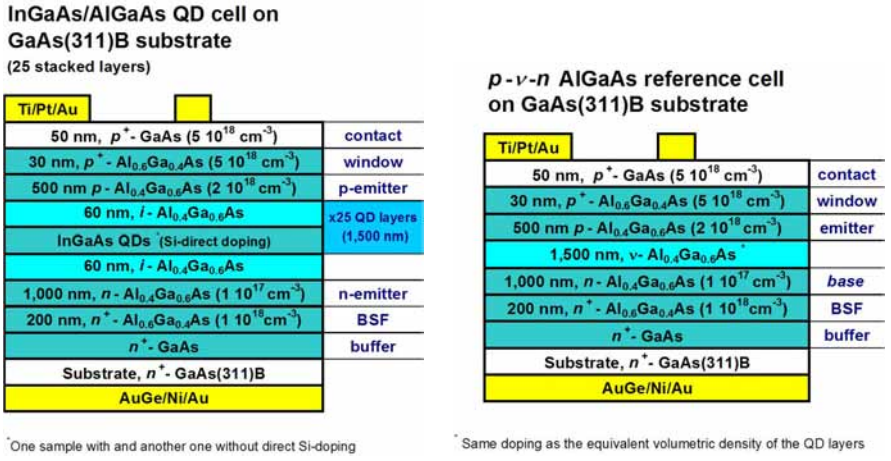

(a) (b)

Figure 5.25: Sketch of the last layer structures proposed in the framework of this collaboration research program with the RCAST. (a) The proposed QD cell is grown on top of GaAs(311)B substrates. It consists of 25 stacked InGaAs/AlGaAs QD layers with 60 nm thick spacers. (b) p-ν-n AlGaAs reference cell.

The use of AlGaAs barriers theoretically allows a higher CBO which can produce an IB well separated (in energy) from the CB [Linares et al., 2011], leading to isolated electronic populations in both bands. Furthermore, IBSCs with larger fundamental bandgaps (i.e. closer to the optimum of 1.95 eV) account for larger limiting efficiencies. A BSF layer is also proposed as another improvement with respect to previous designs. It has to be implemented by means of a highly-doped AlGaAs layers with an increased Al content in order to create the appropriate minority carrier potential barrier (the same reasoning has to be followed for the window layer). A thicker emitter is also prescribed so that the cell has a better collection of the supra-bandgap part of the solar spectrum. The last modification affects the reference cell, which is meant to reproduce the conditions of the QD cell by hosting a 1,500 nm thick ν-region, instead of an intrinsic one. This ν-region is a lightly-doped region with the same doping level as the equivalent volumetric density of the direct-doped IB material region.

5.5 Summary

The fundamentals of the IBSC implemented with QDs are reviewed in this chapter, where a research line including the growth, processing and characterization of strain-compensated QD solar cells is carried out. Several batches of InAs/GaAs(N) stacked QD layer solar cells have been fabricated, processed and tested, leading to the general conclusion that the nitrogen introduced in the spacer layers limits the performance of the QD-IBSC because it reduces the effective bandgap of the device from approximately 1.4 eV to 1.2 eV. This strain-compensation layers can be substituted by thicker GaAs layers which dilute the strain and block the electronic tunnel escape. The performance of Si-direct doping in this structures is also studied. Finally, a new QD-IBSC structure based on an InGaAs/AlGaAs QD solar cell grown on a GaAs(311)B substrate is proposed to enhance the IR absorption and to effectively reduce the thermal escape component.

Chapter 6

Low temperature concentrated light characterization system applied to IBSCs

6.1 Introduction

CPV is nowadays an increasingly important field for both research and industry [Sala and Antón, 2011]. The use of concentrated light techniques allows for significant reduction of the solar cell size, leading to a dramatic decrease of the amount of semiconductor used in a PV system [Swanson, 2003]. Within this paradigm, cheaper PV module components (e.g. lenses) are used in exchange for a significant part of solar cell area, together with the yet-large room for improvement of the concentrator solar cell itself (and of the whole system).

The specific conditions of operation of concentrator solar cells require the use of ad-hoc I-V characterization tools, that will be described in this chapter. Electrical characterization applied to CPV is useful and necessary for the improvement of the concentrator solar cell performance in general, both at material growth and processing levels. Besides, for reasons that have been discussed elsewhere throughout this document, the characterization of IBSCs under concentrated light can also provide valuable information on whether these devices operate in the way the IB theory predicts. Thus, the electrical characterization under concentrated light is an indispensable tool for the research on IBSCs.

The use of ad-hoc concentrated light characterization techniques is not new in itself [Emery, 1986]. Furthermore, many research groups worldwide have focused on this topic throughout recent years and even some companies that belong to the PV industry are willing to have reliable concentrator cell and CPV module characterization set-ups [Keogh

et al., 2004, Pravettoni et al., 2010, Domínguez et al., 2008]. Therefore, after a brief description of the concentrator cell characterization technique and the different possible strategies for implementation, this chapter will deal with the specific features that our concentration set-up incorporate in order to adapt it to the IBSC research needs.

6.2 Concentrated light characterization systems

When a new IB material is proposed and engineered, optical measurements, such as PR, PL, X-ray diffraction (XRD) or FTIR) can be carried out prior to the processing of the solar cell with the purpose of identifying whether the IB exists and if it does, where is it located with respect to the CB and VB edges. Once the solar cell processing has been carried out, electrical characterization is required in order to verify the IBSC concept fundamentals. Concentrated light I-V characterization is an important tool for such purpose and that is why it is worthwhile reviewing the intricacies of the technique. Furthermore, as it has been reviewed in chapter C, this kind of measurements are better carried out when the solar cell processing is adapted to operation under concentrated light, i.e. the whole cell is characterized by a low r_{S}.

The concentrated light characterization system designed and implemented during this Thesis work [Linares et al., 2012c] resembles a conventional multi-flash system [Emery, 1986] except for the features that are specific to the characterization of IBSCs. We will begin this chapter with a review of some of the choices made during the conception of the system. This section may then be useful for any reader undertaking the task of implementing an I-V concentrated light characterization system adapted to IBSCs.

6.2.1 The light source

The light source can be considered as one the most relevant and distinctive elements of a concentration system. The characterization of IBSCs requires a light source that fulfills the following requisites:

- being as powerful as possible, in order to reach the maximum possible irradiance
- the spectrum of the light must be as close as possible to the sunlight spectrum, so that it resembles the AM1.5D spectrum or the one used in CPV standards [Domínguez, 2012, Domínguez et al., 2008]
- it must prevent unnecessary overheating of the sample, since the experiment has to be as sensitive as possible with respect to the IBSC V_{OC} and this is temperature T-dependent

- repeatability and reproducibility of the light source (at least to some extent)

The choice of a commercial Xe flash as light source instead of the many other options has deeply impacted the final design of the system. To make such important decision, several alternative approaches were first explored at laboratory scale. Hereafter, some of the options that were considered regarding the nature and use of the light source will be discussed. Among the different options explored, some were categorically rejected and the respective reasons will be presented.

6.2.1.1 Continuous vs pulsed light systems

The use of a continuous source of light for a steady state concentrated light set-up was initially considered for its stability and relatively simple hardware and software data acquisition requirements. A provisional continuous light system was implemented with a relatively powerful (1,000 W) light bulb, which power was controlled by a 4-quadrant 28 A and 36 V Kepco power supply. A metallic light condenser mirror was located at approximately 1 cm behind the light bulb and aligned with the axis that connects the center of the mirror, the light bulb and the solar cell, so that the light beam was as collimated as possible. A 20x20 cm plastic Fresnel lens was then placed within the optical axis, between the light source and the solar cell, in order to concentrate the pseudo-collimated rays on the solar cell, which was in turn located at its focus. The solar cell, which is typically around 2×2 mm large and had been previously mounted on a 3.5 cm copper disk, had to be cooled down to room temperature for which a Peltier thermoelectric assembly was used. The *I*-*V* characteristic is then measured with the 4-quadrant Keithley source-meter. The whole system is sketched in Fig. 6.1.

In order to accurately fix the temperature of the solar cell junction, it would have not been sufficient to set required temperature in the Peltier controller. The reason is that the amount of heat generated by the continuous light is very significant and the device under test would be affected by a dramatic T gradient between the illuminated side and the refrigerated one. The appropriate way to control the solar cell temperature consisted of placing a shutter, between the cell and the light source, thus blocking the light beam from the lamp (so that the light bulb filament reaches a constant temperature for a fixed supplied power). Then, the shutter was opened (t=0) while the V_{OC} was measured at a sufficiently high sampling rate so that the $V_{\mathrm{OC}}(t = 0^+)$ (i.e. right after being impinged by the light beam) could be measured prior to its reduction due to the increase of the temperature of the solar cell junction. Afterwards, the shutter remained opened and the temperature increased, but the Peltier temperature was then set to a temperature as low as to recover the previous $V_{\mathrm{OC}}(t = 0^+)$ value. Only at this stage, the steady-state

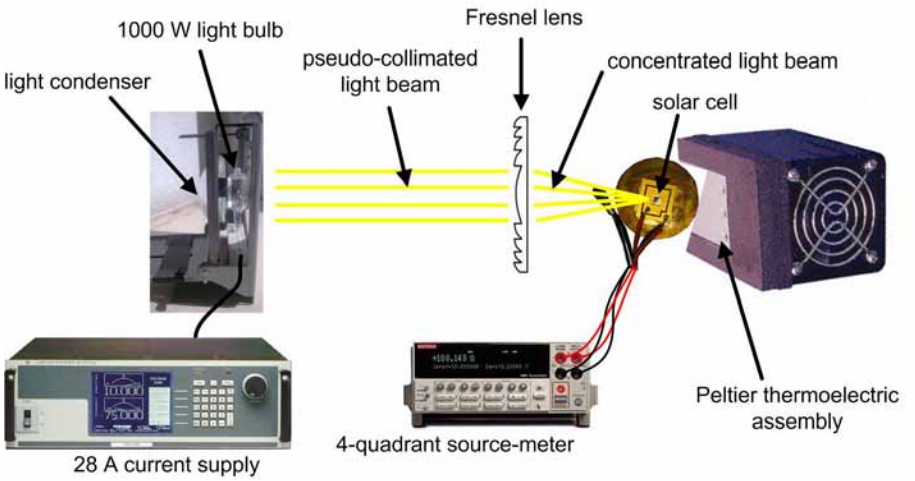

Figure 6.1: Sketch of the continuous light characterization system implemented at IES-UPM. About 300 suns were reached in an approximately 2x2 cm^2 spot thanks to a high current source and a high power light bulb together with a concentrating Fresnel lens. All the system elements are indicated in the figure.

measurement could be acquired. This is a simple and effective way to accurately control the appropriate solar cell temperature, thus allowing the measurement of the whole *I-V* curve in steady state regime. Different concentration factors could be reached just by setting different current values on the lamp power supply, as shown in Fig. 6.2, where several concentrated light *I-V* curves are shown.

Nevertheless, some difficulties and limitations were identified in this continuous light set-up:

- the maximum concentration factor (which may be regarded as one of the most important figures of merit) was too low (below 400 suns), even when different Fresnel lens and rear-mirror configurations were tried
- the operation of the set-up was intrinsically very time-consuming for measuring at many different concentration levels, since it required adjusting the Peltier temperature for each of them
- it was found uncomfortable and not very handy because of the high brightness of the lamp (which had to be operated continuously);
- a noticeable instability of the measurement was identified at high concentrations, maybe due to the inherent fluctuation of the lamp when subjected to high voltages. Such measuring errors are shown in Fig. 6.2
- a reasonably good spectrum (i.e. close to the AM1.5D one) can only be obtained using high power filtered Xe lamps [Domínguez, 2012], which are also difficult to handle (e.g. they can produce ozone and they are complicated to install)

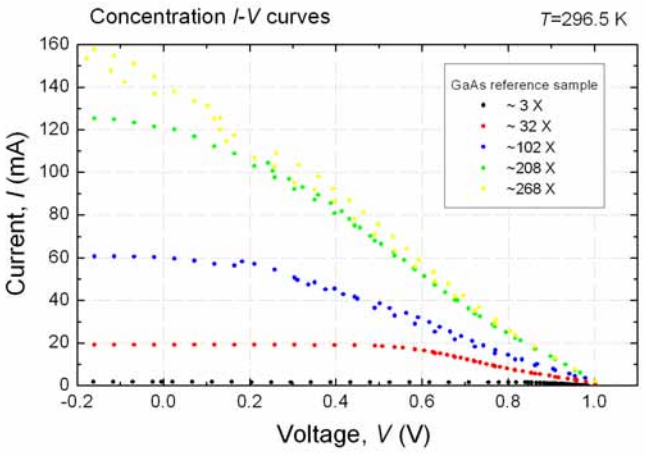

Figure 6.2: Concentrated light I-V plot of a GaAs reference sample using a continuous concentrated light set-up. The voltage applied to the light bulb is varied to obtained different light intensities. Important measuring errors are found when high light intensities apply.

Some other concentrated light systems based on continuous light sources without the inherent instability of incandescent filament light bulbs can be considered. An original idea consists of designing a printed circuit board (PCB) hosting several dozens of closely packed light-emitting diodes (LED) of different emission wavelengths (so that the AM1.5D is somewhat reproduced [Bliss et al., 2009, Kohraku and Kurokawa, 2006]) and power them with enough current for a relatively strong emission. Such lighting appliance has some advantages over conventional incandescent lamps, namely: better stability, easier handling, better light directionality, higher spectral control, lower power consumption, higher scalability, etc. However, its maximum achievable irradiance may not result high enough for our requirements [Bliss et al., 2009] and the implementation of such set-up is too complicated compared with the Xe flash lamp that was ultimately selected.

The light source that was finally chosen for our concentrated light I-V characterization system consisted of a commercial compact flash lamp which provided pulsed-light flashes of approximately 20 ms long (although 90% of the energy is discharged approximately within the first 5 ms). Flash lighting offers several advantages that make it the preferred option for most modern concentration systems worldwide [Sturcbecher and Larue, 1994, Sala and Antón, 2011]. A very important feature is its capability for yielding very high irradiances with a small energy supply, together with a reasonable reproducibility and a light spectrum fairly similar to that of the sun. Furthermore, there are multiple commercially available flash families, which makes it a flexible and economic solution. The very short pulse of the flash can be regarded as drawback regarding its practical implementation, nevertheless it can be easily solved by means of a fast data acquisition system (DAQ), a precise and fast polarization circuit hardware, a versatile data processing software, the appropriate data

processing algorithms and an automatic system controlling unit. Nevertheless, making a virtue of necessity, the fast irradiance decay of the flash light can be useful to explore a wide range of concentrations in each single flash shot.

6.2.1.2 Multi-flash vs single flash systems

There are different strategies for the implementation of a concentrated light flash-based I-V characterization systems: single-flash and multi-flash. A good review of these two strategies can be found in Ref. [Keogh et al., 2004]. In this subsection, a brief description and comparison between them will be addressed, as well as the main reasons that made the multi-flash strategy to be selected for our system.

- **The multi-flash strategy** consists of applying a constant bias to the solar cell throughout the whole flash pulse [Keogh and Cuevas, 1997, Sala and Antón, 2011], so that the irradiance at which the solar cell under measurement is exposed varies from maximum irradiance to zero. Therefore, a single polarization point from the I-V curve is acquired for all the available concentration levels in each flash pulse, providing a family of complete I-V curves at different concentrations after some flash discharges (with the same number of polarization points as flash shots). The aforementioned operating mode is sketched in Fig. 6.3. An important advantage of this technique consists of disregarding the measuring error related to the transient effects produced by a fast variation of the voltage and due to a violent rearrangement of the charge [Keogh et al., 2004]. The latter implies that the cell can be considered as to remain under quasi-steady state regime during the whole flash discharge if a constant voltage is applied, even if the solar cell is subjected to a high irradiance, i.e. a high electron-hole pair generation. This strategy also allows a very fast measurement of the I_{L}-V_{OC} pairs at a wide range of light concentrations (which is an important figure of merit in our concentration set-up), because it can be performed with only two flashes. The multi-flash system does not require a flash irradiance profile with a constant plateau, which ultimately simplifies the measurement, although an external reference cell is also required in order to synchronize the constant irradiance I-V pairs from the different flash pulses (measured at different voltage bias).

- **The single-flash concentrated light I-V characterization strategy** can be subdivided into two different techniques: one of them is based on a flash discharge characterized by a flat plateau irradiance profile (i.e. the flash light intensity is approximately constant during several milliseconds) throughout which different points of the I-V curve are measured [Fanetti, 1981]; the other technique consists of tracing

the I-V curve during a relatively short time lapse of non-constant (although not very varying) irradiance and then extrapolating all data points to a constant irradiance level by means of a calibrated reference cell and the corresponding analytical model that also takes into account the spectrum non-uniformities. This last single-flash technique can be specially useful for industrial production testing and can be implemented by means of a capacitor, which is charged by the photocurrent of the module under test [Askins et al., 2008]. Any of these single-flash techniques requires varying rapidly the cell voltage, which also implies a fast charge redistribution and in turn may lead to transient errors. The magnitude of these errors is variable and depends on the nature and structure of the solar cell under test. Within the IB research context, we may deal with many different semiconductors, and solar cell configurations, which makes the single-flash approach, less appropriate. Furthermore, the fact that the concentration factor remains constant during each measurement also makes it unattractive for our interests.

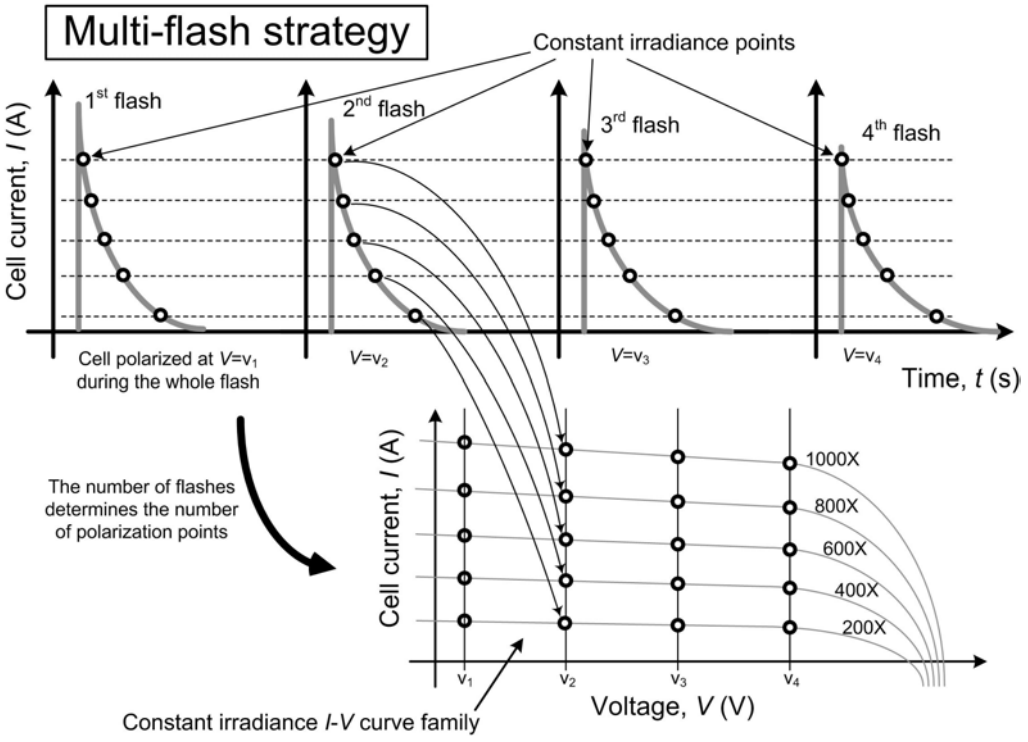

Figure 6.3: The multi-flash strategy is based on the biasing of the solar cell at a fixed voltage during the flash discharge, so that a family of constant irradiance curves are obtained with the same number of I-V pairs than flashes.

6.2.1.3 Sizing and other considerations regarding the flash unit

Different criteria have to be considered when analyzing the appropriate choice of the flash unit:

- **Spectrum**. Most flash tubes are based on Xe lamps, which provides a spectrum reasonably similar to that of the sun [Domínguez, 2012]. Besides, the spectrum constraint will not be very restrictive regarding our design specifications, as it will be later discussed in section 6.3.2.

- **Power**. This feature influences the maximum irradiance that the lighting source can provide at the surface of the solar cell to be measured, which is a very important criterion regarding the final choice of the lamp.

- **Collimation of the light beam**. In conventional CPV characterization systems, the collimation of the light received by the module (or cell) is a figure of merit that is related to the acceptance angle [Domínguez et al., 2008]. In our concentration system applied to IBSCs, this figure has to do with the the maximum concentration factor that can be achieved on the surface of the cell. The more collimated the light coming from the flashlamp, the better the light can be concentrated by means of an external concentrator lens (which will be included in our experimental set-up). Generically speaking, the light rays escape from the Xe flash tube in every direction and therefore, their collimation depends on the optics associated to it. In some cases, this optics is integrated in the compact flash unit and in others, an external metallic reflector has to be used. A couple of commercial reflectors have been used together with a torch flash light trying to enhance the concentrator factor. Fig. 6.4(a) represents an optical paraboloidal reflector aimed to redirect to the front some of the rays emitted towards other directions. This strategy showed some improvement, although the concentrator factor reached was still low, probably because the illumination spot was too large. Another more sophisticated optical device (Fig. 6.4(b)) was tried with the purpose of collimating and homogenizing the light from the torch to a relatively small spot. However this accessory reduced the irradiance of the spot, probably because the light was forced to suffer multiple of reflections inside the device and the efficiency of the reflection was poor.

- **Size of the flash strobe**. The power density of the incident light (i.e. irradiance) at the surface of the flash tube does not only depend on the power supply, but also depends on the size of the Xe strobe tube, i.e. in a general way and for a given power value, the smaller the size of the flash tube, the higher the irradiance that

(a) (b)

Figure 6.4: a) Reflector used to redirect to the front some of the rays emitted by the flash strobe (Elinchrom, model 26149 Reflector Maxi Spot 40 cm). b) Flash tube accessory to homogenize and concentrate the flash beam (Elinchrom, model Mini Spot 26420).

can be reached. Besides, the conservation of brightness theorem applied to strobe bulbs, states that the maximum irradiance at the target surface (the solar cell in this case) is ultimately limited by the maximum irradiance at the surface of the light source (flash bulb). The latter implies that the irradiance received by a PV device may not be augmented by selecting a more powerful flashlamp (if for example, the area of such flashlamp is also augmented). On the contrary, the bright of the flashlamp will increase if 1) the supply power increases and the size of the flash bulb is not increased or 2) the size of the bulb decreases and the power is not reduced. Furthermore, regarding the trade-off between size and power of the flash tube, smaller (more precisely: less energetic) systems, are more adequate for IBSC concentrated light characterization because they furnish lower energy to the environment (i.e. to the surroundings of the cell) and therefore, less heat is transferred to the solar cell. As a consequence, large mono-light flash units (e.g. the ones used in professional photography studios) have been identified as unsatisfactory for our purposes.

- **The length of the light pulse**. This is another important figure of merit of the Xe flash bulb used for concentration set-ups. If a single-flash system is not to be considered, a long flash pulse does not show any advantage. On the contrary, a larger integration area of the irradiance profile implies a larger energy and thus a greater heat transferred to the sample. As a consequence, there is no need for long flash pulses, unless the biasing system and the DAQ are not fast enough to properly register all the required I-V points of the measurement.

- **Automation of the flash triggering**. It is also important that the flashlamp used in the system allows automatic triggering (actuated by an external signal), as it will be reviewed in section 6.2.2.3.

- **Reproducibility of the flash pulses**. Some reproducibility in the flash pulse irradiance profile (with respect to the time) as well as in the maximum irradiance level is required, although, slight variations can be tolerated and corrected by means of the external reference photocell, as it will be explained later.

6.2.2 The hardware

In this section, we will discuss which are the different criteria that one has to consider when it comes to choosing the electronics of the system.

6.2.2.1 The DAQ

The DAQ has to fulfill at least the following requirements:

- Automatic control by software.

- The sampling rate has to be fast enough so that all I-V points (corresponding to the different concentrations) can be acquired throughout each flash pulse. Sampling rates above 1 Mhz have shown excellent results.

- The signal sensitivity has to be high enough so that a wide range of the I_{L} signal can be acquired along each flash. Otherwise the whole I_{L} signal would have to be scanned by means of a large number of flashes (each of them covering a narrow range of currents).

- At least three simultaneous and independent analog acquisition channels are required for the different signals (voltage, current and reference irradiance).

- At least one output channel is recommended so that a trigger signal can be sent to the flash once the DAQ is ready.

A commercial 4-quadrant Keithley 2400 source-meter was originally used as DAQ, but this was found not to be a suitable solution since such source-meter did not allow three simultaneous analog input channels (the fact that the three signals are acquired with respect to the same temporal reference is very important). Besides, it was found not to be sufficiently fast because its sampling rate was in the range of 10 kHz. On the contrary, a National Instruments 6132 peripheral component interconect (PCI) DAQ card (to be

integrated into a PC) with up to 3 Msample/s, a sensitivity of 14 bits, 4 independent analog inputs and 8 digital outputs was found to fulfill all the aforementioned requirements. A simplified sketch showing the different components used for the DAQ is represented in Fig. 6.5, where the PCI DAQ card is shown together with the elements required to control it, i.e. a PC (and the corresponding software). The only difficulty found with such DAQ was that only voltage and not current could be acquired with the analog inputs. As a consequence, the use of a shunt was required so that the I_{L} was proportionally converted into a voltage that could then be measured by the DAQ system. A National Instruments 2110 Bayonet Neill-Concelman connector block (also shown in Fig. 6.5) was used as the interface between the analog and digital input/outputs of the DAQ system and the different terminals of the solar cell circuit. Coaxial cables were used to link the BNC connector block to the circuit.

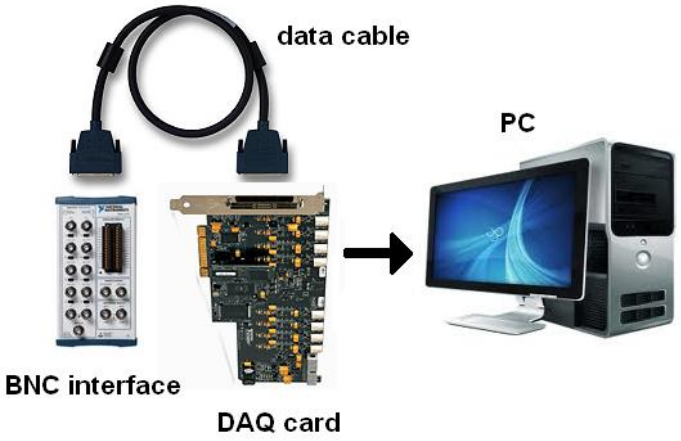

Figure 6.5: Composition of the main elements of the DAQ system, including the PCI DAQ card, the PC used to control the card and the BNC interface together with the data cable.

6.2.2.2 Biasing hardware

A very fast biasing system is required in order to bias the solar cell at a fixed voltage during the flash. In this case, the Keithley 2400 source-meter was found to be a good choice, since it allowed 4-wires biasing, assuring the solar cell to remain at a truly constant voltage despite the violent variations of the voltage throughout the rest of the circuit.

When the light of the flash reaches the solar cell, it induces a violent perturbation on its polarization circuit: prior to that point, a typically low dark current flows (assuming it is reverse or low forward biased), but right after the flash light reaches its surface, a large I_{L} is induced. This current has to be drained by the source-meter at the same time its "sense" probes provide the necessary feedback for the 4-wire algorithm, so that the source-

meter "force" probes rapidly modify the solar cell bias, correcting the voltage perturbation induced by the abrupt change of the current-voltage conditions of the circuit. This process is run recursively in a loop, until the perturbation is counteracted and the desired bias is obtained in the solar cell. The initial voltage perturbation is typically corrected in approximately 1 μs thanks to the very fast response of the Keithley 2400 source-meter.

When choosing the biasing subsystem, besides the aforementioned response time, special attention must be also paid to the voltage and current sensitivity and also to the maximum current that the source-meter can assume, because (depending on the solar cell I_{L} under maximum concentration) this may limit the maximum concentration that the system can reach. Another limitation of this kind of commercial source-meters is related to the maximum voltage difference that can be applied between the sense and the force probes, which in turn limits the size of the shunt used for each measurement.

6.2.2.3 Triggering

An output signal must command the flash trigger. For that purpose, the flashlamp has to be equipped with a switch with which the flash can be automatically triggered. In the case of our commercial flash, this switch is accessed by two cables that trigger the flash light when they are short-circuited (i.e. physical contact is made between them). A trigger signal synchronized with the DAQ is easily obtained from one of the digital outputs of the DAQ card. This trigger signal has to turn an (always opened when de-energized) electromechanical relay on to trigger the flash. Such relay is controlled by the 5 V transistor-transistor logic (TTL) digital output signal from the DAQ card (as shown in the flash trigger system box of Fig. 6.6(a)). However, the maximum current from the digital output of a DAQ card is typically lower than 1 mA, which is too low to energize the relay. Therefore, an amplification circuit has to be placed in between, so that the current from the digital output is increased up to approximately 70 mA. The amplification circuit is based on a Darlington pair, which consists of two transistors in cascade used for current amplifications characterized by a typical gain of $\beta_{\mathrm{Darlington}} \simeq {\beta_{\mathrm{transistor}}}^2$. The simple Darlington pair circuit first used to amplify the current from the DAQ digital output is shown in the picture of Fig. 6.6(b) and was later optimized for the more refined trigger system box of Fig. 6.6(a).

The concentration system also requires the reception of another trigger signal to launch the data acquisition. All analog inputs are set by software and remain ready until a trigger is received and starts the simultaneous reading of the voltage and current signals. This secondary trigger function can be performed with the same trigger signal generated by the digital TTL output of the DAQ that is used to trigger the flash lamp. The latter presents

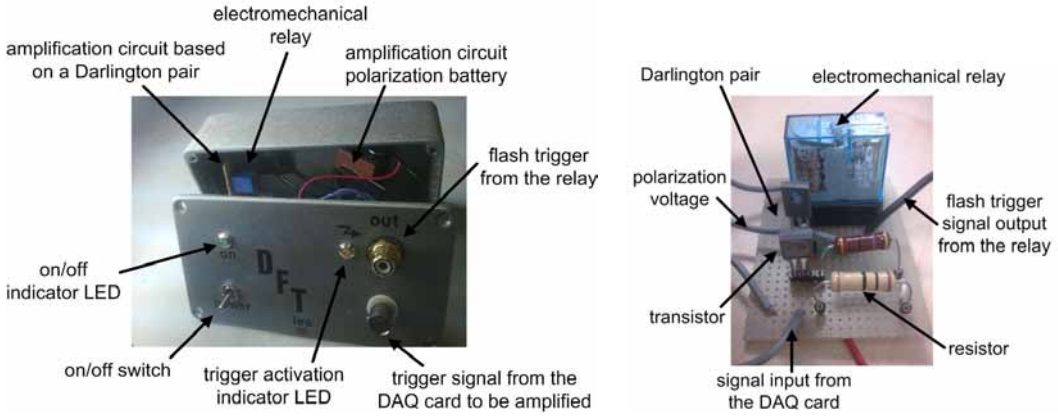

(a) (b)

Figure 6.6: Flash trigger system. (a) Image of the flash trigger system implemented in a metallic box and with labels indicating each of the parts. (b) Detail of the amplification electronic circuit (including the Darlington pair and the electromechanical relay) implemented in another version of the triggering system box.

a problem: the all-digital process of the data acquisition trigger is faster than the digital-analog process that triggers the flash (because of the delay related to the electromechanical relay). The latter causes the data acquisition to start a few milliseconds before the flash is actually triggered. The problem is that during this lapse of time, large sequences of noise are acquired, which can be avoided by setting an automatic delay in the beginning of the DAQ reading.

6.2.3 Automation and irradiance monitoring

The automation of the characterization system does not only aim to make its operation easier and more comfortable, but also to achieve more reproducibility of the measurements.

6.2.3.1 Software and hardware automation

One of the necessary hardware automation strategies consists of the fabrication of a flash control unit that can be, in turn, controlled by software. This flash control unit basically consists of the flash tube triggering unit (including an ad-hoc electronic circuit) that has been already described in section 6.2.2.3.

Another automation is required for the solar cell biasing system: the source-meter automatically modifies the electrical current scale and the dramatic boost in I_{L} can be appropriately handled prior to the saturation of each of the scale ranges. This can be automatically controlled by means of the auto-scale function of the source-meter in our system. Another advantage of this function is that it allows measuring I_{L} without heating

the solar cell: during the time the cell is biased prior to the coming of the flash, a source-meter without this autoscale function would have to remain at the highest current scale (e.g. over one ampere) in order to drain the largest I_{L} value that s going to be generated. At this current scale a relatively high current (of up to several hundreds of microamperes) is fluctuating in the circuit because of the inaccuracy of this high scale in the neighboring of a quasi-zero current (e.g. the source-meter may not have a sensitivity higher than 1 mA when it is set to the 6 A scale). The result of the flow of such relatively high currents through the cell is that it could be unnecessarily heated.

The use of appropriate software tools is crucial for the automation of the system. Many devices have to be controlled and synchronized, as well as many functions have to be performed by software:

- **Command of the DAQ card**. The DAQ card has to be set to the appropriate values: e.g. sampling rate, number of analog channels, magnitude to be measured and corresponding channel to be assigned to it, range of values to acquire from each channel, value of the shunt used in the current-to-voltage conversion, type and value of the trigger signal for each channel, etc.

- **Synchronization of the concentration level**. The I-V pairs from each flash have to be synchronized with the I-V pairs from the subsequent flashes depending on the concentration levels. This is carried out thanks to an external photocell that receives an illumination from the flash proportional to the one received by the solar cell under test. Each I-V pair acquired during a flash shot is assigned to an irradiance level detected by the photocell and once the whole measurement is finished, the I-V pairs with the same irradiance level are set together to produce each of the concentration I-V curves. This method is valid if the relative position and distance between photocell and flash tube is kept constant.

- **Storage and processing of the data**. Every signal acquired through the analog ports is initially stored in a buffer, although it has to be appropriately stored in memory prior to the acquisition of the following signal. Then, the signals are smoothed by a first order low-pass elliptic (digital) filter with a cut-off frequency of 10 kHz.

- **Repetitions**. In order to increase the signal to noise ratio of the acquisition, the system has to be able to make repetitions over the same signal. These repetitions, which require software implementation, imply a longer measuring time.

- **Real-time monitoring**. The temporary results have to be displayed on the computer screen in real-time. The final result (after averaging, filtering and interpolation of the data) is also displayed on the screen.

- **Triggering management**. The trigger signals also have to be programmed, set, sent and detected by software.

An excellent software tool capable of performing all these functions, including data processing and signal synchronization is the graphical development environment from National Instruments called Labview (Laboratory Virtual Instrumentation Engineering Workbench). The "*interactive measurement software for acquiring, analyzing, presenting,*

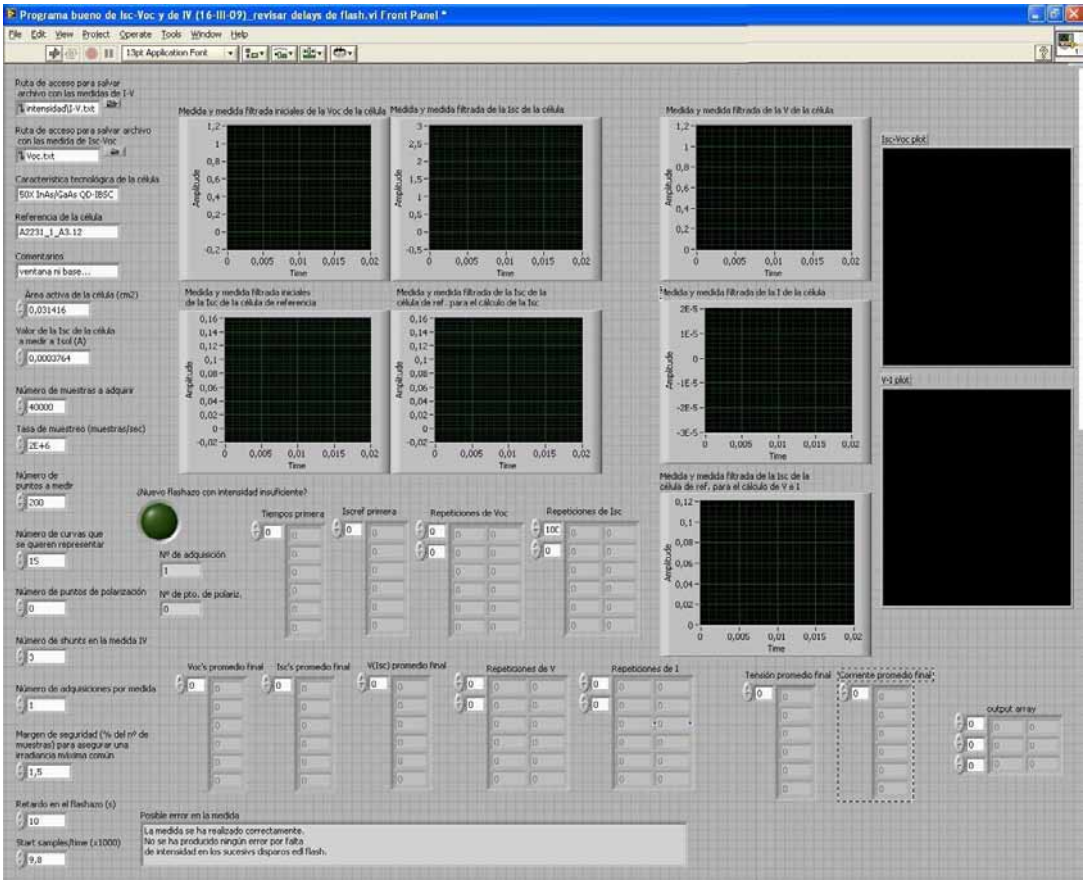

Figure 6.7: Front panel of the Labview software used to command all the concentration set-up subsystems as well as to process the acquired data and present it on the PC screen. On the left side of the panel, the input values are introduced to define the measurement options. On the central part, four screens show the evolution of the measurement on real-time. On the right part, the final result is presented.

and logging data" software tool Labview Signal Express, also from National Instruments, allows controlling the DAQ card and managing the data, including real-time display. A program based on Labview environment with embedded Labview Signal Express modules was carried out in order to control the system. The Labview front panel of this program is

shown in Fig. 6.7. The user can modify the different variables of the concentration set-up by introducing different values in the boxes on the left side of the panel. The evolution of the measurement is presented in the central screens and the final result is shown in the screens on the right.

6.2.3.2 Irradiance monitoring

The irradiance monitoring is a key operation feature for the synchronization between the different flash pulses. This function is performed by means of a commercial 1 cm^2 silicon photodiode, placed in a simple circuit where it is reverse biased. Such reverse bias makes the photodiode to remain in a flat region of its I-V curve, so as to assure an I_L that is proportional to the irradiance. A small resistor is located in series so that the DAQ channel devoted to irradiance monitoring (and connected in parallel to that resistor) reads a voltage that is proportional to the I_L of the photodiode.

In the general case, the irradiance level detected by the photodiode will not be equivalent to the irradiance received by the solar cell under test. The reason is that, for practical reasons, both devices are located at a different distance from the light source. Anyway, a concentrating lens is placed between the flash tube and the solar cell, producing a light spot (of concentrated light) that is too small to accommodate both the cell and the photodiode. As a result, only the solar cell (and not the photodiode) is located within the concentrated light spot under the cell. Besides, the optical path of the light beam that reaches the solar cell is different from that reaching the photodiode and the light may suffer different reflections before impinging either one or the other. Consequently, the purpose of the photodiode cannot be to measure directly the irradiance on the solar cell, but the synchronization of the different flashes, i.e. I-V pairs from different flashes and with equal irradiance levels are matched to each other. As a matter of fact, the concentration factor of our concentrated light I-V measurement can only be indirectly reported from internal reference once we have obtained the 1 sun characteristic from a calibrated sun simulator.

6.2.3.3 Manual handling of shunts and resistor box

The DAQ card does not perform direct current measurements and thus, shunts with different values are required for the wide range of currents that we want to explore, which implies modifying the circuit every time we want to measure a different current range. This shunt replacement function could also be automatically carried out, not only between flashes in which a different concentration range is going to be explored, but also within the same flash, so that the different intensities of the photocurrent are properly measured. Nevertheless, so far the effort and complications derived from such improve-

ment do not justify the automation of this function in this laboratory scale implementation of the concentration set-up.

As it will be explained next, the biasing of the different forward-bias points of the concentrated light I-V curve is done in a passive way. This implies removing any active electronic device from the solar cell circuit, except for the solar cell itself, which in practice consists of replacing the 4-quadrant source-meter by a variable resistor from a decade resistor box. The value of this resistance is modified so that a different slope for the load line is obtained, imposing a different biasing.

6.3 Description of the implemented concentrated light characterization system

In this document, a complete description of the operation principles of the concentrated light system have not been detailed because it would not represent any novelty with respect to what has been already published in this field. However, the main features that make this set-up unique and probably the first used to characterize IBSCs will be addressed.

6.3.1 Design constrains

Besides the general features of a conventional concentrated light solar cell I-V tracing system, the one we have developed has other ad-hoc features for measuring IBSCs [Linares et al., 2012c], which are discussed next.

- **Very high concentration factor**. A very high irradiance is necessary to explore the high voltage range of the solar cell under test. Our concentration set-up employs a concentrator lens located between the flash tube and the solar cell, focusing the light beam in the solar cell surface and achieving a concentration factor of approximately 10,000 suns. The inconvenient derived from the use of this lens is the non-constant irradiance profile of the small illumination spot.

- **Passive biasing**. In our system, the concentrated illumination I-V curve is performed with passive biasing of the forward-biased points. In the active biasing strategy (i.e. with a source-meter) the cell has to be biased prior to the triggering of the flashlamp and in case of high forward bias (which, under dark conditions, implies large forward currents) the cell can be artificially heated up even before the light impinges its surface. The passive biasing strategy consists of introducing a polarization resistance in the solar cell circuit instead of the source-meter. This configuration, imposes a forward-bias biasing that depends on the value of the resistor and that could

not possibly heat the sample up prior up during the time the cell is "waiting" to the coming of the flash under dark conditions. This last configuration is suitable for our interests, although the reverse and low forward voltage ranges, the active biasing is required because the load curve imposed by an arbitrarily low polarization resistance (even of zero ohms) does not cross the illumination I-V curve in such ranges and thus, the cell cannot be passively biased at such voltages. This is sketched in Fig. 6.8, where a family of concentrated light I-V curves are shown together with the load curves corresponding to the passive biasing with resistors. Anyway, the current flowing through the solar cell under dark conditions, when reverse and low forward active biasing is applied is small and produces a negligible cell heating.

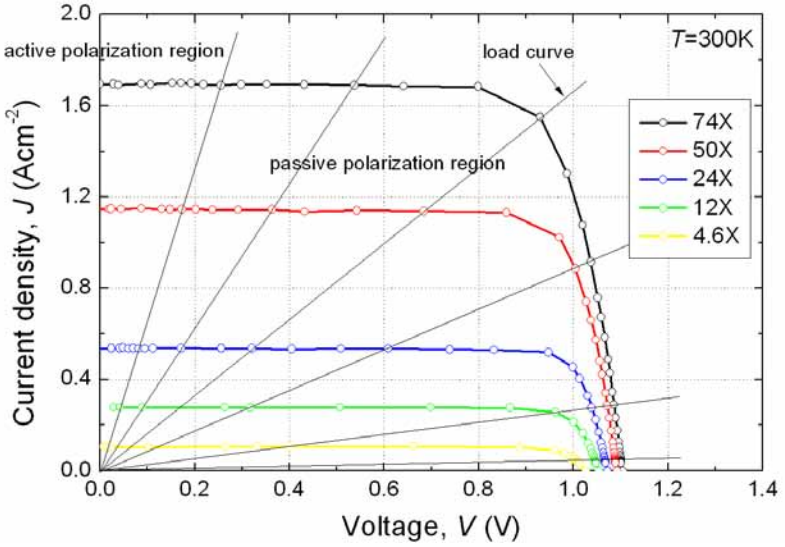

Figure 6.8: Family of I-V curves acquired with passive biasing. Different resistor values are used to bias the cell in the high voltage range, whilst an active biasing performed with a source-meter is used for the reverse and the low voltage ranges. The circuit load curves imposed by the resistors are also shown in the graph.

- **Low temperature operation**. One of the novelties this set-up presents is the possibility of performing low-temperature-high-concentration measurements. The low temperature operation of the InAs/GaAs QD cell is indispensable for its performance as an IBSC. The low temperature concentrated light characterization is a useful tool to analyze the electrical performance of the IBSC, since the I_{L}-V_{OC} measurement allows a deeper understanding of the recombination taking place in the solar cell. Besides, the evolution of the V_{OC} with respect to both concentration level and low temperature, reinforces the verification of the operation fundamentals regarding the IB concept [Linares et al., 2012b]. The concentration set-up has been adapted to cryogenic temperatures (down to 6 K) thanks to a closed-cycle He cryostat. The

optics in this case can only be optimized to reach 1,000 suns. A picture of the concentration system adapted to low temperature is shown in Fig. 6.9.

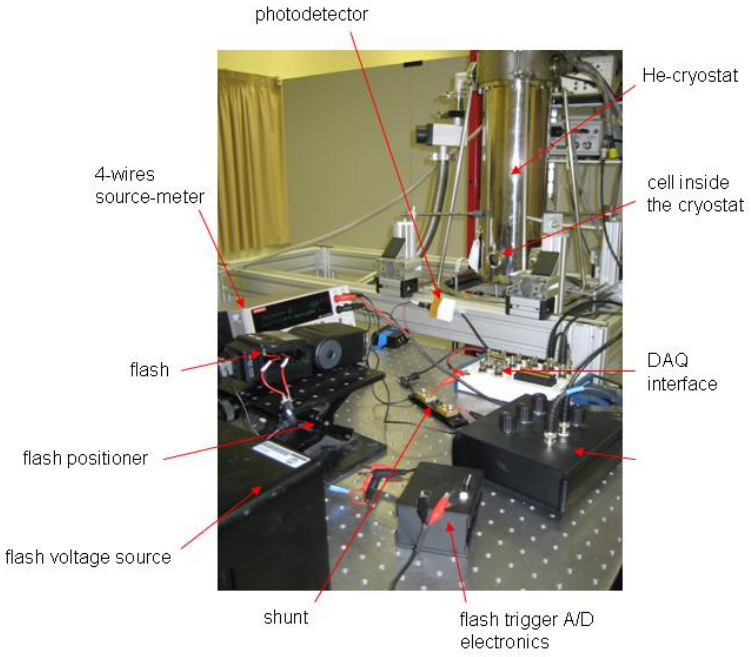

Figure 6.9: Picture of the low temperature concentration system. The labels indicate each part of the system hardware. The solar cell under test is inserted inside the He cryostat and the massive concentration lens of the room temperature system is replaced by a cryostat window acting as a concentrator lens. The different optics of this set-up only allow a maximum concentration of 1,000 suns.

- **Characterization of I_{L}-V_{OC} curves.**. Another distinctive feature of this characterization system is that it is optimized for the acquisition of I_{L}-V_{OC} curves. The main difference is that the I_{L}-V_{OC} curve requires a very wide range of concentrations, e.g. our system is capable of exploring approximately up to seven orders of magnitude of I_{L}, from 10,000 suns down to approximately 10^{-3} suns (depending of the size and photocurrent delivered by the cell).

6.3.2 Simplifications of the system

A general-purpose concentrated light characterization system or an accurately calibrated one are not pursued in this Thesis work. Therefore, a number of simplifications have been carried out in order not to make it very cost and time intensive.

6.3.2.1 Small illumination spot

The light passing through the lens and being concentrated on the cell or the sample holder of the Peltier assembly (in the absence of cell) forms a relatively small spot. Such spot,

where the solar cell has to be located is large enough to illuminate our cells, i.e. most of the IBSCs which IES-UPM work with have been designed for high concentration, so they have a relatively small area, in the range of 3 to 4 mm^{-2}. In case the irradiance of such spot were inhomogeneous, this should not significantly affect the results regarding the IBSC theory.

6.3.2.2 Discrepancy with respect to the AM1.5D spectrum

The same argument can be used with respect to the spectrum with which the cell is illuminated. The flash tube is based on a Xe lamp and its spectrum is reasonably similar to the AM1.5D [Domínguez, 2012], although the flashlight beam crosses several elements before impinging the cell surface (e.g. the plastic front lens of the compact flash, the concentration lens and in some cases, neutral density filters for achieving very low concentrations). The light reflected in the set-up walls as well as in other elements of the system may also vary its spectrum. Even a small contribution of the phenomenon known as chromatic aberration could be affecting the measurement. In spite of all this casuistry, two important things are exclusively mandatory regarding the spectrum. On the one hand, what has already been mentioned about the repeatability among all flashes corresponding to the same measurement. On the other hand the constraints regarding the spectrum can be relaxed to assure that a reasonable part of the light reaching the cell has the appropriate energy for each of the three main transitions involved in the IBSC supra-bandgap and sub-bandgap operation.

6.3.3 Concentrated light I_L-V_{OC} characterization

Several points of the I_L-V_{OC} curve can be ideally acquired with only two flashes: one with the source-meter off and opening the cell circuit so that no current flows through either the cell, nor the calibrated shunt (measurement of the V_{OC} at different concentrations) and the other one closing the circuit and connecting the source-meter in the voltage source mode in series with the circuit. In the first of them, the circuit shown in Fig. 6.10(a) is used. In this mode, the source-meter is disconnected from the circuit and there is no need for the DAQ to read the solar cell current channel, $V_{current}$, since no current flows through r_{shunt}. The voltage channel of the solar cell, V_{cell}, measures V_{OC} and in this case, the source-meter terminals V_{sense} and V_{force} are disabled. The second flash excites the solar cell when it is polarized at a reverse voltage in which the I_L (and not just the I_{SC}) is obtained. In this case, the source-meter is connected to the circuit (as shown in 6.10(b)) and set to 4-wires configuration with the appropriate current limit values before it is turned on. The source-meter V_{force} terminal biases the solar cell, for which the V_{sense} terminal provides feedback

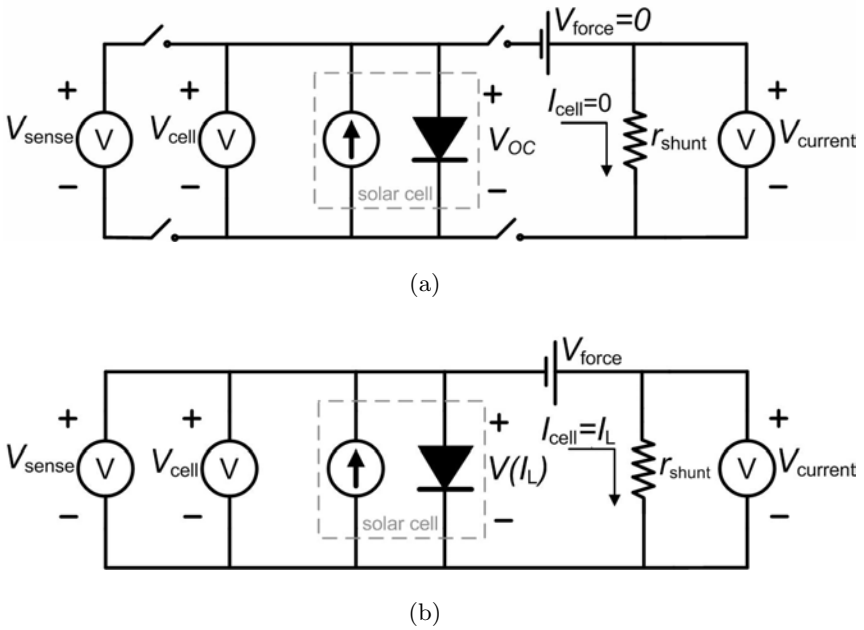

Figure 6.10: Solar cell bias circuit for the acquisition of the I_L-V_{OC}. (a) Bias circuit of the acquisition of the V_{OC}. (b) Bias circuit for the acquisition of the I_L.

on the real voltage measured at the solar cell (i.e. preventing the voltage drop taking place in r_{shunt} to alter the desired biasing of the solar cell). In this mode, I_{cell}=$V_{current}/r_{shunt}$ and it also equals I_L when it is appropriately biased.

In the circuit configurations of Fig. 6.10, the different DAQ input channels are represented as voltmeters, for which an infinite input impedance is considered. In reality, this impedance has a very large value, in the range of 1 GΩ, which should, in principle, be sufficiently low to drain a negligible current.

Once the acquisition of the I_L-V_{OC} data during the two flashes is completed, the software performs the digital filtering of the data and then synchronizes the I_L and V_{OC} pairs that correspond to equal concentrations. This synchronization can be carried out by means of the irradiance signal from the photodiode that is acquired simultaneously to the current and voltage signals from the solar cell, i.e. each I_L and V_{OC} point is assigned to an irradiance value measured by the photodiode within the same temporal axis. The synchronization algorithm is explained in Fig. 6.11, where a simplified sketch of the process is shown:

1) The 1st flash is received, assigning each value from the V_{OC} signal (red curve) to the corresponding irradiance value measured with the photodetector (gray curve). 2) The 2nd flash impinges the cell and the I_L signal (blue curve) is obtained, assigning its values to other irradiance values. 3) The I_L values from the 2nd flash are matched to the V_{OC} values from the 1st flash corresponding to a predefined set of concentration factors. This

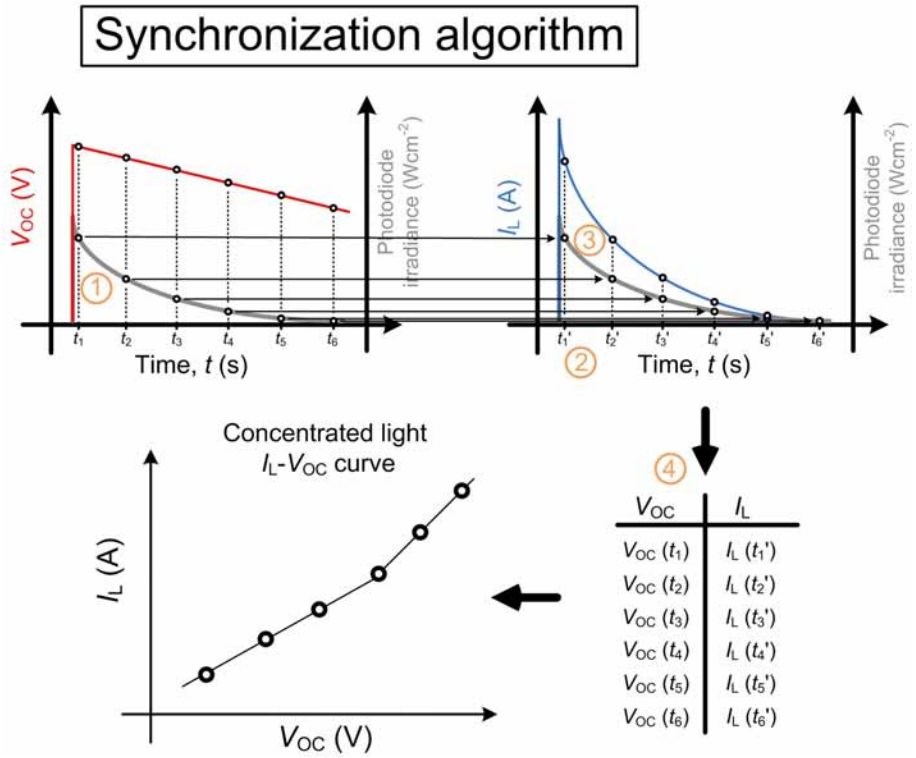

Figure 6.11: Sketch of the synchronization algorithm used to match solar cell I_L-V_{OC} pairs of the same concentration factor in the concentrated light I_L-V_{OC} measurement. The labels 1) to 4) symbolize the different steps of the algorithm.

matching is carried out by means of the eternal photodetector signal. 4) A table with the I_L-V_{OC} pairs at different concentrations is generated and the curve is plotted.

In practice, the measurement cannot be properly carried out only with these two flashes because it has to be assured that the true I_L is being obtained. For that purpose, an iterative verification procedure is followed. It begins by acquiring the I_L-V_{OC} curve at $V(I_L)$=0 V, i.e. with I_L=I_{SC}, as shown in Fig. 6.12(a). If the maximum concentration is too high and/or the solar cell is not adapted to concentration, it is very likely that the upper part of curve #1 is 'bent' to the right because the value of the acquired current does not correspond to the flat section of the I-V curve under such concentrated-light operation conditions, i.e. the I_L value has not been reached yet (at least in the highest concentration range). This indicates that a more negative bias has to be imposed in order to reach the true I_L. This is carried out with an initially small bias. The new I_L-V_{OC} curve is plotted together with the previous one (curves $V(I_L)$=0 V and $V(I_L)$=-1 V in Fig. 6.12(b)) to verify whether the real I_L has been already reached or not. If the two curves accurately match, then I_L=I_{SC}, implying that the I_L-V_{OC} curve is appropriately measured at $V(I_L)$=0 V. However, if the upper part of the second curve ($V(I_L)$=-1 V in the example) does not match the first one, it implies that a more negative bias is still required. A third curve

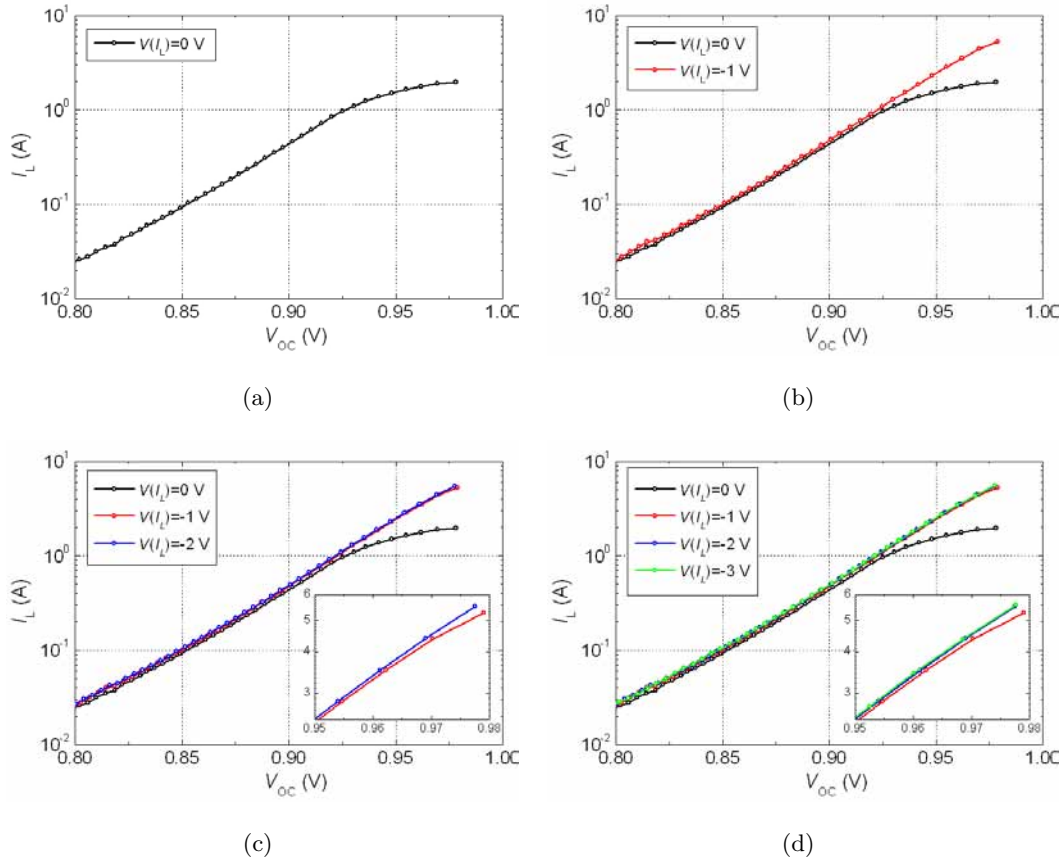

Figure 6.12: Example of the iterative mechanism used to measure the I_{L}-V_{OC} characteristic of a QD-IBSC. (a) The first I_{L}-V_{OC} curve is acquired at $V(I_{\mathrm{L}})$=0 V. (b) The I_{L}-V_{OC} curve with $V(I_{\mathrm{L}})$=-1 V is included, showing that a more reverse bias is required. (c) The $V(I_{\mathrm{L}})$=-2 V curve shows that it is converging towards the appropriately measured values. (d) The last curve ($V(I_{\mathrm{L}})$=-3 V) matches the previous one, meaning that the I_{L} has saturated and the true I_{L} has been obtained.

is measured at a more negative bias, starting an iterative reverse bias measuring process that will finish when two consecutive I_{L}-V_{OC} curves (with progressively more negative bias) superimpose, meaning that the penultimate bias is appropriate for a true I_{L}. Fig. 6.12(c) represents a third curve ($V(I_{\mathrm{L}})$=-2 V) that does not completely overlap to the previous one, meaning that the $V(I_{\mathrm{L}})$=-1 V bias is not appropriate yet. Nevertheless, the gap between the last two curves ($V(I_{\mathrm{L}})$=-1 V and $V(I_{\mathrm{L}})$=-2 V) has been reduced with respect to the gap between the first two curves ($V(I_{\mathrm{L}})$=0 V and $V(I_{\mathrm{L}})$=-1 V), indicating that the I_{L} saturation threshold is about to be reached. Fig. 6.12(d) finally shows the curve $V(I_{\mathrm{L}})$=-3 V, which totally matches the $V(I_{\mathrm{L}})$=-2 V curve, meaning that the -2 V reverse bias is negative enough to obtain the real I_{L}. Either the curves $V(I_{\mathrm{L}})$=-2 V or $V(I_{\mathrm{L}})$=-3 V are correctly measured as I_{L}-V_{OC}, although the lower in absolute value is chosen to minimize possible damaging of the cell.

The wide range of concentrations that we want to measure, together with the fact that the DAQ card has a maximum input voltage and also a minimum one (regarding the sensitivity and the noise to signal ratio) for the acquisition of the I_L signal, imply that the whole I_L-V_{OC} curve cannot be entirely acquired at once. Actually, the curve has to be divided into several sections corresponding to different different flashlight intensities, (which can be obtained lowering the intensity of the flashlamp or placing neutral density filters in the optical path). Different shunt values, adequate for each current range have to be used as well to measure I_{cell}. The highest part of a I_L-V_{OC} section has to match the lowest part of the following section. This verification is shown in the plot of Fig. 6.13.

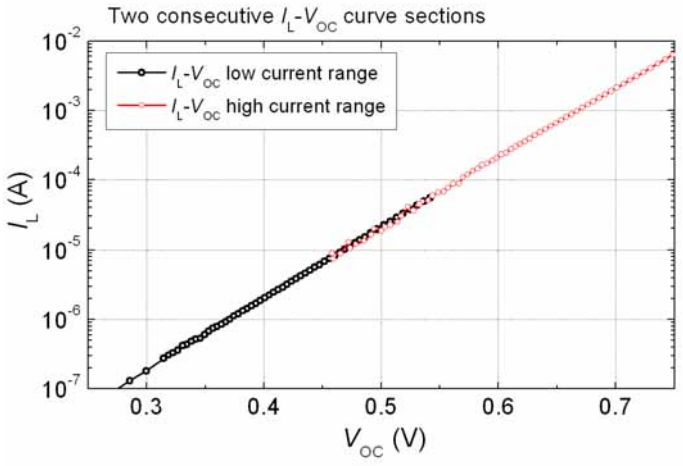

Figure 6.13: I_L-V_{OC} plot showing two consecutive superimposed curve sections that correspond to different concentrated light ranges. This figure verifies that the measurement is being appropriately acquired.

6.3.3.1 Possible problems of the I_L-V_{OC} measurement

It has been stated that temperature control is an important issue regarding the characterization of IBSCs at high concentrated light. However, some heating of the solar cell when subjected to very high irradiance is unavoidable. For concentrations over 2,000-3,000 suns, which are always related to the highest section of the I_L-V_{OC} curve, the sample is inherently heated. There is no way to dissipate this heat instantly and hence, the cell temperature increases and affects the measurement of the V_{OC}, because the same light that excites the sample and makes it reach very high photogeneration rates, causes this heating. Besides, the time-scale corresponding to the discharge of the flash is too small for the heat to be efficiently evacuated during the measurement, because approximately 90% of the light is released in the first 5 ms. Thus, the heat will invariably affect the measurement along the excitation, even if an arbitrarily large sink is connected to the solar cell. The good news is that in most cases, specially when dealing with reasonably good

devices (with a relatively good thermal conductivity), the solar cell heating is produced instantly, i.e. in the very first time after the flash light impinges the surface of the solar cell. As a result, this heating can be considered as constant throughout the whole measurement. The latter can be experimentally verified in the upper part of Fig. 6.14(a) [Linares et al., 2012c] where a complete I_{L}-V_{OC} curve is represented (black, red and blue) together with another curve section (green), corresponding to the highest concentration, that has suffered from a constant heating, thus, displacing it in parallel to the appropriately measured high concentration range of the curve (blue). The only way to properly carry out the measurement is by cooling the solar cell down in advance the same ΔT that will be equivalently increased by means of the flash light. This cooling has to be done prior to the acquisition of the heated I_{L}-V_{OC} curve section. The measurement corresponding to the high current section of the I_{L}-V_{OC} curve can be appropriately performed (blue), compensating the flash-induced heating (in this case, of ΔT=5 K). The fact that the lowest part of the blue curve accurately matches the highest part of the red curve verifies that the anomaly found when measuring the green curve corresponds to a V_{OC} loss produced by a constant ΔT increase (derived from an inherently and instantly heating of the cell due to high irradiance exposure).

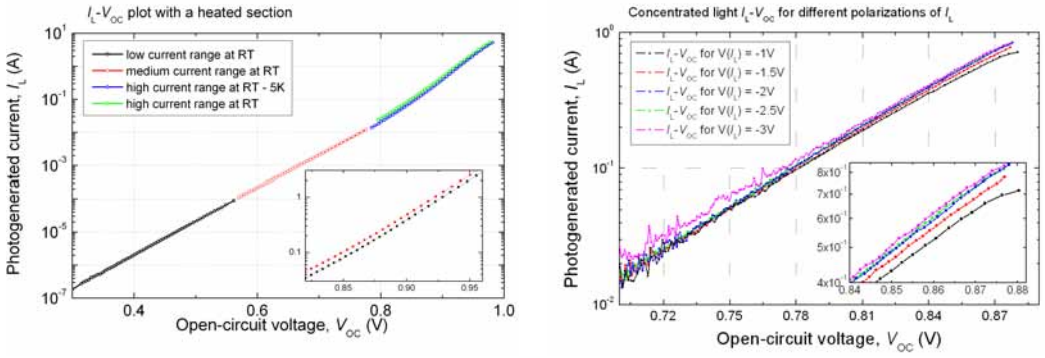

(a) (b)

Figure 6.14: a) Example of I_{L}-V_{OC} plot where the highest curve section is heated (green) and requires decreasing the temperature during the acquisition of that current range, so that the extra heat is compensated and the measurement is properly performed. b) The reverse breakdown is produced at V=-3 V (pink curve) and a certain current is added to the photogenerated component, implying that the measurement could not have been performed for such reverse bias.

Besides the heating of the solar cell, the high concentrated light I_{L}-V_{OC} experiment has to overcome another type of problems. It appears when a one of the following cases (or both at the same time) apply: 1) the solar cell is characterized by a relatively small r_{P} and 2) the reverse breakdown of the cell occurs at a relatively low (in absolute value) reverse

voltage. When the acquisition of the I_L at a certain concentration requires the reverse biasing of the cell, either mechanism 1) or 2) can cause the addition of a non-photovoltaic component to the I_L, thus increasing the value of I_L (the added current component flows in the same sense than I_L) and altering the proper shape of the I_L-V_{OC} curve. This effect is shown in Fig. 6.14(b) [Linares et al., 2012c], where a plot with five I_L-V_{OC} curves measured at different reverse bias is represented. The $V(I_L)$=-3 V curve (pink solid line in Fig. 6.14(b)) has begun the conduction in reverse (e.g. due to the disruption of the p-n junction), which means that the sample cannot be reverse biased at such negative voltage. When either the reverse conduction or the existence of a high parallel resistance cause the addition of an extra current component at a voltage at which the real I_L has not been yet reached, the I_L-V_{OC} curve cannot be properly measured. The only solution is then measuring it at a lower concentration, where a lower reverse bias is required. However, in the case exemplified in the figure, the I_L is correctly measured when applying $V(I_L)$=-2 V, because at this bias, as well as at $V(I_L)$=-2.5 V, both curves superimpose.

Another type of problem can occur during the measurement of the high irradiance I_L-V_{OC} range in solar cells with a relatively high equivalent capacitance. This may be the case of solar cells with a high density of defects, such as thin-film chalcopyrite solar cells, where grain boundaries can provide a large number of intermediate states distributed throughout the bandgap. When a very high irradiance flash light illuminates one of these devices, the large-capacitance may prevent the V_{OC} to evolve as fast as the illumination (which can dramatically increase from 0 to close to 10,000 suns when the flash light is received), so that the electrical response is delayed with respect to the illumination. This effect can be observed in the simultaneous signals of the reference photocell (which measures the evolution of the irradiance) and the cell's V_{OC}, both represented in Fig. 6.15. The second signal is notably delayed with respect to the first one (the time scale, represented in the horizontal axis is the same for both plots).

When this problem is very pronounced, the I_L-V_{OC} may not be possibly acquired in this irradiance range and a lower flash intensity has to be used. However, it is also possible that the measurement is appropriately carried out even if the V_{OC} signal is slightly delayed (or desynchronized) with respect to the illumination.

The last problem regarding the acquisition of the I_L-V_{OC} curve that will be reported is related with an unavoidable heating of the cell during its measurement at very high irradiance (see curve T=77 K from Fig. 2.6(b) and Fig. 2.7(c) as example). It is possible that in case the solar cell under test has a very bad thermal contact, the energy from the flash light cannot be appropriately evacuated and the V_{OC} signal gets very affected because of it, which is manifested by a large voltage drop in the very first microseconds

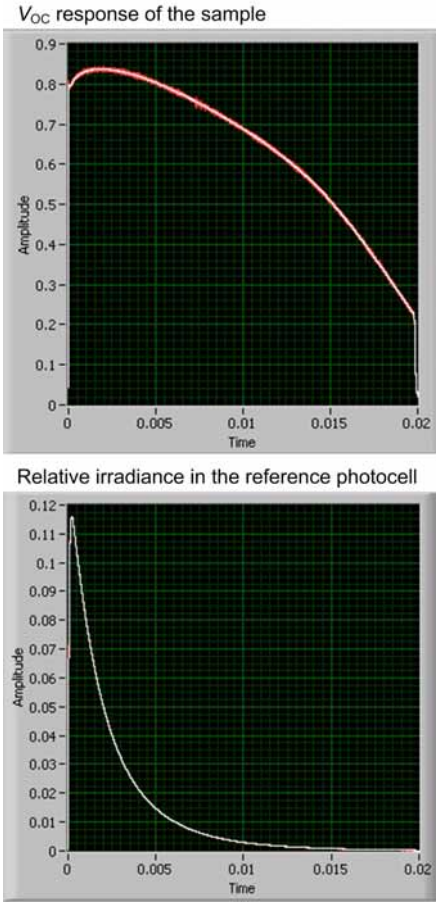

Figure 6.15: Electrical signals simultaneously acquired corresponding to the photocell photogenerated current and the V_{OC} of the sample under test. The second one is delayed with respect to the illumination received from the flash light.

after the flash light has impinged the solar cell surface. We have denoted this effect as "unavoidable" so that it is differentiated from the aforementioned constant heating, because this one cannot be corrected by cooling down the cell prior to the measurement. The reason is that the V_{OC} signature is not constantly altered throughout the flash pulse (i.e. the heating does not cause a constant voltage loss), but it is very much affected in the beginning of the flash pulse and less affected as the flash light vanishes. If this problem occurs, a lower concentration will have to be used, because nothing can be done to properly acquire the device electrical characteristic under such high irradiance.

6.4 Summary

In this chapter, an analysis of a concentrated light I-V characterization set-up has been carried out, including the classification of the different type of concentrated light systems. The more precise case of an IBSC ad-hoc system has been exposed, in which the specific

treatment of some of the properties is required (e.g. accurate temperature control, very high irradiances, etc.). The insights of the I_{L}-V_{OC} measurement have been exposed. The novel low temperature concentrated light technique (that uses a cryostat combined with the conventional concentrated-light I-V characterization system) is also presented as an upgrade of the characterization system developed during this Thesis work.

Chapter 7

Conclusions and recommendations for future research

The following conclusions can be extracted from this Thesis:

- It was predicted that the increased recombination and the associated strong reduction of the device V_{OC} observed in the IBSC operating at 1 sun could be counteracted by the use of concentrated illumination. This theory has been verified experimentally by means of characterization at low temperature, which is necessary to slow down the fast IB-CB thermalization rate that takes place in InAs/GaAs QD-IBSCs at room temperature.

- Several QD-IBSC technologies have been characterized leading to important verifications regarding the IBSC operation principle known as "voltage preservation":

  - InAs/GaAs QD-IBSCs with thick spacers fabricated at the University of Glasgow have shown a V_{OC} $\sim$1.5 V that corresponds to a QFL separation that is very close to E_G/q at T=20 K and that largely exceeds the photon energy absorption threshold.

  - InAs/GaAs QD-IBSCs with thin spacers also show complete voltage recovery although the progression of its V_{OC} under low temperature and concentrated light is different from the QD sample with thick spacers.

  - InAs/GaAs QD-IBSC strain-balanced with N and fabricated at RCAST at the University of Tokyo experience a limited voltage recovery probably due to the lowering of the energy of the CB, which is related to the BAC effect produced by the dilute nitride alloy of the barrier material.

  - InAs/GaAs QD-IBSC strain-balanced with GaP and fabricated at the Rochester Institute of Technology show an almost complete voltage recovery, thus making the GaP an appropriate strain balance material from the point of view of the preservation of the voltage.

- Other characterization techniques also carried out thanks to the acquisition of J_{L}-V_{OC} curves under concentrated light and low temperature have been presented in this Thesis:

  - Determination of the material bandgap by means of electrical characterization.
  - Fitting of multiple-level IBSCs for the determination of the different components of the recombination in an IBSC.

- Several bulk-IBSC technologies have also been measured with the low-temperature concentrated light technique:

  - The $CuInS_2$:Ti and $CuGaS_2$:Fe thin-film cells studied in this Thesis do not fulfill the voltage preservation principle, likely because their IB material was not isolated from the contacts and also because the band alignment of the heterostructure limited the maximum effective bandgap.
  - Si:Ti HIT IBSCs show a noticeable increase of the V_{OC} from 387 mV at room temperature to 540 mV at T=20 K at maximum concentration, although this voltage remains far from the energy (divided by q) of the absorption threshold of approximately 730 meV at room temperature.
  - $In_{0.21}Ga_{0.79}N$:Mn IBSCs have been fabricated with a Mn concentration of approximately 1%. They have been subjected to concentrated light J_{SC}-V_{OC} characterization under low temperature, obtaining a maximum V_{OC} of 386 mV for T=20 K. This value, although largely improved with respect to the 150 mV measured at room temperature, is still very far from the absorption threshold of approximately 1 eV. The reason may be likely related to the fact that the heterojunction band alignment between the GaAs rear emitter and the $In_{0.21}Ga_{0.79}N$:Mn i-region or the GaN front emitter creates such discontinuity that prevents further splitting of the QFLs.
  - GaAs:Ti IBSCs have also been fabricated. The SIMS signature shows an incorporation of Ti above 10^{20} atoms/cm^3 and the TEM characterization indicates the absence of structural defects. External QE measurements show subbandgap photoresponse, although the reference cell (without Ti) also presents this type of absorption. The As antisites very likely produced during the low

temperature growth and not the Ti of the IB region may be responsible for this sub-bandgap response. The initially degraded V_{OC} at 1 sun and room temperature (136 mV) increases to 690 mV under the operation under concentrated light and it suffers a dramatic recovery at low temperature, reaching 1,361 mV, which is above the absorption threshold and actually almost as large as the host material bandgap divided by q.

  - GaAs:Fe IBSCs have also been implemented. They surprisingly obtained larger V_{OC} than their reference counterparts under concentrated light and room temperature, although the low temperature response was clearly favorable to the GaAs benchmark. The maximum V_{OC} obtained by the GaAs:Fe cell does not surpass its absorption threshold.

- A new characterization technique has been developed that brings together the measurement of solar cells under concentrated light and low temperature.

  - The low temperature concentrated light characterization technique is a powerful tool for the verification of the "voltage preservation" principle in IBSCs.
  - The measurement of concentrated light J_L-V_{OC} curves under low temperature allows to deepen on the study of the recombination of a solar cell, which is specially useful for the analysis of potential IBSC candidates.
  - Several problems, such as the different degree in the fulfillment of the superposition principle, the desynchronization between illumination and V_{OC} produced by the large capacitive effects or the unavoidable heating of some of the cells subjected to very high concentrations, have been identified and described regarding the low temperature concentrated light J_L-V_{OC} characterization of different IBSC technologies.

- A theoretical model capable of a fast analysis of III-V compound semiconductors has been developed in order to predict their suitability as QD systems for an IBSC. It consists of a calculation method based on three main steps:

  - 1) computing the band alignment of the heterojunction formed by the barrier and QD material and also computing some important parameters from the alloy such as the effective mass.
  - 2) determining the confined states of the QD in order to calculate the effective bandgap distribution so the three possible transitions can be calculated.
  - 3) determining the efficiency limit in the framework of the detailed balance theory to estimate the suitability of the QD system to perform as an IBSC.

- The theoretical model for III-V alloyed material screening for their application to the QD-IBSC has allowed the identification of several candidate materials, such as $InAs/Al_xGa_{1-x}As$, $InAs/Ga_xIn_{1-x}P$, $InAs_{1-x}N_x/GaAs$, $InAs_{1-y}N_y/AlAs_xSb_{1-x}$, $InAs_{1-z}N_z/Al_x[Ga_yIn_{1-y}]_{1-x}P$, $InAs_{1-y}N_y/Ga_xAs_{1-x}P$, type-II VBO compounds and PbSe/ZnTe are identified and their optimum QD sizes are calculated. Limiting efficiencies over 60% are calculated at maximum light concentration.

- Strain-compensated InAs/GaAsN QD-IBSCs have been fabricated, processed and characterized for CPV applications in collaboration with the University of Tokyo, where the processing of concentrator cells has been adapted to concentration, including the development of a model for the design of concentrator of solar cell circular grids.

From these conclusions, the following recommendations are addressed for future work:

- Possible improvements of the concentrated light characterization system:
  - The software could account for a higher degree of automation, e.g. the operation of the source-meter could be included in the program, which so far is manually performed.
  - Enhancement of the maximum concentration factor reached by the system. This could be implemented by means of different strategies: improving the flash tube which is related to a higher power or/and to a flash tube accounting for an internal optics that increases the degree of collimation of the light beam; improving the concentrator lens (e.g. larger transmitivity); or even including an optical accessory to the flash strobe, so that the light is redirected and homogenized into the spot that is then focused on the entrance of the concentrating lens.
  - A spectrum analyzer and a set of filters could also be included to track and correct the spectrum of the light (with respect to the standard AM1.5D).

- Development of high density InAs/AlGaAs QD-IBSCs grown on high index substrates for the increase of the sub-bandgap photon absorption and the fulfillment of the operation principle related to the current at room temperature. The increase of the photon absorption should also be possible by means of the application of light trapping techniques related to the use of diffraction grids or/and the introduction of metal nanoparticles.

- Fabrication of QD-IBSCs with type-II VBO for the inhibition of the Auger interband relaxation by means of the extension of the wavefunction of the holes in

the VB. This type-II QD structures have been suggested by the implementation of $InAs/Al_xGa_{1-x}As_ySb_{1-y}$ QDs.

- Improvement of the GaAs:X bulk-based IBSC by means of the more rigorous control over the growth at low temperature (with the Ga:As atomic ratio close to 1 and with intentional n-doping) to produce good quality material. Besides, the so-called Migrated Enhanced Epitaxy [Horikoshi et al., 1986, Horikoshi et al., 1987] technique could be used to better adjust the low temperature Ga:As atomic ratio. New X transition metals could also be studied as candidate materils to be incorporated in the GaAs matrix.

Appendix A

The integrated EL experiment

The integrated (non-spectral) EL technique applied to the determination of the r_S component limiting the performance of a concentrator solar cell [Reyna et al., 1998] will be reviewed in this appendix. This technique is based on the study of the so-called "crowding effect" which is related to the non-uniform radiative recombination throughout the solar cell surface originated by the voltage drop produced by the lateral flow of current in the emitter.

The most typical EL characterization applied to the semiconductor field consists of measuring the intensity of the luminescent response for each of the emitted wavelengths along the scanned light range. In this regard, the EL signature shows a number of picks that correspond to the photons emitted due to radiative recombination processes between the different electronic transitions involved in the energy band structure of the device. Nevertheless, in the present case, our EL set-up does not perform such spectral measurement but what we will refer to as integrated EL, meaning that the whole spectral range of the emitted light is simultaneously received and measured by the detector. As a result, the detector electrical response will be proportional to the ensemble of the photons emitted by the electrically excited sample that escape from its front surface.

This experiment, the characterization of the crowding effect, is aimed to verify whether the r_S is dominated by the lateral flow of current, i.e. r_E (which is usually the largest component) and, in case it is, at which equivalent concentration it limits the performance of the solar cell. The physics behind the crowding effect and its corresponding equations are thoroughly explained in Ref. [Reyna et al., 1998].

The hardware of the set-up is sketched in Fig. A.1, together with a graphical explanation of the crowding effect. In Fig. A.1(a) a small bias current (I_{bias}) is applied to the solar cell under test. This current polarizes the sample and forces the QFL to split over the active volume of the device. As a result a radiative recombination is induced in a

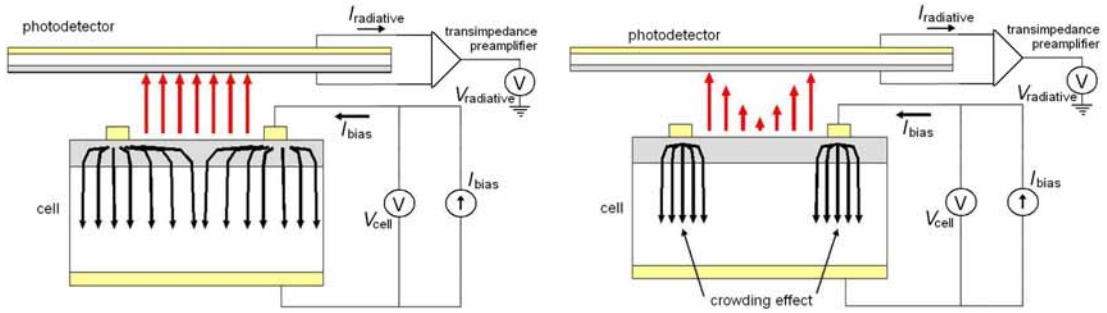

Figure A.1: Sketch of the integrated EL experiment where the physical mechanism known as crowding effect is also depicted: (a) a small I_{bias} is applied to the cell and the radiative recombination escaping from the cell produces $I_{\text{radiative}}$ which is pre-amplified and measured. (b) The crowding effect is depicted in this sketch. It occurs when I_{bias} is large enough so that the recombination current is preferentially redistributed in the vicinity of the metal contacts.

relatively homogeneous way throughout the active area and a maximized portion of this recombination escapes from the front surface of the cell (qualitatively represented with vertical red arrows in the figure). This light, which at this stage is proportional to the radiative recombination, is received by a large area photodetector located on top of the sample, converting it to an electrical current ($I_{\text{radiative}}$). The problem is that we cannot accurately measure small currents and hence we need to use a low-noise current preamplifier (with a transimpedance transference function, as shown in the figure). Our DAQ system, which exclusively reads voltage signals will acquire $V_{\text{radiative}}$ as the preamplifier output. $I_{\text{radiative}}$ will be then obtained as $V_{\text{radiative}}\, A_{\text{trans}}$, where A_{trans} is the preamplifier gain, expressed in A/V.

The crowding effect is represented in Fig. A.1(b) and appears when I_{bias} is large enough so that the voltage drop produced by r_{E} causes the redistribution of the recombination current preferentially in the vicinity of the metal contacts. This reduces the lateral trajectory of the electrons in the emitter layer (and the corresponding voltage drop). Nevertheless, a smaller portion of the radiative recombination escapes from the cell, since it is majoritary located in the surroundings of the metal contact, including the region under the contacts, which reflects the photons from the radiative recombination. It is also true that by means of the photon recycling mechanism, this reflected photons can be reabsorbed again by the semiconductor and eventually re-emitted, but this re-emission can be also reflected again, in summary, the probability of non-radiative recombination increases.

The crowding effect can be visually observed when an EL experiment is performed on a solar cell fabricated with a semiconductor which (preferentially direct) bandgap energy

is in the range of the visible spectral range or when a digital camera with a small-bandgap detector semiconductor technology is used. If the I_{bias} is large enough, a more intense luminescence will be noticeable in the semiconductor regions close to the fingers and specially next to the bus-bar of the cell. This effect will be more pronounced as I_{bias} increases and should be negligible for an I_{bias} within an injection regime equivalent to the J_{L} produced at any concentration lower than that for which the solar cell has been fabricated. For example, a 1,000 suns concentrator solar cell which I_{L}(1sun)=1 mA should not show crowding effect for I_{L} <1 A. The integrated EL experiment is intended to quantitatively verify whether the r_{E} is corresponds to that theoretically calculated for maximum concentration.

A software is implemented by Labview in order to control a 4-quadrant source-meter which is activated in the current-source mode only a few milliseconds before the electrical response of the photodetector is measured. A very small current pulse is used so that the sample is not heated by the forward bias imposed by the source. Two signals are acquired with the same kind of DAQ unit used for the concentration set-up (see chapter 6) and recorded as measurement outputs: on the one hand the output voltage of the cell, which together with the I_{bias} signal, represents the dark I-V curve of the cell and on the other hand the current generated by the photodetector, $I_{\text{radiative}}$, which is proportional to the radiative recombination of the solar cell under test.

The result of this experiment is presented in Fig. A.2, where the $I_{\text{radiative}}$ signal obtained from a GaAs solar cell measured at room temperature is represented with respect to the I_{bias} signal. A sub-linear dependence of the $I_{\text{radiative}}$ signal with respect to the I_{bias} would imply that the crowding effect is taking place and less light is coming out of the front surface of the cell because a significant part of the carriers recombine under the metallization and hence cannot escape from the cell. But in our case the curve obtained can be fitted by a straight (solid dark) line, which indicates that the r_{E} is not limiting the solar cell performance in the whole range in which I_{bias} is applied, and this reaches a value as high as the I_{L} that corresponds to 1,000 suns: $I_{\text{bias}} \approx I_{\text{L}}(X{=}1{,}000)$.

Fig. A.3(a) shows the dark J-V curve together with the $J_{\text{radiative}}$-V curve (plotted with different colors for each of the I_{bias} ranges) obtained from the integrated EL experiment. A factor 1,600 is found to rule dependence between the radiative components of the two curves as it can be deduced from the fitting shown in Fig. A.3(b). Nevertheless, this fitting value is not directly proportional to the relationship between radiative and non-radiative recombination, because the following losses have to be taken into account: 1) Most photons originated by radiative recombination are directed toward the rear side of the cell because of the difference in the refraction index, n, between the cell and the air. Actually a factor

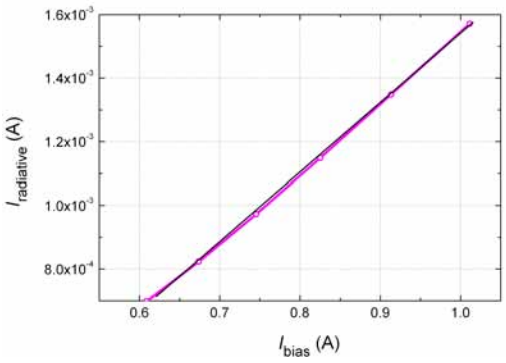

Figure A.2: Integrated EL experiment verifying that the solar cell is not limited by its r_{E} at any concentration below the maximum one for which it has been designed. I_{bias} is plotted with respect to $I_{\mathrm{radiative}}$, showing a linear dependency throughout the whole range.

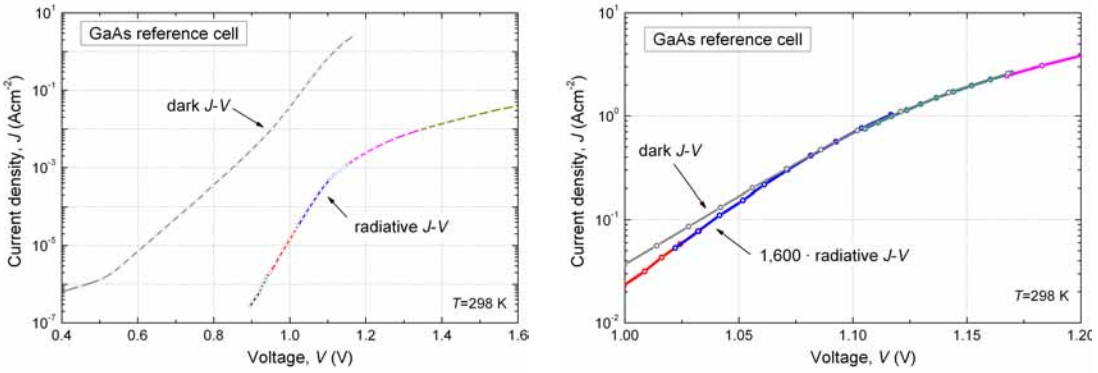

(a) (b)

Figure A.3: (a) Dark J-V of a GaAs solar cell and $J_{\mathrm{radiative}}$-V curve obtained from the integrated EL experiment. (b) Fitting of the radiative part of the dark curve with respect to the radiative J-V obtained from the EL experiment, where a factor 1,600 is found to exist between the two curves.

of approximately 13, obtained as n^2_{GaAs}+1, where n_{GaAs} ≈3.5 is the refractive index of the GaAs, has to be applied to the losses because of the higher n of the GaAs with respect to the air. 2) A large photodetector placed very close to the front surface of the solar cell will collect most of the light exiting the device, but a loss due to the non collection of part of these photons also has to be assumed. 3) The front grid metallization corresponding to both the solar cell and the photodetector have to be accounted as another loss. 4) The photodetector responsivity corresponding to the radiative recombination photon emission energy has to be also considered.

Appendix B

Modeling of concentrator solar cell grids

This Thesis is mainly focused on the application of concentrated light characterization techniques to the research on IBSCs and hence, it tries to get a deeper insight into the performance of these devices under concentrated light. Such conditions allow high rates of photogenerated carriers, which should be collected without a significant voltage drop. For such task, the so-called concentrator solar cells must be implemented, which implies understanding and tunning the different components of the r_S of a solar cell. This can be done by means of device modeling, which allows the design of front metal grids adapted to high concentrations.

In this appendix, several aspects concerning the processing of concentrator solar cells will be studied. A theoretical model for the optimization of the circular front grid of a concentrator solar cell will be presented, including the study of the different components of the r_S: the front metal grids, the metal-semiconductor interfaces and the different semiconductor layers of the layer structure (emitter, base, etc.). This will allow, not only the optimization of the design of the front grid metallization, but also the understanding of the impact of other design features such as layer thicknesses and doping levels (n_n/p_p for donors/acceptors in an n-type/ p-type semiconductor) on the total r_S of the cell and consequently. All these features influence the maximum concentration factor (X) at which the cell is adapted.

B.1 Distributed vs lumped parameter in the modeling of r_S

Two types of modeling can be distinguished: one based on distributed parameters [Galiana et al., 2005] and capable of simulating the solar cell electrical performance and another one

conceived from lumped parameters [Araújo et al., 1986]. On the one hand, the first one requires a quite thorough analysis of the device, basically using finite element calculations, solving the equations corresponding to the electrical performance within each element and relating their behavior to the operating conditions of the rest of the adjacent elements (i.e. by means of a boundary or continuity conditions). In this case, besides the study of the r_S produced by the opposition of the material to the current flow, other effects are studied in parallel, such as the I-V characteristic (locally, within each element, as well as globally, as a two-terminal device), which in turn depends upon the type of semiconductor. This type of model can then be used to analyze the solar cell performance under dark conditions as well as under illumination conditions. As a matter of fact, the effect of different illumination conditions can also be studied, such as variations in the concentration level or in the sunlight spectrum, as well as light spot inhomogeneities. Even the solar cell operation under different polarization conditions can be studied when using the distributed parameter model. On the other hand, the lumped parameter model, which consists of grouping the different components of the r_S by classifying them with respect to their different origin (the different parts of the solar cell where they come from), can be exclusively focused on the study of the r_S without the need for such number of variables. A few simplified solar cell working conditions have to be defined, e.g. determination of the total photogenerated current, assumption of a homogeneously produced photogenerated current throughout the device, a preferential direction and sense of the current flow at any point of the device, etc.

The first of the methods is more accurate. It is also more powerful in the sense that it is more versatile with respect to the conditions of operation of the solar cell. But it is obviously more complicated to implement and it is very sensitive and dependent of the nature and characteristics of the different semiconductor layers. However, the second method, although more simplified, may result more suitable for the design of a concentrator IBSC front grid pattern. The reason for such statement is that there is still a large variability about the performance of the IB materials that already exist and their precise electrical performance cannot be easily implemented by the distributed parameter model. However, the lumped parameter model allows a rough optimization of the design by means of the estimation of the mobilities calculated from the doping level concentrations and the data of the metallization, which under this approach basically depends upon the front grid design.

B.2 The power dissipation model

There are also two kind of lumped models depending on the way r_S is calculated: the voltage drop model [Araújo et al., 1986] and the power dissipation model [Luque, 1989]. Perhaps, the easiest of them in order to simulate the r_S under the lumped parameter realm is the power dissipation model, since it allows the easy calculation of grids of relatively complex structures, where the voltage loss model is difficult to apply.

The r_S modeling based on power dissipation consists of calculating the resistivity (ρ) and guessing the current flow throughout the whole solar cell. Different expressions for these magnitudes will have to be obtained for the different parts of the solar cell where either ρ has a different nature and the current density, j, flows in a different direction. The sum of these components results in the total r_S of the device, which expression is presented in equation B.1, where r_B corresponds to the base layer component, r_{subs} to the substrate layer, r_E to the emitter, r_M to the metallization and $r_{m\text{-}s}$ corresponds to the metal-semiconductor interface.

$$r_S = r_B + r_{subs} + r_E + r_{m\text{-}s} + r_M \tag{B.1}$$

Each of these r_S component are sketched in Fig. B.1, where a cross section of a portion of a solar cell is depicted, also showing the different device layers and their representative dimensions regarding the calculation of their r_S values.

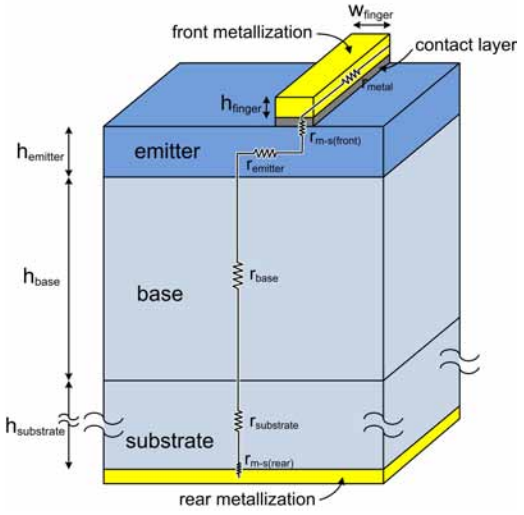

Figure B.1: Sketch of the different components of the r_S of a solar cell considered in our lumped parameter model.

In our model, r_B and r_{subs} are originated by the flow of current in the vertical direction. These components are hardly ever limiting the r_S of GaAs-based solar cells, because

the equivalent resistance section (i.e. the solar cell surface) is very large, the equivalent resistance length (the layer thickness) is short (with respect to the section dimension), at least in the case of r_{B}, since GaAs cells usually account for a few μm thick base and/or the doping concentration is very high (in the case of most of the commercial GaAs substrates used). A simplification in the modeling of the r_{B} has been made by not taking into account the contribution of the BSF layer. The reason is that the IBSC layer structure design made from a new IB material is usually oversimplified and does not include this layer. Besides, the electrons also flow vertically within the highly doped BSF layer and its contribution to the total r_{S} should be very small.

The r_{E} component is usually the one limiting the performance of the device, since it is produced by a lateral flow of current through the emitter layer. This means that the electron flow that is received from the base in the vertical direction, flows then horizontally throughout the emitter layer, until it reaches the metal-semiconductor interface. The emitter thickness is usually relatively thin (in the order of several hundreds of nanometers) and this causes the r_{E} equivalent section to be small. Therefore, if the metal fingers of the front grid metallization are not close enough to each other, the emitter equivalent length "seen" by the carriers when they are photogenerated approximately in the center of the inter-finger region makes r_{E} to be large. As a matter of fact, one of the figures of merit of the front grid pattern design is the gap between adjacent fingers throughout the solar cell surface. But a trade-off exists between the number of fingers and J_{L}, because a high number of fingers produce a large shadowing factor, f_{s} (defined as the ratio between the area of the front grid metallization and total active area) which reduces J_{L}. Consequently, the number of fingers cannot be arbitrarily increased and they also have to be optimized. In the case where the electrons flow laterally, it has to be recalled that a simplification equivalent to that of the BSF has been made with respect to the window layer.

The $r_{\mathrm{m\text{-}s}}$ should not limit the performance of the solar cell provided that the solar cell processing has been appropriately carried out. It depends on the quality of the metal-semiconductor junction that has to be tunneled by the carriers before reaching the metal contact. Its quality is defined by the specific contact resistance (R_{c}) of each of the metal-semiconductor contacts: the one corresponding to the rear contact, denoted as $R_{\mathrm{c,rear}}$ and the one corresponding to the front contact, $R_{\mathrm{c,front}}$. Both of them will be treated as fixed parameters in our model and their value will be extrapolated from experimental data. The total value of the $r_{\mathrm{m\text{-}s}}$ component is then a function of this R_{c} (in turn dependent from the semiconductor and metallic materials involved, the annealing, etc.) and the metallization area.

r_{M} is also one of the most important components of the r_{S}. It is originated by the current flowing throughout the metallizations, which are reached by the electrons once they have flown through the emitter and the metal-semiconductor interface. Within this power dissipation model, this r_{S} component also depends on the amount of current collected and flowing by each of the front grid stretches. Therefore, the number of fingers in each of the sections in which the front surface is divided will also have to be optimized taking into account the trade-off between r_{S} and the photogenerated current previously discussed. The variables involved in the calculation of r_{M} are in this case: the metal resistivity (ρ_{M}), the metal finger thickness (denoted as h_{f} in Fig. B.1), the metal finger width (w_{f}) and the front grid design. This last feature determines the current flow through each finger and the average length from where the photogenerated carriers reach the fingers until they are collected by the bus-bar (assumed as equipotential in our model).

Each r_{S} component is deduced from the calculation of the power dissipated by the flow of carriers throughout its volume, according to the general equation of the Joule effect:

$$r\,[\Omega\,cm^2] = \frac{P_{\mathrm{diss}}\,[W]}{j^2\,[\frac{A^2}{cm^4}]\cdot S_{\mathrm{cell}}[cm^2]} \tag{B.2}$$

where the resistance r is calculated from the dissipated power, P_{diss} divided by j squared (j being the current density that flows through r) and by the solar cell surface (S_{cell}). The units are included in the equation for the sake of an easier understanding.

P_{diss} is calculated from the volume integral using cylindrical coordinates

$$P_{\mathrm{diss}} = \iiint_{\mathrm{V}} |j\,(r,\varphi,z)|^2\;\rho\,dV \tag{B.3}$$

where $j\,(r,\varphi,z)$ is the current density expressed in cylindrical coordinates (because, as it will be explained later, the front grid designs proposed in this Thesis will have circular symmetry), V is the volume through which the current flows and ρ is the resistivity of the metal (in the case of r_{M}) or the semiconductor (in the case of r_{B}, r_{subs} and r_{E}). ρ will be considered either as a fixed parameter (first of the cases, e.g. gold metallizations) or a variable calculated from the doping concentration and the mobilities (second of the cases, where semiconductor resistivities apply), according to equation B.4

$$\rho_{\mathrm{n}} = \frac{1}{q\,N\,\mu} \tag{B.4}$$

where q is the electron charge, N is the carrier concentration and μ is the carrier mobility (as a majority).

B.3 Features of the design

The optimization of a concentrator solar cell front grid metallization can be an endless task because of the very large number of variables and therefore a number of features have to be preset:

- **The shape of the metallization pattern**. It will be circular since the first approximation for a point-focus CPV system is usually characterized by a circular symmetry. The different effect on the r_S of these two different shapes are analyzed in Ref. [Algora and Díaz, 2000].

- **The size of the front grid design**. Values between 1 mm^2 and 1 cm^2 are common in commercial concentrator solar cells. In our case, we will focus on 1 mm radius front grids (3.14 mm^2), although other designs with 0.5 mm and 2 mm radii will also be considered.

- **The distribution of fingers within the metallization**. In our case, a circular symmetry pattern will be used. The separation between fingers has to remain relatively alike throughout the device surface, the number of fingers has to increase in the radial direction. Otherwise, if the number of fingers remained constant throughout the structure, either too much metal would accumulate in the reduced area close to the center of the circle and/or the finger separation would be too large in the regions close to the bus-bar. Hence, the area enclosed by the circular bus-bar is divided in concentric circular annuli. Each of these annuli are separated by metal rings from which the number of radial fingers increases by a factor of two.

- **Unicity of the final design**. For the sake of simplicity, only one front grid design has to be finally implemented for the processing of concentrator solar cells at IES-UPM and therefore, a set of parameters will be defined, according to the typical values of the standard GaAs solar cell. These parameters are basically the thicknesses and doping concentrations of the different layers in the structure.

- **Metal rings separating each annuli**. The suitability of the use of metal rings that separate the different annuli and connect the fingers that arise from the inner ring (that circumscribes the inner circle, which has no fingers) to the bus-bar through the outer rings (as depicted in Fig. B.2) has also been studied. It confirms the results from Ref. [Cánovas et al., 2006], where a model is developed for the calculation of the r_S applied to concentrator solar cell front grids. The conclusion of this work is that the use of metal rings is important and reduce the r_S that can be achieved for

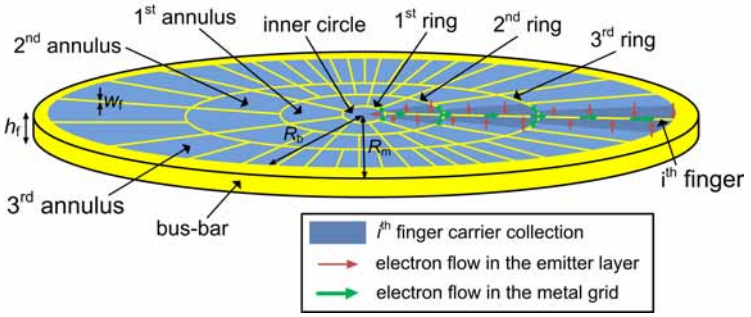

Figure B.2: Sketch of an example of the front grid design used for optimization. The different annuli and their respective rings are indicated. The carrier collection area corresponding to the generic i^{th} finger is represented with stripes as an example. The current directions in the emitter and metal regions corresponding to such i^{th} finger are represented with arrows in the striped area.

a given f_{s}. The reason for such reduction is that the current is better distributed throughout the fingers and hence, the P_{diss} by the r_{M} component is reduced. The previous conclusion is a quantitative argument in favor of the inclusion of the metal rings, however qualitative reasons can also be argued: in case of finger breakage (e.g. because of a problem with the lift-off or during the solar cell manipulation) the metal rings can redistribute (among the adjacent fingers) the current that was circulating through it, however, in the fingerless design the broken finger current will have to flow first through the emitter and then through the adjacent fingers before reaching the bus-bar, which will increase both the r_{M} and the r_{E} components and not only r_{M} as in the first case.

In Fig. B.2, R_{b} refers to the radius of the area inside the circular bus-bar and R_{m} is the radius corresponding to the active area of the cell, i.e. to the mesa. The different parts of the active area are also indicated in the figure, e.g. the bus-bar, the fingers, the inner circle (without fingers), the concentric annuli, the metal rings, etc.

B.3.1 Model variables

In principle, many variables can be optimized, but we will reduce them to a small number, provided that the thicknesses and doping concentrations of the different semiconductor layers are fixed and the optimization of most of them (e.g. w_{f} or h_{f}) may result too expensive and difficult to implement in this early stage of the IBSC research.

The semiconductor resistivities calculated from equation B.4 are considered, in principle, as variables, since they are a function of the carrier mobility (μ). The mobility is, in turn, calculated from other variables, such as the temperature (T), the doping concentrations and the compensation rate (c_{r}), this last one defined as the ratio between electron and

hole concentration in an n-type semiconductor or between hole and electron concentration in a p-type semiconductor. The following equations [Walukiewicz et al., 1979] explain how the electron mobility (μ_n is calculated in an n-type semiconductor (i.e. as a majority) in our model

$$\mu_\mathrm{n} = \mu_\mathrm{min}(c_\mathrm{r}) \left(\frac{T}{300}\right)^{-0.57} + \frac{(\mu_\mathrm{max}(c_\mathrm{r}) - \mu_\mathrm{min}(c_\mathrm{r})) \left(\frac{T}{300}\right)^{-2.3}}{\left(1 + \frac{n_\mathrm{n}}{n_\mathrm{ref}(c_\mathrm{r})} \left(\frac{T}{300}\right)^{-2.4}\right)^{\xi(c_\mathrm{r})} \left(\frac{T}{300}\right)^{-0.146}} \tag{B.5}$$

where

$$\mu_\mathrm{min}(c_\mathrm{r}) = -2201\, c_\mathrm{r}^3 + 5362\, c_\mathrm{r}^2 - 5092\, c_\mathrm{r} + 1942 \tag{B.6}$$

$$\mu_\mathrm{max}(c_\mathrm{r}) = -6933\, c_\mathrm{r}^3 + 3581\, c_\mathrm{r}^2 + 76\, c_\mathrm{r} + 9157 \tag{B.7}$$

$$n_\mathrm{ref}(c_\mathrm{r}) = -4.36\,10^{16}\, c_\mathrm{r}^3 + 1.43\,10^{17}\, c_\mathrm{r}^2 - 1.8\,10^{17}\, c_\mathrm{r} + 8.49\,10^{16} \tag{B.8}$$

$$\xi(c_\mathrm{r}) = 0.506\, c_\mathrm{r}^3 - 0.262\, c_\mathrm{r}^2 + 0.132\, c_\mathrm{r} + 0.365 \tag{B.9}$$

In our case, the electron concentration of the n-type substrate layer is $2\,10^{18}$ cm^{-3}, the temperature used for the calculation is T=300 K and the compensation rate c_r=0 because the solar cell is grown in an MBE and this technique allows very accurate doping concentrations with negligible amounts of the complementary doping.

The hole mobility can also be calculated from the interpolation of theoretical data, however, in this case, it is more accurate to extract the data from experimental data. For this reason, Fig. B.3 is plotted from a set of data obtained from the measurement of the hole Hall mobility of a set of Be p-type GaAs growths with different hole concentrations (covering three orders of magnitude, from 10^{16} up to 10^{19} cm^{-3}). The data have been extracted from MBE experiments carried out at the University of Glasgow. The hole Hall mobility (which is similar as a majority as well as a minority) is plotted with respect to the hole concentration, in a semilogarithmic scale.

In our case, the hole concentration of the p-type layer is $2\,10^{18}$ cm^{-3}, which corresponds to 140.7 cm^2 V^{-1} s^{-1}.

The variables to be optimized are interrelated: the f_s, the number of fingers, the number of annuli and the radii defining the size of each annulus (which defines the length of the fingers inside that annulus).

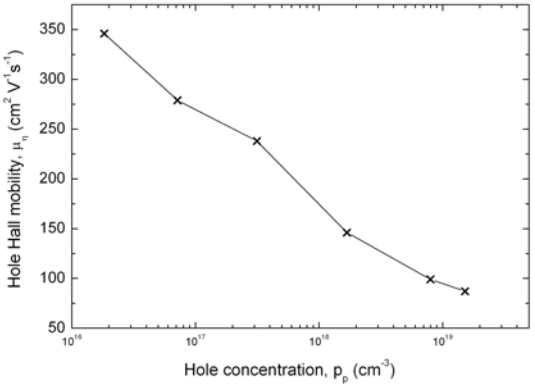

Figure B.3: Experimental data of the hole Hall mobility obtained from a set of Be p-type GaAs growths carried out by MBE at the University of Glasgow.

B.3.2 Model parameters

Regarding the metallization, the thinner the w_f the better, although a trade-off exists between the width of the metal fingers and the processing yield. This means that an arbitrarily low w_f cannot be chosen for practical reasons related to the metal evaporation process i.e. the photolithography and the lift-off processes are more difficult and the fingers can break and/or the resistive coating can be inappropriately removed. A similar reasoning can be followed regarding h_f: the thicker the better, although a special technique (such as electroplating) is usually required for metal thickness depositions higher than 1 μm (the evaporation technique is too inefficient for the deposition of such thicknesses). The implementation of the electroplating technique adds another degree of complexity to the solar cell processing.

Table B.1 presents the fixed parameters used in the optimization of our front grid design. The width of the different metal rings is the same as that of the metal fingers (w_f). The gold deposited in the front grid is porous and its resistivity is assumed to be five times higher than the resistivity of pure gold found in the literature, $\rho_{\mathrm{Au(electrolytic)}}$=2.22 10^6 Ωcm.

The fact that the doping concentrations of the different semiconductor layers are fixed imposes fixed mobilities both for electrons as holes, which is why these data have been included in the parameter list.

B.3.3 The algorithm

In this subsection, the algorithm leading to the calculation of the different components of the r_S will be presented.

Table B.1: Fixed parameters used in the front grid design optimization algorithm

Parameter	Symbol	Value
Temperature	T	300 K
Radius to the bus	R_{b}	1,000 μm
Radius to the mesa	R_{m}	1,145 μm
Finger width*	w_{f}	4 μm
Finger thickness*	h_{f}	4 μm
Substrate concentration	n_{S}	2 10^{18} cm^{-3}
Base concentration	n_{B}	2 10^{17} cm^{-3}
Emitter concentration	p_{E}	2 10^{18} cm^{-3}
Substrate thickness	h_{S}	250 μm
Base thickness	h_{B}	3.1 μm
Emitter thickness	h_{E}	0.9 μm
Specific contact resistance	$R_{\mathrm{c,front}}$, $R_{\mathrm{c,rear}}$	2 10^{-5} Ωcm^2
Metal resistivity	ρ_{m}	11.1 10^6 Ωcm**
Compensation rate	c_{r}	0
Hole mobility in the emitter	μ_{E}	140.7 cm^2 V^{-1} s^{-1}
Electron mobility in the base	μ_{B}	6579.94 cm^2 V^{-1} s^{-1}
Electron mobility in the substrate	μ_{S}	4184.96 cm^2 V^{-1} s^{-1}

*Also applicable to the metal rings
**Chosen as $5{\cdot}\rho_{\mathrm{Au(electrolytic)}}$

- **Power dissipated by the base and the substrate**. These components are calculated applying equation B.3 on the total volume of the base and the substrate, for which the respective resistivities (ρ_{B} and ρ_{S}) are previously calculated using equation B.4 and μ_{B} and μ_{S} (see Table B.1). The volume integral in the base layer is

$$P_{\mathrm{B}} = \int_0^{\mathrm{R_m}} \int_0^{2\Pi} \int_0^{\mathrm{h_B}} |j_{\mathrm{z}}|^2 \; r \, dr \, d\varphi \, dz = j_{\mathrm{z}}^2 \, \frac{1}{q \, n_{\mathrm{B}} \, \mu_{\mathrm{B}}} \, h_{\mathrm{B}} \, \Pi \, R_{\mathrm{m}}^2 \tag{B.10}$$

  where j_{z} is the current photogenerated per unit volume flowing in the vertical direction. A similar result is produced for the substrate layer

$$P_{\mathrm{S}} = \int_0^{\mathrm{R_m}} \int_0^{2\Pi} \int_0^{\mathrm{h_S}} |j_{\mathrm{z}}|^2 \; r \, dr \, d\varphi \, dz = j_{\mathrm{z}}^2 \, \frac{1}{q \, n_{\mathrm{S}} \, \mu_{\mathrm{S}}} \, h_{\mathrm{S}} \, \Pi \, R_{\mathrm{m}}^2 \tag{B.11}$$

- **Power dissipated by the emitter**. The emitter region collects current component that flows in the vertical direction (j_{z}), which, once in the emitter, flows laterally

until it reaches the metal contacts. Two regions can be distinguished. On the one hand, a component corresponding to the inner circle, where the current flows in the radial direction (i.e. perpendicular to the 1st ring) and is expressed as

$$j_{\mathrm{E,in}}(r < R_1) = \frac{j_{\mathrm{z}}\, r}{2\, h_{\mathrm{E}}} \tag{B.12}$$

R_1 being the radius of the 1st ring (which encloses the inner circle, as depicted in Fig. B.2). And on the other hand, one corresponding to the different annuli, where the current flows in the angular direction (i.e. parallel to the rings and perpendicular to the fingers) in the way it is represented in Fig. B.2. This approximation slightly overestimates the r_{E} component because the carriers photogenerated close to the metal ring would find a less resistive path if they flew in the radial direction towards the ring. Nevertheless, the larger the relation of the distance between adjacent rings with respect to the distance between adjacent fingers, the more accurate the approximation. The current density expression of the annulus components is

$$j_{\mathrm{E,out}}(r > R_1) = \frac{j_{\mathrm{z}}\, r\, \varphi}{h_{\mathrm{E}}} \tag{B.13}$$

The current flowing throughout the inner circle dissipates a power according to the following equation

$$P_{\mathrm{E,in}} = \int_0^{\mathrm{R_1}} \int_0^{2\Pi} \int_0^{\mathrm{h_E}} |j_{\mathrm{E,in}}|^2\, \rho_{\mathrm{E}}\, r\, dr\, d\varphi\, dz = \frac{\Pi\, R_1^4 j_{\mathrm{z}}^2}{8\, q\, h_{\mathrm{E}}\, p_{\mathrm{E}}\, \mu_{\mathrm{E}}} \tag{B.14}$$

The reason for choosing R_1 as the integration limit in the r dimension instead of $R_1 - w_{\mathrm{f}}/2$ (which actually defines the vertical plane of the metal-semiconductor interface) is that the carrier trajectory of the current flowing through the emitter is uncertain. Actually, not all the carriers enter the metallization at that plane, but many of them enter the metal throughout the whole ring width. For this reason, R_1, i.e. the vertical plane at the center of the ring, has been selected as an average value for the end of the emitter flow.

The power dissipated by the emitter current components corresponding to each of the annuli can be expressed by the following equation

$$P^{\mathrm{i}}_{\mathrm{E,ext}} = 2\, f_{\mathrm{i}} \int_{\mathrm{R_i+w_f/2}}^{\mathrm{R_{i+1}\text{-}w_f/2}} \int_{0}^{\Pi/\mathrm{f_i}} \int_{0}^{\mathrm{h_E}} |j_{\mathrm{E,out}}|^2\, \rho_{\mathrm{E}}\, r\, dr\, d\varphi\, dz = \frac{\Pi^3\, j_{\mathrm{z}}^2}{6\, f_{\mathrm{i}}^2\, q\, h_{\mathrm{E}}\, p_{\mathrm{E}}\, \mu_{\mathrm{E}}} \left[(R_{\mathrm{i+1}} - w_{\mathrm{f}}/2)^4 - (R_{\mathrm{i}} + w_{\mathrm{f}}/2)^4\right] \tag{B.15}$$

where the subindex i of $P^{\mathrm{i}}_{\mathrm{E,ext}}$ indicates the i^{th} annulus from which the P_{diss} is calculated. f_{i} is the number of fingers of each annulus and R_{i} and $R_{\mathrm{i+1}}$ are the smaller and the larger rings delimiting the annulus. In the case of the outermost annulus, $R_{\mathrm{i+1}}$=R_{b}. Finally, if the total number of rings (and annuli) is denoted as N_{rings}, the total power dissipated by the emitter layer will be the sum of all the emitter components

$$P_{\mathrm{E}} = P_{\mathrm{E,in}} + \sum_{\mathrm{i=1}}^{\mathrm{N_{rings}}} P^{\mathrm{i}}_{\mathrm{E,ext}} \tag{B.16}$$

- **Power dissipated by the metal grid**. The calculation of this component represents the most complex part of the r_{S} analysis. A circuital analysis of the front grid has to be carrier out, so that the current flowing at each single section of the front grid can be deduced. For that purpose, the metal front grid is regarded as an electrical circuit, as the one shown in the example of Fig. B.4. The circuit represents a quadrant of a simplified front grid, in which each finger and ring section is represented by a resistance: R_{Ri} for each section of the i^{th} ring defined by two adjacent fingers arising from it and R_{Fi} for each finger section contained between two consecutive rings, i.e. within the i^{th} annulus. The value of these resistances, as well as the value of some of the current components (e.g. I_0 and I_1) do not depend on other features from the design, because the current flows from the inner to the outer part of the cell. Hence, they can be directly calculated so that the circuit can be solved in order to infer the rest of the I_{i} components and eventually calculate the power dissipated by each of them. The circuit in Fig. B.4 is intended as an example that could be extrapolated to more complex designs (i.e. with more annuli and more fingers per annulus).

  It must be noticed that no current coming from the emitter is collected by the rings because, as explained before, the emitter current component in the radial direction has been neglected in our model. As a consequence, only one type of current component flows through each ring section (R_{Ri}): the one coming from the inner metal fingers connected to each ring section (except for the 1^{st} ring, which

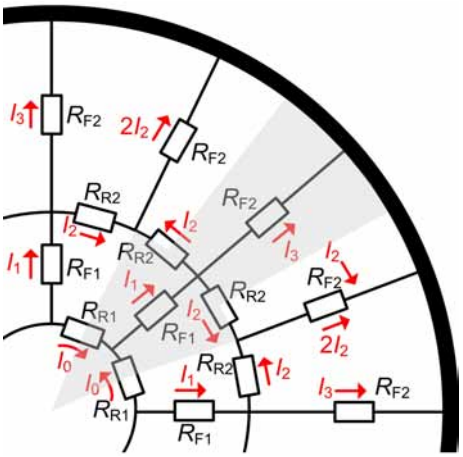

Figure B.4: Example of the metal front grid of the concentrator solar cell represented as an electrical circuit.

encloses no fingers and collects the current from the inner circle). Conversely, two current components are added to each finger section (R_{Fi}): 1) the one coming from the metal ring (and from the same finger, in case it comes from an inner annulus) and 2) the one coming from the emitter (collected throughout the finger). Therefore, the second of these components also has to be calculated prior to the calculation of the power dissipated by the metal grid fingers.

First of all, the value of each resistance appearing in the circuit has to be calculated using the conventional procedure for metallic resistances (by means of its resistivity, section and length in each case):

$$R_{\mathrm{Ri}} = \frac{1}{f_{\mathrm{i}}}\,\rho_{\mathrm{m}}\,\frac{2\,\Pi\,R_{\mathrm{i}}}{w_{\mathrm{f}}\,h_{\mathrm{f}}} \tag{B.17}$$

$$R_{\mathrm{Fi}} = \rho_{\mathrm{m}}\,\frac{R_{\mathrm{i+1}} - R_{\mathrm{i}}}{w_{\mathrm{f}}\,h_{\mathrm{f}}} \tag{B.18}$$

In order to solve the very simple circuit of Fig. B.4, only two equations are required from the circuit analysis. The first of them is derived from Kirchhoff's nodal rule

$$I_1 = 2\,I_2 + I_3 \tag{B.19}$$

and the other one is derived from Kirchhoff's mesh rule

$$I_2\,R_{\mathrm{R2}} + 2\,I_2\,R_{\mathrm{F2}} - I_3\,R_{\mathrm{F2}} = 0 \tag{B.20}$$

I_1 can be calculated from the current component coming from the emitter and collected throughout the finger, plus the current coming from the first metal ring and labeled I_0

$$I_1 = 2\int_{\mathrm{R_1+w_f/2}}^{\mathrm{R_2\text{-}w_f/2}}\int_{\mathrm{w_f/R_2}}^{\mathrm{\Pi/f_1}} j_z\,r\,dr\,d\varphi + I_0 \tag{B.21}$$

and

$$I_0 = 2\int_{0}^{\mathrm{R_1\text{-}w_f/2}}\int_{0}^{\mathrm{\Pi/f_1}} j_z\,r\,dr\,d\varphi \tag{B.22}$$

The integration limit in the radial dimension is again extended to $R_{\mathrm{i}} \pm w_{\mathrm{f}}/2$ because no current is extracted from the metal region corresponding to the ring. The same argument can be used in the case of the φ dimension, where the integration limit is restricted to $w_{\mathrm{f}}/R_{\mathrm{i+1}}$ so that the area corresponding to the metal finger is not considered for the calculation of the current collected from the emitter. In this case, $w_{\mathrm{f}}/R_{\mathrm{i+1}}$ is an approximation of the angle expressed as the sine of the angle (only valid for very small angles).

Once all the currents are known, the current densities (J_0, J_1, J_2 and J_3) can be calculated and the power dissipated by them can be deduced using equation B.3. Then, the total power dissipated by the metal grid can be calculated multiplying the power dissipated by these finger and ring sections by the number of them in the grid.

- **Power dissipated by the metal-semiconductor contact**. The r_{S} component corresponding to the metal-semiconductor contact is directly calculated from the specific contact resistance values and the relation between the total area of the device and the area covered by metal. The series resistance corresponding to the front grid metal-semiconductor contact is

$$r_{\mathrm{m\text{-}s,front}} = \frac{R_{\mathrm{c,front}}}{f_{\mathrm{S}}^{\mathrm{tot}}} \tag{B.23}$$

where f_S^{tot} is defined as the shadowing factor of the whole active area of the cell, i.e. calculated to the mesa and hence also including the bus-bar. And the rear component, $r_{m\text{-}s,rear}$ is simply $R_{c,rear}$, since the shadowing factor is equal to 1 in the rear side of the cell. The total series resistance of the metal-semiconductor contact is

$$r_{m\text{-}s} = r_{m\text{-}s,front} + r_{m\text{-}s,rear} \tag{B.24}$$

Finally, equation B.2 is applied to all P_{diss} components, where $S_{cell} = \Pi R_b^2$ and $j{=}j_z$. The total r_S of the device is then calculated applying equation B.1.

B.4 Results and discussion

Once the algorithm for the calculation of the r_S of a concentrator solar cell has been developed (upgraded for a larger number of annuli and fingers with respect to the example above), it can be implemented so that it automatically evaluates different sets of variables providing different r_S and f_s pairs.

One could think of getting an arbitrarily low r_S value, but the question of whether this value is small enough to appropriately implement solar cell grids adapted for a given concentration would remain unclear. For that reason, a standard definition of the maximum loss allowed for a concentrator cell as a function of the sunlight concentration must be established. Equation 4.27 from Ref. [Luque, 1989] can be used for this purpose

$$X_M \simeq \frac{V_T}{r_S J_L} \tag{B.25}$$

where X_M is the maximum concentration ratio, V_T is the so-called thermal voltage, expressed as kT/q, being k the Boltzmann constant and T the cell operating temperature. If we aim for a maximum concentration of 1,000 suns, J_L is set to the typical value for conventional GaAs solar cells (25 $mAcm^{-2}$) and T is the room temperature, we obtain a maximum r_S of approximately 1 $m\Omega cm^2$, which will be the target for our calculations.

Our algorithm has also been run using a simplified version adapted for the modeling of a grid design without rings. The number of fingers and the length of the different radii defining the annuli were the variables screened with the algorithm for each of the cases studied, which comprised 2, 3, 4 and 5 rings. Several conclusions can be drawn from these simulations: 1) The cases without rings were systematically poorer than their counterparts with rings, as expressed in the general conclusions of Ref. [Cánovas et al.,

2006] 2) The optimum number of rings, N_{rings}, (and corresponding annuli) in the design is 4. A smaller number does not appropriately distribute the current throughout all the fingers and requires a too large number of 'primary fingers' (i.e. the ones arising from the 1st ring) and a larger number introduces a too large f_s, allowing a reduced number of primary fingers (because the finger multiplicative factor from one ring to the next one imposes an exponential trend in the number of fingers). This seems to be in disagreement with the result presented in Ref. [Algora and Díaz, 2000] (Fig. 2), which predicts (although does not calculate) a solar cell efficiency improvement in the whole concentration range for a five-ring design with respect to a four-ring one. This efficiency improvement is invariably related to an improvement of the f_s vs r_S trade-off (provided that it has been calculated optimizing the rest of the parameters), i.e. their algorithm provides a smaller r_S for N_{rings}=5 instead of N_{rings}=4, for a given f_s. Nevertheless, the discrepancy may come from the fact that a different total device area is used and especially that a different (smaller) w_f has been chosen, making the results from both analyzes not comparable. 3) The aforementioned statement regarding the goodness of smaller finger widths is confirmed (the statement regarding the finger thickness is obvious because it does not present any disadvantage, except for the increase of the processing complexity). A thinner finger allows the number of fingers to increase for a fixed f_s, keeping r_M approximately the same (because the reduction in J_L collected by each finger is proportional to the reduction in w_f) and reducing r_E approximately by a factor proportional to the square of the relative w_f reduction (e.g. if $w_{f,final}$=$w_{f,initial}$/2, then, $r_{E,final}$=$r_{E,initial}$/4). The reason for such reduction is that the emitter current density in the annuli, $j_{E,out}$, is a function of φ (see equation B.13) and the corresponding dissipated power, $P^{i}_{E,ext}$ is calculated by integrating the square of this $j_{E,out}$. 4) The total area of the device is critical for the trade-off between f_s and the maximum X that the front grid design can be adapted to. The larger the area of the device, the higher the value of the optimized r_S that can be obtained. This is also shown in Fig. 2 of Ref. [Algora and Díaz, 2000], although the exact result cannot be extrapolated to our case because the assumptions for the fixed parameters are different. 5) Provided the parameters in our model are the ones represented in Table B.1 and taking into account the constraints we have imposed in the solar cell grid design (multiplicative factor between fingers in consecutive annuli, device area, J_L of the cell, etc.), the optimum front grid design for X=1,000 suns is achieved for a f_s=9% and the following R_i values: R_1=60 μm, R_2=150 μm, R_3=300 μm and R_4=560 μm. The number of primary fingers is 13, which implies that the 4th annulus has 104 fingers. The optimized front grid design is presented in Fig. B.5.

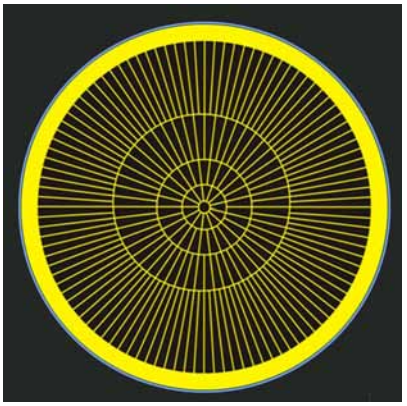

Figure B.5: Optimum front grid design calculated with our algorithm.

B.5 Experimental testing of the r_S components

In the past, we received solar cells from our partners and we needed them fully processed, however, we are now endowed with the capability to process III-V concentrator solar cells at IES-UPM and also to do it with the optimized solar cell front grid design explained in the previous subsection. Hereafter, the main solar cell processing steps will be summarized.

B.5.1 First step: from wafer level to photolithography masks

Once the solar cell structure has been epitaxially grown on the wafer, we need to get ready for the photolithography process, which implies designing and fabricating a photolithography mask from the calculated concentrator devices (shown in Fig. B.5).

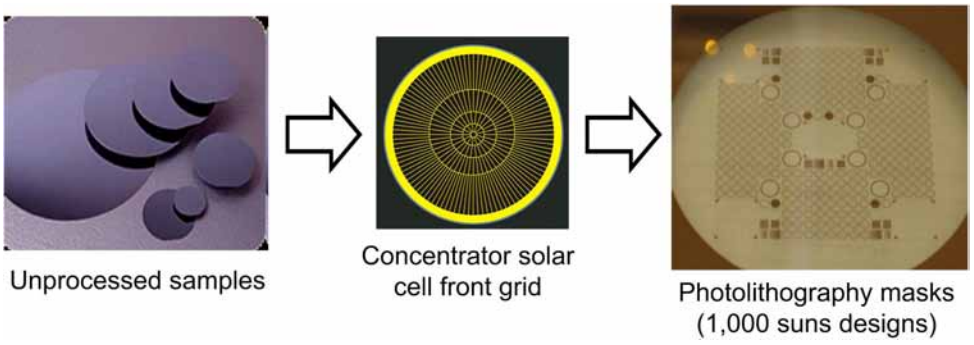

Figure B.6: Sketch of the first part of the processing line, which comprises the calculation and design of the metal contacts (front grid) for the concentrator solar cells and the fabrication of the photolithography masks. These masks are designed by cloning the concentrator solar cell front grid pattern. This processing step begins, in turn, with the plain wafers where the device is previously grown.

The photolithography masks are shown in Fig. B.6, where the first part of the processing line is shown, including the wafers and the photolithography mask designed and

fabricated by cloning the front grid design and some other device, such as diodes (with a f_s=100%) to measure the dark current and QE devices (with a f_s=0%).

B.5.2 Second step: from photolithography to metal evaporation

Fig. B.7 represents the second part of the processing line, which uses the elements shown

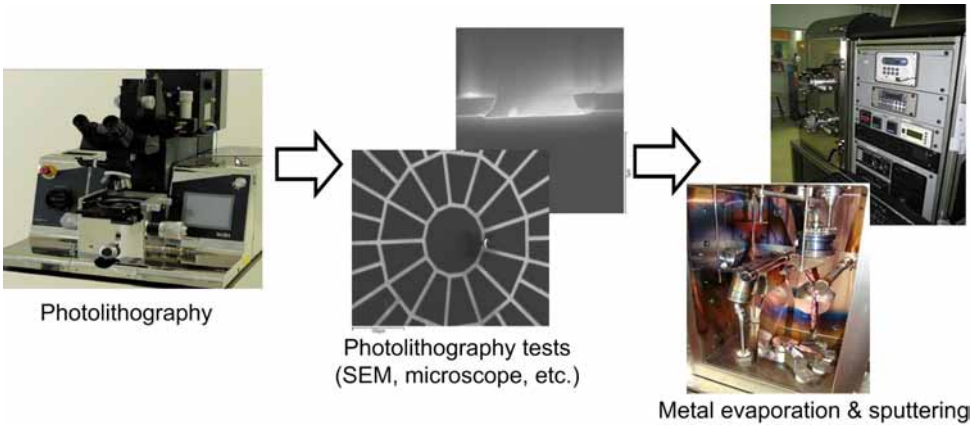

Figure B.7: Sketch of the second part of the processing line, which comprises .

in Fig. B.6 together with the aligner set-up shown in the first of the images of Fig. B.7 to perform the photolithography process. This aligner, with a resolution in the range of tenths of micrometers, holds the wafer and accurately aligns the photolithography mask on top of it so that a light and the subsequent chemicals develop the resistive coating deposited on the exposed side of the wafer, creating on it the pattern of the photolithography mask. The design of the front grid pattern shown in Fig. B.5 can be seen engraved with resistive coating in the middle microscope image of Fig. B.7. A scanning electron microscope (SEM) image of the deposited resistive coating profile can be observed in the second of the middle images of the figure. The third part of the figure represents the new evaporator system installed in the facilities of IES-UPM. This system evaporates, by Joule effect, the metals that constitute the front and rear contacts of the solar cells. The images show the inner and outer parts of the evaporation system.

B.5.3 Third step: from metal contacts to encapsulated solar cells

Once the metallization of the contacts has been carried out, the wafer presents the aspect of an array of solar cells (as the one shown in the first of the images of Fig. B.8), however, the metal-semiconductor contact cannot be adequately optimized until it is annealed in the rapid thermal annealing (RTA) system shown in the middle part of Fig. B.8 . Prior to the annealing process, another photolithography step is required for the implementation of the mesas, which in our case consist of a ring located very close to the external side

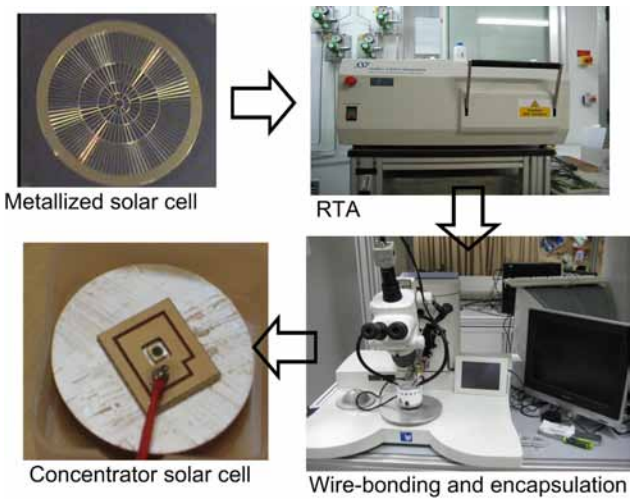

Figure B.8: Sketch of the third part of the processing line, which comprises .

of the bus-bar. These mesas aim to electrically isolate the active part of the device from the rest of the semiconductor and they are implemented by means of a chemical etching. The following step consists of separating the cells from the wafer, for which a diamond tip cutting station is used due to the reduced size of the devices. After the solar cells have been separated from the wafer, they need to be encapsulated so that the electrical current can be easily extracted from the contacts. The most important part of the encapsulation process is the wire-bonding of the cell, which is carried out with the wire-bonding station shown on the lower right part of Fig. B.8. The solar cell is also soldered to a copper disk which is electrically connected to its rear contact. The final aspect of the encapsulated cell is the one shown in the lower left part of the figure, which includes the gold PCB and the electrical cables corresponding to the front contact. The cell is then ready to be measured.

B.5.4 Example of the experimental testing

Concentrated light J-V experiments are useful to acquire a deeper insight on the PV device performance, putting emphasis on the r_S imposed by the concentrator solar cell front grid design and the emitter layer specifications, which determine the maximum concentration level. Fig. B.9(a) shows a family of J-V curves obtained under various concentration levels and measured in the concentration set-up presented in chapter 6. The efficiency is calculated from each J-V curve depends upon the current and voltage maximum power points (I_{mpp} and V_{mpp}, respectively) and the total incident light power, which in turn depends upon the concentration level and the solar cell area, according to equation B.26

$$\eta = \frac{P_{extracted}}{P_{incident}} = \frac{V_{OC} \cdot J_{SC} \cdot FF}{E_{dir} \cdot A_{cell}} = \frac{V_{mpp} \cdot I_{mpp}}{X \cdot E_{dir}(1\,sun) \cdot A_{cell}} \tag{B.26}$$

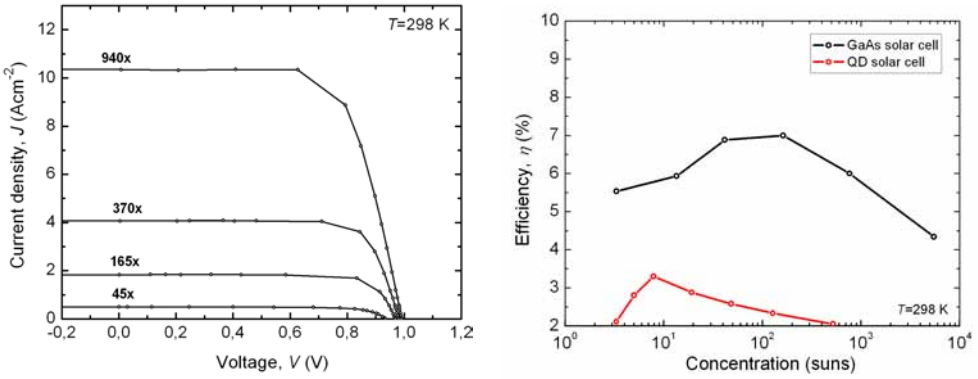

(a) (b)

Figure B.9: (a) Example of a family of J-V curves under concentrated light. (b) Efficiency of the GaAs reference cell and the QD cell plotted with respect to the concentration ratio. The pick of each curve indicates the maximum concentration for which the solar cells are optimized in practice.

where $P_{\text{extracted}}$ (W) is the total power obtained at the solar cell terminals, P_{incident} (W) is the total power of the light that impinges on the solar cell surface, FF is the fill factor of the solar cell defined, in turn, as the ratio between the voltage and current maximum power point and the product between V_{OC} and I_{SC} (with dimensionless units), E_{dir} (Wm^{-2}) is the direct component of the irradiance impinging on the solar cell surface, A_{cell} is the solar cell surface (m^2), X is the concentration factor measured in "sun" units (number of times higher than 1 sun under the standard irradiance conditions) and $E_{\text{dir}}(1sun)$ is the E_{dir} with the AM1.5D spectrum, which corresponds to the standard of 900 mWm^{-2}. The efficiency is then obtained from each of the J-V curves at different concentrations and the data are plotted, showing two curves with the efficiency of each cell in the vertical axis with respect to the concentration level in logarithmic scale in the horizontal axis (Fig. B.9(b)). Moving from left to right along any of the two curves, the efficiency increases until a maximum is reached. This value depends on the total r_{S} of the device, in turn dependent upon the quality of the processing, the encapsulation, the front grid design and the design of the solar cell layer structure. For concentrations higher than this maximum, the efficiency-concentration curve drops because the voltage loss due to the product of the current generated by the solar cell (at the maximum power point) and the r_{S} is larger than the ΔV derived from the (logarithmic) increase of V with the illumination increase. The efficiency of the GaAs reference cell (black curve) is notably higher than that corresponding to the QD cell. Besides, the black curve picks at 162 suns (η=7%), while the red curve picks at 8 suns (η=3.3%), confirming that the QD cell has a higher r_{S}. Anyway, the maximum efficiency picks at a concentration well below X=500 mainly because the metal thickness is lower than that defined in the specifications and also because the rest of the

elements in the device (layer thicknesses and dopings) are not yet optimized. In addition, the problems that occurred during the processing of this first batch of samples has to be taken into account.

B.6 Other applications of the modeling of the r_S

Our model has not only been used to optimize the front grid design of the new cells processed at IES-UPM, but also to model the r_S of other solar cells that were being used in the framework of previous collaborations. An example of this is the modeling carried out for the different front grid designs that were being used by the University of Glasgow to process the GaAs and QD solar cells that were ultimately sent to IES-UPM for further characterization.

Table B.2: Dimensions and results of the different front grid designs used for the fabrication of concentrator solar cells at the University of Glasgow.

Type	R_1	R_2	R_3	R_4	R_5 [μm]	rings	f_{last}	f_s [%]	r_S [mΩcm^2]*
A	50	181	306	560	-	no	64	7.5	11.41
F	50	181	306	560	-	yes	64	8.7	8.88
B	30	108	184	336	641	no	128	13.7	5.04
G	30	108	184	336	641	yes	128	15.2	3.63
I	120	-	-	-	-	no	54	9.1	10.3
J	140	-	-	-	-	no	81	13.3	6.07

*All front grids are calculated with w_f=6 μm and h_f= 0.2 μm in these real examples

Different types of solar cell grid designs have been analyzed, which pictures are shown in Fig. B.10 (the cell labeled as "grid type F" has a slightly different processing, although the only important feature here is the front grid design).

All the aforementioned solar cells, which active area is a 2 mm long diameter circle and which fixed parameters (layer doping levels, layer thicknesses, etc.) are very similar to those exposed in Table B.1, have been modeled using our algorithm. The main dimensions as well as the f_s and r_S results are presented in Table B.2. For this task, all the dimensions were previously measured using a microscope. n_{last} in Table B.1 refers to the number of fingers in the last annulus (i.e. that are directly connected to the bus-bar)

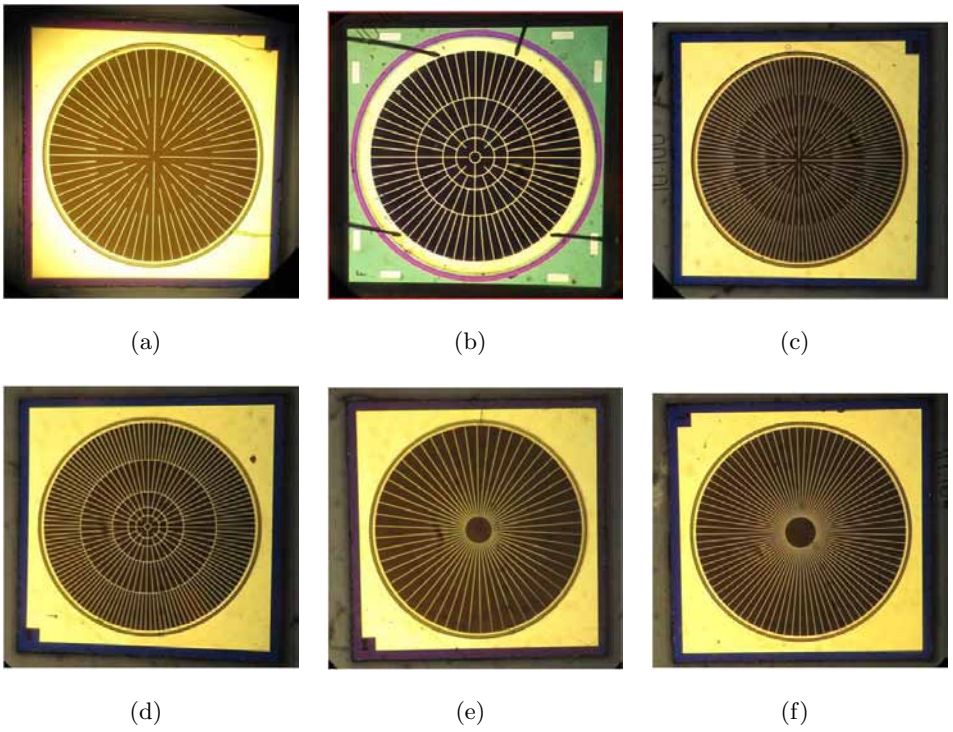

(a) (b) (c)

(d) (e) (f)

Figure B.10: Microscope images of the different solar cell front grid designs fabricated in the University of Glasgow and sent to IES-UPM for their characterization. (a) Grid type A, (b) Grid type F, (c) Grid type B, (d) Grid type G, (e) Grid type I, (f) Grid type J.

Appendix C

Advances in the processing of QD-IBSCs

The special processing required for the fabrication of concentrator solar cells is reviewed in this appendix, summarizing the work carried out at RCAST to adapt their former solar cell processing to high concentrated light.

The Okada Lab at RCAST has three MBE reactors with which they grow, among other type of devices, QD-IBSCs. But their solar cell processing was quite simple and did not use concentrator technology. This section explains the processing upgrading carried out by the author of this Thesis in order to endow this laboratory with the capability for processing concentrator devices.

C.1 Grid designs and photolithography masks

The r_S model described in the previous section was used for the optimization of three 500 suns concentrator solar cells with 1 mm, 2 mm and 0.5 mm of radius. In this case, the main differences in the model parameters used were the thickness and doping concentrations of the solar cell layer structure. The optimized front grid patterns corresponding to the three aforementioned solar cell sizes accounted for 72, 192 and 40 fingers (in the outer annulus). Their designs are represented in Figs. C.1(a), C.1(b) and C.1(c), respectively.

When most variables and parameters can be freely varied for the optimization, the minimum f_s for a given concentration should be a function of the cell size, being minimum for the smallest cell. Nevertheless, because of the design constraints, specially due to the limitations in w_f and h_E, the lower f_s in this case is obtained for the medium size design (R_b=1 mm), with f_s=8.08%. In the case of the large size cell, f_s(R_b=2 mm)=9.94% and in the case of the small one f_s(R_b=0.5 mm)=9.15%.

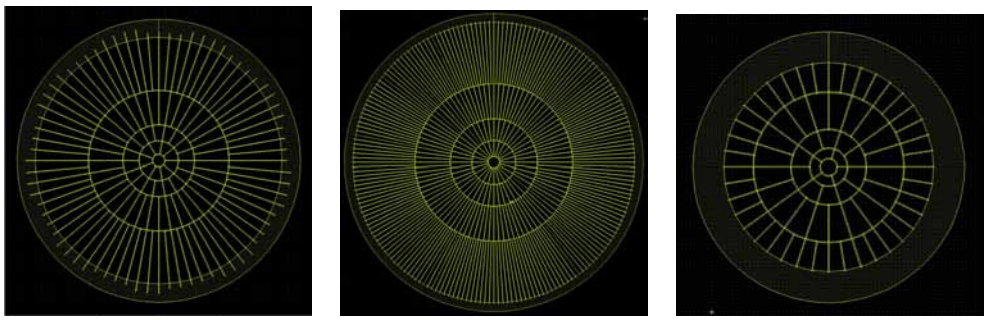

(a) (b) (c)

Figure C.1: Front grid designs of the three 500 suns concentrator solar cells optimized at RCAST. Three different circular front grid sizes were calculated (expressed with the radius): (a) 1 mm; (b) 2 mm and (c) 0.5 mm.

The images shown in Fig. C.1 were performed with a computer-aided design (CAD) free software tool. A combination of this cell grids (8 medium grids, 3 small grids and 1 large grid) were used for the fabrication of the photolithography mask, which also included 4 QE devices and several small diodes to accurately perform dark measurements. All of the previous devices integrated in the photolithography mask are shown in Fig. C.2.

(a) (b) (c)

Figure C.2: Photolithography masks calculated, designed and fabricated for the concentrator solar cells grown at Okada Lab. (a) Photolithography design used for the fabrication of the mask; (b) front grid photolithography mask used for the metallization of the wafer; (c) photolithography mask used for the mesas.

The first of the figures (C.2(a)) represents the CAD design of the whole front mask. Fig. C.2(b) and C.2(c) respectively show pictures of the photolithography mask fabricated for the front metallization and for the mesas.

C.2 Time exposures of the chemical reactions

A new processing technology routine also had to be developed at RCAST for the incorporation of the concentration technology into the fabrication of solar cells. The main difference between this technology and the preexisting non-concentrating one concerns the size of the devices: devices larger than the ones used for concentration were previously used. The latter implies that this time we would need a higher photolithography resolution (fingers in the range of 5 μm), which also makes the finger lift-off more difficult. The different process parameters to optimize were: the amount of resistive coating deposited on the wafer before it is spread thanks to the spin coating machine (also called spin coater or spinner), the revolutions per minute and time programmed in the spin coater, the light exposure times for the development, the chemical proportions in the dissolutions, the time the wafer is immersed in the development dissolutions, etc. At the beginning, the development experiments regarding the resistive coating were unsuccessful because of the thin fingers. This is shown in Fig. C.3(a), where a microscope picture shows how the resistive coating has not properly been deposited on the wafer. The resistive coating corresponding to the fingers and rings is practically nonexistent and only the metal at the intersections is visible, which would eventually cause a deficient metallization and lift-off.

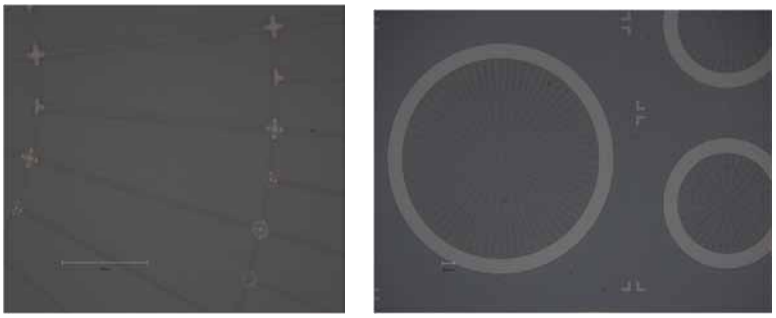

(a) (b)

Figure C.3: Microscope images of the processing optimization experiments. (a) The resistive coating is not properly deposited because some parameters from the photolithography process (such us the exposure times, the chemical proportions in the dissolutions, etc.) still had to be optimized. (b) The photolithography processes is finally optimized and the resistive coating pattern looks exactly as the photolithography mask design.

After all the processing steps were optimized for these concentration mask designs, the result of the metallization experiments looked like the photolithography mask, as it can be observed in the picture of Fig. C.3(b).

The pictures in Fig. C.4 show the clean room at Okada Lab, where most of the processing steps were carried out. Fig. C.4(a) shows the aligner system used for the pho-

(a) (b)

Figure C.4: Clean room at Okada Lab. (a) Aligner system; (b) chemicals table used for the resistive coating development, including a spin coater and a heating plate.

tolithography and Fig. C.4(b) shows the laboratory table with all the chemical products used, as well as the spin coater and the heating plate.

C.3 Evaporation and annealing

Once the resistive coating patterns were appropriately controlled and accurately deposited on the wafer, the evaporation process could be performed. AuGeNi/Au alloy was used for the rear metallization and Ti/Pt/Au alloy was used for the front metallization. Fig. C.5(a) shows the inside of the high-vacuum evaporator system with the basket containing

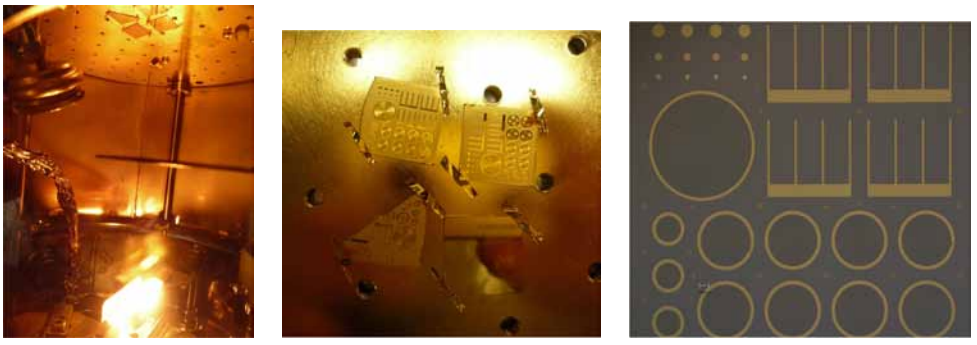

(a) (b) (c)

Figure C.5: Evaporation process at Okada Lab. (a) Image of the inside of the evaporator during the metallization of the wafers. (b) Detail of the wafers inside the metallization. (c) Microscope image of the complete wafer metallization.

the molten metal alloy being heated by Joule effect (the basket is red-hot). The wafers are attached to the ceiling of the evaporator vacuum chamber and the shutter (that prevents the evaporated metal to reach the samples) is removed from the evaporation direction.

Fig. C.5(b) shows a detail of the vacuum chamber where the wafers are attached. It can be observed how the metal alloy has completely covered the front surface of the wafers.

After the metal deposition, the lift-off process is carried out in order to remove the resistive coating from the wafers, thus also removing the metal sticked to it and showing the metallized front grid pattern on the front surface of the wafer. Once the metal contacts have been already deposited, they have to be annealed. This is performed on a small annealing system endowed with a quartz chamber, where the wafer is placed. A nitrogen flux is circulated through the chamber to prevent the oxidation and contamination of the sample.

Publications related to the thesis

Patents

– E. Antolín, A. Martí, A. Luque, I. Ramiro, **P.G. Linares**, Método para la fabricación de una célula solar de banda intermedia con puntos cuánticos no tensionados (Fabrication method for non-strained quantum dot intermédiate band solar cells), Patente P201100708

Book chapters

– **P.G. Linares**, E. Antolín, A. Martí, A. Luque. Intermediate band solar cells - modeling and simulation. In L. Fara and M. Yamaguchi (Eds.), Advanced Solar Cell Materials, Technology, Modeling and Simulation, ch. 11, 188-213, IGI Global, Hershey, 2012

Publications in international journals

– M. Mendes, H. Hernández, E. López, **P.G. Linares** et al., Self-organized colloidal quantum dots and metal nanoparticles for plasmon-enhanced intermediate band solar cells, *submitted to Energy Environ. Sci.*, 2012

– A. Luque, E. Antolín, **P.G. Linares** et al., Interband optical absorption in quantum well solar cells, *submitted to IEEE J. Photovolt.*, 2012

- I. Tobías, A. Luque, E. Antolín, **P.G. Linares** et al., Realistic Performance Prediction in Nanostructured Solar Cells *submitted to J. Appl. Phys.*, 2012

- A. Luque, A. Mellor, I. Tobías, E. Antolín, **P.G. Linares** et al., Virtual-bound, filamentary and layered states in a box-shaped quantum dot of square potential form the exact solution of the effective mass Schrödinger equation, *J. Appl. Phys. (accepted)*, 2012

- **P.G. Linares** et al., Low Temperature Concentrated Light Characterization applied to Intermediate Band Solar Cells, *IEEE J. Photovolt. (accepted)*, 2012

- **P.G. Linares** et al., Extreme voltage recovery in GaAs:Ti intermediate band solar cells, *Sol. Energy Mat. Sol. Cells* 108, pp. 175-179, 2013

- A. Martí, E. Antolín, **P.G. Linares** and A. Luque, Understanding experimental characterization of intermediate band solar cells, *J. Appl. Phys.* 22, pp. 22832-22839, 2012

- A. Luque , **P.G. Linares** et al., Understanding the operation of quantum dot intermediate band solar cells, *J. Appl. Phys.* 111, pp. 044502, 2012

- A. Luque, A. Mellor, E. Antolín, **P.G. Linares** et al., Symmetry considerations in the empirical k.p Hamiltonian for the study of intermediate band solar cells, *Sol. Energy Mat. Sol. Cells* 103, pp.171-183, 2012

- **P.G. Linares** et al., Voltage recovery in intermédiate band solar cells, *Sol. Energy Mat. Sol. Cells* 98, pp. 240-244, 2012

- I. Ramiro, E. Antolín, **P.G. Linares** et al., Application of photoluminescence and electroluminescence techniques to the characterization of intermediate band solar cells. *Energy Procedia* 10, pp. 117-121, 2011

- A. Luque, A. Martí, E. Antolín, **P.G. Linares** et al., New Hamiltonian for a better understanding of the quantum dot intermediate band solar cells, *Sol. Energy Mat. Sol. Cells* 95, pp. 2095-2101, 2011

- A. Luque, A. Martí, E. Antolín, **P.G. Linares** et al., Radiative thermal escape in intermediate band solar cells, *AIP Adv.* 1, pp. 022125, 2011

- **P.G. Linares** et al., III-V compound semiconductor screening for implementing quantum dot intermediate band solar cells. *J. Appl. Phys.* 109, pp. 014313, 2011

- A. Luque, A. Martí, E. Antolín, **P.G. Linares**, Intraband absorption for normal illumination in quantum dot intermediate band solar cells, *Sol. Energy Mat. Sol. Cells*, 94, pp. 2032-2035, 2010
- A. Luque, **P.G. Linares** et al., Multiple levels in intermediate band solar cells, *Appl. Phys. Lett.* 96, pp. 013501, 2010
- E. Antolín, A. Martí, C.D. Farmer, **P.G. Linares** et al., Reducing carrier escape in the InAs/GaAs quantum dot intermediate band solar cell, *J. Appl. Phys.* 108, pp. 064513, 2010
- **P.G. Linares** et al., Inx(GayAl1-y)1-xAs quaternary alloys for quantum dot intermediate band solar cells, *Energy Procedia* 2, pp. 133-141, 2010
- E. Cánovas, A. Martí, N. López, E. Antolín, **P.G. Linares** et al., Application of the photoreflectance technique to the characterization of quantum dot intermediate band materials for solar cells, *Thin Solid Films* 516, pp. 6943-6947, 2008
- E. Antolín, A. Martí, E. Cánovas, N. López, **P.G. Linares** et al., Low temperature characterization of the photocurrent produced by two photon transitions in a quantum dot intermediate band solar cell, *Thin Solid Films* 516, pp. 6919-6923, 2008
- Martí, E. Antolín, E. Cánovas, N. López, **P.G. Linares** et al., Elements of the design and analysis of quantum dot intermediate band solar cells, *Thin Solid Films* 516, pp. 6716-6722, 2008
- A. Martí, E. Antolín, C.R. Stanley, C.D. Farmer, N. López, P. Díaz, E. Cánovas, **P.G. Linares** and A. Luque, Production of Photocurrent due to Intermediate-to-Conduction-Band Transitions: A Demostration of a Key Operating Principle of the Intermediate-Band Solar Cell, *Phys. Rev. Lett.* 97, pp. 247701-4, 2006

Contributions to international conferences

- I. Ramiro, E. Antolín, **P.G. Linares** et al., Oral Presentation: InAs/AlGaAs quantum dot intermediate band solar cells with enlarged sub-bandgaps, 38th IEEE Photovoltaic Specialists Conference, Austin, Texas, USA, 2012

- Y. Okada, K. Yoshida, Y. Shoji, A. Ogura, **P.G. Linares** et al., Oral Presentation: Effect of concentration on the performance of quantum dot intermediate band solar cell, 8th Concentrating Photovoltaic Systems, Toledo, Madrid, Spain, 2012
- A. Ogura, T. Morioka, **P.G. Linares** et al., Oral Presentation: Modeling of Quantum Dot Solar Cells for Concentrator PV Applications, 37th IEEE Photovoltaic Specialists Conference, Seattle, USA, 2011
- **P.G. Linares** et al., Oral Presentation: Characterization of quantum dot intermediate band solar cells under very high light concentration and low temperature, E-MRS 2011 Spring Meeting and Bilateral Energy Conference, Nice, France, 2011
- I. Ramiro, E. Antolín, **P.G. Linares** et al., Oral Presentation: Application of photolumiscence and electroluminescence techniques to the characterization of intermediate band solar cells, E-MRS 2011 Spring Meeting and Bilateral Energy Conference, Nice, France, 2011
- E. Antolín, A. Martí, **P.G. Linares** et al., Oral Presentation: Advances in quantum dot intermediate band solar cells, 35th IEEE Photovoltaic Specialists Conference, Honolulu, Hawaii, USA, 2010
- **P.G. Linares**, et al. Visual: Modeling and characterization of multiple level intermediate band solar cell, 25th European Photovoltaic Solar Energy Conference, Valencia, Spain, 2010
- E. Antolín, A. Martí, **P.G. Linares** et al., Oral Presentation: Raising the efficiency limit of the GaAs-based intermediate band solar cell through the implementation of a monolithic tandem with an AlGaAs top cell, 25th European Photovoltaic Solar Energy Conference, Valencia, Spain, 2010
- **P.G. Linares** et al., Oral Presentation: Inx(GayAl1-y)1-xAs quaternary alloys for quantum dot intermediate band solar cells, E-MRS 2009 Spring Meeting, Strasbourg, France, 2009
- A. Martí, E. Antolín, **P.G. Linares**, et al., Oral Presentation: IBPOWER: Intermediate band materials and solar cells for photovoltaics with high efficiency and reduced cost, 34th IEEE Photovoltaic Specialists Conference, Philadelphia, Pensilvania, EEUU, 2009
- A. Luque, A. Marti, E. Antolin, E. Cánovas, **P.G. Linares** et al., "New approaches to the intermediate band solar cell concept, 24th European Photovoltaic Solar Energy Conference and Exhibition, Hamburg, Germany, 2009, pp. 7-14

- E. Cánovas, A. Martí, D. Fuertes Marrón, E. Antolín,**P.G. Linares** et al., Visual Presentation: Optical characterization of Quantum Dot Intermediate Band Solar Cells, 23rd European Photovoltaic Solar Energy Conference and Exhibition, Valencia, Spain, 2008

- D. Fuertes Marrón, A. Martí, C. Tablero, E. Antolín, E. Cánovas, **P.G. Linares** and A. Luque, Oral Presentation: Thin Film Intermediate Band Chalcopyrite Solar Cells, 23rd European Photovoltaic Solar Energy Conference and Exhibition, Valencia, Spain, 2008

- E. Antolín, A. Martí, **P.G. Linares** et al. Oral Presentation: Demonstration and Analysis of the Photocurrent Produced by Absorption of Two Sub-Bandgap Photons in a Quantum Dot Solar Cell, 23rd European Photovoltaic Solar Energy Conference and Exhibition, Valencia, Spain, 2008

- A. Martí, E. Antolín, E. Cánovas, **P.G. Linares**, and A. Luque, Oral Presentation: "Light management issues in intermediate band solar cells, MRS 2008 Spring Meeting, San Francisco, California, USA, 2008

- E. Cánovas, A. Martí, N. López, E. Antolín, **P.G. Linares** et al., Visual Presentation: Application of the photoreflectance technique to the characterization of quantum dot intermediate band materials for solar cells, E-MRS 2007 Spring Meeting, Strasbourg, France, 2007

- E. Antolín, A. Martí, E. Cánovas, N. López, **P.G. Linares** et al., Oral Presentation: Low temperature characterization of the photocurrent produced by two photon transitions in a quantum dot intermediate band solar cell, E-MRS 2007 Spring Meeting, Strasbourg, France, 2007

- A. Martí, E. Antolín, E. Cánovas, N. López, **P.G. Linares**et al., Oral Presentation: Elements of the design and analysis of quantum dot intermediate band solar cells, E-MRS 2007 Spring Meeting, Strasbourg, France, 2007

Bibliography

[Akahane et al., 1998a] Akahane, K., Kawamura, T., Lan, S., Okada, Y., and Kawabe, M. (1998a). Control of size and density of self-organized quantum dots grown on GaAs(311)B by atomic hidrogen-assisted molecular beam epitaxy. *J. Surf. Anal*, 4(4):255–258.

[Akahane et al., 1998b] Akahane, K., Kawamura, T., Okino, K., Koyama, H., Lan, S., Okada, Y., Kawabe, M., and Tosa, M. (1998b). Highly packed InGaAs quantum dots on GaAs(311)B. *Appl. Phys. Lett.*, 73(23):3411–3413.

[Akahane et al., 2002] Akahane, K., Ohtani, N., Okada, Y., and Kawabe, M. (2002). Fabrication of ultra-high density InAs-stacked quantum dots by strain-controlled growth on InP(311)B substrate. *J. Cryst. Growth*, 245(1-2):31 – 36.

[Algora and Díaz, 2000] Algora, C. and Díaz, V. (2000). Influence of series resistance on guidelines for manufacture of concentrator p-on-n GaAs solar cells. *Prog. Photovolt: Res. Appl.*, 8(2):211–225.

[Alonso-Álvarez et al., 2008] Alonso-Álvarez, D., Taboada, A. G., Ripalda, J. M., Alén, B., González, Y., González, L., García, J. M., Briones, F., Martí, A., Luque, Sánchez, A. M., and Molina, S. I. (2008). Carrier recombination effects in strain compensated quantum dot stacks embedded in solar cells. *Appl. Phys. Lett.*, 93(12):123114.

[Antolín, 2010] Antolín, E. (2010). *Development of Experimental Techniques for the Demonstration of the Operation Principles of the Intermediate Band Solar Cell*. PhD thesis, Instituto de Energía Solar - Universidad Politécnica de Madrid.

[Antolín et al., 2006] Antolín, E., Martí, A., and & Luque, A. . P. p. a. t. . (2006). Energy conversion efficiency limit of series connected intermediate band solar cells. *Proc. of the 21st European Photovoltaic Solar Energy Conference, Dresden, Germany.*

[Antolín et al., 2010a] Antolín, E., Martí, A., Farmer, C. D., Linares, P. G., Hernández, E., Sánchez, A. M., Ben, T., Molina, S. I., Stanley, C. R., and Luque, A. (2010a).

Reducing carrier escape in the InAs/GaAs quantum dot intermediate band solar cell. *J. Appl. Phys.*, 108(6):064513.

[Antolín et al., 2010b] Antolín, E., Martí, A., Linares, P., Ramiro, I., Hernández, E., and Luque, A. (2010b). Raising the efficiency limit of the GaAs-based intermediate band solar cell through the implementation of a monolithic tandem with an AlGaAs top cell. *Proc. of the 5th World Conference on Photovoltaic Energy Conversion and 25th European Photovoltaic Solar Energy Conference, Valencia, Spain*, pages 65–68.

[Antolín et al., 2010c] Antolín, E., Martí, A., Linares, P. G., Ramiro, I., Hernández, E., Farmer, C. D., Stanley, C. R., and Luque, A. (2010c). Advances in quantum dot intermediate band solar cells. *Conference Record of the 35th IEEE Photovoltaic Specialists Conference, Honolulu, USA*, pages 000065–000070.

[Antolín et al., 2011] Antolín, E., Martí, A., and Luque, A. (2011). The Lead Salt Quantum Dot Intermediate Band Solar Cell. *Conference Record of the 37th IEEE Photovoltaic Specialists Conference, Seattle, USA*.

[Antolín et al., 2009] Antolín, E., Martí, A., Olea, J., Pastor, D., González-Díaz, G., Mártil, I., and Luque, A. (2009). Lifetime recovery in ultrahighly titanium-doped silicon for the implementation of an intermediate band material. *Appl. Phys. Lett.*, 94(4):042115.

[Araújo et al., 1986] Araújo, G., Cuevas, A., and Ruiz, J. (1986). The Effect of Distributed Series Resistanceon the Dark and Illuminated Current-Voltage Characteristics of Solar Cells. *IEEE Trans. Electron Devices*, 33(3):391–401.

[Araújo and Martí, 1994] Araújo, G. and Martí, A. (1994). Absolute limiting efficiencies for photovoltaic energy conversion. *Sol. Energy Mat. Sol. Cells*, 33:213–240.

[Askins et al., 2008] Askins, S., Taylor, S., Domínguez, C., and Anton, I. (2008). Realization of a solar simulator for production testing of HCPV modules. *Proc. of the 23rd European Photovoltaic Solar Energy Conference, Valencia, Spain*, pages 137–141.

[Basore,] Basore, P. A. PC1D. *URL:http://www.pv.unsw.edu.au/info-about/our-school/products-services/pc1d. Accessed: 2012-04-15. (Archived by WebCite at http://www.webcitation.org/66w55ytSa).*

[Bimberg et al., 1999] Bimberg, D., Grundmann, M., and Ledentsov, N. N. (1999). *Quantum Dot Hetrostructures*. John Wiley & sons, Chichester.

[Bliss et al., 2009] Bliss, M., Betts, T., and Gottschalg, R. (2009). An LED-based photovoltaic measurement system with variable spectrum and flash speed. *Sol. Energy Mat. Sol. Cells*, 93(67):825 – 830.

[Bockelmann and Bastard, 1990] Bockelmann, U. and Bastard, G. (1990). Phonon scattering and energy relaxation in two-, one- and zero-dimensional electron gasses. *Phys. Rev. B*, 42(14):8947–8951.

[Bremner et al., 2008] Bremner, S. P., Levy, M. Y., and Honsberg, C. B. (2008). Limiting efficiency of an intermediate band solar cell under a terrestrial spectrum. *Appl. Phys. Lett.*, 92:171110.

[Campion et al., 2003] Campion, R. P., Edmonds, K. W., Zhao, L. X., Wang, K. Y., Foxon, C. T., Gallagher, B. L., and Staddon, C. R. (2003). High-quality GaMnAs films grown with arsenic dimers. *J. Cryst. Growth*, 247(1):42–48.

[Chun et al., 1996] Chun, Y. J., Nakajima, S., Okada, Y., and Kawabe, M. (1996). The role of atomic hydrogen for formation of quantum dots by self-organizing process in MBE. *Physica B: Condensed Matter*, 227(14):299 – 302.

[Cuadra, 2004] Cuadra, L. (2004). *Development of Intermediate Band Solar Cells*. PhD thesis, Universidad Politécnica de Madrid.

[Cuadra et al., 2000] Cuadra, L., Martí, A., and Luque, A. (2000). Modeling of the absorption coefficients of the intermediate band solar cell. *Proc. of the 16th European Photovoltaic Solar Energy Conference, Glasgow, UK*, pages 15–21.

[Cuadra et al., 2004] Cuadra, L., Martí, A., and Luque, A. (2004). Influence of the overlap between the absorption coefficients on the efficiency of the intermediate band solar cell. *IEEE Trans. Electron Devices*, 51(6):1002–1007.

[Cánovas et al., 2006] Cánovas, E., Martí, A., and Luque, A. (2006). Design of circular metal grid patterns for concentration solar cells. *Proc. of the 21st European Photovoltaic Solar Energy Conference, Dresden, Germany*.

[Cánovas et al., 2008] Cánovas, E., Martí, A., López, N., Antolín, E., Linares, P. G., Farmer, C. D., Stanley, C. R., and Luque, A. (2008). Application of the photoreflectance technique to the characterization of quantum dot intermediate band materials for solar cells. *Thin Solid Films*, 516(20):6943–6947.

[Dahal et al., 2010] Dahal, S. N., Bremner, S. P., and Honsberg, C. B. (2010). Identification of candidate material systems for quantum dot solar cells including the effect of strain. *Prog. Photovolt: Res. Appl.*, 18:233–239.

[Datta, 1989] Datta, S. (1989). *Quantum Phenomena*, volume VIII of *Modular Series on Solid State Devices*. Addison-Wesley, Reading, MA,.

[del Cañizo et al., 2009] del Cañizo, C., del Coso, G., and Sinke, W. (2009). Crystalline Silicon Solar Module Technology: Towards the 1Eur Per Watt-Peak Goal. *Prog. Photovolt: Res. Appl.*, 17:199–209.

[Domínguez, 2012] Domínguez, C. (2012). *Optical and electrical characterization of high-concentration photovoltaic systems*. PhD thesis, Instituto de Energía Solar - Universidad Politécnica de Madrid.

[Domínguez et al., 2008] Domínguez, C., Antón, I., and Sala, G. (2008). Solar simulator for concentrator photovoltaic systems. *Opt. Express*, 16(19):14894–14901.

[Donaty et al., 2003] Donaty, G. P., Kaspi, R., and Malloy, K. J. (2003). Interpolating semiconductor alloy parameters: Aplication to quaternary III-V band gaps. *J. Appl. Phys.*, 94:5814–5819.

[Ekins-Daukes and Schmidt, 2008] Ekins-Daukes, N. J. and Schmidt, T. W. (2008). A molecular approach to the intermediate band solar cell: The symmetric case. *Appl. Phys. Lett.*, 93:063507.

[Emery, 1986] Emery, K. (1986). Solar simulators and IV measurement methods. *Sol. Cells*, 18(34):251–260.

[Fanetti, 1981] Fanetti, E. (1981). Flash technique for GaAs concentrator solar cell measurement. *Electron. Lett.*, 17:469–470.

[Galiana et al., 2005] Galiana, B., Algora, C., Rey-Stolle, I., and García, I. (2005). A 3-D model for concentrator solar cells based on distributed circuit units. *IEEE Trans. Electron Devices*, 52(12):2552–2558.

[González-Díaz et al., 2009] González-Díaz, G., Olea, J., Mártil, I., Pastor, D., Martí, A., Antolín, E., and Luque, A. (2009). Intermediate band mobility in heavily titanium-doped silicon layers. *Sol. Energy Mat. Sol. Cells*, 93(9):1668–1673.

[Grimmeiss and Koelmans, 1961] Grimmeiss, H. G. and Koelmans, H. (1961). Analysis of p-n Luminescence in Zn-Doped GaP. *Phys. Rev.*, 123(6):1939.

[Hall et al., 2010] Hall, J., Kent, A., Foxon, C., and Campion, R. (2010). Temperature effects during the growth of $In_xGa_{1-x}N$ films through the whole compositional range by plasma-assisted molecular beam epitaxy. *J. Cryst. Growth*, 312(14):2083 – 2088.

[Harrison, 2005] Harrison, P. (2005). *Quantum Wells wires and dots. Theoretical and computational physics of semiconductor nanostructures (2nd Ed.).* John Wiley and Sons, New York.

[Heiss et al., 2006] Heiss, W., Groiss, H., Kaufmann, E., Hesser, G., Böberl, M., Springholz, G., and Schäffler, F. (2006). Centrosymmetric PbTe/ CdTe quantum dots coherently embedded by epitaxial precipitation. *Appl. Phys. Lett.*, 88:192109.

[Horikoshi et al., 1986] Horikoshi, Y., Kawashima, M., and Yamaguchi, H. (1986). Low-temperature growth of gaas and alas-gaas quantum-well layers by modified molecular beam epitaxy. *Jpn. J. Appl. Phys.*, 25(Part 2, No. 10):L868–L870.

[Horikoshi et al., 1987] Horikoshi, Y., Kawashima, M., and Yamaguchi, H. (1987). Photoluminescence characteristics of algaas-gaas single quantum wells grown by migration-enhanced epitaxy at 300 ℃ substrate temperature. *Appl. Phys. Lett.*, 50(23):1686–1687.

[Howe et al., 2004] Howe, P., Ru, E. C. L., Clarke, E., Abbey, B., Murray, R., and Jones, T. S. (2004). Competition between strain-induced and temperature-controlled nucleation of InAs/GaAs quantum dots. *J. Appl. Phys.*, 95(6):2998–3004.

[Hubbard et al., 2009] Hubbard, S. M., Bailey, C. G., Aguinaldo, R., Polly, S., Forbes, D. V., and Raffaelle, R. P. (2009). Characterization of quantum dot enhanced solar cells for concentrator photovoltaics. *Conference Record of the 34th IEEE Photovoltaic Specialists Conference, Philadelphia, U.S.A*, (12):000090–000095.

[Hubbard et al., 2008] Hubbard, S. M., Cress, C. D., Bailey, C. G., Raffaelle, R. P., Bailey, S. G., and Wilt, D. M. (2008). Effect of strain compensation on quantum dot enhanced GaAs solar cells. *Appl. Phys. Lett.*, 92(12):123512.

[Keogh et al., 2004] Keogh, W. M., Blakers, A. W., and Cuevas, A. (2004). Constant voltage I-V curve flash tester for solar cells. *Sol. Energy Mat. Sol. Cells*, 81(2):183 – 196.

[Keogh and Cuevas, 1997] Keogh, W. M. and Cuevas, A. (1997). Simple flashlamp I-V testing of solar cells. *Conference Record of the 26th IEEE Photovoltaic Specialists Conference, Anaheim, USA*, pages 199–202.

[Kohraku and Kurokawa, 2006] Kohraku, S. and Kurokawa, K. (2006). A fundamental experiment for discrete-wavelength LED solar simulator. *Sol. Energy Mat. Solar Cells*, 90(1819):3364 – 3370.

[Lang and Henry, 1975] Lang, D. and Henry, C. (1975). Nonradiative Recombination at Deep Levels in GaAs and GaP by Lattice-Relaxation Multiple Phonon Emission. *Phys. Rev. Lett.*, 35(32).

[Levy et al., 2005] Levy, M., Honsberg, C., Martí, A., and Luque, A. (2005). Quantum dot intermediate band solar cell material systems with negligible valence band offsets. *Conference Record of the 31st IEEE Photovoltaic Specialists Conference, Orlando, USA*, pages 90–93.

[Levy and Honsberg, 2008a] Levy, M. Y. and Honsberg, C. (2008a). Solar cell with an intermediate band of finite width. *Phys. Rev. B*, 78:175122.

[Levy and Honsberg, 2008b] Levy, M. Y. and Honsberg, C. B. (2008b). Nanostructured Absorbers for Multiple Transition Solar Cells. *IEEE Trans. Electron Devices*, 55:706–711.

[Linares et al., 2012a] Linares, P. G., Antolín, E., Martí, A., and Luque, A. (2012a). Intermediate band solar cells - modeling and simulation. In Fara, L. and Yamaguchi, M., editors, *Advanced Solar Cell Materials, Technology, Modeling and Simulation*, chapter 11, pages 188–213. IGI Global.

[Linares et al., 2010a] Linares, P. G., Farmer, C. D., Antolín, E., Chakrabarti, S., Sánchez, A. M., Ben, T., Molina, S. I., Stanley, C. R., Martí, A., and Luque, A. (2010a). $In_x(Ga_yAl_{1-y})_{1-x}As$ quaternary alloys for quantum dot intermediate band solar cells. *Energy Procedia*, 2(1):133–141.

[Linares et al., 2012b] Linares, P. G., Martí, A., Antolín, E., Farmer, C. D., Ramiro, I., Stanley, C. R., and Luque, A. (2012b). Voltage recovery in intermediate band solar cells. *Sol. Energy Mat. Sol. Cells*, 98(1):240–244.

[Linares et al., 2011] Linares, P. G., Martí, A., Antolín, E., and Luque, A. (2011). III-V compound semiconductor screening for implementing quantum dot intermediate band solar cells. *J. Appl. Phys.*, 109(1):014313.

[Linares et al., 2010b] Linares, P. G., Martí, A., Antolín, E., Ramiro, I., Hernández, E., Farmer, C. D., Stanley, C. R., and Luque, A. (2010b). Modeling and characterization of multiple level intermediate band solar cell. In Sant, G., Ossenbrink, H., and Helm, P.,

editors, *5th World Conference on Photovoltaic Energy Conversion and 25th European Photovoltaic Solar Energy Conference*, pages 468–471, Valencia, Spain. WIP-Renewable Energies, Munich.

[Linares et al., 2012c] Linares, P. G., Martí, A., Antolín, E., Ramiro, I., López, E., Farmer, C. D., Stanley, C. R., and Luque, A. (2012c). Low Temperature Concentrated Light Characterization applied to Intermediate Band Solar Cells. *IEEE J. Photovolt. (to be published)*.

[Linares et al., 2013] Linares, P. G., Martí, A., Antolín, E., Ramiro, I., López, E., Hernández, E., Fuertes Marrón, D., Artacho, I., Tobias, I., Gérard, P., Chaix, C., Campion, R. P., Foxon, C. T., Stanley, C. R., Molina, S. I., and Luque, A. (2013). Extreme voltage recovery in GaAs:Ti intermediate band solar cells. *Sol. Energy Mat. Sol. Cells (accepted)*, 108:175–179.

[Liu et al., 1995] Liu, X., Prasad, A., Nishio, J., Weber, E. R., Liliental-Weber, Z., and Walukiewicz, W. (1995). Native point defects in low-temperature-grown GaAs. *Appl. Phys. Lett.*, 67(2):279.

[Loehr and Manasreh, 1993] Loehr, J. P. and Manasreh, M. O. (1993). *Semiconductor quantum wells and superlattices for long-wavelength infrared detectors*, pages 37–40. Artech House, Boston, MA.

[Lucena et al., 2008] Lucena, R., Aguilera, I., Palacios, P., Wahnón, P., and Conesa, J. (2008). Synthesis and Spectral Properties of Nanocrystalline V-Substituted In2S3, a Novel Material for More Efficient Use of Solar Radiation. *Chem. Mater.*, 20(16):5125–5127.

[Luque, 1989] Luque, A. (1989). *Solar Cells and Optics for Photovoltaic Concentration*. The Adam Hilger Series on Optics and Optoelectronics. Adam Hilger, Bristol.

[Luque, 2001] Luque, A. (2001). Photovoltaic markets and costs forecast based on a demand elasticity model. *Prog. Photovolt: Res. Appl.*, 9:303–312.

[Luque et al., 2012a] Luque, A., Linares, P. G., Antolín, E., Ramiro, I., Farmer, C. D., Hernández, E., Tobías, I., Stanley, C. R., and Martí, A. (2012a). Understanding the operation of quantum dot intermediate band solar cells. *J. Appl. Phys.*, 111:044502.

[Luque et al., 2010a] Luque, A., Linares, P. G., Antolín, E. Cánovas, E., Farmer, C., Stanley, C., and Martí, A. (2010a). Multiple levels in intermediate band solar cells. *Appl. Phys. Lett.*, 96:013501.

[Luque et al., 2003] Luque, A., Martí, A., and Cuadra, L. (2003). Impact-ionization-assisted intermediate band solar cell. *IEEE Trans. Electron Devices*, 50(2):447–454.

[Luque et al., 2008] Luque, A., Marti, A., Mendes, M. J., and Tobias, I. (2008). Light absorption in the near field around surface plasmon polaritons. *J. Appl. Phys.*, 104(11).

[Luque and Martí, 1997a] Luque, A. and Martí, A. (1997a). Entropy production in photovoltaic conversion. *Phys. Rev. B*, 55(11):6994–6999.

[Luque and Martí, 1997b] Luque, A. and Martí, A. (1997b). Increasing the efficiency of ideal solar cells by photon induced transitions at intermediate levels. *Phys. Rev. Lett.*, 78(26):5014–5017.

[Luque and Martí, 2001] Luque, A. and Martí, A. (2001). A metallic intermediate band high efficiency solar cell. *Prog. Photovolt: Res. Appl.*, 9(2):73–86.

[Luque and Martí, 2010a] Luque, A. and Martí, A. (2010a). On the Partial Filling of the Intermediate Band in IB Solar Cells. *IEEE Trans. Electron Devices*, 57(6):1201–1207.

[Luque and Martí, 2010b] Luque, A. and Martí, A. (2010b). The Intermediate Band Solar Cell: progress toward the realization of an attractive concept. *Adv. Mater.*, 22:160–174.

[Luque et al., 2011a] Luque, A., Martí, A., Antolín, E., Linares, P., Tobías, I., and Ramiro, I. (2011a). Radiative thermal escape in intermediate band solar cells. *AIP Adv.*, 1(2):022125.

[Luque et al., 2010b] Luque, A., Martí, A., Antolín, E., and Linares, P. G. (2010b). Intraband absorption for normal illumination in quantum dot intermediate band solar cells. *Sol. Energy Mat. Sol. Cells*, 94:20322035.

[Luque et al., 2011b] Luque, A., Martí, A., Antolín, E., Linares, P. G., Tobías, I., Ramiro, I., and Hernandez, E. (2011b). New Hamiltonian for a better understanding of the quantum dot intermediate band solar cells. *Sol. Energy Mat. Sol. Cells*, 95(8):2095–2101.

[Luque et al., 2006a] Luque, A., Martí, A., Antolín, E., and Tablero, C. (2006a). Intermediate bands versus levels in non-radiative recombination. *Physica B*, 382(2):320–327.

[Luque et al., 2000] Luque, A., Martí, A., and Cuadra, L. (2000). High efficiency solar cell with metallic intermediate band. *Proc. of the 28th IEEE Photovoltaic Specialists Conference (PVSC), Glasgow, UK.*

[Luque et al., 2002] Luque, A., Martí, A., and Cuadra, L. (2002). Thermodynamics of solar energy conversion in novel structures. *Physica E*, 14(1-2):107–114.

[Luque et al., 2005] Luque, A., Martí, A., López, N., Antolín, E., Cánovas, E., Stanley, C., Farmer, C., Caballero, L. J., Cuadra, L., and Balenzategui, J. L. (2005). Experimental analysis of the quasi-Fermi level split in quantum dot intermediate-band solar cells. *Appl. Phys. Lett.*, 87(8):083505.

[Luque et al., 2006b] Luque, A., Martí, A., López, N., Antolín, E., Cánovas, E., Stanley, C. R., Farmer, C., and Díaz, P. (2006b). Operation of the intermediate band solar cell under nonideal space charge region conditions and half filling of the intermediate band. *Journal of Applied Physics*, 99(1):094503.

[Luque et al., 2004] Luque, A., Martí, A., Stanley, C., López, N., Cuadra, L., Zhou, D., and Mc-Kee, A. (2004). General equivalent circuit for intermediate band devices: potentials, currents and electroluminescence. *J. Appl. Phys.*, 96(1):903–909.

[Luque et al., 2012b] Luque, A., Martí, A., and Stanley, C. R. (2012b). Understanding intermediate-band solar cells. *Nat. Photonics*, 6:146–152.

[Luque et al., 1991] Luque, A., Miñano, J. C., Davies, P., Terrón, M. J., Tobías, I., Sala, G., Alonso, J., and Oliva, J. (1991). Angle-limited cavities for silicon solar cells. *Conference Record of the 22nd IEEE Photovoltaic Specialists Conference, Las Vegas, Nevada, U.S.A.*, 1:99–104.

[Madelund et al., 1986] Madelund, O., von der Osten, W., and Rössler, U. (1986). *Semiconductors: Intrinsic Properties of Group IV Elements and III-V, II-VI and I-VII Compounds*, volume 22 of *Landolt-Börnstein, Numerical Data and Functional Relationships in science and technology, New Series*, chapter 2, pages 52–159. Springer-Verlag, Berlin.

[Marsen et al., 2010] Marsen, B., Steinkopf, L., Singh, A., Wilhelm, H., Lauermann, I., Unold, T., Scheer, R., and Schock, H.-W. (2010). Effects of Ti-incorporation in CuInS2 solar cells. *Sol. Energy Mat. Sol. Cells*, 94(10):1730 – 1733.

[Martí et al., 2008a] Martí, A., Antolín, E., Cánovas, E., Linares, P. G., and Luque, A. (2008a). Light management issues in intermediate band solar cells. *Proc. of the Material Research Society Spring Meeting, San Francisco, USA*, 1101E:KK06–02.

[Martí et al., 2008b] Martí, A., Antolín, E., Cánovas, E., López, N., Linares, P., Luque, A., Stanley, C., and Farmer, C. (2008b). Elements of the design and analysis of quantum-dot intermediate band solar cells. *Thin Solid Films*, 516(20):6716–6722.

[Martí et al., 2009] Martí, A., Antolín, E., Linares, P. G., Cánovas, E., Marrón, D. F., Tablero, C., Mendes, M., Mellor, A., Tobías, I., Levy, M. Y., Hernández, E., Luque, A., Farmer, C. D., Stanley, C. R., Campion, R. P., Hall, J. L., Novikov, S. V., Foxon, C. T., Scheer, R., Marsen, B., Schock, H. W., Picault, M., and Chaix, C. (2009). IBPOWER: Intermediate band materials and solar cells for photovoltaics with high efficiency and reduced cost. *Conference Record of the 34th IEEE Photovoltaic Specialists Conference, Philadelphia, USA*, pages 002486–002491.

[Martí et al., 2012] Martí, A., Antolín, E., Linares, P. G., and Luque, A. (2012). Understanding experimental characterization of intermediate band solar cells. *J. Mater. Chem.*, 22:22832–22839.

[Martí et al., 2006a] Martí, A., Antolín, E., Stanley, C. R., Farmer, C. D., López, N., Díaz, P., Cánovas, E., Linares, P. G., and Luque, A. (2006a). Production of Photocurrent due to Intermediate-to-Conduction-Band Transitions: A Demonstration of a Key Operating Principle of the Intermediate-Band Solar Cell. *Phys. Rev. Lett.*, 97(24):247701.

[Martí et al., 2003] Martí, A., Cuadra, A., and Luque, A. (2003). Intermediate-band solar cells. In Martí, A. and Luque, A., editors, *NEXT GENERATION PHOTOVOLTAICS: High Efficiency through Full Spectrum Utilization*, Series in Optics and Optoelectronics, chapter 7. Institute of Physics Publishing, Bristol.

[Martí et al., 2000] Martí, A., Cuadra, L., and Luque, A. (2000). Quantum dot intermediate band solar cell. *Proc. of the 28th IEEE Photovoltaic Specialists Conference (PVSC), Glasgow, UK*, pages 940–943.

[Martí et al., 2001] Martí, A., Cuadra, L., and Luque, A. (2001). Partial filling of a quantum dot intermediate band for solar cells. *IEEE Trans. Electron Devices*, 48(10):2394–2399.

[Martí et al., 2002] Martí, A., Cuadra, L., and Luque, A. (2002). Design constraints of the quantum-dot intermediate band solar cell. *Physica E*, 14:150–157.

[Martí et al., 2007] Martí, A., López, N., Antolín, E., Cánovas, E., Luque, A., Stanley, C. R., Farmer, C. D., and Díaz, P. (2007). Emitter degradation in quantum dot intermediate band solar cells. *Appl. Phys.Lett.*, 90(23):233510.

[Martí et al., 2008c] Martí, A., Marrón, D. F., and Luque, A. (2008c). Evaluation of the efficiency potential of intermediate band solar cells based on thin-film chalcopyrite materials. *J. Appl. Phys.*, 103(073076).

[Martí et al., 2006b] Martí, A., Stanley, C. R., and Luque, A. (2006b). Intermediate Band Solar Cells (IBSC) using nanotechnology. In Soga, T., editor, *Nanostructured Materials for Solar Energy Conversion*, chapter 17, pages 539–566. Elsevier, Amsterdam.

[Martí et al., 2008d] Martí, A., Tablero, C., Antolín, E., Luque, A., Campion, R., Novikov, S., and Foxon, C. (2008d). Potential of Mn doped In1-xGaxN for implementing intermediate band solar cells. *Sol. Energy Mat. Sol. Cells*, 93:641–644.

[Mellor et al., 2011] Mellor, A., Tobías, I., Martí, A., Mendes, M., and Luque, A. (2011). Upper limits to absorption enhancement in thick solar cells using diffraction gratings. *Prog. Photovolt: Res. Appl.*

[Mendes et al., 2009] Mendes, M., Luque, A., Tobías, I., and Martí, A. (2009). Plasmonic light enhancement in the near-field of metallic nanospheroids for application in intermediate band solar cells. *Appl. Phys. Lett.*, 95:071105.

[Messiah, 1960] Messiah, A. (1960). *Mécanique Quantique*. Dunod, Paris.

[Missous, 1995] Missous, M. (1995). Stoichiometric low temperature gaas and algaas: A reflection high energy electron diffraction study. *J. Appl. Phys.*, 78(7):4467–4471.

[Missous, 1996] Missous, M. (1996). Stoichiometric low temperature (slt) gaas and algaas grown by molecular beam epitaxy. *Microelectron. J.*, 27(4-5):393–409.

[Olea et al., 2008] Olea, J., Toledano-Luque, M., Pastor, D., González-Díaz, G., and Mártil, I. (2008). Titanium doped silicon layers with very high concentration. *J. Appl. Phys.*, 104(1):016105.

[Oshima et al., 2008] Oshima, R., Takata, A., and Okada, Y. (2008). Strain-compensated InAs/GaNAs quantum dots for use in high-efficiency solar cells. *Appl. Phys. Lett.*, 93(8):083111.

[Palacios et al., 2007] Palacios, P., Sánchez, K., Conesa, J. C., Fernández, J. J., and Wahnón, P. (2007). Theoretical modelling of intermediate band solar cell materials based on metal-doped chalcopyrite compounds. *Thin Solid Films*, 515(15):6280–6284.

[Popescu et al., 2008] Popescu, V., Bester, G., Hanna, M. C., Norman, A. G., and Zunger, A. (2008). Theoretical and experimental examination of the intermediate-band concept for strain-balanced (In,Ga)As/Ga(As,P) quantum dot solar cells. *Phys. Rev. B*, 78:205321.

[Pravettoni et al., 2010] Pravettoni, M., Galleano, R., Dunlop, E., and Kenny, R. (2010). Characterization of a pulsed solar simulator for concentrator photovoltaic cell calibration. *Meas. Sci. Technol.*, 21:115901.

[Reyna et al., 1998] Reyna, R. F., Martí, A., and Maroto, J. C. (1998). Determination of the origin of the series resistance through electroluminescence measurements of GaAs and $Al_xGa_{1-x}As$ solar cells and LEDs. *Solid-State Electronics*, 42(4):567–571.

[Sala and Antón, 2011] Sala, G. and Antón, I. (2011). *Handbook of Photovoltaic Science and Engineering (2nd Edition)*, chapter Photovoltaic Concentrators, pages 402–451. Wiley.

[Shan et al., 1999] Shan, W., Walukiewicz, W., Ager, J. W., Haller, E. E., Geisz, J. F., Friedman, D. J., Olson, J. M., and Kurtz, S. R. (1999). Band Anticrossing in GaInNAs Alloys. *Phys. Rev. Lett.*, 82(6):1221.

[Shockley and Queisser, 1961] Shockley, W. and Queisser, H. J. (1961). Detailed balance limit of efficiency of p-n junction solar cells. *J. Appl. Phys.*, 32:510–519.

[Strandberg and & Reenaas, 2010] Strandberg, R. and & Reenaas, T. W. (2010). Limiting efficiency of intermediate band solar cells with spectrally selective reflectors. *Appl. Phys. Lett.*, 97(3):031910.

[Strandberg and Worren, 2009] Strandberg, R. and Worren, T. W. (2009). Photofilling of intermediate bands. *J. Appl. Phys.*, 105:124512–8.

[Stranski and Krastanov, 1939] Stranski, I. N. and Krastanov, L. v. (1939). *Akad. Wiss. Lit. Mainz Math. Natur. KI IIb*, 146(797).

[Sturcbecher and Larue, 1994] Sturcbecher, J. and Larue, J. (1994). The mini-flasher: a solar array test system. *Sol. Energy Mat. Sol. Cells*, 36:91–98.

[Sugawara, 1999] Sugawara, M. (1999). *Self-assembled InGaAs/GaAs quantum dots*, volume 60 of *Semiconductors and Semimetals*. Academic Press, San Diego.

[Swanson, 2003] Swanson, R. M. (2003). Photovoltaic Concentrators. In Luque, A. and Hegedus, S., editors, *Handbook of Photovoltaic Science and Engineering*, chapter 11, pages 449–503. Wiley.

[Tablero, 2009] Tablero, C. (2009). Quantum dot energy levels and spectrum for different geometries. *J. Appl. Phys.*, 106(7):074306.

[Tablero and Fuertes Marrón, 2010] Tablero, C. and Fuertes Marrón, D. (2010). Analysis of the Electronic Structure of Modified CuGaS2 with Selected Substitutional Impurities: Prospects for Intermediate-Band Thin-Film Solar Cells Based on Cu-Containing Chalcopyrites. *J. Phys. Chem. C*, 114(6):2756–2763.

[Taguchi et al., 1990] Taguchi, M., Tanaka, M., Matsuyama, T., and et al. (1990). Improvement of the Conversion Efficiency of Polycrystalline Silicon Thin Film Solar Cell. *Proc. of the 5th International Photovoltaic Solar Energy Conference, Kyoto, Japan*, pages 689–692.

[Tanaka et al., 1992] Tanaka, M., Taguchi, M., Matsuyama, T., Sawada, T., Tsuda, S., Nakano, S., Hanafusa, H., and Kuwano, Y. (1992). Development of New a-Si/c-Si Heterojunction Solar Cells: ACJ-HIT (Artificially Constructed Junction-Heterojunction with Intrinsic Thin-Layer). *Jpn. J. Appl. Phys.*, 31:3518–3522.

[Thompson and Woolley, 1967] Thompson, A. G. and Woolley, J. C. (1967). Energy-gap variation in mixed III-V alloys. *Can. J. Phys.*, 45:255–261.

[Tobías et al., 2008] Tobías, I., Luque, A., and Martí, A. (2008). Light intensity enhancement by diffracting structures in solar cells. *J. Appl. Phys.*, 104(3):034502.

[Tobías et al., 2011] Tobías, I., Luque, A., and Martí, A. (2011). Numerical modeling of intermediate band solar cells. *Semicond. Sci. Technol.*, 26(3):014031.

[Tomić, 2010] Tomić, S. (2010). Intermediate-band solar cells: Influence of band formation on dynamical processes in InAs/GaAs quantum dot arrays. *Phys. Rev. B*, 82:195321.

[Tomić et al., 2011] Tomić, S., Martí, A., Antolín, E., and Luque, A. (2011). On inhibiting auger intraband relaxation in inas/gaas quantum dot intermediate band solar cells. *Appl. Phys. Lett.*, 99(5):053504.

[Tsunomura et al., 2009] Tsunomura, Y., Yoshimine, Y., Taguchi, M., Baba, T., Kinoshita, T., Kanno, H., Sakata, H., Maruyama, E., and Tanaka, M. (2009). Twenty-two percent efficiency HIT solar cell. *Sol. Energy Mat. Sol. Cells*, 93:670–673.

[Ustinov et al., 2000] Ustinov, V. M., Zhukov, A. E., Kovsh, A. R., Maleev, N. A., Mikhrin, S. S., Tsatsul'nikov, A. F., Maximov, M. V., Volovik, B. V., Bedarev, D. A., Kop'ev, P. S., Alferov, Z. I., Vorob'ev, L. E., Firsov, D. A., Suvorova, A. A., Soshnikov, I. P., Werner, P., Ledentsov, N. N., and Bimberg, D. (2000). Long-wavelength emission from self-organized InAs quantum dots on GaAs substrates. *Microelectron. J.*, 31(1):1 – 7.

[Van de Walle, 1989] Van de Walle, C. (1989). Band lineups and deformation potentials in the model-solid theory. *Phys. Rev. B*, 39:1871–1883.

[van Roosbroeck and Shockley, 1954] van Roosbroeck, W. and Shockley, W. (1954). Photon-Radiative Recombination of Electrons and Holes in Germanium. *Phys. Rev.*, 94:1558.

[Varshni, 1967] Varshni, Y. (1967). Temperature dependence of the energy gap in semiconductors. *Physica*, 34:149–154.

[Vurgaftman and Meyer, 2003] Vurgaftman, I. and Meyer, J. R. (2003). Band parameters for nitrogen-containing semiconductors. *J. Appl. Phys.*, 94:3675–3696.

[Vurgaftman et al., 2001] Vurgaftman, I., Meyer, J. R., and Ram-Mohan, L. R. (2001). Band parameters for III-V compound semiconductors and their alloys. *J. Appl. Phys.*, 89:5815–5875.

[Wahnón and Tablero, 2002] Wahnón, P. and Tablero, C. (2002). Ab initio electronic structure calculations for metallic intermediate band formation in photovoltaic materials. *Phys. Rev. B*, 65(16):165115.

[Walukiewicz et al., 1979] Walukiewicz, W., Lagowski, L., Jastrzebski, L., Lichtensteiger, M., and Gatos, H. C. (1979). Electron Mobility and Free carrier absortion in GaAs: Determination of the Compensation Ratio. *J. Appl. Phys.*, 50(2):899–908.

[Weiming et al., 2009] Weiming, W., S., L. A., and Phillips, J. D. (2009). Intermediate-band photovoltaic solar cell based on ZnTe:O. *Appl. Phys. Lett.*, 95(1):011103.

[Wolf, 1960] Wolf, M. (1960). Limitations and possibilities for improvements of photovoltaic solar energy converters. Part I. Considerations for earth's surface operation. *Proc. IRE*, 48:1246–1263.

[Wu et al., 2002] Wu, J., Shan, W., and Walukiewicz, W. (2002). Band Anticrossing in highly mismatched III-V semiconductor alloys. *Semicond. Sci. Technol.*, 17(6):860–869.

[Yu et al., 2006] Yu, K. M., Walukiewicz, W., III, J. W. A., Bour, D., Farshchi, R., Dubon, O. D., Li, S. X., Sharp, I. D., and Haller, E. E. (2006). Multiband GaNAsP quaternary alloys. *Appl. Phys. Lett.*, 88(9):092110.

[Zhang et al., 2010] Zhang, Y. M., Evans, J. R. G., and Yang, S. (2010). The prediction of solid solubility of alloys: developments and applications of Hume-Rotherys rules. *J. Cryst. Phys. Chem*, 1(2):103–119.

[Zhao et al., 2005] Zhao, L. X., Staddon, C. R., Wang, K. Y., Edmonds, K. W., Campion, R. P., Gallagher, B. L., and Foxon, C. T. (2005). Intrinsic and extrinsic contributions to the lattice parameter of GaMnAs. *Appl. Phys. Lett.*, 86(7):071902.

[Zhou et al., 2010] Zhou, D., Vullum, P. E., Sharma, G., Thomassen, S. F., Holmestad, R., Reenaas, T. W., and Fimland, B. O. (2010). Positioning effects on quantum dot solar cells grown by molecular beam epitaxy. *Appl. Phys. Lett.*, 96(8):083108.